Observations and inhomogeneity in cosmology

Peter Smale

Department of Physics and Astronomy

University of Canterbury

A thesis submitted for the degree of

Doctor of Philosophy

February 16, 2012

I would like to dedicate this thesis to my loving parents ...

"Just be quiet. My mind is very clear today. So then, what is time?" Hans Castorp asked, bending the tip of his nose so forcefully to one side that it turned white and bloodless. "Will you please tell me that? We perceive with our senses, with vision and touch. But what is the organ for our sense of time? Would you please tell me that? You see, you're stuck. But how are we ever going to measure something about which, precisely speaking, we know nothing at all — cannot list a single one of its properties. We say time passes. Fine, let it pass for all I care. But in order to measure it ...no, wait! In order for it to be measurable, it would have to flow *evenly*, but where is it written that it does that? It doesn't do that for our conscious minds, we simply assume it does, just for the sake of convenience. And so all our measurements are merely conventions, if you please."

Thomas Mann, *The Magic Mountain*, Woods transl.

Acknowledgements

"More servants wait on man than he'll take notice of" – George Herbert

This thesis would not have been possible without the creative spirit and giddying attention to detail of my supervisor David Wiltshire.

Teppo Mattsson made detailed comments on the drafts.

I am grateful for the hospitality of Rick Watkins in Salem, Oregon, USA, and for the COMPOSITE peculiar velocity survey he gave me. This is something I could, and perhaps will, look at for the rest of my life, and never understand.

This work was funded by a University of Canterbury Doctoral Scholarship and the Marsden Fund Council from Government funding, administered by the Royal Society of New Zealand.

It has been a privilege to share an office with Cheng-Yang Lee, Dimitri Schritt, and Ewan Orr (in order from the window to the door). Thanks for all the discussion, distraction and inspiration.

I would also like to acknowledge the support of Jenni Adams, Dharamvir Ahluwalia, and Amanda Ball.

I would like to acknowledge the support of the Department of Physics and Astronomy.

Finally, I wish to acknowledge the unflinching support of my parents, without which I would have achieved nothing.

Abstract

We interpret distance measurements from nearby galaxies, type Ia supernovae, and gamma-ray bursts in the light of a cosmological model that incorporates a spatial averaging technique to account for the inhomogeneous distribution of structure in the late-epoch Universe and the consequent importance of the location of the observer. In the timescape cosmology it is suggested that dark energy is a misidentification of gravitational energy gradients—and consequently of the relative calibration of clocks and rulers—in a complex inhomogeneous structure. This model is consistent with the current supernova and gamma-ray burst data within the limits imposed by our understanding of the systematic uncertainties, to the extent that a Bayesian model comparison with the standard model yields a preference for the timescape model that is "not worth more than a bare mention". In the spirit of the timescape model, of attempting to understand the astrophysics with as few cosmological assumptions as possible, we perform a model-independent analysis of galaxy distances in the local Universe. We find that the rest frame of the Local Group provides a more uniform Hubble expansion field than the rest frame of the CMB. We find that the dipole in the Hubble expansion field coincides with the dipole in the CMB temperature with a correlation coefficient of -0.92, and that this pattern is induced within $60\,h^{-1}$ Mpc, provided the variation in the distance-redshift relation due to the formation of structure is taken into account.

Contents

List of Figures

Chapter 1

Introduction

1.1 "A shot heard around the world"

> *One of the greatest challenges of theoretical physics is to simultaneously entertain multiple visions of how nature could be even if some of them are radical or mutually incompatible, and keep track of what we actually know and how we know it.*
>
> Doug Finkbeiner, comment on Cosmic Variance weblog[1], October 29, 2009

> *...it is not being totally facetious to say that any model that fits all the observational data at any time is probably wrong because, at any given time, at least some of the data are likely to be wrong.*
>
> Coles and Ellis (1997) *Is the Universe Open or Closed?* p. 123

Cosmology underwent a sea-change towards the end of the twentieth century with the advent of high-precision measurements that established cosmology as an empirical, as well as a theoretical, science. This "golden age" could perhaps be said to have begun with the large-scale redshift survey undertaken by the Center for Astronomy at Harvard between 1977 and 1982 (Huchra et al., 1983). These surveys are continuing currently. In early 2011, the Sloan Digital Sky Survey (SDSS), for example, had produced 3-dimensional maps of a quarter of the sky and contained 930,000 galaxies and 120,000 quasars[2]. These observations

[1] `http://blogs.discovermagazine.com/cosmicvariance/2009/10/28/has-fermi-seen-new-evidence-for-dark-matter/`

[2] `http://www.sdss.org/`

of the late Universe are complemented by high-precision satellite measurements of the tiny temperature anisotropies in the cosmic microwave background (CMB) radiation, made initially by the COBE satellite in 1995, by the WMAP satellite until 2011, and continuing with the PLANCK satellite launched in May 2009.

Unsurprisingly, as sufficiently precise measurements accumulated, the conventional cosmological models began to be called into question. Some contenders could be definitively ruled out. For argument's sake, we can take modern cosmology to have begun with the publication of Einstein's theory of general relativity in 1915. In these early years, because of the difficulty of making astronomical measurements, cosmology was a theoretical science, with only a few established empirical constraints, and therefore strongly determined by considerations of mathematical aesthetics and utility. It is nevertheless a beautiful fact that just a few minimal, natural assumptions about the Universe are sufficient, via the machinery of general relativity, to yield a picture of the Universe that could be said to be true, at least within the constraints imposed by what could actually be observed of the Universe during most of the twentieth century (e.g. Wald (1984), Chapter 5). As astronomical techniques have developed, however, the gradual unfolding of the cosmos before the eyes of astronomers has revealed a succession of phenomena whose implications have profoundly changed the human view of the world and the place of humans in it.

Cosmology in a nutshell The early years of the twentieth century saw general relativity set Newtonian mechanics in its rightful cosmological place, and established the possible geometries of the Universe as a whole. In 1912, Vesto Slipher discovered the redshifts of galactic spectral lines. The redshifts were interpreted by Hubble in 1929 as being due to their recessional velocities, and could then be understood as having their origin in the expansion of space. A Universe that is expanding now was smaller in the past, and therefore denser, therefore hotter. The gradual apprehension of this fact began with the work of Alpher, Gamow, Herman and Dicke in the 1940s, to be vindicated by the discovery of the microwave background radiation in 1965 by Penzias and Wilson. Cosmologists now knew, beyond a shadow of a doubt, that the Universe evolves. An invisible "dark matter" was invoked by Fritz Zwicky in the early 1930s to explain a mass deficit calculated from the rotations of galaxies in clusters. In the

1970s a corresponding deficit was found in galactic rotation curves by Vera Rubin. Cosmic evolution could then be described by a Friedmann-Lemaître-Robertson-Walker (FLRW) geometry, in which the rate of cosmic expansion is governed by an energy density comprising contributions from radiation, luminous matter and cold dark matter (CDM). In keeping with the guiding principle of mathematical utility then, the energy density of the Universe, which "tells space how to curve"[1], was held to be critical, making space flat on the largest scales. In mathematical terms, since the radiation density today is negligible in comparison with the matter densities, a spatially flat Universe is represented by the fact that the present values of the dimensionless energy densities sum to one: $\Omega_{\rm b} + \Omega_{\rm dm} \equiv \Omega_{\rm m} = 1.0$. The flatness of the Universe is a puzzle: signals have not had enough time, given our best-fit age of the Universe, to bring regions of the sky at large angular separations to their observed thermal equilibrium. In the 1980s, Alan Guth suggested that an early phase of cosmological inflation could explain why the cosmic microwave background is so uniform across the sky.

In the early 1990s, galaxy clustering statistics suggested a less-than-critical matter density (Maddox et al., 1990): clustering of galaxies is not as strong as that predicted by the standard CDM model. This was an early indication that $\Omega_{\rm m} < 1.0$, but at the time there was a possibility that this result was a statistical artifact. In 1995, the COBE satellite found tiny fluctuations in the otherwise smooth microwave sky. The new science of CMB physics yielded a comprehensive picture of the evolution of the Universe from inflation until the epoch of recombination, when the Universe became transparent to light. In this picture, quantum fluctuations were stretched by inflation to super-horizon scales. The resulting density contrasts in the primordial plasma were enhanced by acoustic oscillations. Once recombination "froze in" the oscillations at particular phases, the photons were free to stream out across the Universe and be redshifted by the expansion of space to become the microwave background that we see today. Luminous matter, the "baryons" could then fall into the potential wells generated by the clumped CDM, eventually to produce the large-scale structure that we see in the galaxy-redshift surveys. The power spectrum of the temperature

[1] "Matter tells space how to curve. Space tells matter how to move." John Archibald Wheeler (1911–2008)

anisotropies in the CMB can be explained by just a handful of parameters—six in the simplest model. For example, the location of the first peak in the power spectrum of the intrinsic temperature anisotropies tells us that the energy density is critical: $\Omega_{\rm tot} = 1$.

In the late 1990s came the "shot heard around the world"[1] the anomalous excess dimming of type Ia supernovae (SNe Ia) out to redshifts of ~ 1 gave observational evidence for an accelerated cosmic expansion that could only be accommodated in a FLRW framework if $\Omega_{\rm m} < 1.0$, requiring $\Omega_\Lambda \neq 0$ to keep space flat. A "dark energy" density $\Omega_\Lambda \simeq 0.7$ explains both the SNe Ia results and those from the CMB and the small-scale matter power spectrum. Subsequent SN Ia surveys have confirmed this result—the shot continues to resound[2].

This is where we stand today. In the light of these observations, the current cosmological standard model is a spatially flat FLRW universe whose energy density comprises, roughly, 70% dark energy, 25% dark matter, with just 5% baryonic matter. Dark energy can be represented in the Einstein equations by the cosmological constant, and its origin is a mystery. Having established that its density is nonzero, however, current observational programmes aim to determine its equation of state, and whether it is in fact constant, or whether it varies with time ("quintessence").

What is dark energy? We should clarify what we mean here by the name "dark energy", because it is easily misunderstood. The central idea is that it is something hitherto unknown to physics, so rather than thinking of it as a *substance*—whether fluid or energy—it is better just to think of it as a name for the phenomenon of cosmic acceleration, no more, no less. It *may* be vacuum fluctuations, or it *may* be some sort of scalar field; these are possibilities that can so far be neither confirmed nor ruled out. It *may* also be the case that the anomalous acceleration indicated by the supernovae is in some way an artifact of matter

[1] Kirshner (2009) uses this phrase in an analogy with the assassination of the Archduke Ferdinand that led to the first World War.

[2] On October 4, Saul Perlmutter, of Lawrence Berkeley National Laboratories, Brian Schmidt at ANU, and Adam Riess from Johns Hopkins University were jointly awarded the 2011 Nobel prize in physics for leading the teams responsible for the discovery of cosmic acceleration and the advent of supernova cosmology.

inhomogeneities that are unaccounted for in the standard model. This possibility has the attractive feature that it does not require that 70% of the Universe is something *completely unknown* to physics. A complete physical treatment of the Universe should ideally incorporate general relativity on all scales. Observations of anomalously large bulk flows on scales of $100\,h^{-1}$ Mpc suggest that the standard conception of small-scale peculiar velocities superimposed on large-scale Hubble expansion may be too simplistic. Could the assumption of a Euclidean space on large scales produce conclusions as profound as that the expansion of the Universe is accelerating?

The inhomogeneous "timescape" cosmological model of Wiltshire (2007) suggests just this: the accelerated expansion is an *apparent* effect brought about by the inhomogeneous matter distribution. More precisely, it comes about because of the assumption that the clocks and rulers of real observers located in matter overdensities record the same times and distances as those of hypothetical observers in volume-average locations, which, in a Universe dominated by voids, will be relatively underdense. In other words, we assume that we are volume-average observers, when we are not. The relativistic effects of density contrasts on scales larger than galaxies may be small, but the increasing differentiation of structure has been operating over cosmological periods of time, leading to potentially significant mis-calibration. There is no single global time, except in some average sense.

How can we test this possibility? We cannot physically put a clock into a void[1]. The only way to test the model is against current observations. In particular, does the timescape relationship between redshift and distance match observations, especially observed supernova distances, which, compared to other distance measures, are relatively reliable over significant distances?

Type Ia supernovae (SNe Ia) provide an unprecedented opportunity to study the expansion of the Universe in detail, not only because they yield precise distances, but they also probe the redshift range over which the universe began to accelerate, which is also the range over which large scale structure formation became non-linear.

[1]Even traveling for 1000 years at the speed of light in a direction perpendicular to the plane of the galaxy would barely take a spacecraft out of the disk of the Milky Way.

Distance measurements are the key to cosmology. Given an age and a separation we can infer velocities and accelerations, but we are still limited to an incomplete snapshot of the Universe as a whole: the view out along the past light cone. General relativity gives us a framework for theorizing about the universe off the past light cone, and provides several different definitions of distance. We cannot measure directly what we consider to be distances in the everyday sense on scales beyond the Milky Way, within which we can determine parallax distances to stars. We rely on standard candles to give distances even to our nearest extra-galactic neighbours, the Magellanic clouds. To properly interpret the standard candle observations we need to properly understand the physics of the light source. Even for SNe Ia, despite the underlying simplicity of the underlying physics, systematic uncertainties such as progenitor composition and evolution still severely constrain the precision of measurements, which in turn limits the extent to which they can be used to distinguish between different cosmological scenarios.

This thesis looks at some current samples of cosmological distance indicators in the light of the timescape model, and discusses some of the questions that the timescape model seeks to address. In the next section, the theoretical underpinnings of the ΛCDM model are discussed with the aim of deriving an expression for the redshift-distance relationship and establishing the terms of the standard cosmological model. Chapter 2 will do the same for the timescape model. Chapters 3 and 4 will use these distance-redshift models to understand observations of SNe Ia and gamma-ray bursts respectively. The last chapter of this study investigates the variability of expansion as observed in the local velocity field. For redshifts much less than one, we conventionally assume that the Hubble law of the recessional velocities of galaxies is purely linear and that there exists a single value of the Hubble constant H_0. On this basis, cosmic expansion can be "subtracted out" of the observed recession velocities, leaving us with the "peculiar velocities" of the galaxies induced by nearby density fluctuations. What can we say about "local flows" without these assumptions, which assume the instantaneous action of Newtonian gravity? We conclude with a summary of results, and a discussion about the status of the timescape model as the this "golden age" of observational cosmology looks set to continue, in particular with the square kilometre array

(SKA) of radio telescopes, which will enable wide-area surveys of unprecedented depth and precision[1].

We begin with a discussion of the theoretical background to distance measurements in cosmology. The essence is that we live in a universe that is expanding from an initial state of high energy and density, in which uniformity has given way to irregularity on small scales through the process of gravitational collapse. Much of the complication of the various models of large-scale structure formation lies in the "middle ground" tension between cosmic expansion on the largest scales and gravitational collapse below the supercluster scale.

1.2 ΛCDM: the cosmological standard model

The Copernican principle asserts that we do not occupy a position in the Universe which is unusual in any way. By this principle, any hypothetical observer should see a universe that looks similar to the one we see. This philosophical assumption has a stronger mathematical counterpart upon which modern cosmology is based. Neglecting local perturbations, the Universe is homogeneous and isotropic. The homogeneity and isotropy of the 3-space in which we live leads (Wald, 1984) to the Friedmann-Lemaitre-Robertson-Walker (FLRW) line element

$$ds^2 = -dt^2 + a^2(t)\left[\frac{dr^2}{1-kr^2} + r^2(d\theta^2 + \sin^2 d\phi^2)\right] \tag{1.1}$$

in spherical coordinates. Here, t is cosmic time and $a(t)$ is the *scale factor*. Despite the very restrictive assumptions of homogeneity and isotropy, eq. (1.1) admits three possible behaviours, parameterized by the value of k. Usually, for clarity, we define (e.g. Padmanabhan (1993), Ch. 2)

$$\chi \equiv \int \frac{dr}{\sqrt{(1-kr^2)}} = \begin{cases} \sin^{-1} r & \text{for } k = 1 \\ r & \text{for } k = 0 \\ \sinh^{-1} r & \text{for } k = -1 \end{cases}, \tag{1.2}$$

[1]It has been said that the SKA will *revolutionize* cosmological studies (Blake et al., 2004). Considering that in the twenty or so years since the advent of galaxy redshift surveys in the late 1980s we have observed $\sim 10^6$ galactic positions (but obtained spectroscopic redshifts for only a subset of these), and that the SKA is forecast to make HI observations of 10^9 galaxies out to $z \lesssim 1.5$ within the first few years of its operation (Rawlings et al., 2004), there is no hyperbole here.

so that the metric becomes

$$ds^2 = -dt^2 + a^2(t)[d\chi^2 + f^2(\chi)(d\theta^2 + \sin^2 d\phi^2)], \tag{1.3}$$

where

$$f(\chi) = \begin{cases} \sin\chi & \text{for } k = 1 \\ \chi & \text{for } k = 0 \\ \sinh\chi & \text{for } k = -1 \end{cases} . \tag{1.4}$$

When $k = 0$, the spatial hypersurface is flat Euclidean 3-space. When $k = 1$, the spatial part of (1.3) is a 3-sphere of radius a. This space is has finite volume but is unbounded. When $k = -1$ the 3-space is a hyperboloid; unbounded and infinite, as in the case of Euclidean flat space. The homogeneity and isotropy of these spaces is expressed by the fact that any point on the submanifold can be mapped to any other point by an appropriate transformation, leaving the metric invariant—all points on the surfaces are physically equivalent.

The constant k and the function $a(t)$ in the FLRW metric can be obtained from Einstein's equations

$$G_{\mu\nu} = R_{\mu\nu} - \frac{1}{2}g_{\mu\nu}R - g_{\mu\nu}\Lambda = 8\pi G T_{\mu\nu} \tag{1.5}$$

given an energy-momentum tensor $T_{\mu\nu}$. The *ideal fluid* energy-momentum tensor follows from the assumptions of homogeneity and isotropy, and has the form

$$T^{\mu}_{\nu} = \text{diag}[-\rho(t), p(t), p(t), p(t)], \tag{1.6}$$

in the rest frame of the fluid. An *equation of state* $p = p(\rho)$ for each of the energy density constituents then completely specifies the nature of the source of energy-momentum. For example, for most of its evolution, a pressureless dust universe contains radiation, for which $p = \rho/3$, and matter, for which $p = 0$. The Λ in (1.5) is the famous and enigmatic cosmological constant, which was introduced by Einstein as a modification to the field equations to ensure a static universe. Later, when it became apparent that the universe really is expanding, he referred to it as his "biggest blunder"[1]. However, Λ has retained its place in the Einstein equations, since the energy density of vacuum quantum fluctuations

[1] Bianchi and Rovelli (2010) give a nuanced interpretation of this statement.

acts like a cosmological constant. The equation of state for such a cosmological constant is $w_\Lambda = p/\rho = -1$. i.e. its density stays the same despite the cosmic expansion. A time-varying cosmological "constant" is known as *quintessence*. Current observations are consistent with a vacuum energy cosmological constant: conservatively, $|1+w_\Lambda| \lesssim 0.2$ (e.g., Kessler et al., 2009; Wood-Vasey et al., 2007).

With the metric defined from equation (1.1), the field equations yield the Friedmann equations which describe the evolution of the universe:

$$\begin{aligned} \left(\frac{\dot{a}}{a}\right)^2 + \frac{k}{a^2} + \frac{\Lambda}{3} &= \frac{8\pi G}{3}\rho, \\ \frac{2\ddot{a}}{a} + \left(\frac{\dot{a}}{a}\right)^2 + \frac{k}{a^2} + \frac{\Lambda}{3} &= -8\pi G p. \end{aligned} \tag{1.7}$$

We call the ratio of $\dot{a}$ to a the *Hubble rate*. i.e.

$$H(t) \equiv \frac{\dot{a}(t)}{a(t)}. \tag{1.8}$$

At the present epoch, we say that $H(t_0) \equiv H_0 \equiv 100\ h$ km s^{-1} Mpc^{-1}, where current measurements indicate that h lies somewhere between 0.65 and 0.75. We will have much to say about the Hubble law, so more detail about its measurement is given in Section 1.3. Since the expansion of the Universe is evident from the redshift of the spectral lines of distant galaxies, we can estimate H_0 using the *Hubble law*

$$z = \frac{H_0}{c} r, \tag{1.9}$$

if we know the (redshift-independent) distance to the galaxy r. In the ΛCDM model, a single Hubble law holds for $z \ll 1$; beyond these redshifts corrections must be made to account for the curvature of space. In Chapter 5 we question the assumption of a single nearby Hubble law, based on the observation that hypothetical observers will determine different average Hubble laws depending on their position within the local large-scale structure.

The present Hubble parameter defines a scale of the Universe, since its inverse gives the *Hubble time*

$$t_H \equiv \frac{1}{H_0} = 9.78\ \times\ 10^9\ h^{-1}\ \text{yr}. \tag{1.10}$$

The *Hubble radius*, the radius of the observable universe, is obtained by multiplying the Hubble time by the speed of light:

$$D_H \equiv \frac{c}{H_0} = 3000\ h^{-1}\ \mathrm{Mpc} = 9.26\ \times\ 10^{25}\ h^{-1}\ \mathrm{m}. \tag{1.11}$$

This is the distance to objects which, due to the Hubble expansion, are today receding from us at the speed of light. Note that this is less than the *particle horizon*, which is given by the maximum distance anything can have travelled since the big bang (in the EdS case, the particle horizon distance is twice the Hubble radius) (Ellis and Rothman, 1993).

With *critical density*

$$\rho_c \equiv \frac{3H_0^2}{8\pi G}, \tag{1.12}$$

the present-epoch Friedmann equations give

$$\frac{k}{a_0^2} = \frac{8\pi G}{3}\rho_0 - H_0^2 \equiv H_0^2(\Omega - 1), \tag{1.13}$$

where the subscript 0 indicates the present-epoch value and $\Omega \equiv (\rho_0/\rho_c)$. If the curvature k given by (1.13) is less than zero, the energy density is less than critical and the universe is open, and expands at an ever increasing rate. If $k > 0$, the universe is closed, and will eventually collapse. If $k = 0$, $\Omega = 1$ and the universe is spatially flat. It continues to expand, but the expansion decelerates. A universe in which the matter density constitutes the entire critical density is called an *Einstein-de Sitter* (EdS) universe. The EdS universe is the simplest model that is consistent with a matter-dominated expanding universe and the assumptions of homogeneity and isotropy.

It is relevant to note that a large empty sub-volume of the Universe will behave like an empty FLRW universe. Its spatial curvature will be negative. The large voids observed in the galaxy distribution should behave like this. Cosmological models with spherical symmetry but with a dust density that varies radially were developed by Lemaitre and Tolman, and later by Bondi (Krasinski, 1997). Although they violate the Copernican principle, these models are useful for describing spherically symmetric averages of variable dust distributions (e.g. Mattsson and Ronkainen, 2008).

The critical density can be represented in different ways:

$$\begin{aligned} \rho_c &= 1.88 \times 10^{-26}\ h^2 \text{ kg m}^{-3} \\ &= 2.8 \times 10^{11}\ h^2\ M_\odot \text{ Mpc}^{-3} \\ &= 7.5 \times 10^{21}\ h^{-1}\ M_\odot\ D_H^{-3}, \end{aligned} \tag{1.14}$$

where $M_\odot$ is the mass of the sun.

Since the energy density determines the time evolution of the metric via Einstein's equations, different FLRW models are distinguished by their energy density components. For calculations it is easiest to turn the energy densities into dimensionless quantities by taking their ratio with the critical density and defining

$$\Omega_{_M} = \rho_0/\rho_c \tag{1.15}$$

and

$$\Omega_\Lambda = \frac{\Lambda c^2}{8\pi G \rho_c}, \tag{1.16}$$

which are often loosely referred to as the "matter density" and the "dark energy density", respectively. The matter density comprises contributions from the dark matter density Ω_{CDM} and the luminous matter density Ω_b, more often referred to as the "baryon" density.

High-precision measurements of the intrinsic temperature variations in the cosmic microwave radiation background favour a spatially flat ΛCDM model in which $\Omega_b = 0.0449 \pm 0.0028$ and $\Omega_{CDM} = 0.222 \pm 0.026$, so that $\Omega_\Lambda = 1 - \Omega_{_M} = 0.734$ (Jarosik et al., 2011). These are roughly the parameter values of the cosmological "Standard model". We wish now to derive a measure of distance in such a flat universe, which contains both matter and dark energy.

A cosmological observation is usually the reception of electromagnetic radiation generated by a distant source. Consider the reception of an electromagnetic pulse by an observer, located at $(t_0, r = 0)$, from a source located at (t_1, r_1). These events are connected in spacetime by a null geodesic which we can take to be radial, so that (1.1) gives

$$0 = dt^2 - a^2(t) dr^2, \tag{1.17}$$

where we have set $k = 0$. Hence,

$$\int_{t_1}^{t_0} \frac{dt}{a(t)} = \int_0^{r_1} dr. \tag{1.18}$$

If the source emits two photons, at t_1 and $t_1 + dt_1$, then these will be received by the observer at times t_0 and $t_0 + dt_0$. Now,

$$\int_0^{r_1} dr \;=\; \int_{t_1}^{t_0} \frac{dt}{a(t)} = \int_{t_1+dt_1}^{t_0+dt_0} \frac{dt}{a(t)}. \tag{1.19}$$

Rearranging the integration limits then gives

$$\int_{t_1}^{t_1+dt_1} \frac{dt}{a(t)} = \int_{t_0}^{t_0+dt_0} \frac{dt}{a(t)}, \tag{1.20}$$

so that

$$\frac{dt_0}{dt_1} = \frac{a(t_0)}{a(t_1)}. \tag{1.21}$$

This means that during the time the radiation takes to travel between source and observer, it will be *redshifted* by the cosmological expansion by an amount

$$(1 + z) \equiv a(t_1)/a(t_0) \tag{1.22}$$

and spread over a spherical surface with area $4\pi a^2(t_0) r_1^2$. If the source has an intrinsic luminosity L, so that in the time interval dt_1 it emits energy $L\ dt_1$, the observer, over the time interval $dt_0 = [a(t_0)/a(t_1)]dt_1$, will measure a flux

$$\begin{aligned} \mathcal{F} &= L\frac{dt_1}{dt_0}\frac{a(t_1)}{a(t_0)}/(4\pi a^2(t_0) r_1^2) \\ &= \frac{L}{4\pi a_0^2 r_1^2}\Big(\frac{a(t_1)}{a_0}\Big)^2 \\ &= \frac{L}{4\pi a_0^2 r_1^2 (1+z)^2}. \end{aligned} \tag{1.23}$$

This flux thereby gives us a means of measuring cosmological distances, given a cosmological model, since it serves to define the *luminosity distance*

$$d_L(z) = a_0 r_1(t_1)(1 + z). \tag{1.24}$$

It turns out that the luminosity distance is simply related to another observable: the *angular diameter distance*. If an object of physical size D subtends an angle δ to the observer, and if δ is small, $D = r_1 a(t_1)\delta = a_0 r_1(t_1)(1+z)^{-1}$, so

$$d_A(z) = a_0 r_1(t_1)(1+z)^{-1} = d_L(z)(1+z)^{-2}. \tag{1.25}$$

To get the source distance r_1, we need to know the functional form of $a(t)$ so that we can use (1.18). We can write this as

$$\int_0^{r_1} dr = \int_{t_1}^{t_0} \frac{dt}{a(t)} = \int_{a_1}^{a_0} \frac{da}{a\dot{a}} \tag{1.26}$$

and substitute for $\dot{a}$ using Einstein's equations, obtaining

$$\int_{a_1}^{a_0} \frac{da}{a\dot{a}} = \int_{(1+z)^{-1}}^{1} \frac{d(a/a_0)}{a_0 H_0 \sqrt{\frac{a_0}{a}\Omega + 1 - \Omega}}. \tag{1.27}$$

In a universe with zero curvature, and neglecting the radiation density (which is several orders of magnitude smaller than the other density components), the luminosity distance is

$$d_L(z) = (1+z)\frac{c}{H_0}\int_0^z \frac{dz}{\sqrt{\Omega_{\rm m}(1+z)^3 + \Omega_\Lambda}}. \tag{1.28}$$

When we discuss the "ΛCDM luminosity distance" elsewhere in this thesis, this is the expression to which we refer.

The connection between the theoretical luminosity distance and the actual distance of an astronomical object is provided by the *distance modulus*, which is defined from the difference between the apparent magnitude of the brightness of an object and its absolute magnitude:

$$m - M \equiv \mu = 5\log\left(\frac{d_L}{10\ \text{pc}}\right), \tag{1.29}$$

or $\mu = 5\log(d_L)+25$ for d_L in Mpc. To determine a distance modulus, we therefore need to understand the physics of a given astronomical object sufficiently to be able to derive an estimate of its absolute magnitude. Such objects are called *standard candles*. Clearly, if two objects with the same absolute magnitude lie at different distances, their apparent magnitudes will be different according to the distance between them.

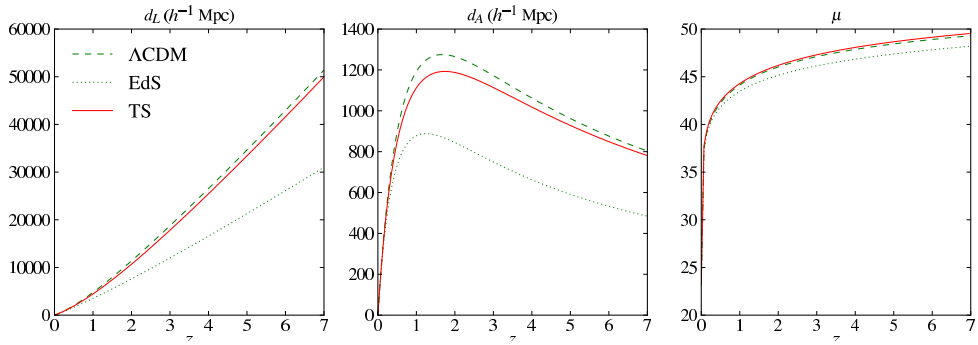

Figure 1.1: Cosmological distance measures: Luminosity distance (left), angular diameter distance, and distance modulus for the spatially flat ΛCDM and EdS, and the TS cosmological models. The parameter values are $H_0 = 71$ km s^{-1} Mpc^{-1}, $\Omega_M = 0.25$ (ΛCDM); $H_0 = 71$ km s^{-1} Mpc^{-1}, $\Omega_M = 1.0$ (EdS); and $\bar{H}_0 = 48.2$ km s^{-1} Mpc^{-1}, $f_{\rm v0} = 0.76$ (TS).

The plots in Fig. 1.1 show the differences between the three measures of distance. The red lines will be explained in Chapter 2. The redshift, on the X-axis, can be measured with great precision spectroscopically—to one part in a thousand or so. The significant measurement uncertainties come about when we try to obtain a redshift-independent distance. It is also clear that the relationship between redshift and distance is model-dependent, although there are similarities in form due to the underlying physics. The luminosity distance, being a distance along the past light cone, always increases with redshift, which makes intuitive sense since more distant objects appear dimmer, and therefore represent a greater intervening distance. The role of dark energy is clear from the difference between the Einstein-de Sitter curve, in which matter makes up the critical density, and the ΛCDM curve, in which the matter density is less than critical, and the remaining density required for flatness is dark energy. Increasing the repulsive dark energy increases the rate of expansion of the Universe, so that a given redshift represents a larger distance.

The angular diameter distance takes the transverse size of an object as the basis for a distance: an object at a redshift of 0.5 will look bigger, and represent a smaller distance, than an object at a redshift at $z = 1$. However, the angular diameter distance is not monotonic with redshift due to the decelerating expansion

of the Universe—see the central panel in Fig. 1.1. A galaxy nearby can appear larger because the distance between it and us is small compared with the Hubble radius. It can also appear large because the distance between it and us was much smaller in the past, when it emitted the light that we now see[1]. There is therefore a redshift at which the angular diameter of an object has a minimum (and where the distance represented by the angular diameter is therefore a maximum). In the EdS model, this redshift is 1.25. With 70% dark energy, this increases to $z_{\rm min} = 1.66$, since the dark energy reduces the deceleration of expansion in the late universe, making the distance to $z_{\rm min}$ larger. It is worth observing that the red lines, depicting Timescape model distances for best-fit parameter values, *look* like accelerated ΛCDM-model distances. The underlying physical interpretation is greatly different, however: briefly, these lines show only *what we observe*, unlike the FLRW models, which claim to represent the true expansion history of the Universe. We will revisit these ideas at the end of Chapter 2 when we have discussed the underpinnings of the timescape model.

The third plot in Fig. 1.1 shows the distance modulus, with magnitudes on the Y-axis. Again, the accelerated cosmic expansion of the ΛCDM model compared to the EdS model means that objects appear dimmer for the same redshift. As we will see in Chapter 3, it was exactly observations of this property from type Ia supernovae, in the redshift range $0.5 < z < 1.5$, which became the "smoking gun" for cosmic acceleration.

We can test a cosmological model by comparing its predictions for the distance-redshift relation with the distances we obtain from standard candles. There are certain fundamental aspects of making observations of objects at cosmological distances that must be accounted for regardless of the model, to do with the fact that we make observations from a single vantage point in space and time. These are known collectively as Malmquist, or Malmquist-like biases (see Teerikorpi, 1997, for a review). The most basic form of Malmquist bias comes about simply because we only register very distant objects if they are bright enough. Hence we observe a larger proportion of brighter objects at greater distances. Secondly, the

[1] In practice, this is not really a degeneracy: a very distant galaxy may have the same angular diameter distance as a nearby one, but it will also be much fainter, with a correspondingly larger luminosity distance.

distance modulus, not being an actual distance, does not give an entirely accurate representation of the distance. Standard candles with the same distance modulus can have a complicated distribution of true distances. Thirdly, a distance nearby corresponds to a much smaller sampling volume than a greater distance. As a consequence, objects seen at large distances may have no nearby counterparts, so that their distances cannot be calibrated absolutely. This applies to gamma ray bursts, which do not occur in the nearby Universe.

We must also account for the fact that we measure a flux $\mathcal{F}$ only within a restricted bandwidth—we cannot obtain a *bolometric* flux measurement. This means that if we wish to study an object in its rest frame we need to make a correction because the flux observed within the bandwidth of a given filter in the observer's frame will be a redshifted version of that emitted in the rest frame. This *K-correction* introduces another term to the distance modulus (1.29). For example (Sparke and Gallagher, 2007), in the B band at 0.44 μm, elliptical galaxies dim rapidly with increasing redshift, since stars in elliptical galaxies emit very little in the ultraviolet. Conversely, in the L band at 4 μm, elliptical galaxies at $z = 1.5$ appear very bright, because they emit strongly in the rest frame H band at ~ 1.6 μm.

This thesis investigates the correspondence between these theoretical distance measures and those obtained from observations in three different expansion regimes. Gamma-ray bursts (GRBs) are said to occur at "large" redshifts because of all the astronomical objects we can currently hope to use as standard candles, they occur at the largest redshifts—$z \lesssim 8$. In this phase of the evolution of the Universe, large-scale structure had yet to form, and cosmic expansion was decelerating. In terms of the standard model, the energy density of the Universe was dominated by matter.

In the redshift range in which SNe Ia occur, the Universe went from being matter-dominated to being dark energy-dominated. This is why understanding SNe Ia has become very important in the last decade or so: they are very accurate standard candles that are bright enough to be seen at the redshifts during which the Universe entered the dark energy-dominated regime and cosmic expansion began accelerating.

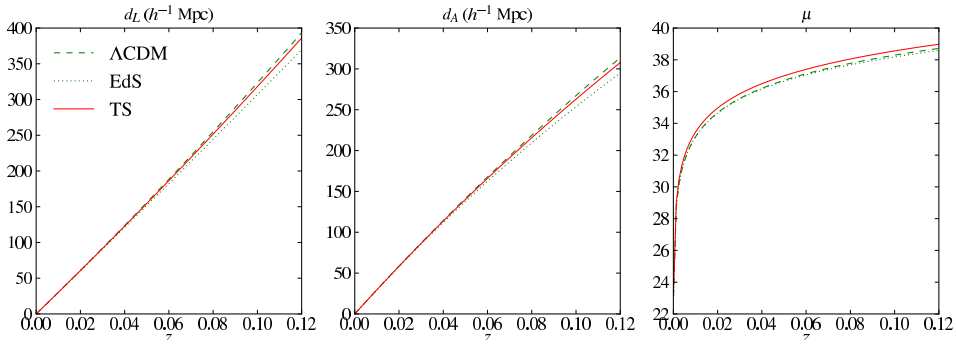

Figure 1.2: Cosmological distance measures (low z): Luminosity distance (left), angular diameter distance, and distance modulus for the spatially flat ΛCDM and EdS, and the TS cosmological models. The parameter values are the same as in Fig. 1.1.

The third redshift range of interest is $z \lesssim 0.1$—the "nearby universe". At such low redshifts, the distance-redshift relationship is effectively model-independent: we should observe galaxies to obey the Hubble expansion law (1.9) provided that their distance is sufficiently large for the galaxy peculiar velocity to be negligible in comparison to its recessional velocity. This nearby region is shown in Fig. 1.2. The linear Hubble law is evident, but it is also apparent that there are different predictions for the value of the Hubble constant within this regime, and that the predictions do not converge until redshifts less than 0.02—in the local Universe (here assuming that "nearby">"local"), measurements of the Hubble constant would furnish us with the true Hubble constant were it not for peculiar velocities generated by the highly irregular and clumped distribution of matter at these scales. In the standard model with dark energy, these peculiar velocities are treated as perturbations about the pure Hubble expansion. In the linear perturbation theory in which matter is treated as a pressureless fluid in comoving coordinates, the peculiar velocity field is written (Peebles, 1993)

$$\mathbf{v}(\mathbf{r}) = \frac{H_0 \Omega_{\rm m}^{0.55}}{4\pi} \int \frac{\mathbf{r}' - \mathbf{r}}{|\mathbf{r}' - \mathbf{r}|^3} \delta(\mathbf{r}') \mathrm{d}^3\mathbf{r}', \tag{1.30}$$

where $\delta(\mathbf{r}) = (\rho - \bar{\rho})/\bar{\rho}$ is the density perturbation and $\bar{\rho}$ is the average density of the Universe. In an EdS universe, the exponent of the matter density is 0.6.

At very small scales, below 8 h^{-1} Mpc in the standard model, perturbations in both velocity and density become non-linear. The relationship between the

distribution of matter and the geometry of space is poorly understood on these scales, and the universe is usually approximated locally as point masses moving in a Euclidean space. Although the observation of the local Hubble constant is confused by peculiar velocities, a more detailed understanding of the peculiar velocity field can potentially elucidate some of the most profound problems in cosmology, such as the distribution of dark matter halos, the relationship between geometry and matter and Mach's priciple. We discuss this matter further in Chapter 5, in which we find significant anisotropy in the Hubble flow from redshift-independent distance measurements of a large sample of nearby galaxies.

1.3 Measurements of the Hubble constant

The Friedmann equations (1.7) that describe the evolution of the Universe on large scales reveal the central role of the Hubble parameter. It encodes the expansion of the Universe. Because of this, measuring its present-epoch value has always been of great interest. Due to the simplicity and success of the homogeneous and isotropic cosmological model, it generally goes without question that H_0 has a single global value to which our measurements will converge given a sufficient sample volume. But this is in fact quite a bold assumption: even if we could directly measure the expansion rate of the entire observable volume, according to the inflationary theory this is but an unknown fraction of the whole Universe. We will see that the timescape model does not make this assumption. Instead, the value of the Hubble "constant" depends on the averaging domain, and rather than having a single global value, there is a range of values which is minimized once the domain size reaches the order of the scale of statistical homogeneity. For completeness, and by way of establishing the general background, we give a very brief overview of the history of the Hubble constant. This history is well documented (for example, in Sandage (1995)). Brief overviews are presented at `https://www.cfa.harvard.edu/~dfabricant/huchra/hubble/)` and in Kirshner (2003).

The discovery of cosmological expansion is usually attributed to Edwin Hubble because of the plot of galaxy velocities versus distances that he published in 1929. The Hubble law (1.9) is linear only nearby, when $z \ll 1$. For larger

redshifts, a cosmological model is needed to specify the way in which distance changes with redshift. Hubble's was the first observational evidence, although he remained sceptical of this result all his life (Sandage, 1995). Lemaître had published an expanding cosmological model in 1927, from which he estimated $H_0 = 625 \pm 50$ km s^{-1} Mpc^{-1}. Hubble's original estimate of the constant that bears his name was $H_0 = 500 \pm 50$ km s^{-1} Mpc^{-1}.

Current estimates are of the order ten times smaller than these first guesses, but the reasons for the discrepancy are not hard to understand. In 1917, it was widely held that the Milky Way comprised the whole universe—the existence of other galaxies had yet to be established. Consideration of the mechanics of such a universe led Einstein to introduce the famous Cosmological Constant to the gravitational field equations (Einstein, 1917) and the prevailing picture of the Universe was at that time one of an infinite and eternal Euclidean volume of "fixed stars" whose velocities were small compared to that of light. It is as easy to see the intuitive appeal of such a picture as it is to see why people once believed the earth was flat. Astronomers at the time were aware of the existence of "spiral nebulae", but there was controversy over whether these objects lay within the Milky Way or outside it: 1920 saw a much-publicized debate about the size of the Universe between Harlow Shapley who held that the Milky Way was itself the universe, and Heber Curtis, who held that the Milky Way is but one of many "island universes"[1]. The controversy was resolved in favour of Curtis' position in 1924 when Hubble used distances deduced from Cepheid variable stars to show that the spiral nebulae were actually extragalactic. He was then able to deduce the expansion of the universe in 1929. In fact, despite being able to make this deduction, modern measurements show that the distances Hubble used in his famous diagram were still too small: although the relative distances were consistent enough for him to claim the linear recessional velocity-distance relationship (Kirshner, 2003). The discovery of Population II stars in the 1950s, and improvements in the treatment of systematic uncertainties reduced estimates of H_0 to between 50 and 100km s^{-1} Mpc^{-1} by the early 1960s. Despite the

[1]This term is attributed to Immanuel Kant, who was convinced of the existence of other galaxies on the basis of the Nebular Hypothesis, which was developed by Swedenborg in the early 18th century.

theoretical possibility of an infinite universe, it took actual observations, requiring new technology, to develop an understanding and intuition of its true size.

We also have an indirect estimate of H_0 from the early Universe. The distance to the last scattering surface, inferred from the physics of the intrinsic CMB temperature anisotropies, depends on H_0 as well as the energy density parameters. The current state-of-the-art standard model "concordance" estimate of the present cosmic expansion rate from the CMB temperature anisotropy power spectrum and the scale of Baryon acoustic oscillations is $H_0 = 71.5 \pm 2.5$ km s^{-1} Mpc^{-1} (Jarosik et al., 2011, WMAP7). From an updated Cepheid calibration of Tully-Fisher (TF), Surface Brightness Fluctuation (SBF), Fundamental Plane (FP) and SNe Ia distances, the Hubble Space Telescope (HST) Key project of Freedman et al. (2001) measured $H_0 = 72 \pm 8$ km s^{-1} Mpc^{-1}. This result was widely adopted as *the* value of H_0, being the most precise direct measurement yet made, and its agreement with the CMB fits is reassuring[1]. The latest determination of the Hubble constant from the HST based on a geometric distance to NGC4258 (more accurate than the Cepheid distances to the Large Magellanic cloud used previously) claims a 3.3% accuracy, finding $H_0 = 73.8 \pm 2.4$ km s^{-1} Mpc^{-1} (Riess et al., 2011).

In the following chapter, we describe a scheme for accounting for an inhomogeneous density distribution: the timescape model.

[1] A plot of the estimates of H_0 versus year (see Kirshner, 2003) shows that the errorbars on the measurements have generally been much smaller than the range of "best" measured values: the systematic errors have always been underestimated. It is true that the systematics generally are now much better understood, but the fact remains that estimates of H_0 still have a much greater range than suggested by the quoted errors, and it is worth keeping in mind the difference between precision and accuracy.

Chapter 2

The Timescape Cosmology: dispensing with the homogeneity assumption

2.1 What is a "typical observer"?

The two central pillars of observational cosmology are the high-precision measurements of the temperature fluctuations in the cosmic microwave background and the galaxy-redshift surveys. From the former, we have a snapshot of the early universe, while the latter provides a picture of the universe at the present epoch. The CMB is remarkably smooth, yet the distribution of galaxies indicates that matter is clumped in a hierarchical structure, perhaps up to the largest scales so far probed by observations. Whether we have yet discerned a maximum clustering scale is the subject of debate (e.g. Blake et al., 2007; Hogg et al., 2005; Kazin et al., 2010; Thomas et al., 2011). Much work needs to be done on the statistical methods by which we address the issue (Gabrielli et al., 2005). Hoyle and Vogeley (2002) and Hoyle and Vogeley (2004) present studies of void statistics in galaxies from the Point Source Catalogue survey, the Updated Zwicky Catalogue, and the 2 degree Field Galaxy Redshift Survey. Their results, summarised as the average void diameters and their average density contrasts $\tilde{\delta}$, are shown in Table 2.1 below. The magnitudes of the density contrasts is greatest at the centres of the voids. Just outside the boundaries of the voids so defined, the mean density

rises sharply but it remains well below $\delta\rho/\rho = -0.5$ out to 150% of the void radius. A more recent study in a similar vein of the SDSS Data Release 7 gives the volume of the Universe taken up by such voids as 61% (Pan et al., 2011). The median void diameter found in this survey was $17\,h^{-1}$ Mpc, with density contrast $\delta < -0.85$ right up to the void edges. Clearly, the voids are extremely empty, and have well-defined boundaries, consistent with a picture of evacuating voids with coalescing walls at their margins. The evolution from smoothness to a certain level of clumpiness is well-described by the linear theory of gravitational instability. But this description becomes inapplicable once density contrasts enter the non-linear regime. The model parameters determined from the late-epoch Universe have unexpected values. Early observations of large-scale structure were interpreted in terms of the EdS model with $\Omega_{\rm m}= 1$, for reasons that were aesthetic rather than physical, but once galaxies could be observed in sufficient numbers, the two-point correlation function revealed that in fact $\Omega_{\rm m}$ has to be significantly less than 1. Although this could indicate an open universe, the concept of a spatially flat universe was considered the more natural model theoretically. The anomalous dimness of type Ia supernovae not only corroborated this result, but suggested (many would say demonstrated) the existence of a large amount of unseen repulsive dark energy. So the visible universe is actually just 4% of all that is. The rest of the matter in the universe is in the form of aggregated non-baryonic dark matter plus a smooth dark energy, the nature of which constitutes a profound question in modern physics.

Survey	Void diameter	Density contrast
PSCz	$(29.8 \pm 3.5)h^{-1}$Mpc	$\tilde{\delta} = -0.92 \pm 0.03$
UZC	$(29.2 \pm 2.7)h^{-1}$Mpc	$\tilde{\delta} = -0.96 \pm 0.01$
2dF NGP	$(29.8 \pm 5.3)h^{-1}$Mpc	$\tilde{\delta} = -0.94 \pm 0.02$
2dF SGP	$(31.2 \pm 5.3)h^{-1}$Mpc	$\tilde{\delta} = -0.94 \pm 0.02$

Table 2.1: Dominant void statistics in the Point Source Catalogue Survey (PSCz), the Updated Zwicky Catalogue (UZC), and the 2 degree Field Survey (2dF) North Galactic Pole (NGP) and South Galactic Pole (SGP), from Hoyle and Vogeley (2002); Hoyle and Vogeley (2004). Table from Wiltshire (2008).

Putting aside this question, there are many observations that are not explained by the standard model. Some examples: galaxies appear to have formed much earlier than predicted (Glazebrook et al., 2004); despite a predicted cut-off in the quasar number density at $z = 5$ (Efstathiou and Rees, 1988) a quasar has been observed at $z = 7$ (Mortlock et al., 2011); we observe the volume of the universe to be dominated by voids which are much emptier than predicted by the theory of structure formation (Peebles, 2001). These could be attributed to the complexity of galaxy evolution, but the question also arises whether the need for dark energy is a sign that the standard model has reached the limit of its application. Given the observed inhomogeneity, it has always been acknowledged that the standard model holds only in some statistical sense, or only up to some point in time, and that only at some sufficiently large scale can the universe be treated as being truly homogeneous and isotropic. The late epoch, local universe has a geometry that is very different from that described by eq. (1.1), yet this geometry seems to describe the observations very well. This particular puzzle Wiltshire (2007) calls the *Sandage-de Vaucoleurs* paradox: large-scale structure is hierarchical at least on the scale of galaxies and clusters (de Vaucoleurs, 1970), and so one expects that in the "very local" universe, within a few megaparsecs, that peculiar motions should swamp the linear Hubble flow. Yet Hubble was able to detect the operation of the law that bears his name in 1929[1] and a local linear Hubble flow is observed (Sandage et al., 1972). There are more questions: How can the average evolution of the universe be derived observationally when local measurements sample only a limited fraction of the Hubble volume? What is the appropriate averaging scheme? What are the implicit assumptions we make when we relate the average FLRW geometry to the measurements we make? These questions are becoming even more important now that cosmological observations can be made with unprecedented precision.

The fundamental complication in any general relativistic treatment of cosmology is that any metric that attempts to directly encode significant inhomogeneous structure will not have the symmetries of a metric like (1.1) that represent conservation principles for the dynamics of the geometry. In the perturbative treatment

[1]There is evidence that Hubble was still questioning the reality of cosmic expansion in 1953 (Sandage, 1995, p. 107).

of linear inhomogeneities, there is always a background possessing the exact symmetries, but once inhomogeneities become nonlinear, there is no such symmetric background. What this means in practice is that we must confront the fact that in a general inhomogeneous geometry there is no unique way to synchronize clocks.

A cosmological model dubbed the "timescape" (Wiltshire, 2007) uses an averaging approach to large-scale structure to address these questions. In attempting to apply the principles of general relativity consistently to cosmology, it confronts foundational questions such as the scales of applicability of the equivalence principle, averaging in cosmology, and what it means to attempt to determine cosmological parameters from observations that are necessarily localised. It claims, with the right approach to averaging and with careful consideration of the location of observers, to obviate the need for dark energy.

This chapter is an introduction to the timescape model. It draws heavily on Wiltshire (2007) and Wiltshire (2008). The aim of the chapter is to write down new expressions for the distances that we will use later in comparison with the FLRW distances (1.25), (1.28), and (1.29). There is a lot of terminology in this chapter, and the reason for this is simple. In the standard cosmological model, we assume by the Copernican principle that we occupy a position that is roughly a volume-average one. Current observations show that in terms of large-scale structure, *we do not*. Not only do we live on the edge of a large local void (Tully et al., 2008), but we also have a picture of the universe as a cosmic web, dominated in volume by voids. This means that a true "typical" observer in a volume average position will make observations from a void. We can however define an hypothetical "isotropic observer" as one who sees an isotropic CMB. Different isotropic observers in the timescape scenario will measure a different mean CMB temperature because of their locations in regions with different expansion histories. To interpret the observations we make, e.g. of accelerated expansion, we must account for the difference between our observations and those of a "typical observer", and this requires a systematic reappraisal of all observed cosmological quantities: whereas there is a single cosmic time in the standard model by virtue of the symmetries of the metric, according to Wiltshire (2007) there are now different notions of time depending on whether one is an isotropic observer located in an on-average void or wall, and the notion of cosmic time is no longer

global but applies within an averaging domain that must be specified. There are, however, only two parameters we will be interested in ultimately: the present matter density Ω_{M0} and the present average Hubble constant H_0, as measured from our location within a wall.

2.2 Inhomogeneity and backreaction: Buchert's averaging scheme

In order to account for the observed density contrasts in the dynamical spacetime of general relativity, the timescape model makes a distinction between underdense *void* regions and *walls* which contain overdense regions. Since the observable universe is dominated by voids, one might think that the global curvature of the universe should be negative, but we should not presume that the observable universe is typical of the universe on scales larger than the particle horizon. Here we use the observed void-domination and the spectral features of the CMB to infer that our observable universe is an underdense, internally inhomogeneous bubble in a spatially flat bulk universe (Wiltshire, 2005). In the standard cosmology, a corollary of the assumption of a spatially flat background geometry is that underdensities are compensated for by overdensities, but there is no such flat background in the timescape model. The assumption of a void-dominated observable universe follows naturally from the theory of primordial inflation, which will have stretched density perturbations to scales many times larger than the present horizon volume (Peacock, 1999, p. 339).

We now outline the scalar averaging scheme of Buchert (Buchert, 2000). The scheme is quite generic, and its application requires assumptions about certain fundamental quantities. For example, the question of what constitutes the "dust" is perhaps the most important of these. We will discuss the way in which these are defined in the timescape model once we have outlined the Buchert formalism. The Buchert scheme is quite intuitive for a real observer, being based on comoving synchronous coordinates, i.e. coordinates do not change for freely falling observers. The underlying geometry and dynamics of space and time are assumed

to be such that the three dimensions of space can be fully defined at a given instant of the cosmic time. This is known as a 3+1 split, and we say that space is time-orthogonal. The evolution of space from one instant of cosmic time to the next — the dynamics of the *spacelike hypersurfaces* — is fully described by the lapse and shift functions of the formalism developed by Arnowitt, Deser and Misner (hereafter ADM) (Arnowitt et al., 2008).

Furthermore, we will here consider a pressureless dust cosmology, which has energy-momentum tensor

$$T^{\mu\nu} = \rho \bar{n}^\mu \bar{n}^\nu, \tag{2.1}$$

where $\bar{n}^\mu = \frac{\mathrm{d}x}{\mathrm{d}t}^\mu$ is the 4-velocity written in terms of the local proper time t. With energy density $\rho(t,\mathbf{x})$, expansion $\theta(t,\mathbf{x})$, and shear $\sigma(t,\mathbf{x})$[1], on a compact domain $\mathcal{D}$ on an appropriately defined spatial hypersurface of constant average time t with spatial 3-metric ${}^3g_{ij}(\mathbf{x})$, the average cosmic evolution is described by the exact equations

$$3\frac{\dot{\bar{a}}^2}{\bar{a}^2} = 8\pi G\langle\rho\rangle - \frac{1}{2}\langle\mathcal{R}\rangle - \frac{1}{2}\mathcal{Q}, \tag{2.2}$$

$$3\frac{\ddot{\bar{a}}}{\bar{a}} = -4\pi G\langle\rho\rangle + \mathcal{Q}, \tag{2.3}$$

$$\partial_t\langle\rho\rangle + 3\frac{\dot{\bar{a}}}{\bar{a}}\langle\rho\rangle = 0, \tag{2.4}$$

where $\bar{a}(t) \equiv \left[\mathcal{V}(t)/\mathcal{V}(t_0)\right]^{1/3}$ and $\mathcal{V}(t) \equiv \int_\mathcal{D} \mathrm{d}^3x\sqrt{\det{}^3g}$ is the volume of the comoving domain. The overdot denotes a derivative with respect to t and angle brackets denote the spatial volume average of a quantity. For example, the volume average spatial curvature is the integral of the Ricci curvature in the domain $\mathcal{D}$: $\langle\mathcal{R}\rangle \equiv \left(\int_\mathcal{D} \mathrm{d}^3x\sqrt{\det{}^3g}\,\mathcal{R}(t,\mathbf{x})\right)/\mathcal{V}(t)$. Equations (2.2) and (2.3) are very like the Friedmann equations (1.7): the difference is that spatial averaging of the

[1]These terms come from considering what happens to a set of neighbouring free-fall trajectories —a *congruence of geodesics*— from one hypersurface to the next in the ADM formalism. The expansion tensor represents their motion relative to one another. The shear tensor is the trace-free part of the expansion tensor. The expansion scalar is the contraction of the expansion tensor with the metric induced on the spatial hypersurface (i.e. the trace of the expansion tensor), and the scalar shear appearing in the Buchert equations is $\sigma^2 \equiv \frac{1}{2}\sigma^a{}_b\sigma^b{}_a$. More details about the ADM formalism can be found in Wald (1984).

parameters results in a *backreaction*

$$\begin{aligned}\mathcal{Q} &\equiv \frac{2}{3}\left\langle(\theta-\langle\theta\rangle)^2\right\rangle - 2\langle\sigma\rangle^2 \\ &= \frac{2}{3}\left(\langle\theta^2\rangle - \langle\theta\rangle^2\right) - 2\langle\sigma\rangle^2 . \end{aligned} \tag{2.5}$$

The backreaction comes about because averaging and time-evolution do not commute with each other. For any scalar Ψ, (Buchert, 2000)

$$\frac{\mathrm{d}}{\mathrm{d}t}\langle\Psi\rangle - \langle\frac{\mathrm{d}\Psi}{\mathrm{d}t}\rangle = \langle\Psi\theta\rangle - \langle\theta\rangle\langle\Psi\rangle. \tag{2.6}$$

The backreaction in (2.5) comes from substituting $\Psi = \theta$ in (2.6). When we take an average of a scalar quantity in Einstein's equations such as the density or the expansion, we are computing the second term on the LHS of (2.6), and, implicitly, the difference with a time-evolved average. Often the time-evolved average is taken to be that derived from an FLRW geometry, but it is important to realise that although there is very good reason to believe the large-scale average is FLRW by virtue of the evidence of the CMB, there is no *a priori* reason for this to be the case.

A necessary condition for the integration of the averaged Raychaudhuri equation (2.3) to yield the averaged Hamiltonian constraint (2.2) provides a relation between curvature and backreaction:

$$\partial_t\left(\bar{a}^6\mathcal{Q}\right) + \bar{a}^4\partial_t\left(\bar{a}^2\langle\mathcal{R}\rangle\right) = 0. \tag{2.7}$$

In a fashion analogous to that resulting in equations (1.15) and (1.16), with an appropriate definition of a critical density to be proposed below, equation (2.2) can be rewritten as

$$\Omega_M^{\mathcal{D}} + \Omega_k^{\mathcal{D}} + \Omega_{\mathcal{Q}}^{\mathcal{D}} = 1, \tag{2.8}$$

where

$$\Omega_M^{\mathcal{D}} \equiv \frac{8\pi G\langle\rho\rangle}{3\bar{H}^2}, \qquad \Omega_k^{\mathcal{D}} \equiv -\frac{\langle\mathcal{R}\rangle}{6\bar{H}^2}, \qquad \Omega_{\mathcal{Q}}^{\mathcal{D}} \equiv -\frac{\mathcal{Q}}{6\bar{H}^2}, \tag{2.9}$$

are fractions of the critical density and the overbar on $\bar{H} \equiv \dot{\bar{a}}/\bar{a}$ indicates that the quantity in question is an average over the domain $\mathcal{D}$.

To apply the Buchert scheme we must make explicit what we mean by "dust". This is a complex issue. A recent review was given by Wiltshire (2011). In the

early Universe one is justified in using baryons as the dust because the Universe was uniform. After last scattering, the dust is usually taken to be galaxies. But once structure starts to form at late times this becomes problematic because of clustering on large scales — the galaxies are not independent. In the early days of general relativity, the dust particles were stars. Once the existence of other galaxies was established, they became the dust particles. The notion of "comoving with the dust" then had an intuitive interpretation. But galaxies cluster and have peculiar velocities. Clearly, if we are to maintain the notion of "comoving with the dust", we need to increase the size of the dust particles to encompass sufficient numbers of galaxies for them to start showing some sort of suitably defined averaged clustering properties. Since we have measured the voids between the clusters to have diameters exceeding $30\,h^{-1}$ Mpc, the size of the "dust" particles should be large. In the timescape model, dust is coarse-grained at the $100\,h^{-1}$ Mpc scale of statistical homogeneity (Wiltshire, 2011), since it is only on these scales that one can neglect the net exchange of energy-momentum between the particles. Within a single dust cell there is therefore significant inhomogeneity, but the hypothesis is made that there exists some notion of average homogeneous expansion. This means that whether isotropic observers within a dust cell are located in a wall or a void, there exists an appropriate set of clocks by which they will measure a uniform average expansion (see Section 2.3).

In the timescape model, the density at a given location is defined relative to a *critical density* defined now as the region-dependent quantity $3\bar{H}^2/(8\pi G)$ (c.f. 1.12), which here does not play its usual role of demarcating the line between a "closed" and an "open" universe. The overbar denotes a Hubble volume average. For a definition of this critical density, we use the density of matter required for gravity to be able to bring the cosmic expansion to zero at the time of last scattering, since at this time local velocity variations were very small and the cosmic expansion would have been uniform. We assume by the Copernican principle that the universe *as a whole* was smooth at last scattering, and not just that fraction of it within our present past horizon volume. In the universe of the present epoch, this critical density sets a universal scale which separates gravitationally bound and gravitationally unbound density perturbations.

The timelike boundaries which separate bound and unbound systems are given the name *finite infinity* (Ellis, 1984). Finite infinity is defined (Wiltshire, 2007) to be the union of the timelike boundaries of disjoint domains within which the average expansion is zero, while being positive without. A schematic picture from Wiltshire (2007) is shown in Fig. 2.1. That $\langle\theta(p)\rangle_{\mathcal{F}_I} = 0$ within comes about is because the inner regions, within finite infinity, are assumed to be virialized or virializing while regions near finite infinity are marginally expanding ($\theta > 0$). Since the average expansion inside a finite infinity region is zero, it must be the case that

$$\rho_c(\tau) = \langle\rho(\tau, \mathbf{x})\rangle_{\mathcal{F}_I}. \tag{2.10}$$

This will serve as the definition of the critical density in what follows. The cosmological parameter values that an observer measures will depend on which side of finite infinity they are located, as well as the size of the averaging domain.

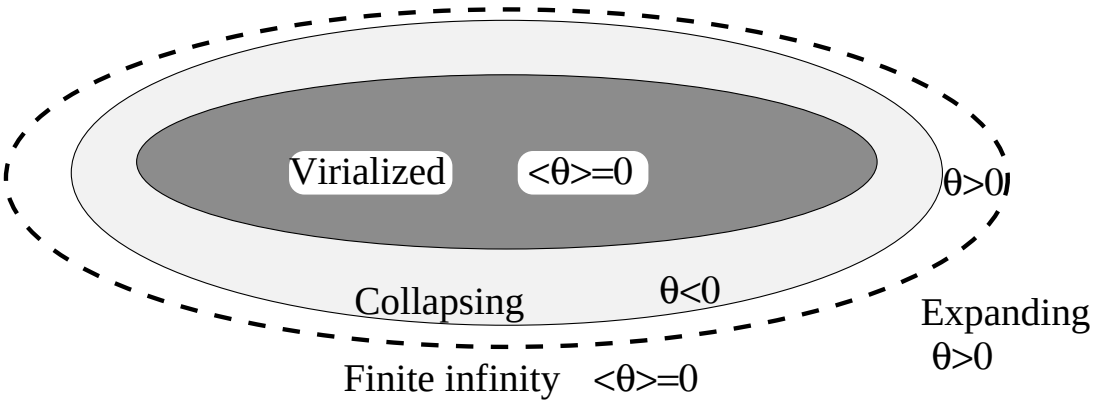

Figure 2.1: Finite infinity See text for details. Figure credit Wiltshire (2007).

What might the typical size be for the region inside finite infinity? By way of illustration: Ellis and Stoeger (2009) define the *matter horizon* of the Solar System as being the comoving region which has contributed matter to the local physical environment. Assuming we can neglect the contribution from cosmic rays from distant galaxies, they argue that the matter horizon lies at about 2 Mpc. This value is roughly consistent with estimates of the zero-velocity radius of the local group from distances to nearby galaxies (Karachentsev et al., 2009; Sandage, 1986). We therefore suggest that the collapsing region sketched in Fig.

2.1 is about 4 Mpc across in our own case, but that it could also be much larger in rich clusters.

Our notion of critical density leads to the distinction between walls and voids via the geometry of finite infinity. In the following section we discuss the interpretation of the relationship between the parameters of the homogeneous averaged geometry and the observations we make.

To establish the synchronous coordinate system for the Buchert average, we begin with a standard 3+1 spacetime split on a globally hyperbolic manifold. The unit normal to the spacelike hypersurface is $n_\alpha = (-\gamma, 0, 0, 0)$, or $n^\alpha = \gamma^{-1}(1, \beta^i)$. If we follow the unit normal from one hypersurface to the next, we arrive at a different point in general from the one we would get to if we followed a worldline with a fixed spatial coordinate. The difference is given by the *shift vector* $\beta^i(\tau, x^k)$. As mentioned above, in Buchert's scheme $\beta^i = 0$, meaning that the normal to the hypersurface is tangent to a worldline with fixed spatial coordinates: the coordinates are *comoving*. In general, there is also a difference between the coordinate time τ and the proper time t on curves normal to the hypersurfaces. The *lapse function* $\gamma(\tau, \mathbf{x})$ encodes this difference. For regions enclosed within finite infinity where the geometry is approximately flat Minkowski, we choose $\gamma(\tau_{\rm w}, \mathbf{x})_{\mathcal{F}_I} = 1$ to be the reference normalization of clocks, which means that for a comoving observer, for whom the unit normal is the 4-velocity, the *wall time* $\tau_{\rm w}$ is the local proper time. For regions $\mathcal{D}_I$ outside finite infinity that are entirely contained within voids, $\gamma(\tau_{\rm v}, \mathbf{x})_{\mathcal{D}_I} > 1$, because of the positive gravitational energy associated with negative spatial curvature. The *void time* $\tau_{\rm v}$ is that measured by hypothetical observers in the centres of the dominant voids. When we average over all spatial scales contained within our present particle horizon volume $\mathcal{H}$ we obtain a "global average"[1] lapse function

$$\bar{\gamma}(\tau) \equiv \langle \gamma(\tau, \mathbf{x}) \rangle_{\mathcal{H}}. \tag{2.11}$$

In practice, in the timescape model this lapse function is *phenomenological*, being defined by observed density contrasts. Order of magnitude estimates for such a lapse function, neglecting backreaction, are calculated in Wiltshire (2008) based

[1] "Global" here means the entire present particle horizon volume, which is actually some fraction of the whole universe – hence the quotation marks.

on the void statistics given in Table 2.1. A full present-epoch average taking backreaction into account gives the lapse difference between walls and voids at the present epoch as $\bar{\gamma} = 1.38^{+0.06}_{-0.05}$ (Leith et al., 2007). The present lapse function differs between walls and voids as a result of the slow divergence of clock rates during ∼10 billion years of structure formation. An absolute upper bound on the difference in clock rates is provided by the lapse function within voids, $\gamma(\tau, \mathbf{x}) < \frac{3}{2}$, which is the ratio of the local expansion rate of a coasting Milne (empty) universe region to a decelerating EdS region.

In the timescape context, there is no exact spatial hypersurface which is time-orthogonal: because there is focussing of geodesics in overdense regions there can be no global comoving coordinate system. The choices $\beta^i = 0$ and $\gamma = 1$ can be understood as requiring that the momentum flux and the variations in the gravitational energy of space can be neglected at the scale of averaging. Hence the specification of the "dust" particles above. We are therefore left with the notion of an *average*, rather than exact, spatial hypersurface, over which the expansion is, on average, homogeneous. No observer resides in a region of locally expanding space. In Chapter 5 we investigate the possibility of determining a rest frame of minimum Hubble flow variance observationally. In each averaging region $\mathcal{D}$, which may or may not contain a finite infinity region, the quasilocally measured expansion is a uniform function of the local proper time.

2.3 The dynamical equations

We average over scales much larger than the domains bounded by finite infinity, and assume that pressure, vorticity and shear can be neglected on these scales. At these scales, we can also neglect non-expanding regions: on large scales the Universe is expanding, but the rates of expansion at different places will differ in general from that at a volume-average position in freely expanding space. Note that there are no observers at volume-average positions in freely expanding space — all actual observers are located in bound systems. The volume-average position in freely expanding space provides us with a reference point against which to refer our measurements: it is simply the location of an observer who by volume

is "typical" in the sense of the Copernican principle, which in a void-dominated universe is most likely to be in a void.

Finite infinity regions are assumed to be contained within walls, and have a locally measured expansion that defines a Hubble flow

$$\bar{H}_{\rm w}(\tau_{\rm w}) = \frac{1}{3}\langle\theta\rangle_{\rm w} \equiv \frac{1}{a_{\rm w}}\frac{{\rm d}a_{\rm w}}{{\rm d}\tau_{\rm w}} \tag{2.12}$$

where the subscript w indicates the quantity is defined with respect to clocks of isotropic observers in walls. In a similar way, the locally measured expansion within the dominant voids defines a different Hubble flow

$$\bar{H}_{\rm v}(\tau_{\rm v}) = \frac{1}{3}\langle\theta\rangle_{\rm v} \equiv \frac{1}{a_{\rm v}}\frac{{\rm d}a_{\rm v}}{{\rm d}\tau_{\rm v}} \tag{2.13}$$

where the void clock rate of isotropic observers is $\tau_{\rm v}$. The uniform proper expansion gauge is represented by the fact that

$$\bar{H}_{\rm w} = \bar{H}_{\rm v} = \bar{H}, \tag{2.14}$$

and because of the gradients in quasi-local gravitational energy, the proper times are different, so

$$\frac{{\rm d}\tau_{\rm w}}{{\rm d}\tau_{\rm v}} \neq 1. \tag{2.15}$$

On the spatial hypersurface of average homogeneity, the entire present particle horizon volume can be represented as the disjoint union of regions corresponding to bubble walls, containing finite infinity regions, and regions corresponding to voids. In other words, $\mathcal{V} = \mathcal{V}_{\rm i}\bar{a}^3$, where

$$\bar{a}^3 = f_{\rm wi}a_{\rm w}^3 + f_{\rm vi}a_{\rm v}^3 \tag{2.16}$$

and the subscript i stands for "initial". The $f_{\rm vi}$ is the initial fraction of the universe taken up by voids and $f_{\rm wi} = 1 - f_{\rm vi}$ is the initial fraction of walls. Clearly, by (2.16), the global average $\bar{a}$ will be less than the scale factor in a Milne universe by virtue of the presence of the spatially flat $\mathcal{F}_I$ regions. It is also the case that $f_{\rm w}(t) = f_{\rm wi}a_{\rm w}^3/\bar{a}^3$ and $f_{\rm v}(t) = f_{\rm vi}a_{\rm v}^3/\bar{a}^3$ are the *wall* and *void fractions* respectively, and that $f_{\rm w}(t) + f_{\rm v}(t) = 1$.

Since Buchert's scheme is given in terms of volume average time parameter t, it is convenient to write all quantities in terms of that parameter. If we define the rate of change of volume average time with local times as

$$\gamma_{\rm w} = \frac{{\rm d}t}{{\rm d}\tau_{\rm w}}, \qquad \text{and} \qquad \gamma_{\rm v} = \frac{{\rm d}t}{{\rm d}\tau_{\rm v}}, \tag{2.17}$$

then we can write the gauge condition (2.14) as

$$\bar{H} = \gamma_{\rm w}\frac{1}{a_{\rm w}}\frac{{\rm d}a_{\rm w}}{{\rm d}t} = \gamma_{\rm v}\frac{1}{a_{\rm v}}\frac{{\rm d}a_{\rm v}}{{\rm d}t}. \tag{2.18}$$

The wall(void) Hubble parameter with respect to volume average time is straightforwardly defined as

$$H_{\rm w} \equiv \frac{1}{a_{\rm w}}\frac{{\rm d}a_{\rm w}}{{\rm d}t}, \qquad \text{and} \qquad H_{\rm v} \equiv \frac{1}{a_{\rm v}}\frac{{\rm d}a_{\rm v}}{{\rm d}t}. \tag{2.19}$$

Note that $H_{\rm w} < \bar{H} < H_{\rm v}$. From Eq. (2.16) we can write $\bar{H}$, the locally measured Hubble parameter of a particle horizon volume average, as

$$\bar{H} = \frac{1}{3}\langle\theta\rangle_{\mathcal{H}} = f_{\rm w}H_{\rm w} + f_{\rm v}H_{\rm v}, \tag{2.20}$$

where the void and wall volume fractions have the definitions given above.

If we define the relative expansion rate

$$h_r(t) \equiv \frac{H_{\rm w}}{H_{\rm v}} < 1, \tag{2.21}$$

then we can write $\bar{H} = \gamma_{\rm w}H_{\rm w} = \gamma_{\rm v}H_{\rm v}$, where

$$\gamma_{\rm w} = 1 + \frac{(1-h_r)f_{\rm v}}{h_r} \tag{2.22}$$

and $\gamma_{\rm v} = h_r\gamma_{\rm w}$. If we also compute the derivative of $f_{\rm vi}a_{\rm v}^3/\bar{a}^3$

$$\begin{aligned} \dot{f}_{\rm v} &= -\dot{f}_{\rm w} = 3(1-f_{\rm v})(1-\gamma_{\rm w}^{-1})\bar{H} \\ &= \frac{3f_{\rm v}(1-f_{\rm v})(1-h_r)\bar{H}}{h_r + (1-h_r)f_{\rm v}} \end{aligned} \tag{2.23}$$

and use (2.16) and (2.20) with

$$\langle\theta^2\rangle_{\mathcal{H}} = 9(f_{\rm w}H_{\rm w}^2 + f_{\rm v}H_{\rm v}^2), \tag{2.24}$$

then for the kinematic backreaction defined in (2.5) we obtain

$$\begin{aligned}\mathcal{Q} &= 6f_{\rm v}(1-f_{\rm v})(H_{\rm v}-H_{\rm w})^2 \\ &= \frac{6f_{\rm v}(1-f_{\rm v})(1-h_r)^2\bar{H}^2}{[h_r+(1-h_r)f_{\rm v})]^2} \\ &= \frac{2\dot{f}_{\rm v}}{3f_{\rm v}(1-f_{\rm v})}\end{aligned}$$

in the absence of shear.

The solution of the third Buchert equation (2.4), analogous to the FLRW case, is $\langle\rho\rangle_{\mathcal{H}} = \rho_0\,\bar{a}_0^3/\bar{a}^3$. To implement Buchert's equations, it only remains to define the average curvature. We can write for the voids $\langle\mathcal{R}\rangle_{\rm v} = 6k_{\rm v}/a_{\rm v}^2$, and for the walls $\langle\mathcal{R}\rangle_{\rm w} = 6k_{\rm w}/a_{\rm w}^2$, so that the average curvature over the particle horizon volume is

$$\langle\mathcal{R}\rangle_{\mathcal{H}} = \frac{6k_{\rm v}f_{\rm v}}{a_{\rm v}^2} + \frac{6k_{\rm w}f_{\rm w}}{a_{\rm w}^2} = \frac{6k_{\rm v}f_{\rm vi}^{2/3}f_{\rm v}^{1/3}}{\bar{a}^2}, \tag{2.25}$$

where we have used $k_{\rm w} = 0$ in the last step.

If the void fraction $f_{\rm v}(t)$ is not constant, the independent Buchert equations (2.2) and (2.7) then give

$$\frac{\dot{\bar{a}}^2}{\bar{a}^2} + \frac{\dot{f}_{\rm v}{}^2}{9f_{\rm v}(1-f_{\rm v})} - \frac{\alpha^2 f_{\rm v}^{1/3}}{\bar{a}^2} = \frac{8\pi G}{3}\bar{\rho}_0\frac{\bar{a}_0^3}{\bar{a}^3}, \tag{2.26}$$

$$\ddot{f}_{\rm v} + \frac{\dot{f}_{\rm v}{}^2(2f_{\rm v}-1)}{2f_{\rm v}(1-f_{\rm v})} + 3\frac{\dot{\bar{a}}}{\bar{a}}\dot{f}_{\rm v} - \frac{3\alpha^2 f_{\rm v}^{1/3}(1-f_{\rm v})}{2\bar{a}^2} = 0, \tag{2.27}$$

where the assumption that the curvature in the voids is negative allows us to put $\alpha^2 \equiv -k_{\rm v}f_{\rm vi}^{2/3}$.

These are the evolution equations for the volume average of the present particle horizon volume. We will see later that for realistic initial conditions the corresponding deceleration parameter is always positive: the volume average backreaction is never large enough to dominate over the other terms in the acceleration equation. But we still have to account for how the volume average evolution is interpreted by observers in galaxies.

2.4 The interpretation of observations

The coupled equations (2.26) and (2.27) are written in terms of the volume average time t. From these equations and from equation (2.9) we get "bare" cosmological parameters, expressed as fractions of the critical density

$$\bar{\Omega}_{\mathrm{m}} = \frac{8\pi G\bar{\rho}_0\bar{a}_0^3}{3\bar{H}^2\bar{a}^3}, \tag{2.28}$$

$$\bar{\Omega}_{\mathrm{k}} = \frac{\alpha^2 f_{\mathrm{v}}^{1/3}}{\bar{a}^2\bar{H}^2}, \tag{2.29}$$

$$\bar{\Omega}_{\mathcal{Q}} = \frac{-\dot{f}_{\mathrm{v}}^{\,2}}{9(f_{\mathrm{v}}(1-f_{\mathrm{v}})\bar{H}^2}. \tag{2.30}$$

"Bare" means that these are the parameters measured by (hypothetical) volume average observers. We wish to derive cosmological parameters appropriate for observations made by actual observers, who will always be located in walls, where the relevant time parameter will be closer to τ_{w}. This "dressing" accounts for the fact that when there are different spatial curvatures, the relationship between area and volume is different depending on the location, implying a variation in the time parameter as well. We construct appropriate metrics for wall and void regions that are FLRW-like, but rather than applying globally, apply in a statistical sense only to disjoint domains on quasilocal scales. The local average geometry near a finite infinity boundary is spatially flat, and is written in terms of wall time τ_{w}:

$$\begin{aligned} \mathrm{d}s^2_{\mathcal{F}_I} &= -\mathrm{d}\tau_{\mathrm{w}}^2 + a_{\mathrm{w}}^2(\tau_{\mathrm{w}})\,[\mathrm{d}\eta_{\mathrm{w}}^2 + \eta_{\mathrm{w}}^2\,\mathrm{d}\Omega^2] \\ &= -\mathrm{d}\tau_{\mathrm{w}}^2 + \frac{(1-f_{\mathrm{v}})^{2/3}\,\bar{a}^2}{f_{\mathrm{wi}}^{2/3}}\,[\mathrm{d}\eta_{\mathrm{w}}^2 + \eta_{\mathrm{w}}^2\,\mathrm{d}\Omega^2]. \end{aligned} \tag{2.31}$$

Here $\mathrm{d}\Omega^2 = \mathrm{d}\vartheta^2 + \sin^2\vartheta\,\mathrm{d}\varphi^2$ is the metric on a 2-sphere, and we have used (2.16) for the volume average scale factor to make the substitution in the second line. In the centre of a void, the metric over a small domain is likewise given by an effective homogeneous isotropic geometry but the appropriate time parameter is

$\tau_{\rm v}$:

$$\begin{aligned} {\rm d}s^2_{\mathcal{D}_{\mathcal{C}}} &= -{\rm d}\tau_{\rm v}^2 + a_{\rm v}^2(\tau_{\rm v})\,[{\rm d}\eta_{\rm v}^2 + \sinh^2(\eta_{\rm v})\,{\rm d}\Omega^2] \\ &= -{\rm d}\tau_{\rm v}^2 + \frac{f_{\rm v}^{2/3}\,\bar{a}^2}{f_{\rm vi}^{2/3}}\,[{\rm d}\eta_{\rm v}^2 + \sinh^2(\eta_{\rm v})\,{\rm d}\Omega^2]. \end{aligned} \tag{2.32}$$

The volume average scale factor $\bar{a}$ that appears in the second lines in (2.31) and (2.32) evolves with volume average time t according to

$$\begin{aligned} {\rm d}s^2 &= -{\rm d}t^2 + \bar{a}^2(t){\rm d}\bar{\eta}^2 + A(\bar{\eta},t){\rm d}\Omega^2 \\ &= -\gamma_{\rm w}^2(\tau_{\rm w}){\rm d}\tau_{\rm w}^2 + \bar{a}^2(\tau){\rm d}\bar{\eta}^2 + A(\bar{\eta},\tau_{\rm w}){\rm d}\Omega^2, \end{aligned} \tag{2.33}$$

in which the area function A is defined by an average over the particle horizon volume, i.e. $\int_0^{\bar{\eta}_{\mathcal{H}}} {\rm d}\bar{\eta}\,A(\bar{\eta},t) = \bar{a}^2(t)\mathcal{V}_{\rm i}(\bar{\eta}_{\mathcal{H}})/(4\pi)$, where $\bar{\eta}_{\mathcal{H}}$ is the conformal distance to the particle horizon relative to an observer at $\bar{\eta}=0$. In what follows we drop the subscript "w" from $\tau_{\rm w}$ and $\gamma_{\rm w}$, since we will no longer refer explicitly to the time in void centres. Henceforth, τ and γ will denote their wall values.

We construct a single geometry that relates metrics (2.31) and (2.33) by matching the radial null geodesics of wall and volume average geometries sharing a common centre. Along these radial null geodesics, we find that

$${\rm d}\eta_{\rm w} = \frac{f_{\rm wi}^{1/3}{\rm d}\bar{\eta}}{\gamma(1-f_{\rm v})^{1/3}}. \tag{2.34}$$

If we define $\eta_{\rm w}$ by integrating this equation on the radial null geodesics of metric (2.33), we can use it to rewrite the "dressed" wall geometry (2.31) as

$$\begin{aligned} {\rm d}s^2 &= -{\rm d}\tau^2 + \frac{\bar{a}^2}{\gamma^2}\,{\rm d}\bar{\eta}^2 + \frac{(1-f_{\rm v})^{2/3}\bar{a}^2}{f_{\rm wi}^{2/3}}\,\eta_{\rm w}^2(\bar{\eta},\tau){\rm d}\Omega^2 \\ &= -{\rm d}\tau^2 + a^2(\tau)\,[{\rm d}\bar{\eta}^2 + r_{\rm w}^2(\bar{\eta},\tau)\,{\rm d}\Omega^2], \end{aligned} \tag{2.35}$$

where $a \equiv b^{-1}\bar{a}$ and $r_{\rm w} \equiv \gamma(1-f_{\rm v})^{1/3} f_{\rm wi}^{-1/3}\eta_{\rm w}(\bar{\eta},\tau)$. This metric extends the wall geometry (2.31) as an average effective geometry to the cosmological scales parameterized by the global average conformal time

$$\bar{\eta} = \int_t^{t_0}\frac{{\rm d}t}{\bar{a}} = \int_\tau^{\tau_0}\frac{\gamma\,{\rm d}\tau}{\bar{a}} = \int_\tau^{\tau_0}\frac{{\rm d}\tau}{a}. \tag{2.36}$$

The volume average Hubble parameter measured by observers in walls that corresponds to metric (2.35) is

$$\begin{aligned} H \equiv \frac{1}{a}\frac{\mathrm{d}a}{\mathrm{d}\tau} &= \frac{1}{\bar{a}}\frac{\mathrm{d}\bar{a}}{\mathrm{d}\tau} - \frac{1}{\gamma}\frac{\mathrm{d}\gamma}{\mathrm{d}\tau}, \\ &= \gamma\bar{H} - \dot{\gamma}, \\ &= \gamma\bar{H} - \gamma^{-1}\frac{\mathrm{d}\gamma}{\mathrm{d}\tau}, \end{aligned} \tag{2.37}$$

(c.f. $\bar{H} = \dot{\bar{a}}/\bar{a} = \frac{1}{a_\mathrm{w}}\frac{\mathrm{d}a_\mathrm{w}}{\mathrm{d}\tau}$, the volume average Hubble parameter with respect to volume average time).

We use the metric (2.35) to define the dressed luminosity distance relation and an effective angular diameter distance in the standard way:

$$d_L = a_0(1+z)r_\mathrm{w}, \qquad \text{and} \qquad d_A = \frac{d_L}{(1+z)^2} \tag{2.38}$$

where

$$\begin{aligned} r_\mathrm{w}(\tau) &= \gamma(1-f_\mathrm{v})^{1/3}\int_\tau^{\tau_0}\frac{\mathrm{d}\tau}{\gamma(1-f_\mathrm{v})^{1/3}\,a} \\ &= \gamma(1-f_\mathrm{v})^{1/3}\int_t^{t_0}\frac{\mathrm{d}t}{\gamma(1-f_\mathrm{v})^{1/3}\,\bar{a}} \end{aligned} \tag{2.39}$$

accounts for the relative difference between the absolute luminosity of a source in a wall region and the observed flux in another wall region. Clearly, at early times, when $f_\mathrm{v} \to 0$ and $\gamma \to 1$, r_w will tend to the conformal time scale (2.36).

Regardless of the physical interpretation of the observable quantities, there exists an exact solution to the Buchert equations (2.26) and (2.27) (Wiltshire, 2007). Applying some physically reasonable assumptions to this general solution yields a late-time attractor solution to which all other solutions converge to within 1% by redshift $z \sim 37$ (Wiltshire, 2009). The physical interpretation of the tracker solution is that in it the void regions expand as Milne universes. In the tracker solution, we find that $h_r = 2/3$ is a constant for all time, and many of the physical observables can be written in relatively simple form. The global average Hubble constant that we measure today, H_0, for example, is related to the bare locally measured Hubble constant $\bar{H}_0$ by

$$H_0 = \frac{(4f_{\mathrm{v}0}^2 + f_{\mathrm{v}0} + 4)}{2(2+f_{\mathrm{v}0})}\bar{H}_0, \tag{2.40}$$

where $f_{\rm v0}$ is the *present void fraction*. The void fraction is

$$f_{\rm v} = \frac{3f_{\rm v0}\bar{H}_0 t}{3f_{\rm v0}\bar{H}_0 t + (1-f_{\rm v0})(2+f_{\rm v0})}, \tag{2.41}$$

and the wall fraction is simply obtained from $f_{\rm w} = 1 - f_{\rm v}$. The mean lapse function is

$$\gamma = 1 + \frac{1}{2}f_{\rm v} = \frac{3}{2}\bar{H}t = \frac{9f_{\rm v0}\bar{H}_0 t + 2(1-f_{\rm v0})(2+f_{\rm v0})}{2\,[\,3f_{\rm v0}\bar{H}_0 t + (1-f_{\rm v0})(2+f_{\rm v0})]^2}. \tag{2.42}$$

The dressed Hubble constant is the one whose value should be close to that which is conventionally determined on scales greater than the scale of statistical homogeneity, $z \gtrsim 0.033$. Using the "Gold" SN Ia dataset of Riess et al. (2007), Leith et al. (2007) found the dressed Hubble constant to be $H_0 = 61.7^{+1.4}_{-1.3}$ km s^{-1} Mpc^{-1}, (and the bare Hubble constant $\bar{H}_0 = 48.2 \pm 2.6$ km s^{-1} Mpc^{-1}). However, since the supernova data magnitudes depend on an overall normalization determined from the local distance ladder, they cannot be used to determine the Hubble constant alone. Joint estimates of H_0 and $f_{\rm v0}$ which fit both the angular diameter distance of the sound horizon in the CMB anisotropy data and the baryon acoustic oscillation scale in galaxy clustering statistics do provide an independent constraint on the value of H_0, however, and on this basis Leith et al. (2007) find the range of values of the dressed Hubble constant to be roughly constrained to lie in the interval $57 \lesssim H_0 \lesssim 68$ km s^{-1} Mpc^{-1}. This is lower than the SH_0ES best estimate of Riess et al. (2011) but that survey relies on the calibration of the distance ladder using objects that lie within the scale of statistical homogeneity, and this may involve complicated systematics given that higher values of H_0 are expected below the statistical homogeneity scale. Estimates of H_0 which do not rely on calibration with nearby objects are often somewhat lower. For example, Courbin et al. (2010) find $H_0 = 62^{+6}_{-4}$ km s^{-1} Mpc^{-1}using the time delay from strong gravitational lensing of quasars, and Beutler et al. (2011) estimate $H_0 = 67 \pm 3.2$ km s^{-1} Mpc^{-1} using the WMAP sound horizon-calibrated BAO signal in the 6dF galaxy survey. These measurements indicate that a value of H_0 consistent with the TS model may still be obtained once systematic errors on distance determinations are reduced.

The bare matter density becomes

$$\bar{\Omega}_{\rm m} = \frac{4(1-f_{\rm v})}{(2+f_{\rm v})^2} = \frac{4(1-f_{\rm v0})(2+f_{\rm v0})\,[3f_{\rm v0}\bar{H}_0 t + (1-f_{\rm v0})(2+f_{\rm v0})]}{[9f_{\rm v0}\bar{H}_0 t + 2(1-f_{\rm v0})(2+f_{\rm v0})]^2}. \quad (2.43)$$

The dressed present-epoch matter density that corresponds to what observers in galaxies will measure can be written in terms of the present void fraction as

$$\Omega_{M0} \;=\; \gamma^3\,\bar{\Omega}_{\rm m0} = \frac{1}{2}(1-f_{\rm v0})(2+f_{\rm v0}). \quad (2.44)$$

All relevant quantities in the timescape model can be written in terms of the present void fraction. Physically, $f_{\rm v0}$ will correspond to some density contrast determined empirically, after the manner of the void statistics analysed by Hoyle and Vogeley (2004) and Pan et al. (2011). The fits to the Gold supernova data of Leith et al. (2007) gave a present void fraction of $f_{\rm v0} = 0.76 \pm 0.05$, corresponding to a dressed matter density $\Omega_{M0} = 0.33^{+0.11}_{-0.16}$. There is no *a priori* reason why this matter density should match the ΛCDM value, but it should be consistent within the constraints imposed by the CMB and the timing of structure formation, which do not change significantly in the TS model.

The luminosity distance can also be written in a relatively simple form using the tracker solution, and we use this form throughout the present studies. First, the redshift determined by wall observers in terms of volume average time is

$$z+1 = \frac{\bar{a}_0\gamma}{\bar{a}\gamma_0} = \frac{(2+f_{\rm v})f_{\rm v}^{1/3}}{3\bar{H}_0 t f_{\rm v0}^{1/3}}, \quad (2.45)$$

where $f_{\rm v}(t)$ is given in (2.41). In practice, this expression is inverted numerically for a given redshift to obtain the expansion age $\bar{H}_0 t$. The luminosity distance integral (2.38) turns out to have an analytic solution:

$$\begin{aligned} \bar{H}_0 d_L &= (1+z)^2(\bar{H}_0 t)^{2/3}\int_t^{t_0} \frac{2\bar{H}_0 {\rm d}t}{(2+f_{\rm v}(t))(\bar{H}_0 t)^{2/3}} \quad (2.46)\\ &= (1+z)^2 y^2\Big[2y + \frac{b}{6}\ln\Big(\frac{(y+b)^2}{y^2-by+b^2}\Big) + \frac{b}{\sqrt{3}}\tan^{-1}\Big(\frac{2y-b}{\sqrt{3}b}\Big)\Big]_y^{y_0} \end{aligned}$$

where $y^3 \equiv \bar{H}_0 t$ and $b^3 \equiv 2(1-f_{\rm v0})(2+f_{\rm v0})/(9f_{\rm v0})$. This expression is plotted for comparison with the ΛCDM distances in Fig. 1.1, with parameter values from Leith et al. (2007).

2.5 Apparent accelerated cosmic expansion

From the tracker solution (Wiltshire, 2007) and the value of the present void fraction from Leith et al. (2007), we obtain the age of the universe in volume average time

$$t_0 = (2 + f_{\rm v0})/(3\bar{H}_0) = 18.7 \pm 0.3 \text{ Gy}, \tag{2.47}$$

while in wall time, to correspond with that measured by observers in galaxies, it is

$$\tau_0 = \frac{2(2 + f_{\rm v0})}{9\bar{H}_0}\left[1 + \frac{(1 - f_{\rm v0})}{3f_{\rm v0}} \ln\left(\frac{2 + f_{\rm v0}}{2(1 - f_{\rm v0})}\right)\right] = 14.7 \pm 0.1 \text{ Gy}. \tag{2.48}$$

Recall that the corresponding ΛCDM age is 13.6 Gy.

From equations (2.3), (2.25), (2.28) and (2.30), we find the volume average deceleration parameter is

$$\bar{q} \equiv \frac{\ddot{\bar{a}}}{\bar{H}^2\bar{a}} = \frac{1}{2}\bar{\Omega}_{\rm m} + 2\bar{\Omega}_{\mathcal{Q}} = \frac{2(1 - f_{\rm v})^2}{(2 + f_{\rm v})^2} \tag{2.49}$$

where the last equality follows from the second line in (2.25) by virtue of the tracker solution. Since this equation is always positive, the volume average observer *detects no cosmic acceleration*. On the other hand, it can also be shown that a wall observer measures an effective deceleration parameter

$$q = \frac{-(1 - f_{\rm v})(8f_{\rm v}^3 + 39f_{\rm v}^2 - 12f_{\rm v} - 8)}{(4 + f_{\rm v} + 4f_{\rm v}^2)^2} \tag{2.50}$$

which is plotted Figure 2.2. Around the time of recombination, the void fraction is small, and the deceleration parameter has the Einstein-de Sitter value. But at $f_{\rm v} = 0.587$ it changes sign, and then approaches the Milne universe value of zero from below at late times. Current indications from SN Ia data (Leith et al., 2007; Smale and Wiltshire, 2011) and gamma ray bursts (Smale, 2011) suggest that the present value of the void fraction is between 0.7–0.85. Hence, an observer in a galaxy at the present epoch registers an *apparent acceleration*. These values for the deceleration parameter from the tracker solution agree with the numerical solution of (2.26) and (2.27).

The comparison of the distance measures of the timescape and ΛCDM models in Fig. 1.1 shows that the timescape distances show less accelerated expansion

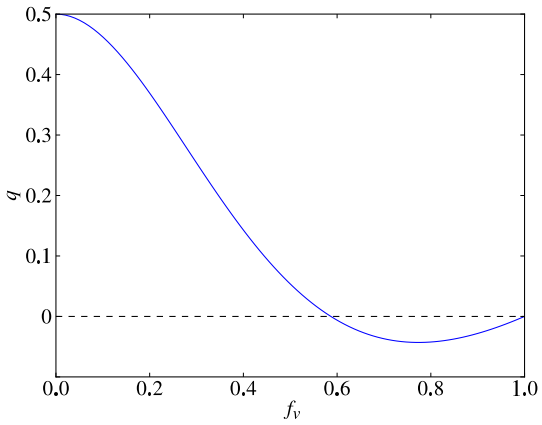

Figure 2.2: Apparent acceleration: Plot showing the deceleration parameter as measured in walls as a function of void fraction, from the equation derived from the tracker solution Eq. (2.50).

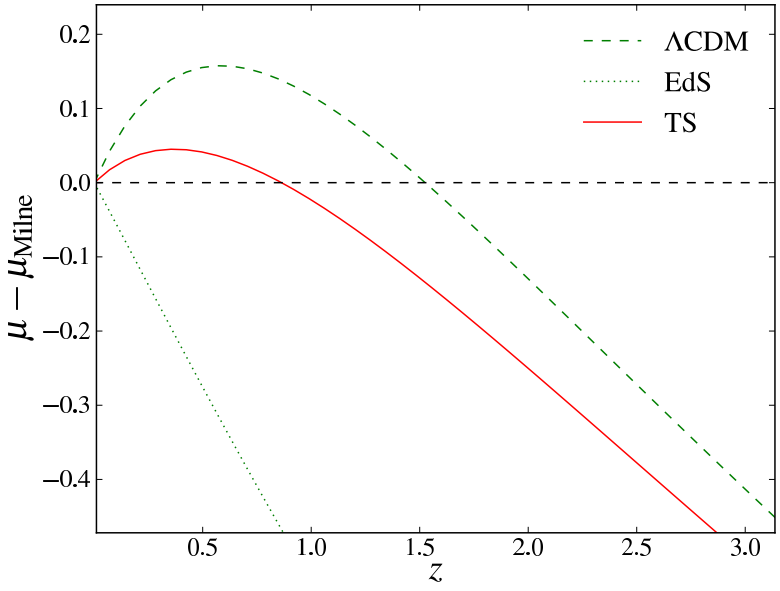

Figure 2.3: Distance modulus differences: The difference in the distance modulus $\mu = 5\log(d_L) + 25$, with d_L in Mpc for the TS, EdS, and ΛCDM models, and that of a Milne universe with the corresponding values of the Hubble constant.

than the ΛCDM model. Figure 2.3 shows the difference $\mu - \mu_{\rm Milne}$ for the ΛCDM, EdS and TS models, with the corresponding values of the Hubble constant used in the Milne distance modulus for an empty universe. At low redshifts the TS residual distance modulus lies between those of the ΛCDM and the Milne. The ΛCDM expansion is accelerated relative to a Milne universe out to larger redshifts than the TS expansion. As noted in Leith et al. (2007), the lower gradient of the theoretical residual in the TS model than in the ΛCDM model reflects the fact that the TS distance modulus approaches that of a Milne universe at late times.

There is also a more subtle philosophical contrast between the models in Figs. 1.1 and 1.2. The ΛCDM model claims to represent the actual expansion history of the universe. An object with a given redshift can be said to occupy a universe in which the deceleration parameter had a particular value, according to whether the prevailing influence on the expansion was matter or dark energy. In the case of the timescape distances, we can only say that distances along the past light cone will appear to have this particular form because the rulers and clocks of observers in gravitationally bound walls will "dress" cosmological parameters according to the present extent of voids by volume.

The timescape distances depicted in Figs. 1.1 and 1.2 are also valid only on scales larger than the *scale of statistical homogeneity*, at which the variance of the density reduces to within certain minimal limits (A rough estimate of $\sim 6\%$ is given in Wiltshire (2009), which fits well with estimates of 7–8% from galaxy clustering statistics on scales larger than the BAO scale (Hogg et al., 2005; Sylos Labini et al., 2009)). Below this scale, local effects, i.e. the unique statistics of voids surrounding a given wall location, will generate variation in (2.38). In the standard model, for $0.033 \lesssim z \lesssim 0.1$, the simple Hubble law applies. There is a single, global Hubble constant, and if a measured velocity cz is not equal to the distance $H_0 d_L$ then the difference is said to be due to random motion induced in the object by nearby density variations—the so-called *peculiar velocity*. In Chapter 5, we take a different approach since the assumption of a single linear Hubble law is restrictive when the density distribution is inhomogeneous. We will calculate the variance in the local expansion rates assuming the existence of some average Hubble law, but without imposing the clear distinction between peculiar

velocities and velocities due to cosmic expansion[1].

In the timescape scenario, there is a different interpretation of local variance. Below the scale of statistical homogeneity we expect to see significant variance in the Hubble flow, because, with respect to any one set of clocks, the underdense voids expand faster than the more dense walls. Since voids dominate the volume of the universe, if we average only on nearby scales we will typically measure a higher value of the Hubble constant than the global average, H_0. A measurement confined to our own local wall, e.g., towards the Virgo cluster, would produce a lower value. As we look out to greater and greater distances, however, a typical line of sight will eventually intersect as many walls and voids as the global average. If we perform a spherically symmetric average over the sky to try to determine the Hubble constant using only nearby measurements within some given finite maximum radius, which is then varied, the inferred Hubble "constant" should peak at the dominant void scale $30\,h^{-1}$ Mpc, i.e. at $z\sim 0.01$, with a maximum value up to 17% greater than the global average and then steadily decrease to near the global average value as the scale of statistical homogeneity is reached. The latter scale, which corresponds to our scale for the coarse-graining of dust, is about $100\,h^{-1}$ Mpc. These expectations are consistent with the data analysis of Li and Schwarz (2007), and future observations would have the potential to either rule out or strongly constrain the TS scenario.

We investigate local variance in the Hubble flow in Chapter 5, but in the next two chapters, we test the timescape luminosity distance (2.38) on scales above the statistical homogeneity scale.

[1]In the definition of peculiar velocity $V_{\rm pec} = cz - H_0 r$ we can measure cz without ambiguity, but H_0 and r depend on the model assumed.

Chapter 3

Testing the distance-redshift relation with type Ia supernovae

3.1 Introduction

It turns out that whether or not the supernova data give meaningful results when applied to the timescape model depends on the method used to process the observations in the supernova dataset. This chapter discusses the use of type Ia supernovae as standard candles, and the subtle questions regarding model dependence that arise when one wishes to test a non-FLRW cosmological model. The material presented here has been published in a paper: Smale and Wiltshire (2011). It is organised as follows. Section 3.2 gives a general history of events that have made possible the use of type Ia supernovae as standard candles. In Section 3.3 there is a discussion of supernova data reduction methods. Their different ways of treating systematic uncertainties are described in Section 3.4—some of these have profound consequences for testing the timescape model. There is much background to cover, so a supernova analysis of the timescape model is not discussed until Section 3.5. There is then a discussion in Section 3.6 and conclusions are presented in § 3.7.

3.2 The advent of supernova cosmology

3.2.1 "...this striking result"

Ever since the early twentieth century, when supernovae were recognized as originating in other galaxies, researchers have wanted to use them as standard candles. Compared with galaxies, whose absolute magnitudes will depend strongly on stellar evolution and galactic mergers, supernovae are much more likely candidates for being standard candles. It has taken the better part of 100 years for technology and our understanding of supernovae to advance sufficiently to make supernova cosmology possible.

It turns out that "Nature has more than one way to explode a star" (Kirshner, 2009). Type Ia supernovae (SNe Ia) are distinguished from other supernovae by spectral analysis: they show a distinctive Si II absorption feature and lack hydrogen and helium lines. Most supernovae explode via core collapse, but SNe Ia are different. They are most likely to result when the mass of a white dwarf in a binary system accretes enough material from its companion star to bring its mass close to the Chandrasekhar limit. Since most stars (about 97% of stars in the Milky Way) will end their lives as white dwarves, and since many stars are in binary systems (Sparke and Gallagher (2007) ironically remark that "three out of every two stars are in a binary"), this is a likely possibility. As the mass of the white dwarf approaches the Chandrasekhar limit, the weight of its outer layers overcomes the electron degeneracy pressure that has been supporting it, triggering runaway nuclear fusion of carbon right up to ^{56}Ni at the iron peak. Energy released in the fusion builds up rapidly and sends a shockwave expanding toward the surface, ejecting the outer layers at speeds of up to 10% that of light. In a SN Ia explosion as much energy is expelled in a few weeks as the sun radiates in its whole lifetime, making them visible over cosmological distances.

This process of slow approach toward the Chandrasekhar limit followed by annihilative explosion wipes out much of the dependence on variations of composition or even mass in the progenitor stars. However, by the early 1990s, with the advent of CCD detectors and sufficient observations, it became apparent that within the type Ia category there is still considerable variability: the explosion

occurs somewhere near the Chandrasekhar limit rather than exactly at it, and their intrinsic luminosity can vary by a factor of three. A correlation between the duration of the SNe Ia light curves and their brightness was discovered by Phillips (1993), and is probably a reflection of the amount of ^{56}Ni produced in the fusion phase. Correction for this "stretch" decreases the dispersion of the SNe Ia about the Hubble line to about 0.3 mag (Kirshner, 2009)—sufficiently precise, given more observations, to shed light on such questions as the cosmic matter density and cosmic expansion.

The first major collection of SNe Ia observations for cosmology was made at the Calán and Tololo telescopes in Chile by Hamuy et al. (1995, 1996). This study of 29 nearby SNe Ia confirmed the Phillips relationship, also noting "significant correlations" between the absolute luminosity and the morphological type of the host galaxy. The Calán/Tololo sample was used to calibrate higher redshift SN Ia samples from the High-Z group (HZT) of Riess et al. (1996) and from the Supernova Cosmology Project at the Lawrence Berkeley Laboratory (Perlmutter et al., 1997). With only seven high-redshift SNe Ia ($0.35 \leq z \leq 0.45$), the SCP found initially that their results were consistent with a flat matter-dominated universe. Then the HZT (Riess et al., 1998; Schmidt et al., 1998) showed the first evidence of accelerating expansion: SNe Ia at $z \simeq 0.5$ are about 0.2 mag dimmer than a spatially flat CDM model predicts—a deviation of just 0.5% from the EdS distance modulus at that redshift. Another SCP paper published very soon after, this time based on a larger high-redshift sample, corroborated the HZT result (Perlmutter et al., 1999). Their Hubble diagram is shown in Fig. 3.1.

Within the context of FLRW models, the best fit to the supernova data required a flat (critical) energy density, roughly 30% of which is matter (both dark and baryonic), and 70% of which comprises an exotic "dark energy", which pushes the universe apart even as the matter induces further collapse. The simplest candidate for the dark energy is a cosmological constant, and the supernova evidence for such a cosmological constant, combined with accumulating evidence from the CMB for a flat universe and evidence from galaxy clustering statistics for a low Ω_{m}, constitute a "concordance" of the ΛCDM cosmological parameters.

This "striking result"[1] was not accepted without question. Such a dimming

[1] Riess et al. (1998)

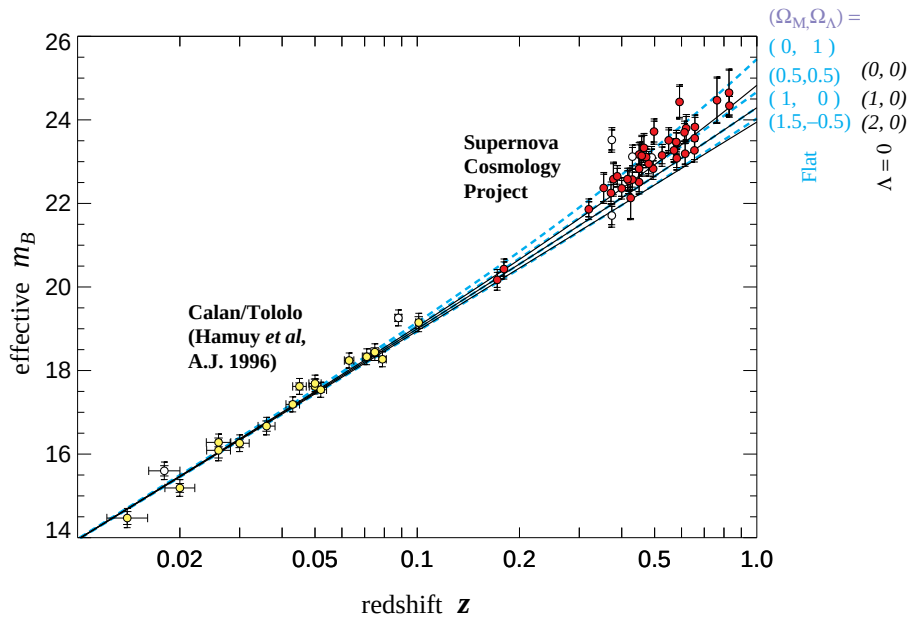

Figure 3.1: SNe Ia Hubble diagram: Hubble diagram published by the SCP (Perlmutter et al., 1999), showing the evidence for a non-zero Ω_Λ. The best fit line is given by the flat cosmology labelled (0.5,0.5).

without reddening could be due to the presence of a uniform high-redshift "grey dust". However, on the basis of the dispersion of a small number of high-quality high-redshift observations made with the Hubble Space Telescope (HST), this could be satisfactorily ruled out (see Fig. 3.2). Calibrating high-redshift SNe Ia using low-redshift ones requires an assumption that the supernovae will be identical, whatever their redshift. There are indications that this assumption is overly simplistic. For example, SNe Ia at high redshifts in the "Union" sample are redder than their low-redshift counterparts (Amanullah et al., 2010). It is conceivable that the type of the progenitor stars, the type of the explosion, and the star-forming activity of the host galaxy could also affect the absolute luminosity. Evidence of the extent of these effects is only now being gathered, however—it is unlikely that evolution could bias measurements at a level greater than the current systematic uncertainties.

3.2.2 "... unique leverage"

Subsequent supernova surveys aimed to check the robustness of these results by increasing the numbers of SNe Ia observed and using follow-up spectroscopy where possible. They also aimed to determine some of the properties of the dark energy by determining its equation of state $w = p/\rho$. For a cosmological constant, $w = -1$, but w could conceivably vary. The "Gold" sample of Riess et al. (2007), a collection of 182 high-quality observations from various telescopes, included 21 SNe Ia observed with the Hubble Space Telescope (HST), and showed that SNe Ia probe not just the "dark energy"-dominated acceleration regime, but also the end of the preceding matter-dominated era of deceleration. The Hubble diagram from this paper is shown in Fig 3.2. The "unique leverage"[1] of these objects ruled out rapidly evolving dark energy, and was consistent with a constant equation of state out to $z \geq 1$.

The SuperNova Legacy Survey (SNLS), with a sample of 71 high redshift events, found $w = -1.023 \pm 0.090 \pm 0.054$ (Astier et al., 2006), where the first error is statistical and the second is due to systematics. The ESSENCE (Equation of State: SupErNovae trace Cosmic Expansion) survey of Wood-Vasey et al. (2007) found $w = -1.05^{+0.13}_{-0.12} \pm 0.13$ from 60 SNe Ia, with empty and matter-only universes ruled out at $> 4.5\ \sigma$.

3.2.3 "... a more perfect union"

The high-redshift observations that have changed the way we think of the universe are critically dependent on the low-redshift sample. Low-redshift observations provide an opportunity to investigate and reduce systematic uncertainties and anchor the Hubble diagram at the redshifts at which it is independent of cosmology—for example, having no low-z SNe Ia increases the uncertainty on a constant $1 + w$ by a factor of two (Linder, 2006).

A sample of 44 nearby SNe Ia was collated by Jha et al. (2007), who developed a version of the Multi-Colour Light curve Shapes (MLCS) light curve fitter used in the HZT studies to incorporate better K-corrections and a detailed, empirical treatment of host galaxy extinction and reddening (see § 3.3.1). This study also

[1] Riess et al. (2007)

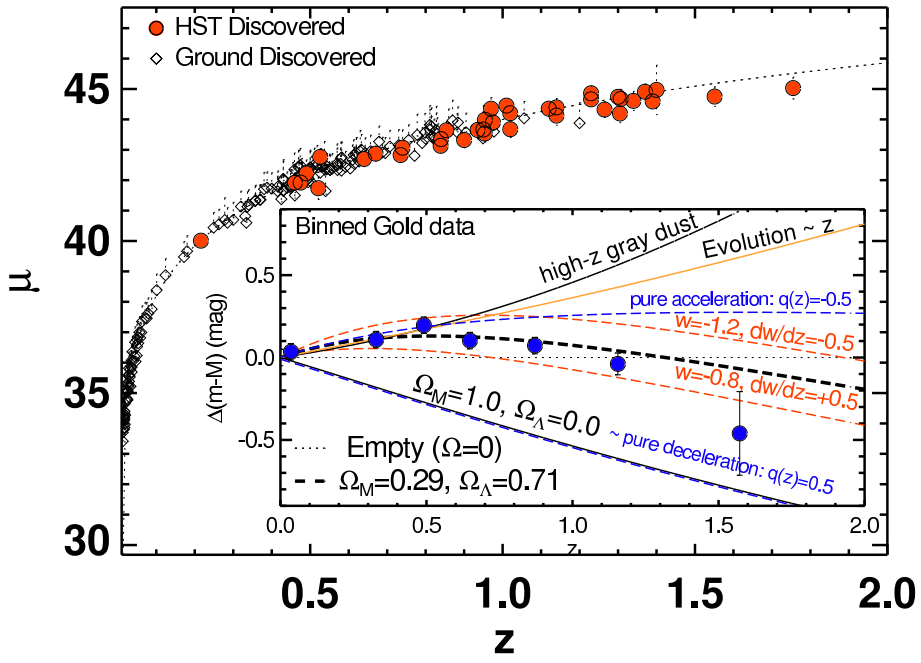

Figure 3.2: SNe Ia Hubble diagram: Hubble diagram published by the HZT (Riess et al., 2007), showing the 21 SNe Ia at $z > 1$ discovered with the Hubble Space Telescope (HST), with a ΛCDM Hubble line derived with $\Omega_M = 0.27$ and $\Omega_\Lambda = 0.73$. The "lever arm" probed by the HST SNe Ia is obvious—objects at these redshifts provided strong constraints on the kinds of cosmological models being tested. The inset shows the differences in Hubble lines for several of these models from an empty (Milne) universe. The SNe Ia have been binned, and the HST SNe Ia at $z > 1$ come from the era *before* cosmic acceleration, when the universe was undergoing matter-dominated *de*celeration.

supported the detected a systematic +6% local deviation from the global Hubble law, first observed and dubbed the "Hubble bubble" in the supernova data of Zehavi et al. (1998). We shall have much more to say about the Hubble bubble later in this chapter (e.g. § 3.4.2) and in Chapter 5.

The Union sample (Kowalski et al., 2008) standardized 307 SNe Ia from various sources, reanalysing them using the Spectral Adaptive Light curve Template (SALT) fitter developed by Guy et al. (2005) for the Legacy survey. The nearby sample from Jha et al. (2007) was united with the Union to form the Constitution

("a more perfect Union"[1]) sample by Hicken et al. (2009), also using the SALT fitter. This study also contained comparisons of large MLCS- and SALT-reduced datasets to investigate the consistency between the fitters. The Union sample was updated in Amanullah et al. (2010) by refining the light curve-fitting process and adding new high-precision high-redshift SNe Ia from the HST. With 557 objects, this "Union2" is the current state-of-the-art sample.

The Carnegie Supernova Project (CSP) (Folatelli et al., 2010; Freedman et al., 2009) aims to increase the numbers of low redshift SNe Ia and include measurements in the near infrared for the resolution of some of the intrinsic colour/extinction degeneracy issues that arise at shorter wavelengths.

There are several light curve fitters in current use. All are based on variations of the Phillips stretch relation, but treat the color evolution and extinction in different ways. Each fitter takes the measured light curves and transforms them into a distance modulus for each supernova. It has been widely noted (e.g., Hicken et al. (2009); Kessler et al. (2009); Kirshner (2009); Komatsu et al. (2011)) that there are discrepancies between datasets reduced with different fitters, and also between different implementations of the same fitters. This is a significant issue for our investigation here.

One direct way of quantifying the differences is to compare the published distance moduli for the 140 SNe Ia common to the Gold, Union and Constitution datasets. In Fig. 3.3 we plot the differences between the published Gold and Constitution distance moduli for the 140 data points they have in common. This shows that $|\mu_{\rm Gold} - \mu_{\rm Const}| \lesssim 1$ mag. Despite being less than the level of the current uncertainties, individually these differences are nearly significant in some cases. In the absence of systematics, there should be exact agreement for a given supernova, so it could be said that even the smaller differences are significant, or potentially could be significant when propagated to parameter fits. Moreover, clearly, as systematic uncertainties are reduced, the discrepancies between fitters will become more important. Even with the uncertainties as they are, it is obviously very important when estimating cosmological parameters from the data from various SN Ia observation programmes that the data reduction process is consistent across the whole dataset. There is no correct fitter: a given fitter

[1] Hicken et al. (2009)

will instead embody certain physical assumptions or be more computationally efficient. These fitters are continually being developed and refined, and their strengths and limitations are revealing new aspects of supernova physics as measurements become more precise. We now describe two fitters currently in general usage.

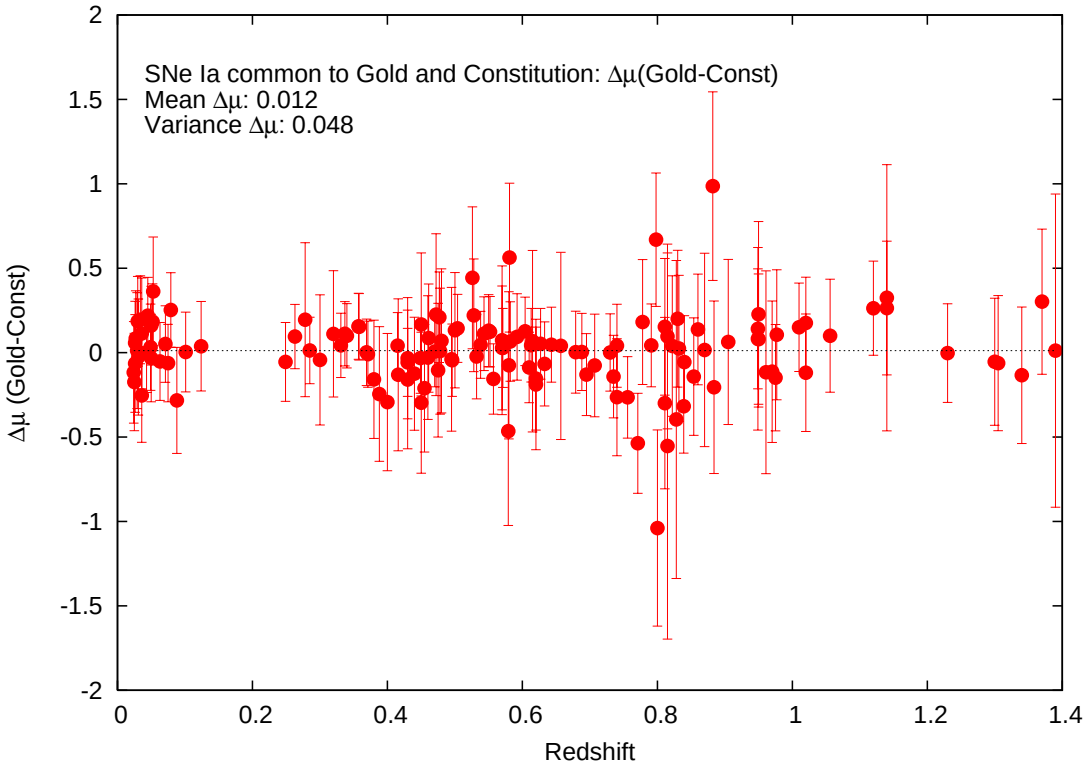

Figure 3.3: Same SNe Ia, different μ: Plot showing the difference between distance moduli published in Gold and Constitution for the 140 SNe Ia common to the two datasests. This shows that $|\mu_{\rm Gold} - \mu_{\rm Const}| \lesssim 1$ mag. However, the differences show no obvious redshift-dependent trend so they should not bias the relative estimates of cosmological parameters.

3.3 From fluxes to magnitudes: Light curve fitters

3.3.1 MLCS2k2

MLCS2k2 (Jha, Riess, and Kirshner, 2007) is the most recent incarnation of the LCS (Light Curve Shapes) fitter developed by the High-Z Supernova Team (Riess et al., 1998; Schmidt et al., 1998). This is the fitter used in the Gold dataset of Riess et al. (2007). For each supernova, MLCS2k2 returns a distance modulus μ and its uncertainty via the MLCS2k2 model magnitude

$$m^{e,f}_{\rm model} = M^{e,f'} + \mu + p^{e,f'}\Delta + q^{e,f'}\Delta^2 + X^{e,f'}_{\rm host} + X^{e,f}_{\rm MW} + K^{e}_{f,f'}. \tag{3.1}$$

A model magnitude is fitted at each time point (indexed by epoch e, and defined relative to the time of maximum brightness), and for each observer-frame filter index f. The model is defined in $UBVRI$ rest frame filters f', with the light curve shape parameter Δ representing the relation between luminosity and duration. Extinction due to dust is divided into host galaxy $X_{\rm host}$ and Milky Way $X_{\rm MW}$ components, and $K_{f,f'}$ is the K-correction that accounts for the redshift-induced pass band discrepancy between rest-frame and observer-frame filters. Obtaining a set of distance moduli takes two steps. One first computes the model vectors $M^{e,f'}$, $p^{e,f'}$, and $q^{e,f'}$ by minimising the distance modulus residuals of a training set of nearby SNe Ia, which lie within the range in which the Hubble line is linear, yet are sufficiently distant for their peculiar velocities to be negligible compared with their Hubble-flow velocity. Secondly, one fits for the distance moduli along with the remaining parameters.

The extinction terms are set up independently of these fits. There is some colour dependence on the brightness incorporated in Δ, but there is also a significant colour dependence on extinction by dust in the host galaxy and in the Milky Way. Following Cardelli et al. (1989), MLSCS2k2 characterizes the extinction by first defining $\zeta^{e,f'} \equiv X^{e,f'}/A_0^{e,f'}$, where $A_0^{e,f'}$ is the extinction in passband f' at maximum light in B. Hence, $\zeta^{e,f'}(t=0)$ is defined to be 1, and $\zeta^{e,f'}$ encapsulates the time dependence of the exinction. Then one fits for the coefficients $\alpha^{f'}$ and $\beta^{f'}$, defined by

$$X^{e,f'} = \zeta^{e,f'}\left(\alpha^{f'} + \frac{\beta^{f'}}{R_V}\right)A_V^0, \tag{3.2}$$

at maximum light, where R_V is the ratio of the extinction in the V-band to the colour excess $E(B-V)$. A "Milky Way-like" reddening law, based on an average over a number of lines of sight, has $R_V = 3.1$. Dust extinction and SNe Ia will be discussed in more detail in § 3.4.1.

In MLCS2k2, the light curve fit is essentially a process of finding a likelihood function of the observed fluxes or magnitudes as a function of four model parameters for each SN Ia: the distance modulus μ, the time of peak luminosity in the rest-frame B-band, the shape-luminosity parameter Δ, and the host galaxy extinction A_V. The estimates and uncertainties of each parameter value are determined by marginalizing over the three other parameter probability distribution functions and taking the mean and rms of the resulting probability distribution for the parameter of interest.

With a distance modulus and its uncertainty for each supernova, cosmological parameter estimates are obtained by minimizing the χ^2 statistic:

$$\chi^2 = \sum_i \frac{[\mu_i - \mu(z_i, H_0, \Omega_{M0})]^2}{\sigma_\mu^2} \tag{3.3}$$

where $\mu(z_i, H_0, \Omega_{M0})$ is the theoretical distance modulus calculated for the redshift of the ith SN Ia, based on a set of cosmological parameters H_0 and $\Omega_{\rm m}$ for a spatially flat universe. Of course, other constraints can be introduced: e.g. in Kessler et al. (2009), $\chi^2_{\rm WMAP}$ and $\chi^2_{\rm BAO}$ terms are added to (3.3) to incorporate prior information from WMAP CMB measurements and SDSS luminous red galaxy BAO measurements respectively. The measurement variance $\sigma^2_{\mu_i}$ must be carefully specified. In MLCS2k2, the distance modulus uncertainty is given by (Kessler et al., 2009)

$$\sigma_\mu^2 = \sigma_{\rm fit}^2 + \sigma_{\rm int}^2 + \sigma_z^2, \tag{3.4}$$

where $\sigma_{\rm fit}$ is the statistical uncertainty from the MLCS2k2 fit, $\sigma_{\rm int}$ is an intrinsic uncertainty computed such that the χ^2 per degree of freedom is one for the Hubble diagram constructed from the (nearby) training sample, and σ_z incorporates redshift and peculiar velocity uncertainties.

3.3.2 SALT

The Union and Union2 datasets use a light curve fitter called **S**pectral **A**daptive **L**ight curve **T**emplate, or SALT (Guy et al., 2005). Whereas MLCS calibrates the higher-z SNe to a nearby training set of SNe Ia assuming a close to linear Hubble law over relevant distances, SALT uses the whole data set to calibrate empirical light curve parameters. To deal with a determination of empirical parameters for objects at unknown distances, the absolute magnitude M and H_0 are combined as

$$\mathcal{M} = M - 5\log_{10} h + 5\log_{10} c + 10. \tag{3.5}$$

In the SALT algorithm, the distance modulus is then modeled as

$$\mu_i = m_{B_i}^{\max} - \mathcal{M} + \alpha(s_i - 1) - \beta c_i. \tag{3.6}$$

The initial light curve standardization results in best fit values for the time of maximum B-band light, t_0, the rest-frame peak magnitude in the B-band, $m_B^{\max}$, a stretch factor s, and a colour parameter c, in which is combined the intrinsic supernova colour and reddening due to dust in its host galaxy.

SALT II (Guy et al., 2007) builds on SALT by including spectroscopic information to improve the wavelength resolution of the spectral templates. Here we use the relationship between the SALT stretch parameter s and the SALT II parameter x_1 given in Guy et al. (2007) in order to compute cosmological parameters for SALT II SNe Ia with the same program as we use for the SALT SNe Ia. In what follows, we use "SALT" to refer to both SALT and SALT II: they incorporate the same assumptions.

In MLCS2k2, the cosmological parameter estimation step is "decoupled" from the distance modulus determination. In SALT, after obtaining the parameters s (or x_0 and x_1 for SALT-II) and c for each SN Ia from the light curve fits, a magnitude for each supernova is fitted via the equivalent expression to eq. (3.3), so that the cosmological parameters are obtained as part of a single minimization process, viz.

$$\chi^2 = \sum_i \frac{[m_{Bi} - m(z_i; \alpha, \beta, \mathcal{M}, \Omega_{M0})]^2}{\sigma_{m_i}^2 + \sigma_{\rm int}^2} \tag{3.7}$$

This process results in *global* estimates of α, β, and $\mathcal{M}$, and a corresponding $\Omega_{\rm m}$. In general, the denominator of eq. (3.7) will also incorporate the full covariance matrix of the parameters from the light curve fits and a contribution from the peculiar velocity dispersion. As before, an intrinsic uncertainty, $\sigma_{\rm int}$, is calculated during the fitting process as having the value required to yield a reduced χ^2 of one (Astier et al., 2006; Guy et al., 2007; Guy et al., 2005), but this time, it is the *global* reduced χ^2 that is set to one, not just that for the nearby sample. The published tables of supernova distance moduli obtained with the SALT fitters therefore have a certain inherent model dependence, because the cosmological parameters are varied to reduce scatter in the Hubble diagram. In the case of the Union and Constitution datasets, the quoted distance moduli were computed for a spatially flat ΛCDM universe with a constant w. The computation of the systematic uncertainty for which the $\chi^2 = 1$ amounts to an assumption that the model is correct, and that any variation of the data around the theoretical line is due to chance alone. This may be practical, but may not necessarily realistically estimate the systematic uncertainties. The effect of the systematic uncertainty values on fits to the (fundamentally different) timescape model will be discussed in § 3.5.1 below. A more detailed alternative treatment of the systematic uncertainties, in addition to the one just described, is presented in Kowalski et al. (2008) in order to check that the χ^2 values are reasonable and to vindicate the use of the intrinsic uncertainties calculated via the $\chi^2/{\rm dof} = 1$ method.

Table 3.1 shows the main differences between the MLCS2k2 and SALT fitters.

3.3.3 Same supernova, different distance?

The differences in Fig. 3.3 are not only to be found in comparing MLCS with SALT. If new data is added to a SALT-reduced sample, a global refit of all the empirical light curve and cosmological parameters has to be performed. What effect does this have on the distance moduli? To see this, we have taken the 140 SNe Ia common to the Gold, Union and Constitution datasets (the same 140 objects as shown in Fig. 3.3) and computed a SALT fit to this subsample

Table 3.1. Summary of main differences between MLCS2k2 and SALT/SALT-II SN light curve fitters.

	MLCS2k2	**SALT/SALT-II**
Training SNe Ia	Nearby	Both nearby and distant
Dust	Any colour variation beyond Δ attributed to dust. Assumption that reddening in host galaxy follows CCM89 MW-like law $R_V = 3.1$	Colour parameter c does not distinguish between intrinsic colour variation & variation due to dust
Intrinsic uncertainties	$\sigma_{\rm int} = 0.16$ obtained from setting χ^2/dof=1 for nearby SNe Ia	$\sigma_{\rm int}$ obtained from setting global χ^2/dof=1
χ^2 *minimization*		Global parameters M, α, and β estimated simultaneously with the cosmological parameters. Includes covariance matrix for shape and colour parameters s (SALT), x_0, x_1 (SALT-II), and c
Distance modulus	Independent μ for each SN	μ_i are correlated

directly, assuming a spatially flat ΛCDM model, using Dr Conley's publicly available `simple_cosfitter` code[1]. In Fig. 3.4 we show the differences between these newly calculated distance moduli and the corresponding distance moduli published in the Constitution compilation. We see that there is still scatter (about half that in Fig. 3.3) even though the SALT method has been applied in each case. This is due to the differences between the values of the parameters α, β and M_B determined from only 140 SNe Ia in the subsample, and those determined from all 397 SNe Ia in the full sample. We note too that the `simple_cosfitter` implementation of SALT is not perfectly identical to that used by Hicken et al. (2009). But running `simple_cosfitter` on the whole Constitution sample and comparing the recomputed distance moduli with the published fits shows small and insignificant variation, as is shown in Fig. 3.5.

Much more detailed studies of these sorts of issues have already been conducted by various researchers, revealing a complex picture.

In their comparison of the different fitters, Hicken et al. (2009) found that SALT, SALT II, and MLCS2k2 produce light curve shape and color/reddening parameters that agree well with each other and that it is in determining the distance modulus that systematic offsets are introduced. For example, SALT produces more scatter in high-redshift distance moduli than MLCS2k2, while nearby MLCS distances are larger than in SALT, depending on the treatment of reddening. Such discrepancies will clearly affect the cosmological parameter fits. Hicken et al. (2009) note that although there exist some trends in some μ(MLCS)$-\mu$(SALT) differences versus shape parameter Δ and color parameter β, there are no trends versus redshift, which would indicate the influence of hidden systematics and affect the cosmological parameter fits (Wood-Vasey et al., 2007). These are grounds for hope that retraining with larger datasets, combined with a better treatment of systematic uncertainties, will perhaps reconcile the differences. In the meantime, however, they observe that for the best cut samples, SALT and SALT II estimates of w differ by 0.05–0.09 from the MLCS estimates.

Kessler et al. (2009) find a mismatch between the rest-frame U-band flux model and the light curve data that affects the nearby SNe Ia with the SALT II fitter and all *except* the nearby sample with the MLCS2k2 fitter, leading to a

[1] `http://qold.astro.utoronto.ca/conley/simple_cosfitter/`

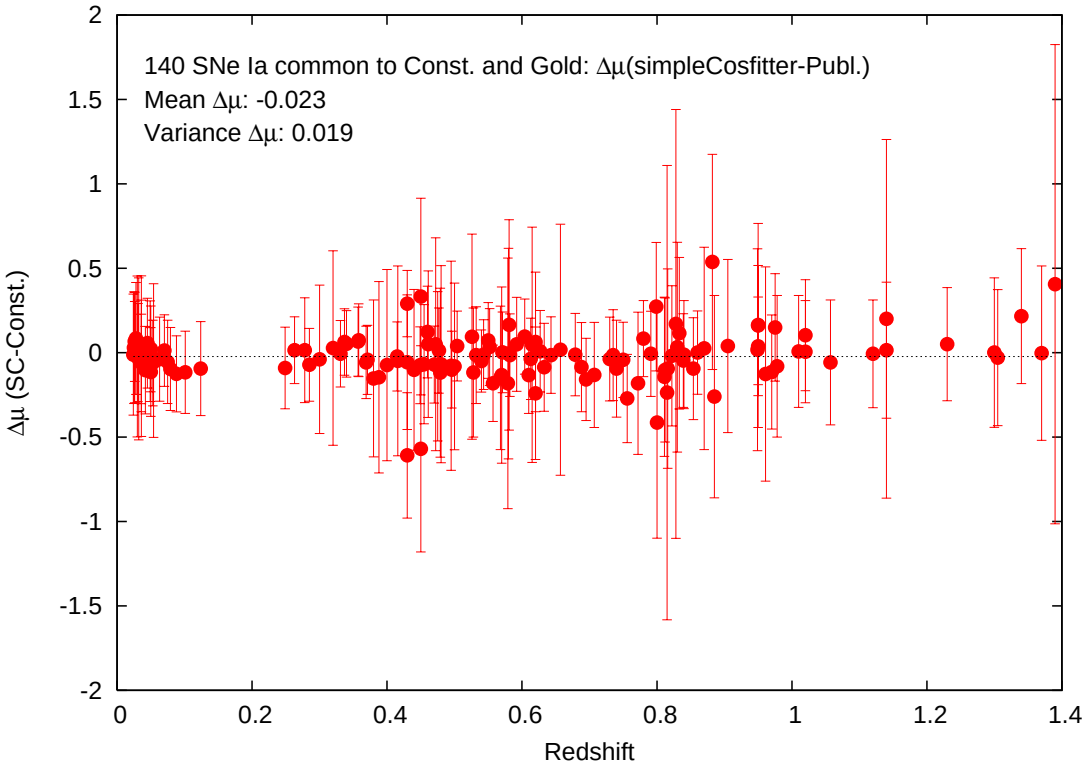

Figure 3.4: Differences in distance moduli between values published in the Constitution sample, and the corresponding values determined with `simple_cosfitter` (ΛCDM) using only the subsample of 140 SNe Ia plotted in Fig. 3.3, as a function of redshift. $H_0 = 65$ km s^{-1} Mpc^{-1}.

discrepancy of 0.31 between the value of w estimated from one of their MLCS2k2 sample combinations and that from the corresponding sample from the MLCS2k2 ESSENCE collaboration (Wood-Vasey et al., 2007). There is clearly a need for the development of better rest-frame U-band models. This is important because the light that we see in the optical bands from high redshift supernovae was emitted in the UV. Recent UV studies of nearby supernovae from *SWIFT* and the HST confirm that there is more variability in the UV light curves than in their optical counterparts (Brown et al., 2010; Wang et al., 2011). Dust strongly absorbs in the UV, re-radiating in the IR, and the consequent bluer $U - B$ would lead to an underestimated host-galaxy reddening and an overestimate of the distance (Wang

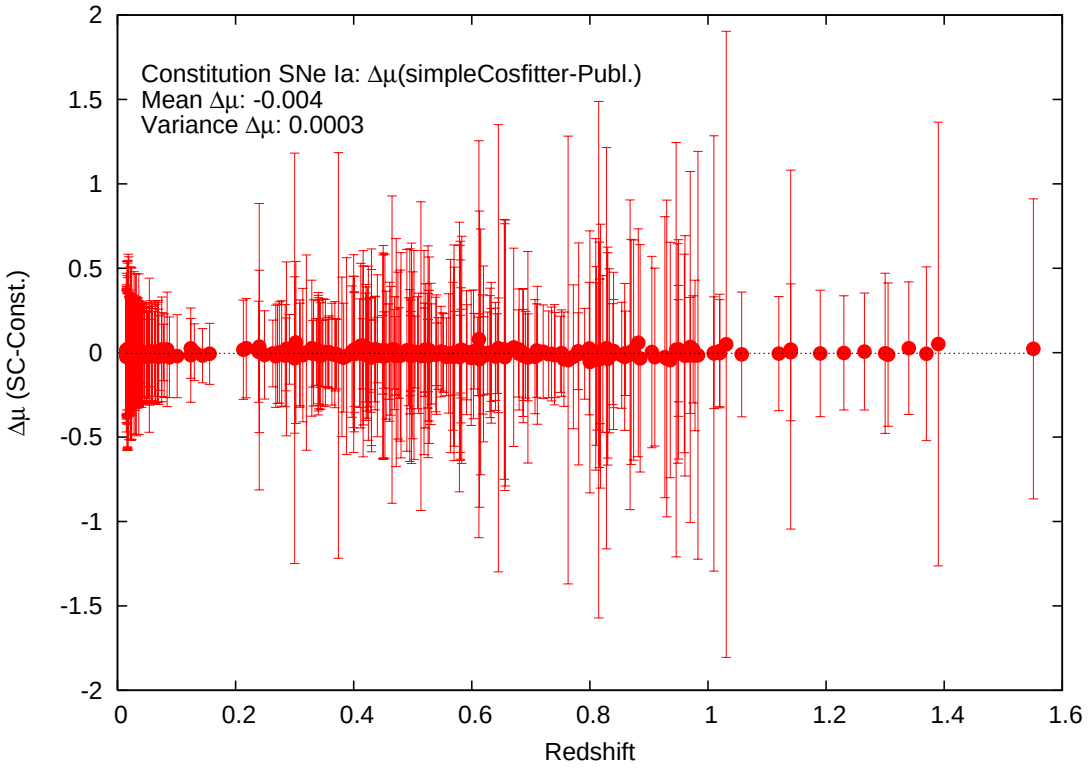

Figure 3.5: Differences in distance moduli between published values in the Constitution sample, and values determined with `simple_cosfitter` (ΛCDM) using the full Constitution sample, as a function of redshift. $H_0 = 65$ km s^{-1} Mpc^{-1}.

et al., 2011). More observations in the UV could help to disentangle the intrinsic colour variation from dust-related colour variation. In any case, UV light curves need to be better understood in order to properly assess their impact on the estimation of cosmological parameters.

When constraining dark energy parameters derived from WMAP7+BAO+SN, Komatsu et al. (2011) find that the parameters of the minimal 6-parameter ΛCDM model change depending on whether the SN Ia compilation used SALT II or MLCS2k2, based on the SN samples of Kessler et al. (2009). The dark energy density values varied by 2.5σ. They note that it is not presently obvious how to properly incorporate systematic uncertainties into the likelihood analysis and thereby reconcile different methods and datasets. Komatsu et al. (2011) use

the Constitution sample when quoting canonical cosmological parameter values, because it is an extension of the Union sample which they used for the 5-year WMAP analysis.

3.3.4 Combining datasets

There are many subtleties in the individual implementations of the SNe Ia reduction, which means that combining samples is not a trivial exercise. For example, the cosmological parameters computed for the Union dataset of Kowalski et al. (2008) are obtained from the χ^2 equation (3.6) above, but with additional nuisance parameters encoding the propagating systematic uncertainties (see their equation (5)). When they augment the Union set with the nearby CfA3 SNe Ia to produce the Constitution dataset, Hicken et al. (2009) first take the SALT parameters of the Union dataset, $m_B^{\max}$, s, and c, "out of the box" and calculate a best-fit cosmology incorporating a BAO prior in the cosmological fit: $\chi^2 = \chi^2_\mu + \chi^2_{\mathrm{BAO}}$. The reason for this is presumably that the BAO prior constrains the range of Ω_{m} better than the SNe Ia alone, and thus provides a more stringent assurance that the new cosmological parameter estimation has been "in line" with the old one. Once the Union results were reproduced with sufficient accuracy, the light curves of nearby Union SNe Ia were run once again through SALT to ensure that the new $m_B^{\max}$, s, and c values agreed with the Union ones, and then the whole CfA3 sample was run through SALT, to be combined with the Union set "without introducing any significant offset". The uncertainty in the distance modulus σ_μ is calculated by Hicken et al. (2009) in a way that differs from Kowalski et al. (2008). Essentially, the σ_μ calculated by Hicken et al. (2009) contains adjustments that ensure reproduction of the same uncertainty in $1+w$ as in Kowalski et al. (2008).

3.4 Systematic uncertainties

Because the results of fitting the timescape model to the supernova data depend on the supernova data reduction method, it is important that the differences between the data reduction methods are understood. The methods treat the systematics in different ways. It is clear from equations (3.1) and (3.6), for

example, that the models employ different assumptions about reddening and extinction in their modification of the distance modulus.

Table 3.2, taken from Wood-Vasey et al. (2007), lists the systematic uncertainties affecting the measurement of the dark energy equation of state w along with their estimated contribution to its uncertainty. The most considerable of these are clearly the treatment of host galaxy extinction and intrinsic SN Ia colour variation. The most important of these are the effects of dust and assumptions about colour, and the possibility of a Hubble bubble. Introductory discussions of these, along with other connected uncertainties like evolution, are given in the next sections as a background to their consideration in the context of the timescape model.

3.4.1 Dust: extinction/reddening

There exist at least four possible sources of dust, a better understanding of any or all of which have the potential to significantly reduce scatter on the Hubble diagram: (i) dust in the Milky Way; (ii) dust in the host galaxy; (iii) dust in the local, circumstellar environment of the supernova; and (iv) dust in the intergalactic medium. These will be discussed in further detail in § 3.6 below, but a general background on Milky Way and host galaxy dust is given here.

Milky Way dust. Extinction by interstellar dust in the Milky Way is relatively well understood: in the Near Infrared (NIR) and optical bands ($\lambda^{-1} \leq 3.5\ \mu\text{m}^{-1}$) it is conventionally understood to follow power laws that can be parameterized by the visual band extinction-reddening ratio $R_V = A_V/E(B-V)$. Extinction curves for lines of sight with various values of R_V are shown in Fig. 3.6. Averaging over many lines of sight gives $R_V = 3.1$ (Cardelli, Clayton, and Mathis, 1989), the standard value for the Milky Way interstellar medium, often referred to as the "CCM89" value.

Host galaxy dust. In the MLCS supernova cosmology papers—in particular those of the Harvard CfA (e.g. Jha et al., 2007; Riess et al., 1996, 2007)—for simplicity, the assumption is made that extinction in supernova host galaxies follows a Milky Way-like extinction curve. Although it is not unlikely that there might be some systematic variation of R_V with redshift, recent SN Ia-independent

Table 3.2. Potential sources of systematic error on the measurement of w

Source	Δx	Δ_w
Photometric errors from astrometric uncertainties of faint objects	0.005 mag	0.005
Bias in differential image photometry	0.002 mag	0.001
CCD linearity	0.005 mag	0.005
Photometric zeropoint differences in R,I	0.02 mag	0.04
Zero-point offset between low and high z	0.02 mag	0.02
K-corrections	0.01 mag	0.005
Filter passband structure	0.001 mag	0
Galactic extinction	0.01 mag	0.01
Host galaxy R_V	0.5	0.01
Host galaxy extinction treatment	prior choice	0.08
Intrinsic color of SNe Ia	0.02 mag	0.06
Malmquist bias/selection effects	0.03 mag	0.02
SN Ia evolution	0.02 mag	0.02
Hubble bubble	0.02	0.06
Gravitational lensing	0.01 mag	< 0.001
Grey dust	0.01 mag	0.01
Subtotal w/o extinction+colour	$\cdots$	0.082
Total	$\cdots$	0.13
Joint ESSENCE+SNLS comparison	$\cdots$	0.02
Joint ESSENCE+SNLS Total	$\cdots$	0.13

Note. The systematic errors for the first ESSENCE cosmological analysis (Wood-Vasey et al., 2007). The issue of treatment of A_V and colour distribution is clearly the dominant systematic effect and will need to be seriously addressed to reduce systematic errors to 5%.

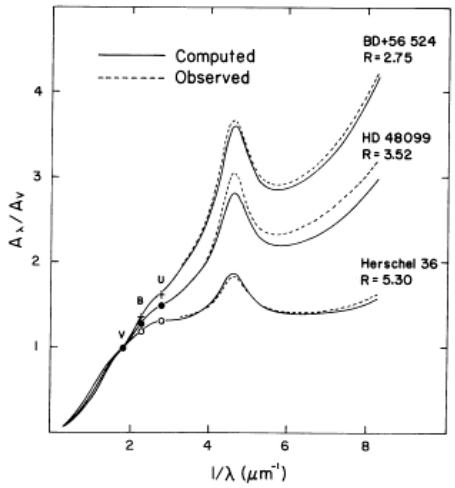

Figure 3.6: Interstellar dust extinction, showing the infrared and optical regions (points labelled V,B and U) where R_V is fitted, the "graphite bump" at 2175 Å, and the strong extinction in the far UV. The plot comes from Cardelli et al. (1989).

studies of some nearby galaxies suggest that in general, extragalactic R_Vs are surprisingly close to the CCM value, at least at low redshifts. A widely used technique for determining extragalactic extinction is to subtract the image of the original galaxy from a dust-free model of a galaxy of the same Hubble type with a smooth distribution of emitted light. This method applies best to early-type galaxies in which inhomogeneities such as spiral arms and HII regions are absent. Patil et al. (2007) noted that despite the simplicity of this technique, extinction curves had been obtained for only a handful of galaxies prior to 2007, and that the optical extinction curves closely resembled that of the Milky Way. In a multiband ($BVRI$) study of 26 early-type galaxies, using observations from various facilities in India, Patil et al. (2007) obtain R_V values in the range 2.03–3.46, with an average of 3.02. A similar method applied to observations made by the South African Large Telescope, including the U-band, yielded $R_V = 2.82 \pm 0.38$ from eight early-type galaxies (Finkelman et al., 2008) and $R_V = 2.71 \pm 0.43$ from seven more (Finkelman et al., 2010), all at redshifts less than 0.033.

Dust in SN Ia host galaxies at higher redshifts may be parameterised by a different R_V, especially considering that the star formation rate (SFR) is thought to increase out to $z \simeq 2$ (see Fig. 9.17 in Sparke and Gallagher, 2007), but the

assumption is made that over the redshift range in which SNe Ia occur, host galaxy extinction is the same everywhere, just as SN Ia evolution is assumed to be negligible. These assumptions appear to apply, at least to a subsample of the events observed so far, based on matching of SN Ia spectra (Hook et al., 2005).

3.4.2 The Hubble bubble

The inhomogeneous distribution of luminous matter revealed to us by large-scale galaxy surveys raises the question of the effect of "local"-scale inhomogeneities on the observations we make. Any light we see from distant objects must traverse the local universe to get to us, and it is reasonable to ask to what extent this will influence our estimations of global cosmological parameters (Sinclair et al., 2010).

Observationally, from a decomposition of the peculiar velocity of the Local Group of galaxies manifested in the CMB dipole into three dominant and "fortuitously almost orthogonal" components, Tully et al. (2008) verified that the Milky Way galaxy is located in a Local Sheet that forms the boundary of a Local Void. Gravitational instability theory in the standard cosmology puts the distance to the centre of the void at least $17\,h^{-1}$ Mpc from us, making the Local Void "extremely large", although the SDSS void statistics suggest this is roughly average for a void size (Pan et al., 2011).

The possible existence of a Hubble bubble is of great interest for the TS model. As discussed in Sec. 2.5 it is a feature of the TS model that we will observe an apparent increase in the value of the Hubble constant on scales less than the scale of statistical homogeneity at $z \sim 0.033$ due to the volume-dominance of the present-epoch Universe by voids. Although it is quite conceivable for the local Hubble rate to be lower than the global average in the direction of a particular overdensity, a spherically symmetric average of the Hubble rate will in general encompass more void than wall. In the TS model, such an average over increasing local volumes will give a peak variance of order 17% above the mean on scales $z \sim 0.01$, which then steadily decreases until the scale of statistical homogeneity is reached.

Usually, very low redshift objects are left out of SNe Ia samples because their peculiar velocities are a considerable fraction of their Hubble flow velocities[1], but depending on the sample events with redshifts as low as $z = 0.01$ have been included. Evidence of a Hubble bubble was found by Zehavi et al. (1998), and confirmed by Jha et al. (2007), using a MLCS2k2 sample with $R_V = 3.1$. Modeling the expansion law in terms of a single inner void region expanding faster than an outer FLRW region, they find a drop in the Hubble constant of $\delta_H = (H_{\rm inner} - H_{\rm outer})/H_{\rm outer} = 0.065$ ($\sim$20%) out to a redshift $z = 0.024$. The reality of the local void in the supernova data was acknowledged to be tentative, and investigations using galaxy clusters found only weak evidence for a Hubble bubble (Giovanelli et al., 1999; Hudson et al., 2004), suggesting that it really is an artifact of the supernova data. Furthermore, Zehavi et al. (1998) and Jha et al. (2007) use (different incarnations of) the same SN Ia light curve fitter, suggesting the possibility that the Hubble bubble is perhaps some kind of artifact of the light curve fitter. However, it is also interesting to note that peculiar velocity surveys of galaxies in the Universe within 150 Mpc clearly show a Hubble bubble feature — this will be discussed in Section 5.3.1.

A comparison of supernova distances computed using other fitters by Conley et al. (2007) revealed that whether or not the Hubble bubble is detected in the data depends on the way that the supernova colours are modeled in the fitter. In the SALT-reduced samples, a Hubble bubble is found if the fit parameter β is held fixed at 4.1 —this is the value believed to roughly correspond to the CCM89 value for reddening in the Milky Way— but disappears if $\beta < 4.1$ (Conley et al., 2007). With their 366-SN MLCS31 sample, which uses the MLCS2k2 fitter and $R_V = 3.1$, Hicken et al. (2009) find very strong evidence for a void at $z = 0.028$ with reduced amplitude $\delta_H = 0.029$. By contrast, in their MLCS17 sample (372 SNe Ia), with $R_V = 1.7$ (a value that is extremely low for a whole galaxy—this value was chosen as minimising the scatter around the Hubble line of a nearby SN sample), they find strong evidence for a *negative* void at $z = 0.034$ with $\delta_H = -0.020$. (The void significance is quantified here as the ratio δ_H/σ, where σ is the uncertainty in the amplitude of the void.) Clearly, unknown systematic

[1]Sometimes attempts are made to correct the peculiar velocities to the Hubble flow using some standard velocity-field model, but this is not the case with the samples under discussion.

uncertainties in reddening and extinction of supernovae *in their host galaxies* will lead to different results regarding *local* inhomogeneities.

Different groups have made different choices about the minimum redshift cut-off in light of these uncertainties. Riess et al. (2007) took a minimum redshift $z = 0.024$, while Hicken et al. (2009) include data down to $z = 0.01$. Kessler et al. (2009), for their full MLCS2k2 Nearby+SDSS+SNLS+ESSENCE+HST sample, took a minimum redshift of $z = 0.0218$, based on the midpoint of a ± 0.06 variation in w with minimum redshift cuts between 0.01 and 0.03. The effects of minimum redshift cuts have also recently been discussed for the Hubble bubble generated by single-void Lemaître-Tolman-Bondi models (Sinclair et al., 2010). This study finds that by not accounting for a Hubble bubble, if it exists, we would measure a lower-than-actual $\Omega_{\rm m}$ and a non-zero Ω_Λ, and that imposing low redshift cutoffs can reduce this error but not remove it entirely: even with a redshift cutoff at $z \sim 0.02$, a $\sim$1% error in Ω_Λ remains—we can expect to achieve this precision from measurements in the near future. With a large enough void ($\sim$Gpc), the apparent acceleration in the supernova data can be explained without dark energy, but considerable fine-tuning is required to place the observer at the centre of such a void in order to match the evidence of the CMB dipole anisotropy (Blomqvist and Mörtsell, 2010), which makes this scenario unikely. Moreover, such a void should also induce an anisotropy in the temperature of CMB photons which inverse Compton scatter off free electrons in galaxy clusters—the kinetic Sunyaev-Zel'dovich effect—an effect which is not observed, providing sufficient evidence to claim a confirmation of the Copernican principle at Gpc scales and above (Zhang and Stebbins, 2011). Although a large Hubble bubble appears to be ruled out, the analysis of Sinclair et al. (2010) shows that systematic effects will persist even with a smaller bubble, which can still potentially result from not properly accounting for nearby peculiar velocities.

Even if the Hubble bubble is just a feature of the supernova data, it is still very important for precision cosmology that it is understood, because the nearby supernovae are used to calibrate the high redshift supernovae. Whether a redshift cut is applied or not makes little difference to the indication of accelerated cosmological expansion from SNe Ia (Riess et al., 2004), but it has a significant effect on measurements of the dark energy equation of state: Jha et al. (2007) use

simulations to show that estimates of w vary by $\sim 20\%$ depending on whether one includes the nearby sample or not—only the full sample gives the value of w that is consistent with its cosmological constant interpretation.

The statistical nature of the apparent Hubble expansion law expected in the TS model differs from the empirical models used in the above analyses of the Hubble bubble, as we are not dealing with a uniformly expanding void inside a background region. However, in general an increased minimum redshift cut *should* be made in the TS model, as we will show in Section 3.5.3. In Chapter 5, we perform a detailed analysis of the radial variation of the Hubble flow, fitting an average Hubble "constant" to galaxy distances in spherically symmetric shells with increasing minimum radial distances. By this means we find significantly larger values of H_0 in nearby bins, and this from a sample of mainly supernova-independent distances. Moreover, we find that the CMB rest frame, relative to which all the supernova redshifts are given in the published datasets, does not yield a minimum-variance Hubble flow—the Hubble flow in the Local Group rest frame is *closer* to uniform than that in the CMB frame. These issues will be discussed in more detail, with reference to supernova systematics, in § 5.5.1 at the end of Chapter 5.

3.4.3 Note regarding the value of H_0 and cosmological fits

The overall normalisation of the luminosity distance depends on the value of the Hubble constant, H_0. But, independently of a knowledge of the intrinsic luminosity of the standard candles, one cannot extract information about the value of the Hubble constant since uncertainties in the parameters M and H_0 are degenerate with one another in the distance modulus. The SALT fitter provides a global estimate of $\mathcal{M}$ in which any uncertainties are combined according to (3.5), and so says nothing about the value of H_0 directly. The value of H_0 must be determined by an independent calibration.

In the MLCS method, the overall distance scale similarly relies on the calibration of the magnitudes of nearby SNe Ia, usually to the Cepheid distance scale (Freedman et al., 2001; Riess et al., 2011; Sandage et al., 2006).

It is impossible therefore to infer the value of the Hubble constant by a fit to SNe Ia data alone. However, for the MLCS method, in which the uncertainties in the intrinsic magnitudes have hopefully already been accounted for, the fit of luminosity distances to a particular cosmological model can still provide an estimate of the *variance* in H_0 values that are admissible for that model. Independent cosmological tests, such as the determination of the angular diameter distance of the sound horizon, or of the comoving baryon acoustic oscillation scale, lead to different constraints on H_0, so in order to compare the potential agreement of different tests Leith et al. (2007) plotted confidence levels for the fit to the Riess07 gold data in their Fig. 2 using the normalization assumed in the data. Riess et al. (2007) stated that a systematic subtraction of 0.32 mag from their distance moduli would match the Cepheid calibration of Riess et al. (2005). At the time there was debate over the Cepheid calibration: Cepheids in the LMC were used as the "first rung" of the distance ladder, but these were of lower metallicity than their counterparts in the spiral galaxies hosting nearby SNe Ia (Riess et al., 2011; Sandage et al., 2006). Since a fit of the spatially flat ΛCDM model to the unmodified Gold SNe Ia distance moduli gave a value $H_0 = 62.6 \pm 1.4$ km s^{-1} Mpc^{-1}, consistent with the value determined by Sandage et al. (2006), Leith et al. (2007) chose to use the unmodified distance moduli. The Cepheid calibration of Riess et al. (2011), is in disagreement with the Sandage et al. (2006) calibration, and the confidence limits depend upon what overall normalization is assumed for the Hubble constant.

Constraints on the Hubble constant from WMAP and baryon acoustic oscillations in the TS model, given in Fig. 2 of Leith et al. (2007), are reproduced here in Fig. 3.7. The constraints from WMAP are estimated by fitting the angular scale of the sound horizon to within 2, 4 or 6%. The BAO constraints are similarly estimated by assuming that the dressed comoving scale of the sound horizon matches the corresponding scale of $104\,h^{-1}$ Mpc for the ΛCDM model to within 2, 4 or 6%. Assuming that these estimates are roughly correct[1] then Fig. 3.7

[1]A direct comparison with the data requires that we compute the expected angular anisotropy power spectrum for the TS model in the case of the CMB, and also that all model dependent assumptions in the data reduction of galaxy clustering data are carefully re-examined in the case of the BAO analysis.

shows that values of $57 \lesssim H_0 \lesssim 67$ km s^{-1} Mpc^{-1} (95% CL) would be admissible in the TS scenario, but values as large as the recent $H_0 = 74.2 \pm 3.6$ km s^{-1} Mpc^{-1} determined by the SH_0ES survey (Riess et al., 2011) would represent a severe challenge to the model.

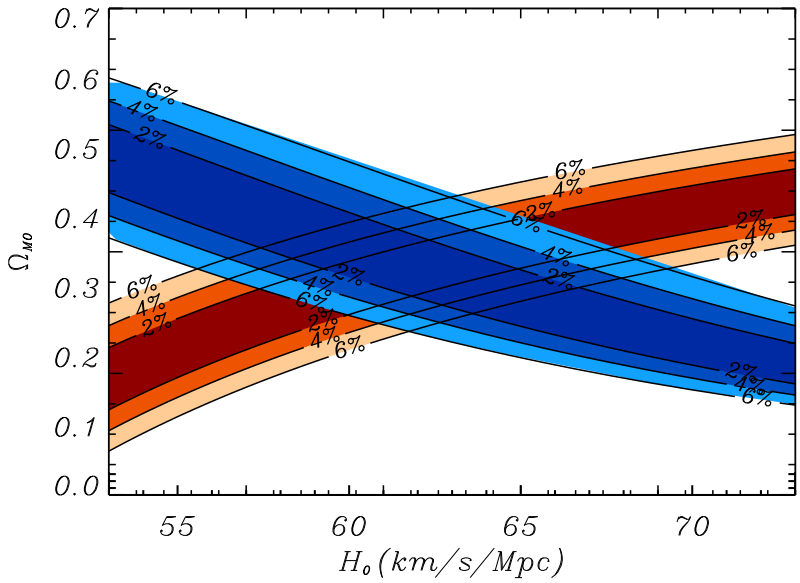

Figure 3.7: Confidence limits for TS model fits to the angular scale of the sound horizon from WMAP (upper left to lower right), and the BAO scale (lower left to upper right).

The determination of the value of the Hubble constant is a complex problem from the viewpoint of the TS model, given that many of the crucial measurements are made below the scale of statistical homogeneity, over scales on which the local Hubble flow should exhibit quite large variability. Indeed, the statistical properties of the observed fractional variability of the Hubble flow (Li and Schwarz, 2008) do seem broadly consistent with the expectations of the TS scenario. For concordance of the geometrical tests of average cosmological parameters, however, the real challenge is the baseline value of H_0.

Ideally the global average Hubble constant should be determined only on scales significantly larger than the scale of statistical homogeneity, $z > 0.033$, by

methods which do not depend on calibrations below that scale. As discussed in § 2.4, methods which do not rely on a local calibration of the distance ladder tend to yield smaller estimates of H_0. For example, the estimate of Beutler et al. (2011) using the WMAP sound horizon-calibrated BAO signal in the 6dF galaxy survey gives $H_0 = 67 \pm 3.2$ km s^{-1} Mpc^{-1}. Another example of such a method is the determination of H_0 via the time delays of multiply-imaged quasars in strongly gravitationally-lensed systems, which gives a large variety of estimates for H_0 (Oguri, 2007). A recent new estimate of H_0 from accurate time delay measurements with six years of data from the quadruply imaged quasar HE 0435-1223 gives $H_0 = 62^{+6}_{-4}$ km s^{-1} Mpc^{-1} (Courbin et al., 2010). In considering such estimates from the perspective of the TS model, one must be careful to examine any assumptions which might assume the standard cosmology.

The analysis of the Sunyaev-Zel'dovich effect and X-ray data of galaxy clusters provides another method of constraining H_0 independently of calibration to standard candles in the extragalactic distance ladder (e.g. Reese et al., 2010). If the standard ΛCDM angular diameter distance is replaced by that of the TS model then this method could be easily adapted to give further constraints in the (H_0, Ω_{M0}) parameter space.

In this chapter we are mainly interested in supernova tests of the timescape cosmology, so we will not consider the question of the value of H_0 further. We instead focus on the comparison of the expansion history for the TS and spatially flat ΛCDM models as determined by the luminosity distances of various SNe Ia datasets.

3.5 Testing the timescape cosmology with SNe Ia

From fits to the MLCS-reduced Riess Gold SN Ia data, the angular scale of the sound horizon at last scattering from the CMB, and the baryon acoustic oscillation scale, Leith et al. (2007) found concordance for $f_{\rm v0} = 0.76^{+0.12}_{-0.09}$, or, equivalently, $\Omega_{M0} = 0.33^{+0.11}_{-0.16}$.

A study by Kwan et al. (2009) investigated fits of the TS model to the Union and Constitution supernova datasets (the state-of-the-art samples at the time) and found that the estimated $\Omega_{\rm m}$ was anomalously low compared to the results

obtained in Leith et al. (2007) for the Gold dataset (which they replicated). They suggested that the reason for this was that the newer supernova datasets had smaller uncertainties than could be accommodated in the possible variation of the distance modulus of the timescape model. In this section we test the TS model against all supernova datasets available as of 2010 and we find that SALT-reduced supernova samples in general do not fit with the TS model, but MLCS-reduced samples do. We find that this is probably due not to the model-dependency in the SALT fitter but to the inclusion of supernovae from within the scale of statistical homogeneity in the SALT datasets.

In view of the SNe Ia systematic uncertainties it is important to consider all the effects of using the different supernova light curve fitters, including the additional possible systematic effects specific to the TS model. In § 3.5.1, we discuss TS fits to eight published datasets "out of the box". In § 3.5.2, we determine the extent to which substitution of the TS luminosity distance calculation for the ΛCDM one in the SALT `simple_cosfitter` code affects parameter estimation. We then investigate the effects of making sample cuts according to the redshift corresponding to the scale of statistical homogeneity in § 3.5.3. Finally, in § 3.5.4 we discuss some systematic issues relevant to MLCS2k2.

3.5.1 "Out of the box" data

Kwan et al. (2009) simply took the published values of the Union and Constitution datasets, produced data fits and concluded that the TS model was a relatively poor fit, with the implication that despite the initial success in fitting the Gold dataset, the TS failed when presented with the newer larger datasets. However, the newer datasets are fit by SALT, which implicitly assumes a homogeneous isotropic cosmology for the distances in its data reduction, so one might expect compatibility issues to arise when testing SALT data against nonstandard cosmological models. In fact, it was for this reason that the MLCS-reduced Gold data was used by Leith et al. (2007) in preference to the SALT-reduced SNLS data.

To illustrate the problem, we first collate TS cosmological parameter fits for eight supernova datasets in Table 3.3 using the data "out of the box". The three

datasets investigated in this manner by Kwan et al. (2009) were the Gold dataset (Riess et al., 2007), and the SALT-fitted Union (Kowalski et al., 2008) and Constitution (Hicken et al., 2009) datasets. To these we add the equivalent parameter fits for the SALT2, MLCS17 and MLCS31 datasets of Hicken et al. (2009), the full 288-supernova[1] sample of Kessler et al. (2009), and the 557-supernova Union2 sample of Amanullah et al. (2010). The MLCS17 and MLCS31 datasets share many SNe Ia in common with the Constitution set, but were fitted by MLCS2k2 with values for the extinction parameter R_V of 1.7 and 3.1 respectively. The value $R_V = 1.7$ was found by Hicken et al. (2009) to give less scatter in the Hubble residuals for a sample of nearby SNe Ia, in keeping with previous studies which found the colour parameter β in eq. (3.6) to be significantly lower than would be expected if the host galaxy reddening law conforms to a Milky Way reddening law ($R_V = 3.1$). The SDSS-II data (Kessler et al., 2009) was fitted by MLCS2k2 with $R_V = 2.18$. The Union2 dataset is fit with SALT II.

We have compiled Table 3.3 by our own analysis of the data, with the prior[2] $0.01 \leq \Omega_{M0} < 0.95$ used by Kwan et al. (2009). For comparison, Table 3.4 shows ΛCDM parameter values that were published with the respective datasets. Note that because the SALT/SALT-II fitters compute an intrinsic distance modulus dispersion by forcing the reduced χ^2 to be unity, there are no χ^2 values given for the Union2 and Consitution samples. The χ^2 shown for the Union data comes from an implementation of SALT peculiar to the study of Kowalski et al. (2008).

The parameter values quoted by Leith et al. (2007) and Kwan et al. (2009) were those corresponding to the peak in the probability distribution, at which the χ^2 statistic is minimised. However, as Fig. 1 of Kwan et al. (included here as Fig. 3.8) illustrates, for the published Union and Constitution datasets the bestfit value is driven to the edge of the parameter space at unrealistically small values of $\Omega_{\rm m}$, an issue we will discuss further in Sec. 3.5.3. Given probability distributions

[1] Nearby+SDSS+ESSENCE+SNLS+HST

[2] Kwan et al. (2009) state that this prior corresponds to taking a prior $10^{-5} < f_{\rm vi} < 10^{-2}$ on the void fraction at last scattering. However, while the value of $\Omega_{\rm m}$ is closely related to $f_{\rm v0}$, it is essentially independent of $f_{\rm vi}$ on account of the existence of the tracker solution. Leith et al. (2007) used the value $f_{\rm vi} = 10^{-4}$ with the exact solution for *all* values of $\Omega_{\rm m}$; the value of $\Omega_{\rm m}$ is essentially insensitive to the value $f_{\rm vi}$.

Dataset	N	χ^2	Ω_m	f_v0
Riess07 (M)	182	162.7	$0.29^{+0.14}_{-0.13}(0.33)$	$0.79^{+0.11}_{-0.12}$
Union (S)	307	319.6	$0.12^{+0.14}_{-0.12}(0.09)$	$0.91^{+0.09}_{-0.08}$
Const. (S)	397	470.8	$0.10^{+0.08}_{-0.09}(0.01)$	$0.93^{+0.06}_{-0.06}$
MLCS17 (M)[1]	372	403.1	$0.18^{+0.12}_{-0.15}(0.20)$	$0.87^{+0.09}_{-0.10}$
MLCS31 (M)[1]	366	432.8	$0.07^{+0.04}_{-0.06}(0.01)$	$0.95^{+0.02}_{-0.04}$
SALT2 (S2)[1]	352	346.8	$0.11^{+0.11}_{-0.10}(0.04)$	$0.92^{+0.08}_{-0.07}$
SDSS-II (M)[2]	288	240.8	$0.38^{+0.11}_{-0.09}(0.40)$	$0.72^{+0.05}_{-0.05}$
Union2 (S2)[3]	557	550.9	$0.08^{+0.05}_{-0.07}(0.01)$	$0.95^{+0.03}_{-0.04}$

[1] Hicken et al. (2009)
[2] Kessler et al. (2009)
[3] Amanullah et al. (2010)

Table 3.3: Timescape model best-fit parameters. Expectation values for the parameters for the timescape model from SNe Ia data, using published SNe Ia data as selected and reduced by the respective SNe Ia collaborations. The bestfit value of Ω_m is quoted in brackets in addition to the expectation value. The MLCS17, MLCS31, and SALT2 datasets were published along with the Constitution dataset in Hicken et al. (2009). The SDSS-II dataset is the full 288-object dataset described in Kessler et al. (2009) and available from `http://das.sdss.org/va/SNcosmology/sncosm09_fits.tar.gz`. The sample size, N, and minimum χ^2 are also tabulated. S=SALT; S2=SALT2; M=MLCS2k2.

Dataset	N	χ^2	Ω_m
Union	307	310.8	$0.29^{+0.05}_{-0.04}$
Constitution	397	—	$0.28^{+0.04}_{-0.02}$
SDSS-II[1]	288	237.9	$0.31^{+0.02}_{-0.02}$
Union2[2]	557	—	$0.274^{+0.040}_{-0.037}$

[1]These values come from table 13 in Kessler et al. (2009).

[2]Statistical and systematic uncertainties combined.

Table 3.4: ΛCDM best-fit parameters. Published values for Ω_m for the ΛCDM model from SNe Ia data, for comparison with Table 3.3. The χ^2 value for the Union sample comes from Table 6 in Kowalski et al. (2008) before applying the iterative "intrinsic" dispersion computation. The uncertainties in the Union Ω_m include a systematic component computed with a method outlined in §5 of Kowalski et al. (2008) (the alternative method alluded to in Section 3.3.2). The Constitution value of Ω_m includes a BAO prior. The SDSS-II value includes BAO and WMAP5 priors. Distance normalisation is arbitrary.

such as these that are significantly skewed relative to a Gaussian distribution, a more typical estimate of any parameter θ is given by the expectation value $\langle\theta\rangle = \int_{-\infty}^{+\infty} \theta\, p(\theta)\, \mathrm{d}\theta$, where $p(\theta)$ is the normalised probability. While the bestfit value gives the most probable individual parameters, the expectation value is the average one would obtain given many measurements of the parameter in many universes. In Table 3.3 we have displayed the expectation values of Ω_m and f_v0, together with the bestfit value of Ω_m for comparison. In the cases in which the bestfit value of Ω_m takes the smallest values, namely the Constitution, SALT2 and MLCS31 samples of Hicken et al. (2009) and the Union2 sample of Amanullah et al. (2010), the bestfit value of Ω_m differs from the expectation value by a factor close to one standard deviation.

The extremely small bestfit values of Ω_m for the Union and Constitution samples—or equivalently the unusually large values of f_v0—match those found by Kwan et al. (2009), which led these researchers to draw unfavourable conclusions about the TS model. Kwan et al. reasoned that this was due to inclusion

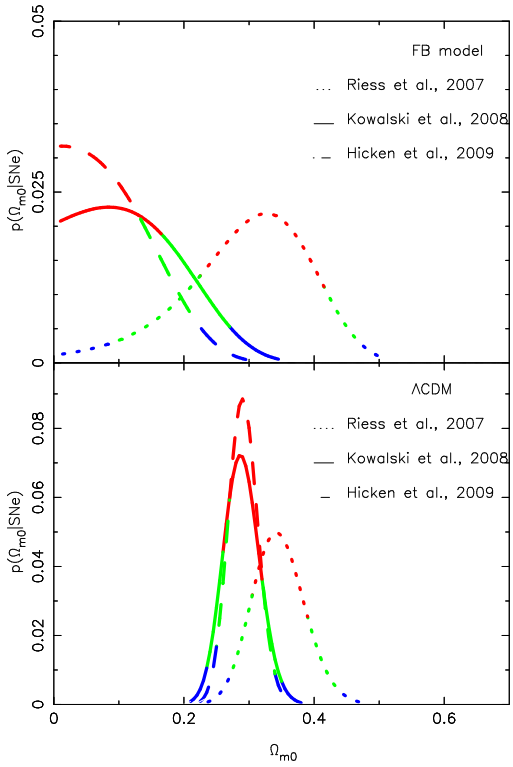

Figure 3.8: *Above*: Marginalised posterior distributions for the TS model using the Union compilation in solid lines, the Gold SNe Ia sample in dotted lines, and the Constitution set in dashed lines. The colours correspond to the confidence limits, red is 1σ, green is 2σ and blue is 3σ. *Below*: As above except using ΛCDM. Source: Kwan et al. (2009)

of extra data in the Union and Constitution samples, compared to the Riess07 sample. In particular, there are a larger number of SNe Ia in the redshift range $0.35 < z < 0.4$ in the Union sample, and in the range $0 < z < 0.2$ in the Constitution sample. While the inclusion of extremely close SNe Ia at distances less than the scale of statistical homogeneity is a separate systematic issue to be investigated later, the results of the MLCS2k2-reduced samples in Table 3.3 refute the claim of Kwan et al. (2009) that it is the greater sample size that is the main issue. The parameters of the TS model are not so much sensitive to small changes in the SNe Ia data, as Kwan et al. maintain, as they are sensitive to the method of data reduction. While the MLCS31 sample, fit with $R_V = 3.1$ produces results close to the SALT/SALT II fits, the MLCS17 sample, with the largest number of SNe Ia fit by the MLCS2k2 method, yields a bestfit value $\Omega_{M0} = 0.20^{+0.10}_{-0.17}$, and the SDSS-II sample of Kessler et al. (2009) a bestfit value of $\Omega_{M0} = 0.40^{+0.09}_{-0.11}$. As for the parameters of the ΛCDM model in the lower part of Fig. 3.8, the parameters found from the MLCS17 and SDSS-II samples for the TS model agree with those of the Riess07 Gold sample to within one standard deviation.

We conclude that the MLCS-reduced SN Ia samples, with appropriate treatment of host galaxy reddening, provide a better fit to the TS model than the SALT-reduced samples. We will see in Sec. 3.5.3 that this carries through to the Bayesian statistical evidence as well. Our results therefore support the observation of Sollerman et al. (2009), who find that for the SDSS-II supernovae of Kessler et al. (2009) reduced with the MLCS2k2 fitter, nonstandard cosmological models can provide a better fit to the data than the ΛCDM model.

3.5.2 Recalibration of the SALT SNe Ia

Having established that the primary issue for the goodness of fit of the TS model relative to the ΛCDM model is which data reduction method is used, we should examine the extent to which implicit use of the ΛCDM model in data calibration affects the SALT/SALT II samples. It is difficult to assess all the ways in which the assumption of a homogeneous cosmology is built into the SALT data reduction procedure. However, it is straightforward to adapt the `simple_cosfitter` code,

Dataset	N	χ^2	Ω_m	f_v0
Union (TS)	307	350.6	$0.13^{+0.10}_{-0.08}(0.09)$	$0.91^{+0.07}_{-0.06}$
Union (ΛCDM)		344.1	$0.28^{+0.03}_{-0.03}(0.28)$	
Const. (TS)	397	319.7	$0.13^{+0.09}_{-0.08}(0.08)$	$0.91^{+0.06}_{-0.06}$
Const. (ΛCDM)		312.9	$0.29^{+0.03}_{-0.03}(0.28)$	

Table 3.5: Recalibrated TS parameter values. Expectation values for the parameters of the timescape model from SALT-reduced SN Ia data, recomputed with the timescape model luminosity distance. Distance normalisation is arbitrary. The bestfit value of Ω_m is in brackets. Note that the ΛCDM values shown here differ from those in Table 3.4 because they were computed without incorporating the estimation of the intrinsic dispersion by setting $\chi^2/\mathrm{d.o.f} = 1$.

which implements the SALT procedure, to use the luminosity distance of other cosmological models.

We replaced the module of `simple_cosfitter` that implements the spatially flat ΛCDM luminosity distance (1.28) by one that computes the TS luminosity distance: equation (2.38). Leaving the rest of the `simple_cosfitter` code unchanged, we reran the parameter fits. This amounts to taking the published stretch and colour parameters for each supernova, and recomputing Ω_m along with the empirical parameters $\mathcal{M}$, α and β of eq. (3.6).

The values of Ω_m and the minimum χ^2 that result from this reanalysis are displayed in Table 3.5. Since the comparable published values for the ΛCDM model often include BAO or WMAP priors, we also show the corresponding parameter values we obtained ourselves using `simple_cosfitter` applied to the spatially flat ΛCDM model. The results indicate that the expectation values of Ω_m increase only very slightly from the values of Table 3.3. However, the bestfit value of Ω_m is much closer to the expectation value for the Constitution sample. The parameters α, β, and M_B (calculated from $\mathcal{M}$ with[1] $H_0 = 65$ km s^{-1} Mpc^{-1}) are shown in Table 3.6. Both the TS and the `simple_cosfitter` results for α

[1] We will simply adopt the same Hubble constant normalization as Hicken et al. (2009), who took this value.

Dataset	α	β	M_B
Union (TS)	$1.32^{+0.12}_{-0.12}$	$2.37^{+0.12}_{-0.12}$	-19.42
Union (ΛCDM)[1]	$1.33^{+0.12}_{-0.12}$	$2.38^{+0.13}_{-0.12}$	-19.46
Const. (TS)	$1.29^{+0.10}_{-0.10}$	$2.49^{+0.11}_{-0.11}$	-19.43
Const. (ΛCDM)[2]	$1.31^{+0.10}_{-0.10}$	$2.50^{+0.11}_{-0.11}$	-19.46

[1]Kowalski et al. (2008) values: $\alpha = 1.24^{+0.10}_{-0.10}$, $\beta = 2.28^{+0.11}_{-0.11}$.

[2]Hicken et al. (2009) values: $\alpha = 1.34^{+0.08}_{-0.08}$, $\beta = 2.59^{+0.12}_{-0.08}$, $M_B = -19.46$ with $H_0 = 65$ km s^{-1} Mpc^{-1}.

Table 3.6: Recalibrated global parameters: Values for the global parameters from SALT-reduced SN Ia data, computed by `simple_cosfitter` with the ΛCDM and TS luminosity distances.

and β are well within the uncertainties quoted in Hicken et al. (2009). Given that the Constitution set contains the Union set, it is not surprising that their corresponding $\Omega_{\rm m}$ values should be the same, when calculated for each model, as Table 3.5 shows. The addition of the new CfA3 SNe Ia to the Union sample changes the fits of the global parameters α, β, and $\mathcal{M}$, and consequently the estimate of $\Omega_{\rm m}$, but Table 3.6 shows these changes are relatively small.

Actually, the differences between Table 3.3 and Table 3.5 are overall relatively small. In particular, whether or not the ΛCDM or TS luminosity distance is assumed, the SALT-reduced data still produces consistently higher fits to the present epoch void fraction $f_{\rm v0}$ than that of the MLCS-reduced samples (other than MLCS31). The resulting $\Omega_{\rm m}$ values depend only very weakly on whether the luminosity distance assumed by the SALT fitter is a TS one or a ΛCDM one. Furthermore, the distance moduli themselves show insignificant differences: the difference between the two measures is plotted in Fig. 3.9 (on the same scale as used in Figs. 3.3 and 3.4 for comparison).

Fig. 3.9 demonstrates that use of the TS luminosity distance reproduces the SALT ΛCDM results to great precision. Thus the differences in the expectation values of cosmological parameters found in Table 3.3 between the MLCS and

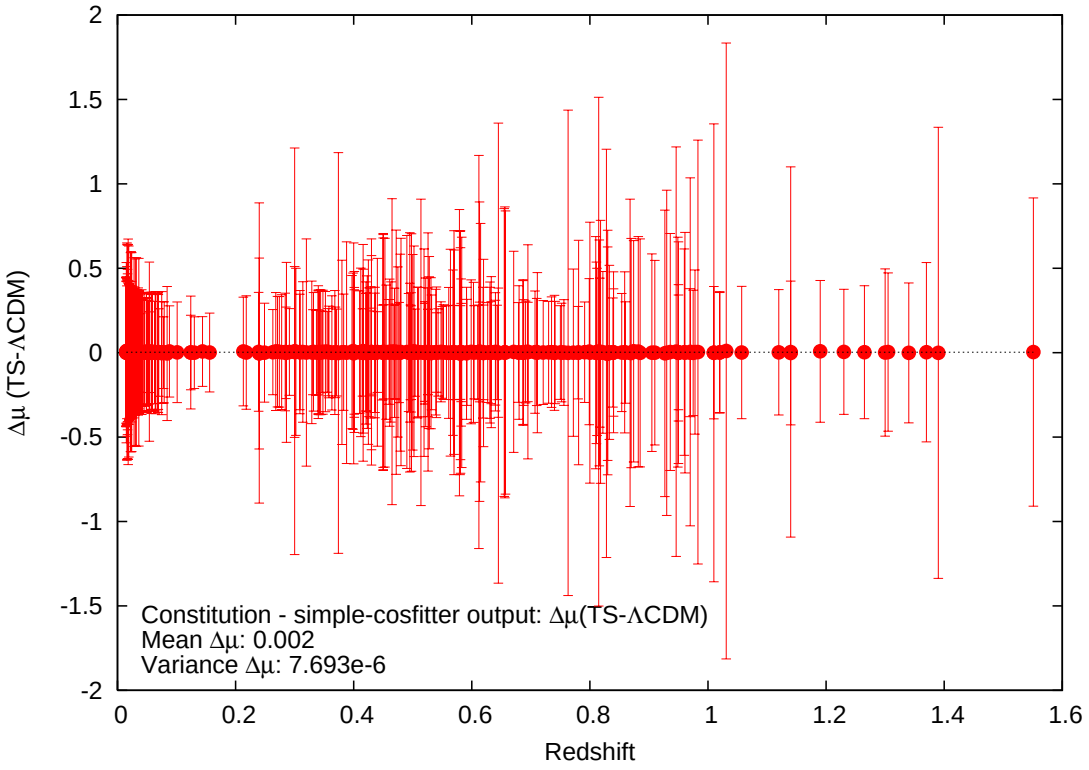

Figure 3.9: Differences in the distance moduli obtained by a SALT fit to the Constitution sample using the `simple_cosfitter` code adapted to: (i) the spatially flat ΛCDM model, and, alternatively, (ii) the TS model; as a function of redshift.

SALT fitters must be a consequence of systematic differences, rather than the luminosity distance relation assumed by SALT.

As a check that the differences between the fitters are not simply a consequence of the inclusion of different SNe Ia subsamples, we have compared the cosmological parameters determined from the subsample of 140 SNe Ia common to the Riess07 Gold, Union, and Constitution datasets, which was used in generating Figs. 3.3 and 3.4. In Table 3.7 we show the TS cosmological parameters determined using both the published data for the Gold dataset[1], Union and Con-

[1]For the subsample of 140 SNe Ia from the Gold dataset a fit of the Hubble constant gives $H_0 = (61.4^{+1.4}_{-1.5},\ 62.3^{+1.4}_{-1.8})$ km s^{-1} Mpc^{-1} for the TS and spatially flat ΛCDM models respectively. c.f. the respective values $H_0 = (61.7^{+1.2}_{-1.1},\ 62.6 \pm 1.3)$ km s^{-1} Mpc^{-1} for the full

Dataset	$\Omega_{\rm m}$	$f_{\rm v0}$	ln B
R140	$0.33^{+0.15}_{-0.14}(0.36)$	$0.76^{+0.13}_{-0.13}$	0.14
U140(p)	$0.21^{+0.17}_{-0.20}(0.23)$	$0.85^{+0.14}_{-0.13}$	0.43
U140(f)	$0.16^{+0.12}_{-0.10}(0.13)$	$0.89^{+0.07}_{-0.09}$	0.14
C140(p)	$0.17^{+0.16}_{-0.16}(0.17)$	$0.88^{+0.11}_{-0.12}$	0.56
C140(f)	$0.18^{+0.12}_{-0.12}(0.17)$	$0.87^{+0.09}_{-0.09}$	0.17

Table 3.7: Parameters from the 140 common SNe Ia. Expectation values of $\Omega_{\rm m}$ (with bestfit values in brackets), for the 140 SNe Ia common to the Riess07 Gold (R), Union (U), and Constitution (C) samples. For the Union and Constitution subsamples the results of fits to the published data (p); and to `simple_cosfitter` fit data (f), are both shown. Bayes factors, with priors $0.01 \leq \Omega_{M0} \leq 0.95$ (and $55 \leq H_0 \leq 75$ km s^{-1} Mpc^{-1} where relevant), for the TS model relative to the spatially flat ΛCDM model are also given. i.e. the TS model is favoured for a positive Bayes factor.

stitution samples, and also our own SALT fit (with the TS luminosity distance) of these 140 points alone. We see that the subsets of published data values produce higher estimates of $\Omega_{\rm m}$ for each sample than each of the complete sets given in Table 3.3, and that the greatest percentage increase is for the Constitution sample. Furthermore, a `simple_cosfitter` fit to the subsample of 140 SNe Ia alone also produces higher estimates of $\Omega_{\rm m}$, which differ somewhat from the subsample of the published values only in the case of the Union sample. However, in all cases the SALT-reduced Union and Constitution subsamples still have a significantly lower value of $\Omega_{\rm m}$ than the MLCS-reduced Riess07 subsample. Consequently, intrinsic differences in the MLCS and SALT methods appear to be the dominating cause of the variance in cosmological parameter estimates for the TS model.

The Bayes factors, representing the integrated likelihood of the TS model over that of the spatially flat ΛCDM model have also been given in Table 3.7. By the Jeffreys scale (Trotta, 2008) these results indicate that the models are statistically

sample of 182 SNe Ia. As remarked in Sec. 3.4.2 this is not an absolute determination of H_0, as the data assumes an overall calibration; but relatively speaking, the favoured value of H_0 is only very slightly reduced by restricting to the subsample.

indistinguishable for the subsample of 140 SNe Ia, regardless of the fitter used. For the Gold data this is interesting, given that the whole sample of 182 SNe Ia gives $\ln B = -1.20$ with mild positive evidence in favour of the ΛCDM model: although the inclusion of the additional 42 SNe Ia in the Gold sample does not greatly affect the values of cosmological parameters, it significantly changes the relative goodness of fit of the TS and ΛCDM models. Since the Constitution sample simply augments the Union sample with more recent data, the reason for the exclusion of the 42 SNe Ia in question from the Union sample is that Kowalski et al. (2008) use different selection cuts to those used in the Gold sample.

3.5.3 The Statistical Homogeneity Scale

There are many potential sources of systematic error which are treated differently in the MLCS and SALT fitters, and might be responsible for the differences in parameter estimates obtained for the TS model. We now investigate the effects on the fits of the different redshift cuts introduced to compensate for Hubble bubble or peculiar velocity effects. We prefer to use the terminology "statistical homogeneity scale" (henceforward, SHS) to the more commonly used "Hubble bubble" terminology, since the latter is often taken to be a single large local void. In the ΛCDM context, such a feature is, strictly speaking, an anomaly. But as mentioned in § 3.4.2, in the TS model an *apparent* Hubble bubble at any typical wall location is expected for averages below the statistical homogeneity scale, given the observed dominance of $30\,h^{-1}$ Mpc diameter voids by volume in the late epoch universe. A rough estimate of the scale of statistical homogeneity is obtained as the radius of the volume within which the variance of locally measured Hubble expansion falls within certain minimal limits. As discussed above, a rough estimate of the scale of statistical homogeneity is obtained as the radius of the volume within which the variance of locally measured Hubble expansion falls within certain minimal limits (Wiltshire, 2008). It should not be more than a few times the size of the largest typical nonlinear structures. Given the observed scale of the dominant voids, a $100\,h^{-1}$ Mpc scale is suitable for the SHS. Hence, in the TS scenario an average Hubble flow is only expected on scales greater than the statistical homogeneity scale, and, for consistency in the parameter fits with

the TS model, a cut should be applied to data at redshifts below the SHS. For future reference, we note that $100\,h^{-1}$ Mpc corresponds to a redshift of 0.033.

For the SALT datasets the inclusion of significant numbers of SNe Ia below the SHS could conceivably bias the global fits of α, β, $\mathcal{M}$ and $\Omega_{\rm m}$. The potential impact of the SHS on the MLCS datasets is less clear, as the fitter is trained using a set of nearby SNe Ia that are far enough into the Hubble flow for peculiar velocities to be negligible, yet still close enough for the linear Hubble law to hold (Jha et al., 2007). In practice, the training set includes some SNe Ia within the SHS, so there may still be some subtle systematic issues associated with the SHS.

As a first check on whether the discrepancy between the values of $\Omega_{\rm m}$ determined by the SALT and MLCS methods can be accounted for by making cuts at the SHS scale, we have determined parameters for fits to the TS model with cuts made: (i) by excluding objects at redshifts $z < 0.024$, which corresponds to the $H_0 d_{\rm SN} \simeq 7400\,{\rm km\,sec^{-1}}$ Hubble bubble partition assumed by Jha et al. (2007); Riess et al. (2007) and Hicken et al. (2009)); and (ii) by excluding objects with redshifts $z < 0.033$, corresponding to the estimated scale of statistical homogeneity, 100 h^{-1} Mpc. The resulting values of $\Omega_{\rm m}$ are compared with the values obtained from the full dataset in Table 3.8. Bayes factors for a fit of the TS model relative to the spatially flat ΛCDM model are also displayed.

Table 3.8: (page 84) **Different minimum redshift cuts.** Parameter values for SN Ia datasets, applying homogeneity scale cuts, the first at the Hubble bubble radius of $z_{\rm min} = 0.024$ (e.g. Jha et al. (2007)), the second at $z_{\rm min} = 0.033$, corresponding to the scale of statistical homogeneity estimated to be $\sim 100\ h^{-1}$ Mpc. Expectation values of $\Omega_{\rm m}$ are shown, with bestfit values in brackets. For the SALT/SALT II fits (Union, Constitution, SALT2, Union2) the parameters have been recomputed by adapting `simple_cosfitter` to the TS model in each case. "CSP" stands for the Carnegie Supernova Project, an IR survey of nearby supernovae documented in Freedman et al. (2009).

Dataset	z cut	N	χ^2	Ω_m	$\ln B$
Gold	≥ 0.024	182	162.7	$0.30^{+0.14}_{-0.13}(0.33)$	-1.20
	≥ 0.033	169	151.8	$0.31^{+0.15}_{-0.13}(0.34)$	-1.18
R140	≥ 0.024	140	102.7	$0.33^{+0.16}_{-0.14}(0.36)$	0.14
	≥ 0.033	132	96.2	$0.26^{+0.20}_{-0.25}(0.30)$	0.78
MLCS17	None	372	401.7	$0.18^{+0.13}_{-0.15}(0.20)$	0.77
	≥ 0.024	282	315.7	$0.17^{+0.13}_{-0.16}(0.19)$	0.37
	≥ 0.033	234	260.2	$0.19^{+0.14}_{-0.17}(0.21)$	0.57
MLCS31	None	366	429.5	$0.07^{+0.05}_{-0.06}(0.01)$	-1.57
	≥ 0.024	278	332.2	$0.09^{+0.08}_{-0.08}(0.01)$	0.13
	≥ 0.033	229	263.3	$0.11^{+0.11}_{-0.10}(0.03)$	1.09
SDSS-II	None	288	240.8	$0.39^{+0.11}_{-0.09}(0.40)$	0.09
	≥ 0.024	284	238.4	$0.40^{+0.11}_{-0.10}(0.41)$	0.27
	≥ 0.033	272	214.5	$0.42^{+0.10}_{-0.10}(0.44)$	0.53
Union	None	307	350.6	$0.13^{+0.10}_{-0.08}(0.07)$	-2.04
	≥ 0.024	288	333.4	$0.15^{+0.10}_{-0.09}(0.14)$	-1.53
	≥ 0.033	275	318.0	$0.18^{+0.11}_{-0.11}(0.20)$	-0.86
Const.	None	397	319.6	$0.13^{+0.09}_{-0.08}(0.06)$	-1.54
	≥ 0.024	351	293.8	$0.13^{+0.09}_{-0.08}(0.09)$	-1.57
	≥ 0.033	309	275.9	$0.16^{+0.10}_{-0.10}(0.15)$	-1.06
SALT2	None	351	402.5	$0.10^{+0.08}_{-0.06}(0.02)$	-2.25
	≥ 0.024	278	342.1	$0.11^{+0.08}_{-0.06}(0.03)$	-2.22
	≥ 0.033	235	305.5	$0.13^{+0.09}_{-0.07}(0.09)$	-1.55
Union2	None	557	520.3	$0.09^{+0.07}_{-0.08}(0.05)$	-2.65
	≥ 0.024	504	483.5	$0.10^{+0.08}_{-0.06}(0.09)$	-2.25
	≥ 0.033	457	428.4	$0.10^{+0.08}_{-0.06}(0.15)$	-3.46
CSP	None	56	62.3	$0.11^{+0.08}_{-0.10}(0.01)$	-4.23
	≥ 0.024	47	69.1	$0.12^{+0.13}_{-0.11}(0.01)$	-4.03
	≥ 0.033	43	46.0	$0.13^{+0.12}_{-0.12}(0.01)$	-3.34

In all cases the relevant cuts lead to somewhat larger values of $\Omega_{\rm m}$, with the exception of the subsample of 140 SNe Ia from the Gold dataset, which was shown in Table 3.7. In the SALT cases the increase in the expectation value of $\Omega_{\rm m}$ is not particularly large. However, the bestfit value of $\Omega_{\rm m}$ increases generally by about a standard deviation from the full sample to the SHS cut sample. Since the bestfit value of $\Omega_{\rm m}$ is much closer to the expectation value for the SALT samples once SHS cuts are made, it shows that the fits are no longer so strongly skewed away from being Gaussian with bestfit values of $\Omega_{\rm m}$ having small values. This demonstrates that once the SHS cut is made, the posterior distributions for the TS void fraction parameter in Fig. 3.8 will coincide within a standard deviation of each other.

In all the MLCS2k2 cases, the Bayes factor improves in favour of the TS model with the redshift cuts, but the improvement is weak and, with the exception of MLCS31, generally not enough to statistically distinguish the models. For the SALT-reduced data, by contrast, the data generally indicate mild positive evidence against the TS model on the Jeffreys scale (Trotta, 2008). For all SALT datasets apart from Union2 the Bayesian evidence in favour of the ΛCDM model is weaker once the SHS cut is applied.

To further test the issue of redshift cuts, we have repeated our analysis by applying a cut at redshifts which range from the minimum value in each dataset up to $z_{\rm min} = 0.08$. The results are shown in Figs. 3.10 and Figs. 3.12. For comparison, the equivalent redshift cut results for the ΛCDM model are shown in Fig. 3.11. The Bayes factor for the SHS ($z_{\rm min} = 0.033$) cut on the Union2 sample turns out to mark the beginning of a downward trough in an otherwise increasing trend.

Fig. 3.10 provides a direct demonstration of how excluding the SNe Ia below the SHS leads to to χ^2 values that are indistinguishable from those of ΛCDM fits in the SALT-reduced datasets. In fact, it also reveals differences between the SALT and SALT II fitters. For the Union and Constitution datasets, reduced by SALT, we see that below the SHS the bestfit value is below the expectation value, i.e., the distribution is negatively skewed. For cuts in the range $0.03 \lesssim z_{\rm min} \lesssim 0.05$ the bestfit and expectation values of $\Omega_{\rm m}$ are roughly comparable for these samples, while for $z_{\rm min} \gtrsim 0.05$ the bestfit value indicates a positive skew. For SALT2 and

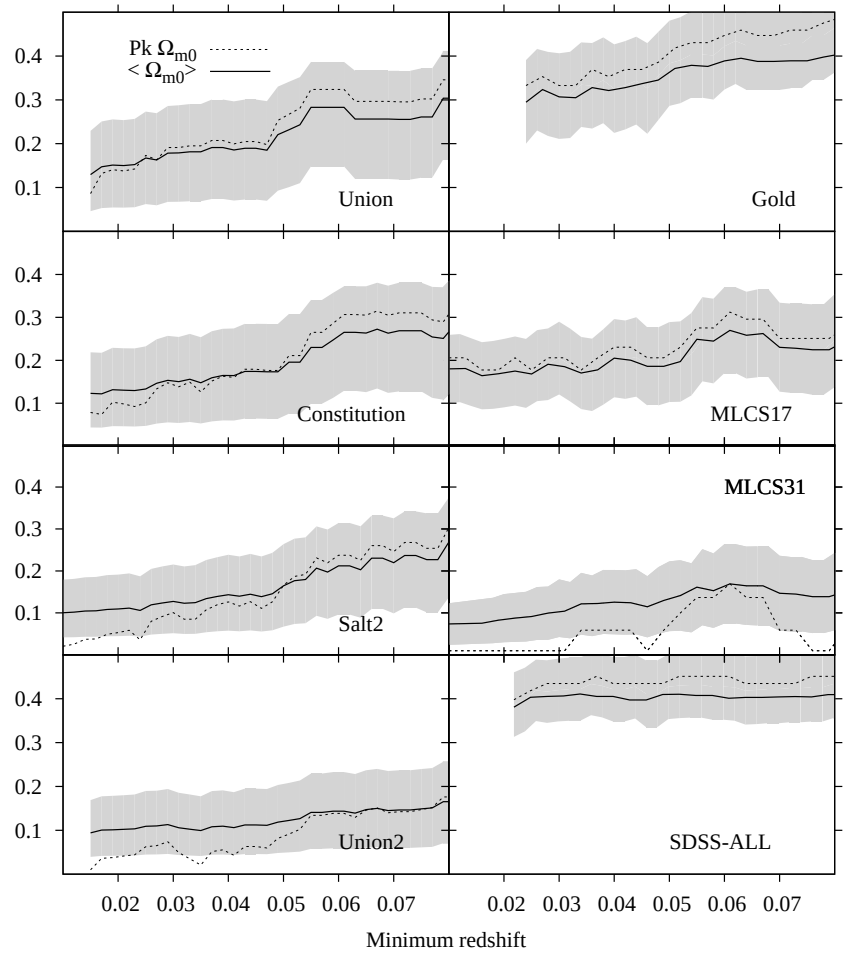

Figure 3.10: TS Minimum redshift cuts. Bestfit values (dotted line) and expectation values (solid line) of Ω_{m} for successive redshift cuts for eight SNe Ia samples. The shaded regions show the 1σ uncertainties around the expectation values. The probability distributions for SALT Ω_{m} fits (left column) make a transition from negative skew to positive skew, while those MLCS samples (right column) which already provide better fits to the TS model are always positively skewed.

Union2, reduced by SALT II, the distribution remains negatively skewed for cuts up to $z_{\mathrm{min}} \lesssim 0.055$.

In the case of the datasets that the TS model fits well — Gold, MLCS17 and SDSS-II — the skew is always positive, i.e., the bestfit value is greater than the expectation value. The skew is larger for the cuts at higher redshifts, particularly

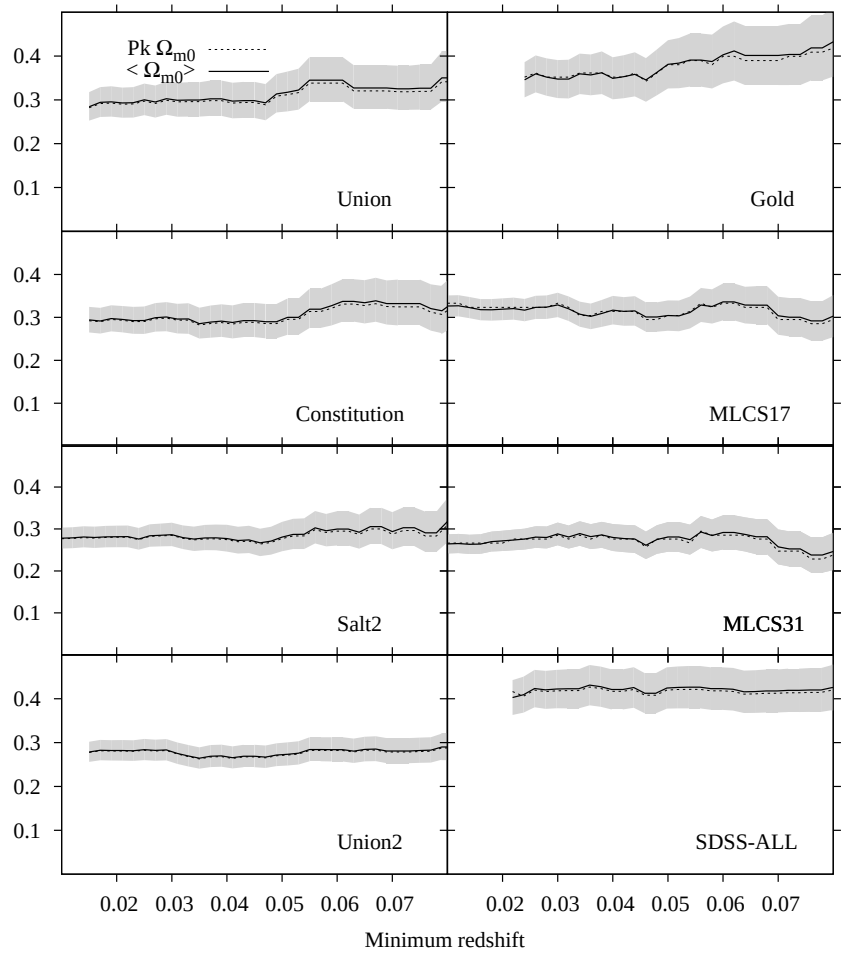

Figure 3.11: ΛCDM Minimum redshift cuts. Bestfit values (dotted lines) and expectation values (solid lines) with 1σ uncertainties in the expectation values indicated by the shaded regions.

for the Gold and SDSS-II samples. For MLCS31, the bestfit value is negatively skewed, and the fit is generally poor, in the sense that this probability distribution is very significantly skewed.

These results suggest that the way that the SALT fitters treat nearby objects — the inclusion of large numbers of them as well as the treatment of their color variations and host galaxy dust — does affect the TS cosmology fits.

Finally, for comparison we have added the first dataset from the Carnegie

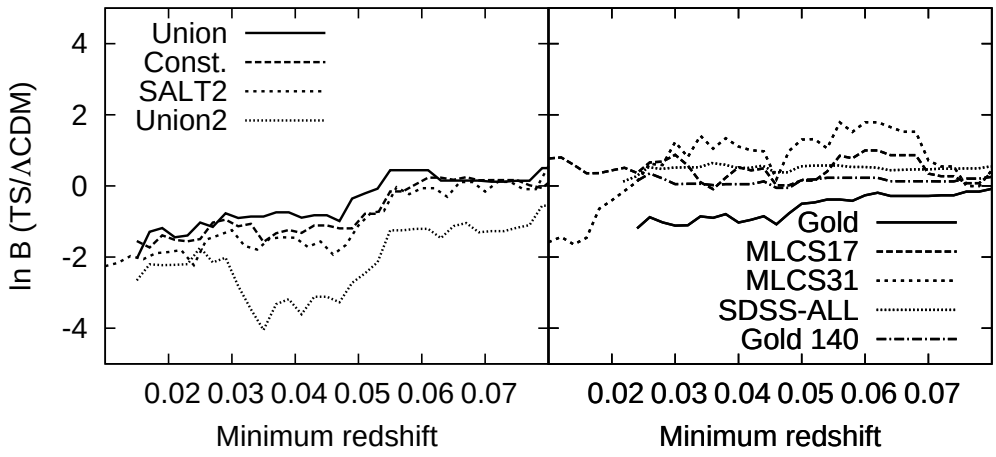

Figure 3.12: Bayesian evidence: $\ln B$ for the TS model relative to the spatially flat ΛCDM model for successive redshift cuts for nine SNe Ia samples. The SALT-reduced sets are in the left panel, the MLCS2k2-reduced samples in the right panel.

Supernova Project (CSP) (Freedman et al., 2009) to Table 3.8. This is a much smaller dataset than the others and it differs from other projects by working in the near infrared, and consequently the data is differently reduced. However, in their analysis Freedman et al. (2009) have adopted a reduced-$\chi^2 = 1$ approach, conceptually similar to that used in the SALT fits. Nuisance parameters, including R_V, are determined by minimising Hubble residuals for the whole diagram. In Table 3.8 we have only presented fits to the TS model for the "out of the box" data of Freedman et al. (2009), which was fit to a FLRW model with constant dark energy equation of state parameter, w. To be more confident about the conclusions we should redo the data reduction for the TS model. However, such a task requires considerable effort, and we will defer this until such a time as significantly more data is available. At this stage we note that Freedman et al. (2009) found a value of $R_V = 1.74 \pm 0.27\,(\mathrm{stat}) \pm 0.01\,(\mathrm{sys})$, considerably lower than the Milky Way $R_V = 3.1$ value, which is consistent with the values of the corresponding values of β typical in the SALT fits. Furthermore, the very low expectation values of Ω_m are consistent with SALT2 and Union2. While the bestfit value of Ω_m is essentially driven to zero, giving an extremely skewed distribution, we must recall that this was also the case for Union2 "out of the box" data in

Table 3.3 before the SALT II parameters were recomputed for the TS luminosity distance. Also, all the SNe Ia in this sample are at very low redshifts, so the SALT-like behaviour is not unexpected.

3.5.4 Systematic issues for MLCS

The bestfit results from MLCS31 ($R_V = 3.1$) for the minimum redshift cuts in Figs. 3.10 and Figs. 3.12 are erratic compared with the other samples. The relatively stable results from MLCS17 ($R_V = 1.7$) and SDSS II ($R_V = 2.18$) suggest that while the MLCS samples are better fit by the TS model, such fits are still highly affected by the treatment of dust extinction and reddening, since these samples use different vales of R_V. However, these samples also use different selection criteria, so the issues are much subtler than simply the value of R_V assumed. In particular, the Gold dataset and the MLCS31 dataset (Hicken et al., 2009) are both fit with $R_V = 3.1$ and yet they produce expectation values of $\Omega_{\rm m}$ which differ by a standard deviation once the SHS cut is made. Similarly, the MLCS17 dataset (Hicken et al., 2009) and SDSS-II dataset are both fit with low R_V values, respectively 1.7 and 2.18, while producing expectation values of $\Omega_{\rm m}$ which differ by nearly one standard deviation, for the SHS-cut samples.

These large differences in the probable values of $\Omega_{\rm m}$ suggest that the different assumptions in sample selection made with different versions of MLCS2k2 have a very significant impact in the determination of TS model parameters. As a check, we have redone the analysis of Table 3.8 for the objects common to the following samples: Sample A contains the 76 SNe Ia common to the Gold and MLCS31 datasets; and Sample B contains the 74 SNe Ia common to the Gold and MLCS17 datasets. These two samples include the same SNe Ia apart from four objects, three of which, SN 1999gp at $z = 0.026$, SN 1991U at $z = 0.033$, and SN 1992J at $z = 0.046$ are in Gold and MLCS31 but not in MLCS17, and one of which, SN 2004D4dw at $z = 0.961$, is in Gold and MLCS17 but not in MLCS31. We have tested both samples both in full and with a SHS cut. Of the four supernovae not common to both Sample A and Sample B, only one, SN 1999gp is below the SHS, though SN 1991U at $z = 0.033$ is borderline. In addition, we make a final cut to include the 66 SNe Ia above the SHS which are common to both samples.

Dataset	z cut	N	χ^2	$\Omega_{\rm m}$	$\ln B$
A Gold	≥ 0.024	76	60.7	$0.20^{+0.20}_{-0.19}(0.13)$	0.73
	≥ 0.033	68	51.0	$0.19^{+0.19}_{-0.18}(0.02)$	0.41
	≥ 0.033	66	41.3	$0.23^{+0.24}_{-0.22}(0.23)$	0.84
A MLCS31	≥ 0.024	76	76.6	$0.14^{+0.13}_{-0.13}(0.01)$	0.09
	≥ 0.033	68	65.7	$0.13^{+0.11}_{-0.12}(0.01)$	-0.73
	≥ 0.033	66	51.9	$0.16^{+0.16}_{-0.15}(0.01)$	0.40
B Gold	≥ 0.024	74	50.5	$0.24^{+0.23}_{-0.23}(0.26)$	0.80
	≥ 0.033	67	41.3	$0.23^{+0.23}_{-0.22}(0.23)$	0.93
B MLCS17	≥ 0.024	76	76.2	$0.18^{+0.20}_{-0.17}(0.11)$	0.93
	≥ 0.033	67	74.5	$0.18^{+0.19}_{-0.17}(0.01)$	0.86

Table 3.9: Parameter values for SN Ia datasets, applying homogeneity scale cuts, to the 76 SNe Ia common to Riess07 Gold and MLCS31 (Sample A); and to the 74 SNe Ia common to Riess07 Gold and MLCS17 (Sample B).

From Table 3.9 we see that the expected and bestfit values of $\Omega_{\rm m}$ for the Riess07 Gold sample are somewhat reduced relative to those of the full sample given in Table 3.9, and that they agree with the corresponding values for the MLCS31 and MLCS17 subsamples within the 1σ uncertainties. Nonetheless there are still some differences in the central expectation values, particularly in the case of the MLCS31 sample. Since the Gold and MLCS31 samples assume the same $R_V = 3.1$, the differences might be a consequence of the different assumptions about extinction priors (Jha et al., 2007) made in the different implementations of MLCS2k2.

While in most cases the Bayesian evidence for the TS model relative to the spatially flat ΛCDM model is improved for the subsamples of Table 3.9, the most striking change comes about when the MLCS17-excluded SNe Ia SN 1991U and SN 1992J are excluded from the SHS–cut Gold and MLCS31 A samples, reducing these from 68 to 66 objects. The effect of this is to substantially increase $\Omega_{\rm m}$ in both cases, to remove a dramatic negative skew of the bestfit $\Omega_{\rm m}$ in the Gold subsample, and to change the Bayesian evidence by an order of magnitude, (a factor 3 in B), in the case of the MLCS31 subsample. We have not investigated the reasons for the exclusion of SN 1991U and SN 1992J in the MLCS17 sample; however, they do indeed appear to be outliers in the present analysis. To test this hypothesis, we have recomputed the Riess07 Gold and MLCS31 entries of Table 3.8 with the three MLCS17-excluded SNe Ia removed. Table 3.10 shows the results. One might expect the effect of removing two SNe Ia on these larger samples to be less. Nonetheless, the SHS-cut samples do show quite a dramatic change. The Bayesian evidence for the TS model is significantly increased in each case.

Finally, given that individual SNe Ia which were excluded from either the MLCS17 or MLCS31 samples by Hicken et al. (2009) are potential outliers, (at least for the ΛCDM model), we recompute Table 3.8 for the 352 SNe Ia common to both MLCS31 and MLCS17 samples, using each R_V normalization. The results are shown in Table 3.11. For the SHS-cut samples, there is no overall change to the $\Omega_{\rm m}$ parameter for the MLCS17 sample, but the bestfit value of MLCS31 sample is increased to be more in line with the Table 3.10 result. There is now positive

Dataset	z cut	N	χ^2	$\Omega_{\rm m}$	$\ln B$
Gold	≥ 0.024	179	151.0	$0.34^{+0.13}_{-0.11}(0.36)$	-0.77
	≥ 0.033	167	139.9	$0.31^{+0.15}_{-0.13}(0.34)$	-0.63
MLCS31	None	363	414.9	$0.08^{+0.05}_{-0.07}(0.01)$	-1.27
	≥ 0.024	276	317.2	$0.10^{+0.08}_{-0.09}(0.01)$	0.50
	≥ 0.033	227	248.4	$0.13^{+0.13}_{-0.12}(0.08)$	1.68

Table 3.10: Recalculation of Table 3.8 for the Riess07 Gold sample and the MLCS31 samples, with three low redshift SNe Ia that were excluded by Hicken et al. (2009) from their MLCS17 sample, SN 1991U, SN 1992J and SN 1999gp, excluded.

Bayesian evidence for the TS model versus the spatially flat ΛCDM model for MLCS17 as well as MLCS31 with the SHS cut.

While the analysis of this section has not been able to resolve the issue of how similar R_V values can lead to quite different expectation values of $\Omega_{\rm m}$, as shown by the case of the Gold sample versus the MLCS31 sample, or by the SDSS-II sample versus the MLCS17 sample, it does show that the question of extinction priors, and the SNe Ia excluded by particular priors, may be crucial to this. Ideally one should re-evaluate the MLCS2k2 parameter fitting using the TS model at the outset.

3.5.5 Parameter sensitivity in the timescape model

The parameter $\Omega_{\rm m}$ is much more sensitive to the method of data reduction in the case of the TS model than it is in the ΛCDM model. Of course, we have not explored the goodness of fit of the ΛCDM model when cuts are made at the SHS in the same way that we have for the TS model, as there is no theoretical rationale for doing so.

In order to understand differences in the degree of sensitivity of parameter estimation between the two models, let us consider the fit of the MLCS2k2 data once a SHS cut is made. In Fig. 3.13 we display confidence contours for the SHS-cut ($z \geq 0.033$) Gold sample of Table 3.10, the SDSS-II sample of Table

Dataset	z cut	N	χ^2	$\Omega_{\rm m}$	$\ln B$
MLCS17	None	352	366.9	$0.16^{+0.13}_{-0.15}(0.17)$	1.20
	≥ 0.024	266	293.8	$0.16^{+0.14}_{-0.15}(0.18)$	1.10
	≥ 0.033	219	238.1	$0.19^{+0.14}_{-0.18}(0.21)$	1.37
MLCS31	None	352	403.4	$0.08^{+0.05}_{-0.07}(0.01)$	-1.31
	≥ 0.024	266	310.0	$0.09^{+0.09}_{-0.08}(0.01)$	0.39
	≥ 0.033	219	242.1	$0.12^{+0.12}_{-0.11}(0.07)$	1.55

Table 3.11: Recalculation of Table 3.8 for the 352 SNe Ia common to both the MLCS31 and MLCS17 samples of Hicken et al. (2009).

3.8, and the MLCS17 and MLCS31 samples of Table 3.11. (In all cases SNe Ia events excluded from either the MLCS17 or MLCS31 samples have been cut.) Corresponding plots for the spatially flat ΛCDM model are shown in Fig. 3.14. Equivalent contour plots for SALT-reduced samples are not shown, since the value of H_0 is marginalised over in the SALT fitting process.

Clearly there are some differences which are intrinsic to the data reduction method, since even in the ΛCDM model the best fit value of the matter density parameter varies from 0.40 ± 0.04 for the SDSS-II sample to 0.26 ± 0.03 for the MLCS31 sample. The fact that the dressed matter density parameter of the TS model is more sensitive than the corresponding value of $\Omega_{\rm m}$ for the ΛCDM model is essentially a consequence of the different manner in which the parameters $\Omega_{\rm m}$ and H_0 affect the luminosity distances in the two models. In the case of the ΛCDM model the confidence contours show a negative covariance between the parameters for the scale chosen in Fig. 3.14. By contrast, although the area of the contours is comparable in both models, on the same scale the confidence contours for the TS model are close to vertical, especially for the smaller values of $\Omega_{M0} \sim 0.3$. Thus in the case of the TS model the parameter H_0 is more tightly constrained than in the ΛCDM model, while the parameter $\Omega_{\rm m}$ is less constrained, given whatever overall normalization of absolute magnitudes is assumed in the data.

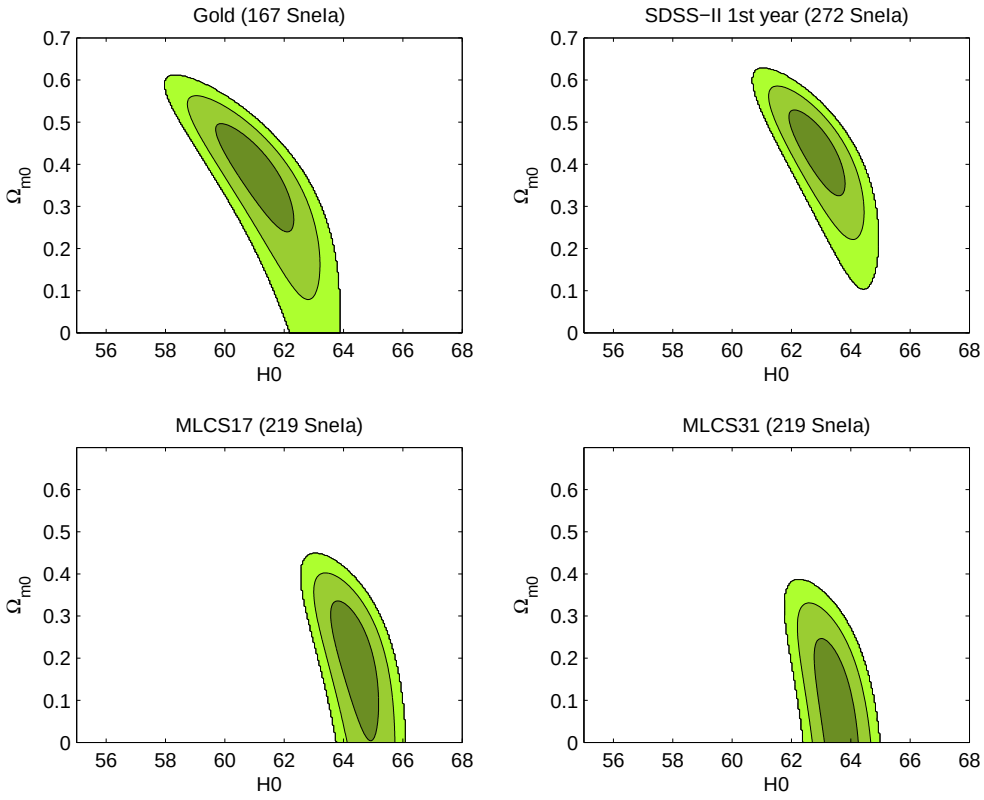

Figure 3.13: Confidence limits for the TS model fits to $z \geq 0.033$ cut samples of Gold (Table 3.10), SDSS-II (Table 3.8), MLCS17 and MLCS31 (Table 3.11). In each case an overall normalization of the Hubble constant and an absolute V magnitude from the published dataset are assumed.

Physically, these differences can be understood to be a consequence of the fact that on one hand the ΛCDM model has actual accelerating expansion, whereas the apparent acceleration in the TS model is less pronounced and its luminosity distance is closer to that of an empty Milne universe.

3.6 Discussion

Even with a SHS cut there remain considerable systematic issues — probably concerning extinction and reddening by dust and intrinsic SNe Ia colour variations — which need to be resolved before one can draw any reliable conclusions about

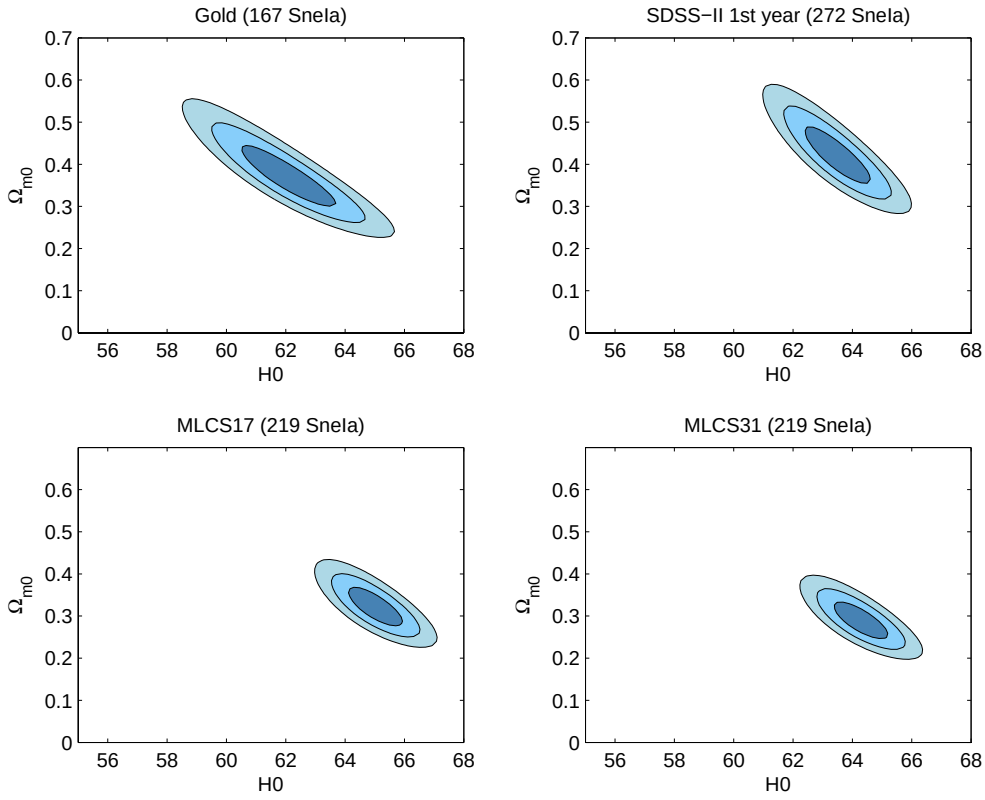

Figure 3.14: Confidence limits for the ΛCDM model fits to $z \geq 0.033$ cut samples of Gold07 (Table 3.10), SDSS-II (Table 3.8), MLCS17 and MLCS31 (Table 3.11). In each case an overall normalization of the Hubble constant and an absolute V magnitude from the published dataset are assumed..

the goodness of fit of one cosmological model over another. These issues have been discussed by many other groups (see, e.g., Freedman et al. (2009); Hicken et al. (2009); Kessler et al. (2009); Lampeitl et al. (2010); Sullivan et al. (2010)).

3.6.1 Reddening by dust

There are at least four possible sources of dust: (i) dust in the Milky Way; (ii) dust in the host galaxy; (iii) dust in the local circumstellar environment of the supernova event; and (iv) dust in the intergalactic medium. Whereas Milky way dust, with the reddening law $R_V = 3.1$ is well understood, we do not have direct

a priori knowledge of the other three possible sources of dust. The present status of our understanding is that while there appears to be no direct evidence of an intergalactic grey dust which would significantly alter the SNe Ia luminosity distance relations, the situation regarding dust within the host galaxy, and within the supernova local environment, is a complex one.

3.6.1.1 Host galaxy dust

The nature of dust in the host galaxy would appear to be the most significant systematic unknown, given that assuming different values of R_V can lead to substantial differences in the MLCS2k2 fitters, and similarly for the value of β in the SALT fitters. Superficially, the results of Table 3.11 might appear to favour the MLCS17 over the MLCS31 sample for the TS model, given the lower value of χ^2. However, it is noticeable that the results for the MLCS17 sample show essentially no change with the cuts made up to the SHS. By contrast, the Bayesian evidence for the TS model over the spatially flat ΛCDM model shows a marked improvement in Tables 3.10 and 3.11 when the SHS cut is applied.

For consistency of the TS scenario an apparent Hubble bubble feature should be seen below the SHS. Consequently the most likely expectation for reddening and extinction by dust consistent with the above results is that, *at least at low redshifts*, the reddening law for dust in other galaxies is close to the $R_V = 3.1$ law of the Milky Way. Independent support for such a conclusion is provided by the recent studies of Finkelman et al. (2008, 2010) and Folatelli et al. (2010) (CSP).

Finkelman et al. (2008, 2010) studied dust lanes in 15 E/S0 galaxies with $z < 0.033$, and determined extinction properties by fitting model galaxies to the unextinguished parts of the images in each of six spectral bands, and then subtracting these from the actual images. They found an average value $R_V = 2.82 \pm 0.38$ for 8 galaxies in their first study (Finkelman et al., 2008), and $R_V = 2.71 \pm 0.43$ for 7 galaxies in their second investigation (Finkelman et al., 2010). These values are a little lower than the Milky Way value but consistent with it within the uncertainties.

Folatelli et al. (2010) investigate the reddening law properties of SNe Ia in host galaxies at $z < 0.08$ using well-sampled, high-precision optical and near-infrared light curves from the CSP. Although a value of $R_V \simeq 1.7$ was obtained

for the whole sample, once two very highly reddened objects SN 2005A and SN 2006X were excluded, a value of $R_V \simeq 3.2$, similar to the Milky Way one, was obtained by comparison of colour excesses. In contrast to the results obtained by comparison of colour excesses Folatelli et al. (2010) found that fits of absolute magnitude gave $R_V \simeq 1$–2, even when the two highly reddened SNe Ia were excluded. This discrepancy suggests that in addition to the normal interstellar reddening produced in host galaxies, there is an intrinsic dispersion in the colours of normal SNe Ia which is correlated with luminosity but independent of the decline rate. This would suggest that the low R_V values inferred in the MLCS17 and SDSS-II analyses may be anomalous, and furthermore that there may be intrinsic systematic problems with the empirical methodology assumed by the SALT fitter.

3.6.1.2 Supernova circumstellar dust

The actual picture is further complicated, however, if the local circumstellar environment of individual SNe Ia is important for a significant subclass of events. That this is potentially the case was borne out by a recent analysis of Wang et al. (2009). They found that within a sample of 158 normal SNe Ia, roughly one third of the objects displayed high photospheric velocities, as determined from Si II λ6355 absorption lines. These high velocity SNe Ia were found to be on average ~ 0.1 mag redder than the larger group of "normal" supernovae. This high velocity sample includes the two very highly reddened objects SN 2005A and SN 2006X, whose exclusion[1] led to the $R_V \simeq 3.2$ estimate of Folatelli et al. (2010). This could either mean that the high velocity sample have intrinsically red $B-V$ colours or that they are associated with dusty local environments. Evidence for the second possibility is directly seen in the case of SN 2006X in the nearby Virgo

[1]Of the events in common to the analysis of Folatelli et al. (2010) and Wang et al. (2009) all apart from three objects SN 2004ef, SN 2005A and SN 2006X are classified by Wang et al. (2009) as normal. Wang et al. (2009) note that there is no sharp division between their normal and high velocity groupings when the photospheric velocity approaches a lower value, so that blending can occur to some extent. The object SN 2004ef is the only one treated as normal by Folatelli et al. (2010) but it is classified as high velocity sample by Wang et al. (2009).

cluster spiral galaxy[1] M100 (Patat et al., 2007; Wang et al., 2008a,b). A model with multiple scattering of photons by circumstellar dust is found to steepen the effective extinction law (Goobar, 2008). Wang et al. (2009) found that their reddened high velocity subsample preferred a lower extinction ratio $R_V \simeq 1.6$, compared with $R_V \simeq 2.4$ for the normal group, which is consistent with this theoretical model. The difference of the R_V value of the normal group from the corresponding value of Folatelli et al. (2010) may be a further hint of a possible intrinsic colour dispersion of the normal group.

If the sample of Wang et al. (2009) is representative then perhaps of order one third of SNe Ia could have different effective R_V values. We note, for example, that 78 objects are common[2] to the sample of Wang et al. (2009) and the MLCS17 sample of Hicken et al. (2009). Of these 27 are classified as high velocity by Wang et al. (2009), and the rest as normal, which are the same rough proportions as the full sample. However, one must take great care in making generalizations based on low redshift samples, as low redshift SNe Ia are often discovered by targeting galaxies of particular types, such as massive galaxies. This could introduce significant selection bias of the sample compared with higher redshift SNe Ia samples.

Furthermore, much needs to be done to understand the astrophysics of non-standard circumstellar dust, as the relative proportion of objects could be affected

[1]The circumstellar material around SN 2006X was identified by the presence of time-variable and blue-shifted Na I D features by Patat et al. (2007), and from a light echo by Wang et al. (2008b). Spectroscopic and photometric analysis of extinction due to circumstellar dust around SN 2006X has been parameterised with $R_V = 1.48 \pm 0.06$ (Wang et al., 2008a). VLT spectropolarimetry (Patat et al., 2009) provides independent confirmation that the intervening dust is different in nature from typical Milky Way dust. SN 2006X is an unusual SN Ia, however, having one of the highest expansion velocities ever observed, as well as being very highly reddened. A further sample of 31 SNe Ia has been studied for the presence of the same Na I D features as SN 2006X by Blondin et al. (2009). The only object in their sample other than SN 2006X which exhibited such features was the highly reddened SN 1999cl, which is classified as a high velocity object by Wang et al. (2009). There are 24 objects in common to the studies of Wang et al. (2009) and Blondin et al. (2009) including SN 2006X and SN 1999cl. Of the 22 objects which do not exhibit variable Na I D features, 17 are classed as normal by Wang et al. (2009) and 5 as high velocity. This suggests Na I D variability may not be systematically related to nonstandard dust.

[2]These objects are all at low redshifts, $z < 0.06$, and some 86% are within the SHS.

by evolution. For example, it has been suggested that the nonstandard dust of SN 2006X might be due to circumstellar material accreted from a companion star in the red giant phase (Patat et al., 2007). If the nature of the companion star to a SN Ia progenitor is important in characterizing nonstandard dust, then the relative statistics of such events may change with redshift.

3.6.1.3 Intergalactic dust

The possibility that the anomalous faintness of SNe Ia could be accounted for by intergalactic "grey dust", that could dim the SNe Ia without reddening them, was ruled out by the HST data (Riess et al., 2007) (see Fig 3.2).

The possible cumulative effect of intergalactic dust ejected from galaxies has been investigated by Ménard et al. (2010), who analysed the reddening of $\sim 85,000$ quasars at $z > 1$ due to the extended halos of 20 million SDSS galaxies at $z \sim 0.3$. They found that on large scales dust extinction has a wavelength dependence described by[1] $R_V \simeq 4.9 \pm 3.2$. The cumulative presence of intergalactic dust along the line of sight turns out not to affect the colour-magnitude-stretch scaling relations, but does bias cosmological parameters in the standard cosmology at a level comparable to current statistical errors, i.e., a few percent (Ménard et al., 2010) — accounting for the intergalactic dust led to a 6% increase in $\Omega_{\rm m}$ for the spatially flat ΛCDM model. Given the increased sensitivity of $\Omega_{\rm m}$ in the TS model to changes in the treatment of SNe Ia systematics, this bias may have an even greater impact, and should be further investigated.

3.6.2 Intrinsic colour variations

As discussed in Sec. 3.6.1.1 above the analysis of Folatelli et al. (2010) suggests that there may be an intrinsic dispersion in the colours of normal SNe Ia which is correlated with luminosity but independent of the decline rate. This may be significant in understanding the dramatic differences for the TS model between the results of the MLCS2k2 fits and the SALT fits, given that the latter rely on

[1]The analysis of Ménard, Kilbinger, and Scranton (2010) assumed the slightly lower value $R_V = 3.9 \pm 2.6$.

an empirical parameterisation in which the effects of intrinsic colour dispersion are degenerate with those of reddening by dust.

Much effort has gone into both theoretical and observational studies which attempt to find direct correlations between SN Ia luminosity and particular effects, including metallicity of the progenitor, age of the progenitor, asymmetries of the explosion, central density and C/O ratio etc[1]. While these effects could account for further secondary corrections to the light curve fitting which need to be performed to account for intrinsic colour variations, a great many more studies are required to sort out the physics. Indeed, there is a possibility that different effects are involved in a manner which may make them difficult to disentangle as the progenitor population evolves over cosmological time scales.

It is well established that the age of progenitor system is a key variable affecting supernova properties, a feature which has been known since the early work of Hamuy et al. (1995), who observed that in their nearby sample, brighter SNe Ia tend to occur in late-type galaxies. A broad division of SNe Ia can be made into "prompt" and "delayed" groups (Scannapieco and Bildsten, 2005), where the "delay time" is the interval between star formation and supernova explosion. The former group comprise intrinsically brighter, slow-declining (large stretch) SNe Ia which come from a young stellar population and have a rate proportional to the star formation rate ($\sim 0.5\,\mathrm{Gyr}$ timescale), while the latter group consists of intrinsically dimmer (smaller stretch) fast decliners, which take several Gyr to explode and come from much older populations with a rate proportional to the mass of the host galaxy (Sullivan et al., 2006). Since star formation rate increases over the redshift ranges in which SNe Ia occur, the number of prompt SNe Ia will increase with redshift, and therefore the mean luminosity of the population should increase with redshift (Howell et al., 2007). The *rate* at which SNe Ia occur has also been found to increase with redshift from a sample extending to $z = 1.45$ (Barbary et al., 2010, 2011) — which would seem to lend weight to the suggestion that SNe Ia are affected by evolution but does not necessarily imply it.

It is quite possible that it is intrinsic effects related to the differences between the prompt and delayed events which are not fully accounted for with the current light curve fitters. However, light curve corrections can reverse the trends in the

[1]For a detailed list of references see Sec. 2 of Höflich et al. (2010).

underlying population if the fitter only assumes a single class of standardizable object, when there are actually more than one. Recent studies by Sullivan et al. (2010) and Lampeitl et al. (2010) both find a statistically significant correlation between SN Ia luminosity and host galaxy type. In particular, more passively evolving galaxies tend to host SNe Ia which, *after light curve correction* are of order 0.1 mag brighter than those in galaxies with high specific star formation rates. The passively evolving galaxies are generally more massive, and so there is a related correlation, which has also been observed in earlier work with smaller nearby samples (Kelly et al., 2010). Sullivan et al. (2010) studied SNLS data using the SiFTO light curve fitter, which uses a similar methodology to SALT. They found that events of the same light-curve shape and colour were on average 0.08 mag brighter, at 4σ confidence, for the the passively evolving subclass of SNe Ia. The passively evolving subclass also favoured smaller values of the SALT-like parameter β than those in galaxies with significant star formation, at the 2.7σ confidence level. Very similar results were obtained by Lampeitl et al. (2010) using SNLS data and both the SALT II and MLCS2k2 fitters. For MLCS2k2, the favoured value of the parameter R_V is found to be different between the two subclasses, with values $R_V \sim 1$ favoured by the passively evolving subclass and $R_V \sim 2$ by the the star-forming hosts.

Both Sullivan et al. (2010) and Lampeitl et al. (2010) recommend correcting light curves based on two sets of SN Ia templates, depending on galaxy types. Since the effective $\Omega_{\rm m}$ parameter of the TS cosmology is more sensitive to the differences between different light curve fitters, it would be extremely interesting to test what effect this would have.

3.7 Conclusions

The broad conclusion of the study undertaken in this chapter is that the principal criticism of the TS cosmology made by Kwan et al. (2009) does not hold up when the issues surrounding the systematics of SN Ia data reduction are thoroughly investigated. In particular, the unreasonably small bestfit values of $\Omega_{\rm m}$ (or equivalently the unreasonably high bestfit values of the void fraction, $f_{\rm v0}$) for the full Union and Constitution datasets are an artifact of failing to exclude SNe Ia below

the scale of statistical homogeneity from the analysis. Such a cut must be made for the purpose of consistency with the TS model, given that an apparent Hubble bubble with certain characteristics will be found below the SHS. The main issue is not the size of the datasets, as Kwan et al. (2009) claimed, but the systematics of the data reduction methods.

We have shown that when suitable cuts are made then the SALT fitters, as currently implemented, provide Bayesian evidence to favour the spatially flat ΛCDM model over the TS model. However, by contrast the MLCS2k2 similarly provide Bayesian evidence that favours the TS model over the spatially flat ΛCDM model. Basically, both models are a very good fit and it is the light curve fitting systematics that underlie the few percent level differences which have to be sorted out to distinguish the two cosmologies.

As yet these systematics are not fully understood, and involve many subtleties. For example, the value of $\Omega_{M0} = 0.42 \pm 0.10$ obtained for the TS model with the SHS-cut SDSS-II sample is twice the corresponding value for the SHS-cut MLCS17 sample, $\Omega_{M0} = 0.19^{+0.14}_{-0.17}$, despite their similar R_V values (although these parameter values are consistent within the errors). It is clear that the differences do not involve a single parameter alone. Nonetheless, given that an apparent Hubble bubble below the scale of statistical homogeneity is a feature of the TS scenario, the differences between SHS cuts applied to the MLCS17 and MLCS31 samples suggest consistency for the TS scenario if galaxies which host normal SNe Ia events have a reddening law with R_V value close to the Milky way value, $R_V \simeq 3.1$, at least at low redshifts. Distinguishing normal SNe Ia from other events may be further complicated by

- the existence of a subclass of events with nonstandard dust, possibly related to circumstellar dust, as in the study of Wang et al. (2009);

- the existence of an intrinsic colour variation, uncorrelated with decline rate, which distinguishes normal SNe Ia in passively evolving galaxies from those in galaxies with significant star formation, as evidenced by many studies including the recent studies of Sullivan et al. (2010) and Lampeitl et al. (2010).

In our opinion systematic questions should ideally be resolved by detailed studies which attempt to understand the astrophysics involved with as few cosmological assumptions as possible, rather than purely empirical correlations based on homogeneous cosmologies. For example, in trying to sort out systematics at the percent level the current approach is often to test how variation of empirical parameters affects Hubble residuals, using a standard ΛCDM model or a homogeneous dark energy cosmology with fixed equation of state parameter, w. However, such a parameterisation has no meaning for the TS cosmology, as was demonstrated in Fig. 3 of Wiltshire (2009), where the equivalent $w(z)$ determined from a perfectly smooth luminosity distance relation was found to be ill-defined at $z \sim 1.7$.

Furthermore, from the viewpoint of the TS model, distinctions based on Hubble residuals should not be used below the scale of statistical homogeneity, $z \lesssim 0.033$, since a natural variance in the Hubble flow is to be expected below this scale. The only scales within which Hubble residuals would be a safe determinant of empirical correlations would be over those scales beyond the SHS over which an effective linear global average Hubble law pertains, e.g., on scales $0.033 \lesssim z \lesssim 0.1$. Beyond such a scale any Hubble residuals, whether based on the ΛCDM model, the TS model or any other model, are cosmology-dependent.

For a simple two model comparison it would be important to fully re-perform the MLCS reduction, including cuts based on extinction priors, using the TS model from the outset. Likewise, the changes to Hubble residuals with different classes of SN Ia light curves for passively evolving galaxies, as opposed to star-forming galaxies, should be investigated.

Given that the issues of dust extinction and reddening are so entangled with the question of intrinsic colour variations, we really require many independent studies, such as those of (Finkelman et al., 2008, 2010), which examine reddening laws in other galaxies without any reference to SNe Ia.

Cosmology is a unique science, in the sense that its most basic quantity — distance—can only be determined by assuming a cosmological model when interpreting measurements such as spectra, apparent magnitudes and angles on the sky. We have to be careful to recognize how the cosmological models we assume

affect our approach to data reduction. The TS model is a well-motivated alternative to the standard ΛCDM model with some very different properties to homogeneous cosmologies and cannot be parameterised by a well-defined dark energy equation of state parameter, even though the luminosity distance is close to that of FLRW models. The differences between the two models are at the same level as the current systematic uncertainties in SN Ia data reduction which need to be disentangled. We therefore hope that the TS model might be used alongside the standard cosmology as a test by which to determine which systematic effects are truly astrophysical, and which might have an origin in cosmological assumptions.

Chapter 4

Gamma Ray Burst distances and the timescape cosmology

4.1 Introduction

Gamma ray bursts (GRBs) can potentially be used as distance indicators, providing the possibility of extending the Hubble diagram to redshifts ~ 7. In this chapter we follow the analysis of Schaefer (2007) (for the remainder of this chapter, S07), with the aim of distinguishing the timescape cosmological model from the ΛCDM model by means of the additional leverage provided by GRBs in the range $2 \lesssim z \lesssim 7$. We find that the timescape model fits the GRB sample slightly better than the ΛCDM model, but that the systematic uncertainties are still too little understood to distinguish the models.

We saw in the previous chapter that the TS model agrees closely with the ΛCDM model over the range of scales probed by the supernova data (Leith et al., 2007), with certain qualifications: parameter values obtained by minimizing χ^2 fits to the TS Hubble curve depend significantly on the process used to reduce the SN Ia light curves (Smale and Wiltshire, 2011).

The current state of knowledge of systematic uncertainties in the SN Ia data precludes discrimination between the TS and ΛCDM models using SNe Ia (Smale and Wiltshire, 2011). In fact, calculation of the effective comoving distance $H_0 D(z)$ shows that in the redshift range probed by SNe Ia there is little to distinguish between the TS model with the best-fit value for the present void fraction

$f_{\rm v0} = 0.762$ from the Gold dataset of Riess et al. (2007). Wiltshire (2009) has noted that over different redshift ranges $H_0D(z)$ for the TS model closely approximates $H_0D(z)$ for spatially flat ΛCDM models with different values of Ω_{M0} and $\Omega_{\Lambda 0}$. It is thus seen to interpolate between different ΛCDM models as the redshift is varied. Fig. 4.1 shows that between $z \simeq 2$ and $z \simeq 6$, the TS $H_0D(z)$ crosses from coinciding closely with the best fit line from the SNe Ia only to that predicted by the joint best fit to WMAP, BAO and the SNe Ia. In principle GRBs, which probe this redshift range, could distinguish the TS and ΛCDM models in this redshift range, although their use as distance indicators is far from established.

This chapter will establish that the TS model is also supported by the current GRB data (Schaefer, 2007), but that, as one might expect from the SNe Ia results, the uncertainties in the data are as yet too large to distinguish the models in the redshift range $2 < z < 6$.

The chapter is organized as follows. Section 4.2 describes the nature of GRBs and the method of "standardizing" them for their use as distance indicators. Section 4.3 describes the results, before a discussion and conclusions are presented in Section 4.4.

4.2 GRB data reduction method

Gamma ray bursts are transient releases of very high-energy electromagnetic radiation. Gamma rays are produced by such high-energy astrophysical sources as pulsars, supernova explosions, and active galactic nuclei. They are also produced by the explosion of nuclear bombs, and astrophysical gamma ray bursts were in fact first observed by American and Soviet satellites designed to detect violations of nuclear testing bans in the late 1960s. The Burst and Transient Source Experiment (BATSE), aboard the Compton Gamma Ray Observatory satellite, operating between 1991 and 2000, revealed the isotropic distribution of GRBs in the sky, thereby demonstrating their cosmological (as opposed to terrestrial or galactic) origin (Melia, 2009). A cosmological origin was confirmed in 1997 when the detection of absorption lines in the spectra of GRB 970508 showed a redshift $z = 0.835$ (Waxman et al., 1998).

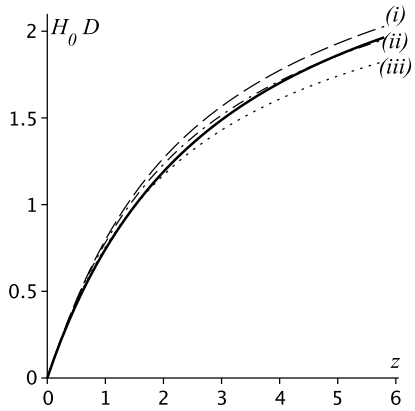

Figure 4.1: Effective comoving distance as a function of redshift for various spatially flat models (dotted lines) and for the TS model with $f_{v0} = 0.762$ (solid line). Parameter values for the dotted lines are (i) $\Omega_{M0} = 0.249$ (best-fit to WMAP only); (ii) $\Omega_{M0} = 0.279$ (joint best-fit to WMAP, BAO and SNe Ia); (iii) $\Omega_{M0} = 0.34$ (best-fit to Riess et al. (2007) SNe Ia only). After Wiltshire (2009).

In contrast to those of the SNe Ia discussed in the previous chapter, the light curves of GRBs are diverse, being highly variable in their time profiles, intensities, and durations, consistent with a diverse morphology of their progenitors. Gamma ray bursts are designated "short" if they occur on time scales of less than a second, and "long" for those lasting seconds to minutes. Their isotropic equivalent luminosities are on the order of 10^{51} erg s^{-1}, or 10^{18} solar luminosities, and they "light up the Universe" about once every minute (van Putten, 2009). These huge energies are consistent with a relativistic jet model for the GRB source — there is no known process that can produce this much energy isotropically in such a short time. Of all GRB events we observe only those for which we lie in the path of the jet. These jets can have bulk Lorentz factors in excess of 100. Such jets are produced by the rotating black hole remnants of core-collapse supernovae which have been linked to GRBs — the long ones most notably — via optical follow-up (van Putten, 2009).

Despite the light curve variability, an empirical fit that has proven successful for many GRBs was presented in Band et al. (1993) in terms of the photon count

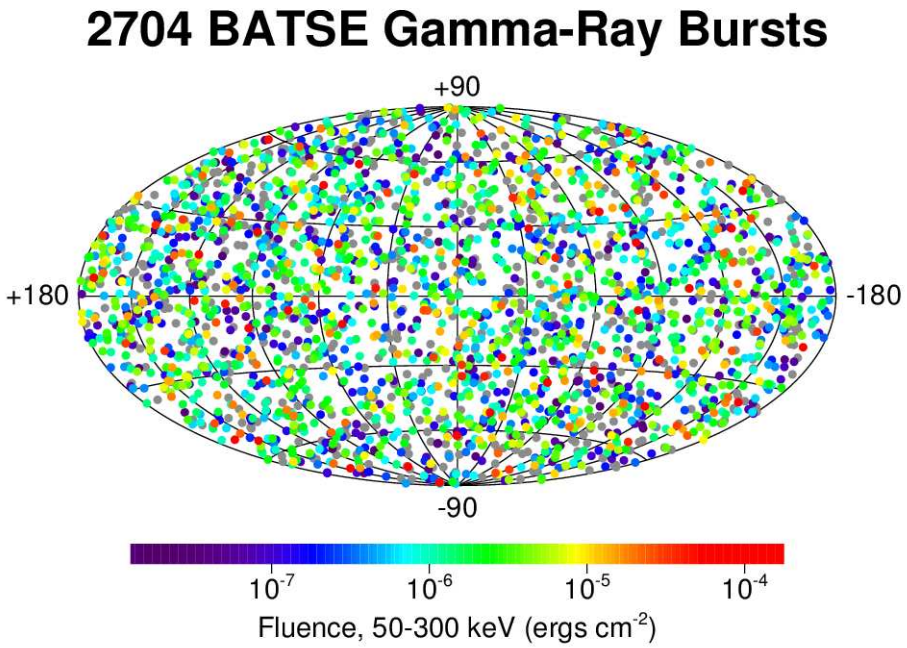

Figure 4.2: The BATSE GRBs are isotropically distributed in the sky and are here shown in galactic coordinates and colour-coded according to their energy. Long duration bright bursts are coloured red, while the shorter faint bursts are coloured purple. Grey points indicate detections with incomplete data. A statistically significant deficit of faint bursts suggests that the BATSE detected the high-redshift edge of the region in which GRBs occur. Source: `http://www.batse.msfc.nasa.gov/batse/grb/skymap/`

N in cm^2 s^{-1} keV^{-1}:

$$N(E) = \begin{cases} E^\alpha \exp\left(-\frac{E}{E_{\rm peak}}\right), & \text{if } E \leq (\alpha-\beta)E_0 \\ [(\alpha-\beta)E_{\rm peak}]^{(\alpha-\beta)}\, E^\beta \exp(\beta-\alpha), & \text{otherwise} \end{cases} \tag{4.1}$$

where E is energy, $E_{\rm peak}$ is the energy at which the fluence spectrum peaks (of order 100-1000 keV (Schaefer, 2007)), α is the asymptotic power-law index for photon energies below the break, and β is the power-law index above the break. The example spectrum of GRB 080916C (the identification number has the format YYMMDD) along with the best fit parameter values is shown in Fig. 4.3.

GRBs are not standard candles, since their luminosities span several orders of magnitude (whether one assumes collimated or isotropic emission). However,

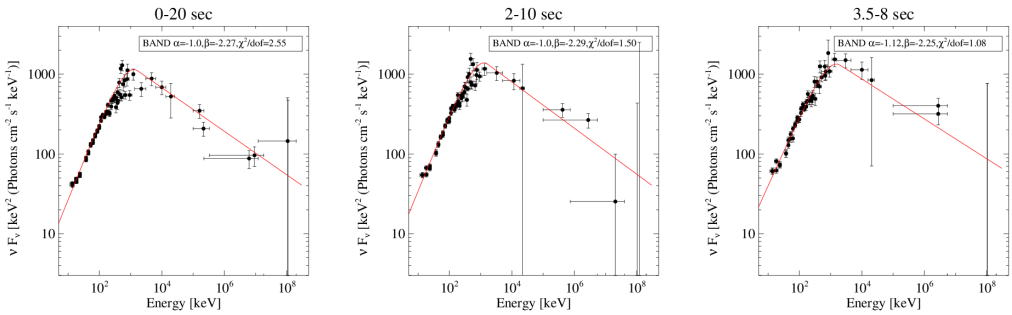

(a) (b) (c)

Figure 4.3: Band parameter fits for GRB 080916C. These observations were made by the Large Area Telescope (LAT) and the Gamma ray Burst Monitor (GBM) aboard the Fermi satellite on 16 September 2008. The smoothly-joint broken power law function is an unusually good fit in this case. Time bins have been reduced in size in order to improve the χ^2 of the fits. Source: Zhang et al. (2011).

there are ongoing attempts to "standardize" GRBs given their promise for cosmology: they occur at higher redshifts than any established standard candles, and radiation in the gamma band ($\geq$ 10 keV) is not subject to the same limitations due to dust extinction as the optical band (Ghirlanda et al., 2006). Certain GRB light curve parameters have been found to correlate with each other, offering the possibility of computing a magnitude, much in the same way as the Phillips stretch-luminosity relation is used to reduce scatter in the SN Ia Hubble diagram.

Here we use a sample of 69 GRBs selected by Schaefer (2007) (henceforward S07) as having sufficient light curve data to compute their placement on a Hubble diagram.

Since there is no nearby GRB sample, there is no GRB calibration of $\bar{H}_0$, so we work with relative distances only. The fitting process therefore results in a best-fit value for the single parameter $f_{\rm v0}$.

Schaefer (2007) uses four light curve parameters that correlate with the luminosity: (1) the lag time $\tau_{\rm lag}$ is the time shift between the hard and the soft light curves; (2) the light curve variability V is the normalized variance of the light curve around a smoothed version of that light curve; (3) the peak energy $E_{\rm peak}$ is the photon energy at which the fluence spectrum is brightest; and (4) the

minimum rise time $\tau_{\rm RT}$ is the shortest time over which the light curve rises by half the peak flux of the pulse. A fifth correlation, $E_{\rm peak} - E_\gamma$, relates the peak energy of the light curve to total photon energy emitted by the burst. This is the tightest of the correlations (Ghirlanda et al., 2004), but it requires measurement of a jet break time by which the measured (isotropic-equivalent) energy can be corrected for the collimation. A "jet break" is an achromatic shift in the GRB afterglow that occurs when the relativistic jet slows down and begins to spread laterally, and most earlier GRB observations were only made after the jet break time, during the spreading phase (Sari et al., 1999). Along with these luminosity indicators a peak flux P is also measured for a wide range of bandpasses. A bolometric flux (or fluence) can be calculated by extrapolating to high and low energies using the Band function (4.1) for the GRB spectrum and integrating over all energies. This brings consistency to the brightnesses, and given a cosmological model, permits the calculation of an isotropic luminosity

$$L = 4\pi d_L^2 P_{\rm bolo}. \tag{4.2}$$

The algorithm goes as follows. The luminosity indicator is the independent variable, and from eq. (4.2) is obtained the Y-coordinate. A linear fit to the logarithms of these quantities gives an empirical relationship between the luminosity indicator and the luminosity. The scatter about the best-fit lines in each case is greater than the measurement uncertainties in both the luminosity and the luminosity indicator, implying the dominance of an additional source of intrinsic scatter over the measurement errors which appears to be independent of luminosity and redshift (Schaefer, 2007). For this reason no weighting is used in the least squares regression, since the weights would bias the best-fit line towards outlying points with smaller uncertainties when in fact there is another physical reason why the point is an outlier.

Since the best-fit slopes would be different depending upon whether we minimize the residuals of the luminosity indicator or of the luminosity itself, we use the *bisector* of the two ordinary least squares fits: that of X against Y, and then vice versa (Isobe et al., 1990), since the relations are not directly causative. We can then use this relationship to calculate a theoretical luminosity curve for each indicator, based on the luminosity distance obtained from eq. (4.2). In cases

where a jet break has been measured, $E_{\rm peak}$ is related to the collimation-corrected energy E_γ, by

$$E_\gamma = 4\pi d_L^2 S_{\rm bolo}(1-\cos\theta_{\rm jet})(1+z)^{-1}, \tag{4.3}$$

for jet opening angle $\theta_{\rm jet}$ and bolometric fluence $S_{\rm bolo}$. The uncertainties in the Y-axis quantities $\log\ L$ and $\log\ E_\gamma$ are obtained from the uncertainties in the X-axis quantities in the standard way. Because the physics of the GRB explosions is not completely understood, the correlations contain some scatter over and above the measurement noise. To account for this, an additional intrinsic uncertainty is estimated such that the reduced χ^2 of the indicator-luminosity calibration curve is unity. The best-fit lines for these relations are given along with their uncertainties in Appendix A.1.

From each calculated L or E_γ we then recalculate a luminosity distance via (4.2) or (4.3), from which we obtain a distance modulus in the standard way: $\mu = 5\log d_L - 25$ for d_L in Mpc. The propagated uncertainties are (Schaefer, 2007)

$$\sigma_\mu^2 = (2.5\sigma_{\log L})^2 + \left(\frac{1.086\sigma_{P_{\rm bolo}}}{P_{\rm bolo}}\right)^2, \tag{4.4}$$

if the bolometric flux $P_{\rm bolo}$ is used, or, if the bolometric fluence is used,

$$\sigma_\mu^2 = (2.5\sigma_{\log E_\gamma})^2 + \left(\frac{1.086\sigma_{S_{\rm bolo}}}{S_{\rm bolo}}\right)^2 + \left(\frac{1.086\sigma_{F_{\rm beam}}}{F_{\rm beam}}\right)^2, \tag{4.5}$$

where the beam factor $F_{\rm beam} \equiv (1-\cos\theta_{\rm jet})$ is calculated from the jet break time $t_{\rm jet}$.

Finally, we take a weighted average of all the five different distance moduli:

$$\mu = \frac{\Sigma_i \mu_i/\sigma_{\mu_i}^2}{\Sigma_i \sigma_{\mu_i}^{-2}}, \tag{4.6}$$

which has uncertainty

$$\sigma_\mu = \left(\Sigma_i \sigma_{\mu_i}^{-2}\right)^{-1/2}. \tag{4.7}$$

Potential issues arise if any of the luminosity relations are correlated: if two of the relations are perfectly correlated then eq. (4.7) means that the weight of what is actually just one correlation is effectively doubled. S07 calculates correlation coefficients between different luminosity relations by calculating the differences between the distance moduli derived from those relations and the

distance modulus of a fiducial cosmological model given the GRB redshift. The only significant correlation turns out to be between the variability-luminosity and the rise time-luminosity relations, but, since these two relations provide relatively little weight for the well-observed GRBs, the actual weight σ_μ is calculated to be only 4% too small. It is calculated that the summed weights are in fact comparable, and since each of the measures carries information, none are rejected.

We avoid circularity by performing a simultaneous fit of both the cosmology and the luminosity relations (Ghirlanda et al., 2004; Schaefer, 2007)— i.e. the luminosity relations are part of the model. The value of H_0 here is arbitrary, since its variation changes the Hubble line and the luminosity calibration of the data in an identical way, resulting merely in a change in the overall normalization of the Hubble diagram. GRBs do not occur in the local universe, so calibrating the GRB Hubble diagram to a value of H_0 with any accuracy is not possible. This is different to the SN Ia case, in which the calibration of light curve and stretch can be done model-independently with nearby SNe Ia, and then extrapolated to objects at higher redshifts. However, regardless of the normalization, the *shape* of the curve in the Hubble diagram depends solely on $f_{\rm v0}$. This means that for a range of values of $f_{\rm v0}$, here between 0.0 and 1.0, we calibrate the luminosity relation and compute the placement of the GRBs on the Hubble diagram, and calculate a corresponding range of χ^2 values. The favoured value for $f_{\rm v0}$ is that for which the χ^2 is minimized.

4.3 Results

We show the results of the linear regressions in Figs. 4.4–4.8 in red. The intercept a and slope b of the TS model calibration line are shown in each figure. For comparison, the ΛCDM-calibrated data points (for a flat Friedmann model with $\Omega_{M0} = 0.27$ and $w = -1$, as calculated in S07) are shown in grey.

The timescape model produces calibrations that are within 1σ of the ΛCDM model in each case. In fact, the TS model regression parameters match those of the concordance model more closely than regression parameters calculated from the variable dark energy equation of state cosmology of Riess et al. (2004)

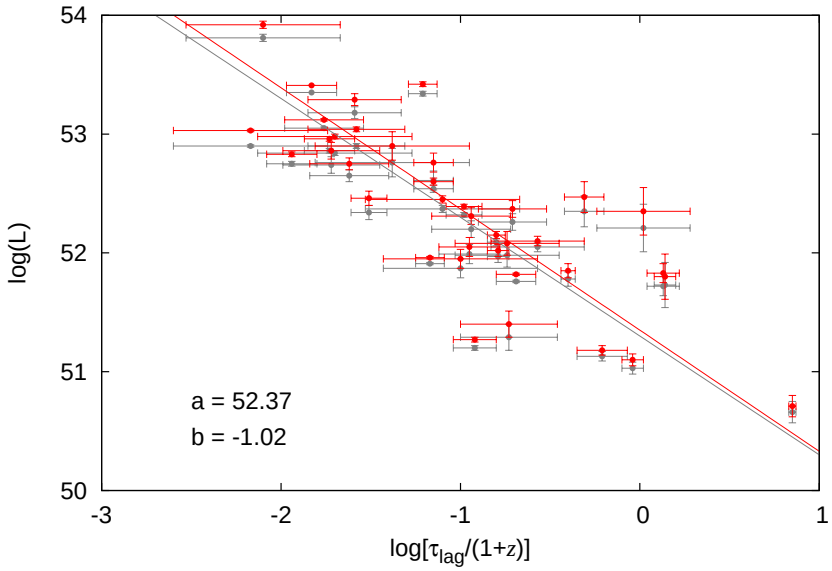

Figure 4.4: Power law relation between lag time $\tau_{\rm lag}$, corrected to the GRB rest frame, and isotropic luminosity, for 38 GRBs. The 1σ measurement uncertainties are used for the error bars. The ΛCDM fit as calculated in S07 is shown in grey. The same colour scheme is also used in Figs. 4.5–4.8. The intercept a and the slope b for the TS calibration are shown on the plot, and the equation of the best-fit line and the expected uncertainty in the luminosity so calculated is given in Appendix A.11.

($w_0 = -1.31$, $w' = 1.48$), computed in S07 to assess the dependence of the calibration on the input cosmology.

The resulting Hubble diagram for the TS model is shown in Fig. 4.9. In the ΛCDM case, with the "concordance" value $\Omega_{M0} = 0.27$, we obtain a reduced χ^2 of 1.05 as in S07. The parameter values that minimize the HD χ^2 are $\Omega_{M0} = 0.21^{+0.22}_{-0.11}$ for the ΛCDM model[1], shown in grey, and $f_{\rm v0} = 0.84^{+0.14}_{-0.21}$ for the timescape model, for which the reduced χ^2 was 1.04 for 68 dof, shown in black. This present void fraction corresponds to a matter density as measured by wall observers via eq. (2.44) of $\Omega_{M0} = 0.23^{+0.25}_{-0.20}$. However, note that there is no *a priori* reason why the ΛCDM and TS values for Ω_{M0} should coincide, since the role of this parameter in each theory is different.

[1]This coincides within a standard deviation with $\Omega_{M0} = 0.39^{+0.12}_{-0.08}$ found in S07, which was found by marginalizing over the slopes and intercepts of the luminosity relations.

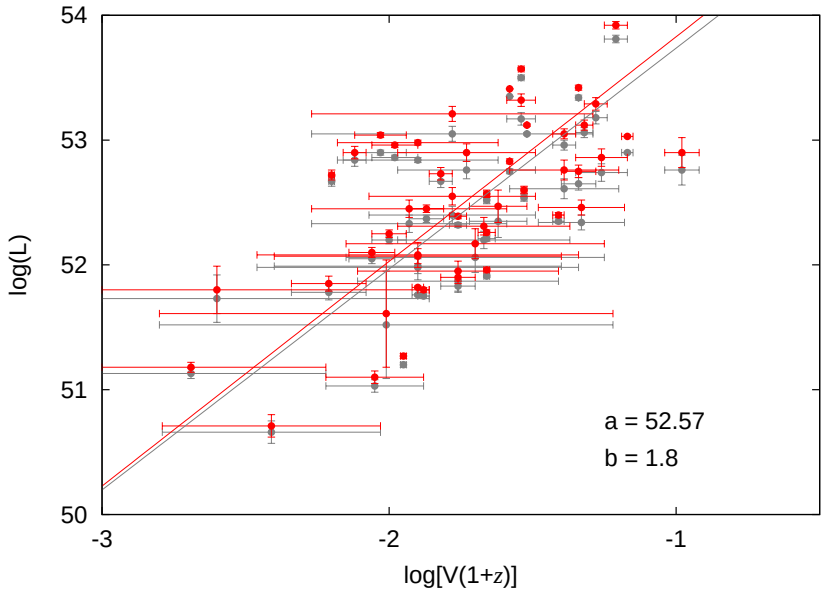

Figure 4.5: Bisector fit of the Variability-Luminosity relation for 51 GRBs. Larger measurement uncertainties in this relation mean it carries less weight in the final luminosity average. The TS intercept a and the slope b are shown, and the equation of the best-fit line and the expected uncertainty in the luminosity so calculated are given in Appendix A.12.

The TS model fits the GRB Hubble diagram slightly better (lower χ^2) than the ΛCDM model. The corresponding Bayes factor $\ln B = 0.18$ indicates Bayesian evidence in favour of the timescape model that is "not worth more than a bare mention" according to the Jeffreys scale (Kass and Raftery, 1995). This is apparent, since the competing predictions of the models lie well within the range spanned by the measurement errors, let alone the systematics, so it can only be concluded that GRB cosmology is not yet precise enough to distinguish between these models.

By contrast, preliminary investigations by Schaefer (2008) indicate that certain modified gravity models and particular exotic forms of dark energy (the Chaplygin gas) provide much poorer fits to the GRB data than the standard ΛCDM model. Amongst the alternatives to the ΛCDM model, the TS model therefore enjoys a degree of phenomenological success which is hard to replicate in a number of other scenarios.

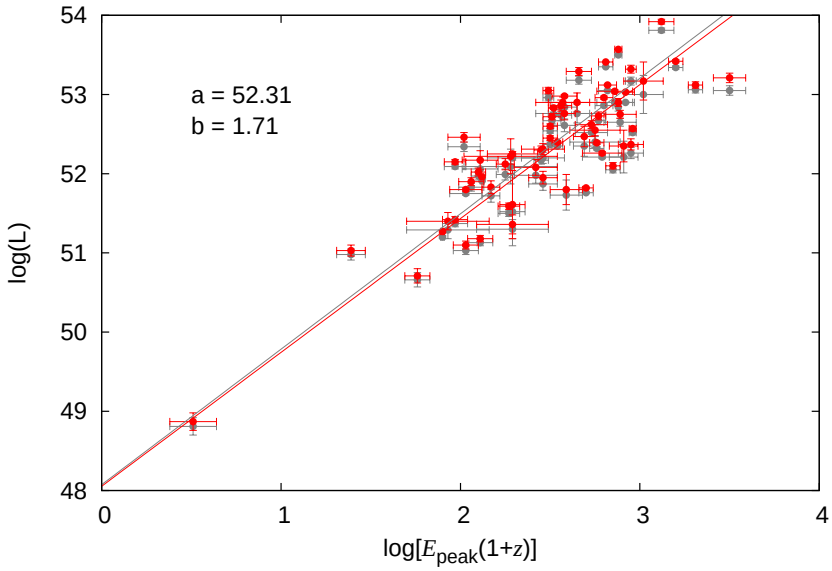

Figure 4.6: Bisector fit of GRB isotropic luminosity to the peak energy $E_{\rm peak}$, corrected to the rest frame of the GRB. $N = 64$. The TS intercept a and the slope b, and the equation of the best-fit line and the expected uncertainty in the luminosity so calculated are given in Appendix A.13.

4.4 Conclusions

Some issues with the use of GRBs as standard candles for constraining cosmological parameters are discussed by Ghirlanda et al. (2006), Ghirlanda, G. (2009), and Petrosian et al. (2009). In particular, the correlations between the isotropic luminosities and the luminosity indicators are weak in a χ^2 sense—physical factors unaccounted for are producing large scatter. Strictly speaking, the $E_{\rm peak} - E_\gamma$ correlation is the only relationship with a sufficiently low reduced χ^2 to admit cosmological parameter estimation, albeit with the caveat that the measurement of the jet break time assumes a particular fireball model (Ghirlanda, G., 2009). Petrosian et al. (2009) point out that the luminosity correlations are statistical in nature, rather than being, as they should ideally, one-to-one relations between uncorrelated quantities. This meant, for example, that the comparatively tight $E_{\rm peak} - E_\gamma$ correlation found by Ghirlanda et al. (2004) actually weakened with the introduction of more data points.

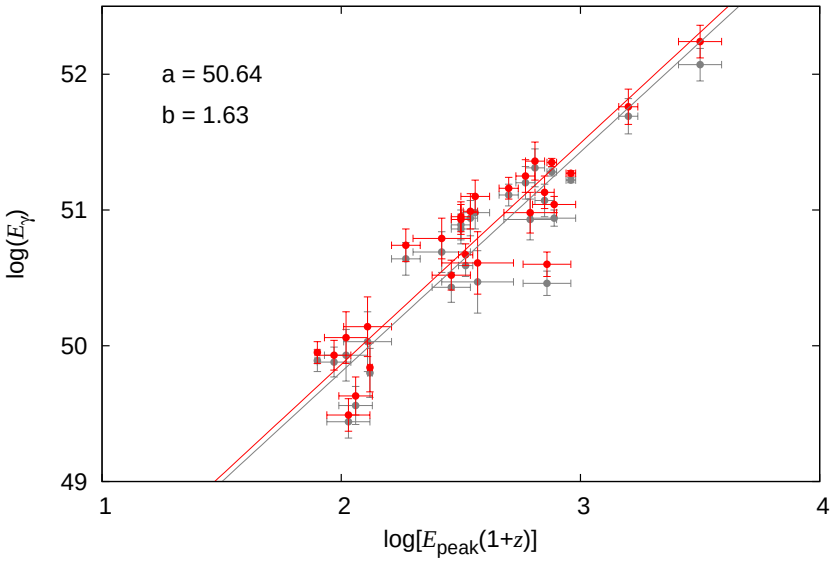

Figure 4.7: $E_{\rm peak} - E_\gamma$ relation for 27 GRBs. This is the tightest of the five power relations but there are fewer data points, since calculation of E_γ requires identification and measurement of a jet break. The TS intercept a and the slope b are shown on the plot, and the equation of the best-fit line and the expected uncertainty in the E_γ so calculated are given in Appendix A.14.

Systematic uncertainties such as dust extinction and evolution constitute considerable limitations to cosmological parameter estimation with SNe Ia. Many of these uncertainties, for example Malmquist bias and gravitational lensing, are considered negligible in the redshift range over which SNe Ia occur. For the redshift range over which GRBs occur, one would expect that Malmquist bias and lensing might cause at least some of the scatter in the GRB Hubble diagram, but these biases are shown in S07 to be negligibly small. Obscuration by dust is not an issue for GRBs (Ghirlanda et al., 2004), but evolution and selection effects can potentially influence the current GRB sample. Petrosian et al. (2009) find evidence for evolution of the GRB peak luminosities, but this should not affect the Hubble diagram, since it is the luminosity relations which should give the right distances for placement on the Hubble diagram. The well-known "Amati" correlation for long-duration GRBs between isotropic-equivalent radiated energy $E_{\rm iso}$, describing the intensity of the burst, and the photon energy at which the

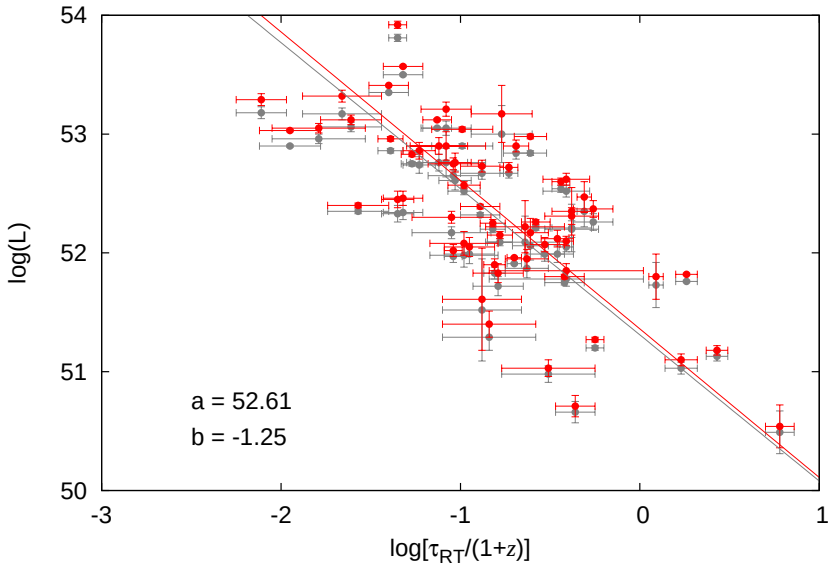

Figure 4.8: Minimum rise time-Luminosity relation for 62 GRBs. The TS intercept a and the slope b are shown, and the equation of the best-fit line and the expected uncertainty in the luminosity so calculated are given in Appendix A.15.

time-averaged spectrum peaks $E_{\mathrm{p,i}}$, although proving to be quite robust (Amati, 2010; Amati et al., 2008), has shown evidence of variation with redshift (Li, 2007) and susceptibility to detector threshold selection effects (Butler et al., 2007). An analysis of 2130 GRBs from the BATSE catalogue (Shahmoradi and Nemiroff, 2011) shows that the $L - E_{\mathrm{peak}}$ relation (so-called Yonetoku relation), is also likely strongly affected and biased by the trigger and the spectral thresholds set on detection, data selection and sampling processes.

It is argued in S07 that the kind of relativistic and geometric effects that underlie the luminosity relations should not be greatly affected by evolution or the metallicity of the progenitor. It is conceivable that a better understanding of GRB physics in the future will allow them to be used as "standardizable" candles, and put their utility for cosmological parameter estimation and discrimination between cosmological models on a firmer basis. Ongoing observational programmes such as *Swift* continue to contribute to this aim. We need to know more about the physics of the GRBs, and we need more high-quality measurements of GRB redshifts, light curves and spectra.

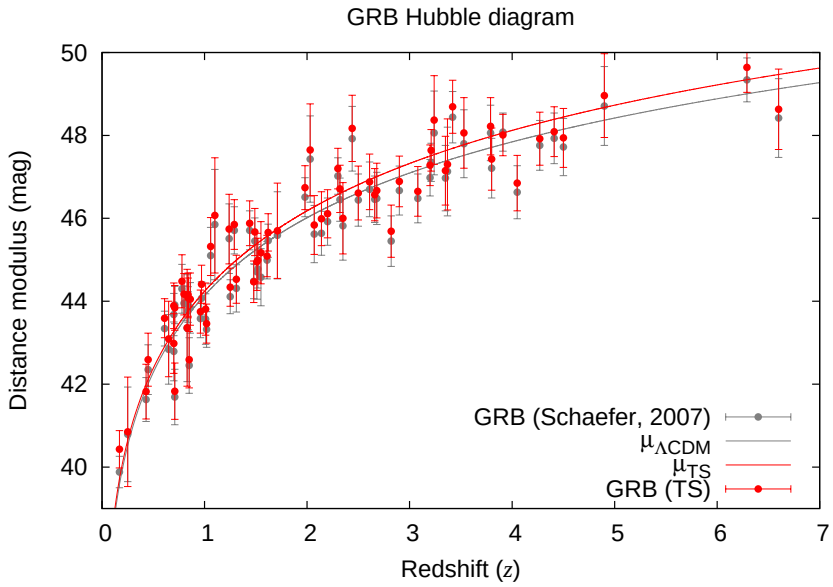

Figure 4.9: Hubble diagram for the 69 GRBs of S07. The ΛCDM best-ft line is shown in grey, and the TS best-fit line is shown in black.

In the meantime, however, we can obtain glimpses of the potential applications of standard candles whose range extends into the era of decelerating cosmic expansion. In the present study, the correlations are forced to be a good fit by incorporating the additional "systematic error" term, computed such that it makes the χ^2 of the best-fit correlation equal to one. This term contributes (in quadrature) to the uncertainty in the log of the isotropic luminosity which propagates through to the Hubble diagram χ^2 via eqs (4.4) and (4.5). A single GRB at a redshift of 5 or 6, with better-determined physical characteristics, potentially carries more statistical power than a single SN Ia at $z = 1.7$ because of the Hubble diagram "lever arm"—the Hubble diagram at redshifts $z > 2$ changes with a different cosmological model or cosmological parameters much more than it does at lower redshifts. We obtain results that are not inconsistent with current models, with certain acknowledged caveats. In particular, there is much scope for progress in improving the GRB Hubble diagram, and much to be gained.

Chapter 5

Hubble variance and the cosmic rest frame

5.1 Introduction

General relativity is a local causal theory, and insofar as the geometry and its expansion are generated by the local sources of energy-momentum, then expanding regions of different density will decelerate by different amounts leading to the development of different regional expansion histories, according to their density. In this chapter we investigate the variation of the Hubble "constant" as measured from a large peculiar velocity survey, the COMPOSITE sample. In the spirit of the timescape model, this will involve implementing spatial averaging techniques with the position of the observer in mind and avoiding Newtonian approximations, but the results are independent of any cosmological model. The only assumption we make is that there exists a suitably averaged Hubble law. Ultimately, this leads us to propose a different mechanism for the origin of the CMB temperature dipole, since without the assumption of a Minkowski background spacetime, the dipole cannot be interpreted as a simple sum of peculiar velocity vectors. Our conclusions support the hypothesis that the expansion of space is not equivalent to a velocity. This work has been written up as a paper (Wiltshire et al., 2012) and submitted to The Astrophysical Journal.

This chapter is organised as follows. In Section 5.1.1 we start with an overview of previous work on the subject (§5.1.1), including four papers in particular that

the work in this chapter builds on. We then motivate this investigation by introducing the dipole anisotropy observed in the CMB (§5.1.1) and then outlining the current picture of the structure in the local Universe (§5.1.1).

Our data is described in Section 5.2. We are very fortunate to have obtained the COMPOSITE peculiar velocity sample (the "largest peculiar velocity survey to date" (Watkins et al., 2009)) from Dr Richard Watkins at Willamette University in Salem, Oregon, US. This is a compilation of supernova and galaxy redshifts, distances and positions from several surveys undertaken between the early 1990s and the middle 2000s.

First, in §5.3 we investigate the Hubble variation in radial spherically symmetric shells, following an analysis by Li and Schwarz (2008) (henceforward LS08) of the HST Key Project data. We make some adjustments to the method we consider appropriate for the larger dataset and consistent with our aim to eliminate dependence on the Newtonian approximation. We find very strong Bayesian evidence that the Local Group reference frame produces a more uniform Hubble expansion field than the CMB frame. We also find that there is a range of distances between roughly 35 and 65 h^{-1} Mpc in which the CMB frame is slightly more uniform than the Local Group frame.

In §5.4 we plot the data on an all-sky map in order to investigate angular variation in the Hubble expansion. The work in this section shows that local inhomogeneity can strongly affect the measured Hubble expansion. We find a clear dipole anisotropy in the Hubble expansion in the LG frame that correlates with the CMB dipole with a Pearson correlation coefficient of -0.92.

This concludes the data analysis section of the chapter. In the concluding section, §5.5, we present discussion and suggestions for future work.

5.1.1 Motivations

Previous work

There have been several recent studies to constrain the peculiar velocity of the Local Group (hereafter, LG) using the supernova data. Two in particular have motivated the work in this chapter. There is a short section in the paper by Jha et al. (2007) (henceforward JRK07) addressing the LG-frame peculiar velocities

of 69 type Ia supernovae from between 1500 and 7500 km s^{-1} whose distances were computed from the light curves using the MLCS2k2 method (see Chapter 3). In their Figure 18, they plot the peculiar velocities on an Aitoff projection of the sky, along with the poles of a best-fit velocity dipole. The direction and magnitude of the dipole they find are consistent with the CMB temperature dipole at approximately the 2σ confidence level, with the difference most likely being due to the sparse sample and the paucity of data from the zone of avoidance. They conclude that the 69 SNe Ia provide evidence for the convergence of the local flow field to the CMB dipole in the redshift range in question. They end with an exhortation to gather more data to fill their gaps. Gordon et al. (2008) used a similar-sized sample of SALT supernovae distances, but with a higher minimum redshift. The aim of this study was to constrain the intrinsic component of the CMB dipole with an accurate determination of the LG motion with respect to the CMB. They use a more sophisticated error analysis to account for the fact that the supernova peculiar velocities are correlated with each other. They find a dipole that is consistent with the earlier study but with much larger errors on the amplitude.

The work in this chapter focuses on the dipole direction, but our aim is not to obtain convergence of the Local Group motion with the CMB dipole, since we wish to avoid assuming a flat background spacetime on large scales. With the COMPOSITE sample, the statistical issues will be different—we will return to these in §5.5—but we are able to obtain a similar dipole, except that we explain it in terms of the variance of the Hubble expansion rather than a large-scale motion with respect to a frame comoving with the cosmic expansion.

The main motivation for recasting the interpretation is that despite the fact that it appears that the motion of the LG in the rest frame of galaxies within 3000 km s^{-1} ($r \lesssim 10\,h^{-1}$ Mpc) is mainly generated within that volume (Lavaux et al., 2010; Tully et al., 2008), bulk flows observed on larger larger scales have yet to show convincing convergence with each other, and estimates of the peculiar velocity of the LG from different implementations of the linear perturbative Newtonian treatment are inconsistent. We can identify two different ways of treating the problem here. The first is the measurement of the bulk flow, which is effectively an average CMB-frame peculiar velocity taken over large scales (e.g.

Kashlinsky et al., 2008, 2009; Nusser and Davis, 2011; Turnbull et al., 2011; Watkins et al., 2009), and the second approach is in terms of the clustering dipole, in which the local peculiar velocity field is computed from the observed density field, to be compared with the observed peculiar velocity field[1]. We now give a brief introduction to some recent work in these areas.

Bulk flows.

A bulk flow is the dipole moment of the CMB-frame peculiar velocity field. There seems to be some agreement between various studies on the direction of the observed bulk flow, but the amplitude of the flow is controversial.

For example, using 4481 peculiar velocities from the COMPOSITE sample, Watkins et al. (2009) (hereafter WFH09) detect a bulk flow of 407 ± 81 km s^{-1} towards $\ell = 287°$, $b = 8°$ within a Gaussian window of $50\,h^{-1}$ Mpc. This result comes from a minimum variance (MV) method which assigns weights to each data point which minimize the variance between a bulk flow measured in the real sample and that which would be measured in a perfectly sampled 3D Gaussian. This weighting scheme addresses the bias in maximum likelihood methods which derive from the increased weights such techniques assign to data points with smaller uncertainties and also up-weights data in regions of low sampling density like the zone of avoidance (see Fig. 5.7). For a Gaussian window of $50\,h^{-1}$ Mpc, the MV weighting scheme is designed to be sensitive only to scales of order $100\,h^{-1}$ Mpc or larger (wavenumbers $k \lesssim 0.06\ h$ Mpc^{-1}). A flow of such a large amplitude, and on such large scales, is unexpected within the WMAP5-normalized ΛCDM model, which, even with the baryon oscillations in the matter power spectrum (Eisenstein and Hu, 1998), predicts a one-dimensional rms velocity of ~ 110 km s^{-1} at these scales. In contrast, Nusser and Davis (2011) find a bulk flow of 333 ± 38 km s^{-1} towards $\ell = 276°$, $b = 14°$ in a top-hat sphere centred on the MW of radius $40\,h^{-1}$ Mpc, and a bulk flow of 257 ± 44 km s^{-1} towards $\ell = 279°$, $b = 10°$ in a MW-centric sphere of radius $100\,h^{-1}$ Mpc, which they find to be *consistent* with the WMAP-normalised ΛCDM model, from the SFI++ velocities, but calculating their own distances. A new version of the COMPOSITE sample, with 245 new MLCS2k2 SN Ia distances (the "First Amendment" compilation),

[1] I am indebted to Maciej Bilicki for clarifying this distinction.

yields a bulk flow of 249 km s^{-1} towards $\ell = 319°$, $b = 7°$ via the Minimum Variance weighting method which is consistent with ΛCDM expectations, but is also marginally consistent with the bulk flow of WFH09 (Turnbull et al., 2011). Union2 supernova distances were used to characterise bulk flows within particular redshift ranges, and even showed evidence of "infall" on to the far side of the Shapley concentration at $z \simeq 0.05$ in the work of Colin et al. (2011). The results of this study support the claim of WFH09: there exists a bulk flow on scales as great as $z \sim 0.06$ that is a problem for the ΛCDM model. At higher redshifts ($z > 0.15$) the agreement with the standard model improves. A reconstruction of the velocity field of the northern SDSS DR7 sample finds a bulk flow in the direction of the Sloan Great Wall ($z = 0.08$) of ~ 100 km s^{-1} over a volume of $\sim 170\,h^{-1}$ Mpc (Wang et al., 2011).

The most controversial bulk flow detection comes from using the frequency shift of CMB photons that pass through hot intracluster gas (the kinetic Sunyaev-Zel'dovich (kSZ) effect). From a sample of more than 800 clusters, Kashlinsky et al. (2008, 2009) detect a very strong bulk flow on scales larger than $800\,h^{-1}$ Mpc, towards $\ell = 296°$, $b = 39°$. This is dubbed the "dark flow", since it suggests the presence of long wavelength inflationary remnants and therefore an intrinsic component in the CMB dipole. Both the magnitude and the direction of this bulk flow are considerably different from any of the other measurements. By contrast, a kSZ study of 715 ROSAT galaxies out to $z \sim 0.45$ finds no significant power at multipoles less than $l = 5$ (Osborne et al., 2011), showing consistency with the predictions of the homogeneous and isotropic model at these larger scales. These groups use different techniques for filtering the CMB, and in a recent review article, Kashlinsky et al. (2012) suggests that Osborne et al. (2011) are in fact filtering out some of the signal that they wish to measure. However, the original kSZ large-scale bulk flow remains controversial and has not been reproduced.

In summary, there is considerable variation in the magnitude of the detected bulk flows. Moreover, because of the relative sparseness of data at the relevant distances, and because the mass of the Shapley concentration is estimated to be insufficient to generate the observed LG motion (Bolejko and Hellaby, 2008; Muñoz and Loeb, 2008), supporting evidence for the picture of a vector sum of peculiar velocities due to particular identifiable mass concentrations eventually

converging on the CMB dipole direction is rather unsatisfactory. We prefer the picture suggested by general relativity of a variable expansion field governed by density gradients that are not localized.

In the standard picture of the local Universe, the peculiar velocities can be decoupled from the cosmic expansion, which amounts to a separation of motions occurring on two different scales. In such a picture, bulk flows are a problem because they occur at an intermediate scale. In a fully relativistic treatment there are motions on many scales and their separation is a more subtle exercise. Here we wish ideally to account for these motions at all scales, and unify their effects by an analysis in terms of variance in the Hubble expansion.

The acceleration or peculiar velocity of the Local Group, apparent in the SN Ia analyses discussed above, is also often called the "clustering dipole". It has a history going back to the first galaxy-redshift surveys of the 1980s (see Bilicki et al. (2011) for a comprehensive introduction). It is this motion that in the Newtonian picture should converge to the CMB dipole direction. However, as discussed in Bilicki et al. (2011); Erdoğdu et al. (2006); Lavaux et al. (2010), there is disagreement over the scale of convergence and even on whether there is convergence at all. Some recent examples: Erdoğdu et al. (2006) claim convergence of the 2MRS dipole converges at $\sim 60\,h^{-1}$ Mpc; Lavaux et al. (2010) do not find convergence even at $120\,h^{-1}$ Mpc; then Bilicki et al. (2011) show that the former result is actually at odds with ΛCDM, as the convergence is expected no sooner than about $200\,h^{-1}$ Mpc. They find that even at $300\,h^{-1}$ Mpc the dipole has not converged to the CMB dipole. All these analyses rely on the linear Newtonian gravitational instability framework that relates the peculiar velocities of galaxies to their peculiar gravitational accelerations (eq. (1.30)).

The lack of demonstrable convergence of bulk flows and the inconsistencies in the estimates of the clustering dipole convergence to the CMB dipole suggests a return to first principles. Based on general relativity, peculiar velocities should be better interpreted as the differential expansion of space that results from the varying expansion history of regions of different density. There are two groups who have investigated the scale dependence of Hubble variation from this perspective, and our work in this chapter builds on their work.

Li and Schwarz (2008) (hereafter LS08), and more recently Wiegand and Schwarz (2011), apply Buchert's averaging scheme to assess the extent of cosmological backreaction that should be expected by virtue of the fact that any local estimation of H_0 is essentially a process of averaging over some spatial domain. Their results are consistent with Newtonian models. We note that the approach of LS08 uses a very different interpretation of the Buchert average to the one proposed in the timescape model. While LS08 calculate Buchert averages of linear perturbations evolved on an Einstein-de Sitter background, a theory of structure formation has yet to be developed for the timescape model, which does not possess an exact highly symmetric background. The aim of this exercise is not to distinguish cosmological models, but simply to assess the Hubble variability in a model-independent way. LS08 test their theory using the statistics of the high-precision Hubble rates measured by the HST Key project (Freedman et al., 2001). In the first part of our study, we investigate the radial Hubble variation adapting the statistical method used in LS08 with the HST Key data to the much larger COMPOSITE sample.

The second part of our study investigates the angular variation of the Hubble expansion following an analysis by McClure and Dyer (2007) (henceforward MD07) that again is based on the HST Key sample. This analysis is based on projections of the smoothed Hubble expansion field on the sky. They find a statistically significant variation of the Hubble constant over the sky for the whole HST Key dataset of 9%.

With the COMPOSITE sample, we are able to build on the results of the studies discussed above. We are able to acquire results with better statistical significance because of the large sample size, but we must be careful to treat the errors appropriately, since they are much larger than those in the HST Key data.

The aether drift and the cosmic rest frame

Any local motion within a sea of blackbody radiation will result in a dipole anisotropy (Peebles, 1993). Radiation received from the direction towards which the observer is moving will be hotter than that received from the opposite direction. The uniform background of relict microwave radiation from the "primeval

fireball" was predicted in the mid-1960s to show just such a dipole due to the motions of the sun and of the Milky Way. In this way the CMB radiation can be said to provide a "cosmic rest frame" similar to the rest frame of absolute space that exists in Newtonian cosmology, independently of the contents of the Universe. The temperature field of the microwave background due to this "aether drift" can be calculated: special relativity leads (Peebles and Wilkinson, 1968) to

$$T_{\theta\phi} = \frac{T_{CMB}}{\gamma(1 - v\cos\theta_{\hat{\mathbf{v}}})}, \tag{5.1}$$

where, in units of $c = 1$, $\gamma = (1 - v^2)^{-1/2}$, and $\theta_{\mathbf{v}}$ is the angular separation of the grid point from the direction of motion.

The COBE and WMAP satellite measurements have converged on a CMB temperature dipole amplitude of 3.35 mK (e.g. 3.346 ± 0.017 mK (Bennett et al., 2003)). Although the possibility exists that the temperature variation might at least in part be intrinsic, the usual, simplest explanation is that the dipole is entirely a consequence of our peculiar velocity in the reference frame of the CMB, which constitutes a surface of average homogeneity. More precisely, the dipole magnitude $\Delta T = 3.35$ mK implies a velocity of about 370 km s^{-1} in the direction of the constellation of Leo (Kogut et al., 1993). The cleanness of the dipole (see Fig. 5.27) is suggestive of such an origin, although it is worth remembering that galactic foregrounds have been subtracted from the sky map, and these cover a significant fraction of the sky in some frequency bands (see Fig. 2 in Tegmark et al., 2003).

Just as our motion results in an enhancement of the radiation field in the direction of motion, it should also result in a $\sim 1\%$ enhancement of the surface density of distant galaxies in the direction of motion. This has been observed in a sample of radio galaxies with a median redshift of $z \sim 1$, after compensating for the possible effects of a clustering dipole on smaller scales (Blake and Wall, 2002).

This motion arises due to density fluctuations on many scales. In cosmology, the boost that results in an isotropic CMB is assumed to also result in a frame in which the variance of the cosmic expansion is minimized: in the "cosmic rest frame", at redshifts $z \ll 1$, the cosmic expansion is governed by a linear Hubble

law about which local density gradients produce scatter. In papers written about the local Universe, a reference frame comoving with the cosmic expansion is generally used, so that one often reads that we are "moving towards" something, or "moving away" from it. But this terminology can be misleading. Many authors state (Tully et al., 2008), for example, that we are "moving towards" the Virgo cluster. It is important to remember that this statement is only true of our velocity relative to a hypothetical idealised uniform expansion, because, of course, all objects beyond the "zero-velocity" radius of the Local Group are moving away from us with the cosmic expansion. Extrapolating the present expansion, the Milky Way will never collide with the Virgo cluster. Even less likely is it that it will ever "fall into" the Great Attractor, at $\sim 50\,h^{-1}$ Mpc, or the Shapley concentration at $\sim 125\,h^{-1}$ Mpc.

These considerations show the difficulty in talking about relative motions. Strictly speaking, in general relativity one cannot compare two velocities except at a point, and so it is meaningless to speak about the velocity of the Milky Way relative to the Virgo cluster. The statement that "in the Local Group frame the cosmic expansion is less than average in the direction of Virgo" is agnostic with respect to the underlying geometry of space, except to say that it is expanding.

For these reasons, in the discussion that follows we discuss the COMPOSITE data not in terms of peculiar velocities $cz - H_0 r$, but in terms of what the ratios cz/r say about the average cosmic expansion H_0. In this way we avoid making assumptions about the nature of the underlying geometry. In particular, in this treatment we can defer, if not circumvent, the question of gauge choice that determines what fraction of the measured velocity of a galaxy can be attributed to cosmic expansion and what fraction is due to local density fluctuations.

Structure in the local Universe

The theoretical prediction from linear perturbation theory for the peculiar velocity field derived by treating the contents of the Universe as an ideal pressureless fluid in comoving coordinates is given by Eq. (1.30), which we introduced at the end of Chapter 1.

In the Euclidean treatment, the Milky Way peculiar velocity vector in the CMB reference frame is built up from contributing motions from several scales. The picture we put together from observations is therefore as follows. The sun has a velocity with respect to the rest frame of the Local Group (LG) of approximately 310 km s^{-1} towards $(\ell, b) = (107°, -7°)$ (Yahil et al., 1977). If the dipole anisotropy in the temperature of the CMB is interpreted as being entirely due to our velocity with respect to the CMB, then the sun is moving at 370 km s^{-1} towards $(\ell, b) = (264.4°, 48.4°)$—i.e. in the opposite direction to that of the sun's motion within the LG. The velocity of the LG in the rest frame of the CMB is then obtained as the difference $\mathbf{v}^{\rm LG}_{\rm CMB} = \mathbf{v}^{\odot}_{\rm CMB} - \mathbf{v}^{\odot}_{\rm LG}$: 627 km s^{-1} toward $(\ell, b) = (279°, 29°)$. The origin of this motion was originally thought to be a large mass concentration hidden behind the MW disc in the direction of Centaurus: the so-called "Great Attractor". From this point, Tully et al. (2008) (henceforth T08) assemble the remaining pieces of the local jigsaw as follows[1]. Figure 5.1, which comes from this paper, is useful for orientation. The Local Group of galaxies is surrounded within 7 Mpc by 150 or so more galaxies with very small velocities relative to the Local Group. Because of its flattened morphology this structure is called the Local Sheet (LS). Thus the LG and the LS share roughly the same motion in the rest frame of the CMB. In the rest frame of the average motion of galaxies in the Local Supercluster (which contains both the Local Sheet and the nearest dense cluster, Virgo) in the peculiar velocity framework the LS is "moving toward" a loose collection of a few galaxies called the Leo spur. The residual of this motion and a vector pointing toward the Virgo cluster is a vector that points directly away from the centre of the Local Void. The expansion of the Local Void contributes a significant component to the motion of the LS centre of mass. The residual of the Local Sheet motion toward the Leo Spur and its motion in the CMB rest frame calculated above points toward objects beyond the survey volume. The nearest large structures in this direction are the Centaurus-Horologium cluster in the region of the Great Attractor, and, still further beyond, at $150\,h^{-1}$ Mpc or so, the Shapley concentration.

[1]There is even a movie associated with this paper that is very useful for orientation. It can be found at http://ifa.hawaii.edu/~tully/pecv_12min_sound_qt.mov

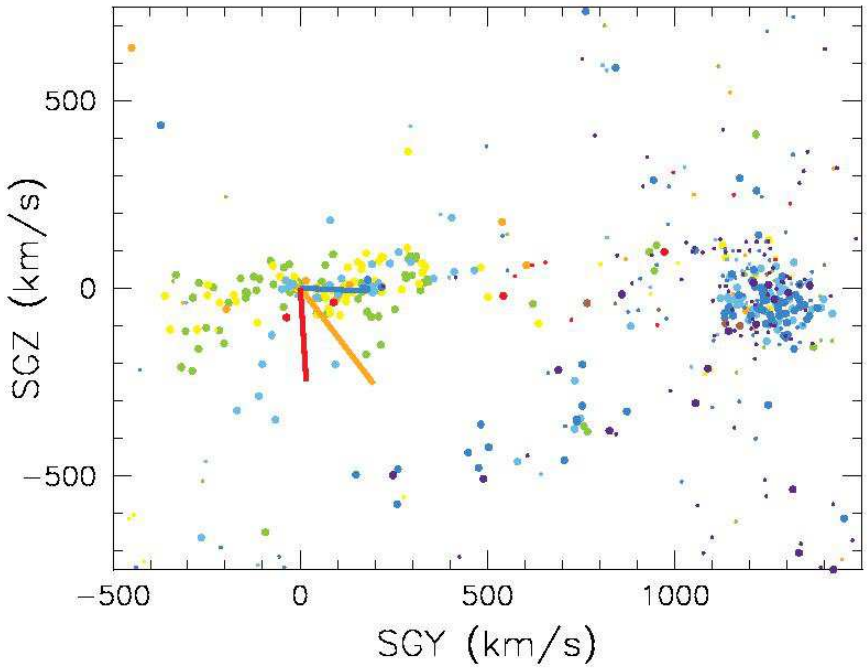

Figure 5.1: Galactic motions within the Local Supercluster. In this figure, in supergalactic coordinates, are shown the Local Sheet (the collection of mostly yellow and green points), the Virgo cluster (the collection of mostly blue and purple points in the +SGY direction, and the Leo Spur (the loose collection of points along (SGY,SGZ) = (200-600,-500) km s^{-1}. The points are colour-coded so that yellow and green represent small peculiar velocities, while blue and purple represent larger peculiar velocities that are directed toward us, while the point size is inversely proportional to its uncertainty. The orange vector pointing towards the Leo spur shows the motion of the Local Sheet in the Local Supercluster rest frame. The blue vector points toward the Virgo barycentre. The residual of these two vectors is shown in red. This vector points roughly radially away from the centre of the Local Void, which is the empty region in the upper left of the figure. Figure credit: Tully et al. (2008).

Although the cosmic web structure has been established and a Local Void has now been clearly delineated in surveys of galaxies in the local volume (Courtois et al., 2011; Tully et al., 2008), a void signature in the local distance measurements is still rather elusive because of selection and volume effects. A large ($\sim 30\,h^{-1}$ Mpc-diameter) nearby void is to be expected from studies of void statistics in the 2dF (Hoyle and Vogeley, 2004) and SDSS (Pan et al., 2011) galaxy redshift surveys which indicate an average void radius of $15\,h^{-1}$ Mpc. For example, the expansion of the Local Void was tested directly by Iwata and Chamaraux (2011) who used new TF distances to 15 galaxies on the far side of the void. This study is an extension of the analysis of T08 discussed above who calculate that the galaxies in the Local Sheet move away relative to the centre of the Local Void with a velocity of 259 km s^{-1}. They find a mean velocity with respect to the Local Group of -419^{+208}_{-251} km s^{-1}, which, although of roughly the right magnitude to support the comparatively fast expansion of the Local Void, is rendered inconclusive by the intrinsically large uncertainties in the TF relation. This study gives an idea of how far we are from a direct confirmation of the increased expansion rate in voids: a larger sample size is needed to reduce errors. It turns out that in the case of the Local Void, only about 50 galaxies are actually suitable for computing TF distances, so a more accurate distance indicator is also needed.

Detections of anomalies in the Hubble flow

We have discussed non-uniformities in the Hubble flow in §1.3 above. In brief summary, the supernova data is ambiguous about the existence of a Hubble bubble. Supernova data reduced with MLCS2k2 makes the assumption that reddening and extinction by dust in the supernova host galaxies is similar to that in the Milky Way, and a $\sim 6\%$ increase in the Hubble rate is found within $z = 0.024$. Supernova data reduced with the SALT fitter, however, include the extinction-reddening ratio R_V as one of the fit parameters, and find no Hubble bubble when host galaxies have $R_V = 1.7$. Supernova-independent direct measurements of dust in other galaxies suggest that their reddening laws do roughly conform to the Milky Way model. A Hubble bubble-type feature is expected in the timescape

model because of the volume dominance by voids below the scale of statistical homogeneity.

A Gpc-scale central void in an LTB model can explain the acceleration we attribute to dark energy, but such a large void is very unlikely, particularly since the consequent anisotropy in the kinetic SZ effect is not observed on such scales (Zibin and Moss, 2011).

Excess clustering on large scales has been measured in SDSS luminous red galaxies (LRGs) by Thomas et al. (2011) after hints of excessive power were observed in an earlier release of the same dataset (Blake et al., 2007). This effect turned out to be due to spurious correlations being made between improperly masked foreground M-stars and the LRGs (Ross et al., 2011) and is not observed in independent-volume measurements from the WiggleZ and 6dF galaxy surveys (Blake et al., 2011).

The theory of inflation predicts that the large-scale universe is homogeneous, and yet the galaxy distribution appears to be correlated up to very large scales. There is some controversy over whether we have yet observed the end of inhomogeneity. Hogg et al. (2005) use the SDSS LRG sample to determine number counts in completely-surveyed spheres between $0.16 < z < 0.47$ and find a slow transition to homogeneity between 70 and $100\,h^{-1}$ Mpc. Conversely, Sylos Labini et al. (2009) find a distribution that is still incompatible with homogeneity at up to $100\,h^{-1}$ Mpc in the SDSS Main Galaxy sample, claiming that erroneous assumptions of uniformity are built into the statistical methods that find the onset of homogeneity. This raises questions for the standard model because in the CMB-normalized theory of structure formation such large structures do not have time to form.

The kinematic interpretation of the redshift cz as a velocity, and of $cz - H_0 r$ as a peculiar velocity, depends on the validity of the approximation of spacetime by a Euclidean space, with small boosts, over the range in question. This leads to a paradox, since one would naturally expect large statistical scatter in peculiar velocities below the statistical homogeneity scale, but this is not observed. The paradox was first described by de Vaucoleurs (1970) and Sandage et al. (1972): Why is the local Hubble flow so quiet? Deeper galaxy surveys (see Figure 5.1) show us why. The Milky Way and the Local Group are located within a larger

concentration of galaxies notable for their small relative peculiar velocities—the Local Sheet. The Sandage-de Vaucoleurs paradox can be resolved if we accept that space on local scales is not flat.

If we dispense with the description of space as Euclidean, we no longer know how much of a measured radial velocity is due to peculiar motion and how much is due to cosmic expansion. In fact we do not know what the metric is, and we show in this chapter that actually we can make progress without one. We only require a notion of an average linear Hubble law, which will hold beyond the zero-velocity radius of the Local Group. There will be no single underlying average linear Hubble law, but it will instead vary locally with the size of the averaging domain until the scale of statistical homogeneity is reached. If H_0 becomes a function of the spatial coordinates, being greater here or lesser there due to the non-uniform density distribution, then the distance must have a corresponding intrinsic variation if we are to maintain the assumption of an underlying linear Hubble law. How much variation is there in the Hubble expansion within the scale of statistical homogeneity? Can we see the transition to statistical homogeneity in the decline of expansion variability with radial distance? To what extent is the void/wall density distribution apparent in the local variation of H_0? Is there a particular reference frame in which the variation is minimized? We begin to address all these questions in this chapter.

5.2 The data

We use a sample of 4536 galaxy and group redshifts, distances, and positions from the COMPOSITE peculiar velocity survey of Watkins et al. (2009). The samples that make up the COMPOSITE compilation are summarized in Table 5.1.

The distances come from both field galaxies and groups. Where galaxies have been identified as members of groups, the group peculiar velocity is given. This analysis was undertaken in the original surveys and their data is available in the references given in Table 5.1.

In this sample the velocities are given in the CMB reference frame and without corrections for our local velocity field. We henceforth exclude two nearby galaxies whose distances are less than $1\,h^{-1}$ Mpc since they are within the zero-velocity

Survey	*N*	*Depth*	*Type*	*Ref.*
SBF	88	17	SBF	Tonry et al. (2001)
ENEAR	697	29	FP	Bernardi et al. (2002); da Costa et al. (2000); Wegner et al. (2003)
EFAR	50	93	FP	Colless et al. (2001)
SFI++	3456	34	TF	Springob et al. (2007)
SMAC	56	65	FP	Hudson et al. (2004, 1999)
SC	70	57	TF	Dale et al. (1999); Giovanelli et al. (1998)
SN	103	32	SN	Tonry et al. (2003)
Willick	15	111	TF	Willick (1999)

Table 5.1: Subsurveys of the COMPOSITE sample (Watkins et al., 2009). N is the number of objects in the survey. The depth is the characteristic depth of the survey, defined as the mean distance weighted by the square of the peculiar velocity error. Type indicates the distance method: TF=Tully-Fisher, FP=Fundamental Plane, SBF=Surface Brightness Fluctuation, SN=Type Ia supernovae.

radius of the Local Group (Karachentsev et al., 2009), and we want to investigate local/cosmic expansion. Redshift-independent distances are given in units of h^{-1} Mpc, where h is defined via $H_0 = 100\,h$ km s^{-1} Mpc^{-1}. With $N = 4534$, the statistical uncertainties in this sample are greatly reduced compared to those for the $N = 54$ HST Key data, but the distances —obtained via Surface Brightness Fluctuations (SBF), Tully-Fisher (TF) and Fundamental Plane (FP) methods— are much less precise, with measurement errors as large as 20% in some cases.

5.3 Radial variation in the cosmic expansion rate

The scale dependence of cosmological backreaction was investigated in Li and Schwarz (2008) using a Buchert average over linear perturbations about a standard EdS model. Cosmological backreaction is a more general effect than just peculiar velocities and flows, being due to variations in the geometry and matter distribution (see § 2.2). However, flows certainly contribute to it. In the backreaction picture, the Buchert equations (2.2–2.4) explicitly relate the variance of the volume expansion rates to the volume average scale factor. Exactly how this

volume average scale factor relates to observable quantities is a complex question, and different researchers take different approaches.

Many studies have investigated the possibility that this relationship could result in cosmic acceleration, real or apparent (e.g. Behrend et al., 2008; Kolb et al., 2005; Li and Schwarz, 2007; Umeh et al., 2011; Wiltshire, 2007). In order to compare theory with observations, the assumption is generally made that the spatial hypersurface average coincides approximately with that on the past light cone, which restricts the analysis to small redshifts.

A common approach has been to average over first- and second-order perturbations of a background FLRW universe—assumed to be the average—to obtain corrections to the background that depend on the gauge. The success of the linear perturbation theory in describing the temperature anisotropies of the CMB and the matter power spectrum suggests that these corrections will be small, and this is indeed found to be the case, but many backreaction analyses neglect higher order terms in the perturbations, and these are potentially significant (Clarkson and Umeh, 2011).

In the timescape model the average is not assumed to be a FLRW model at all. Rather, the Buchert equations are solved directly for an ensemble of voids and walls. For realistic initial conditions the contribution of the backreaction term to the global expansion never exceeds 4.5% at any particular epoch. However, the integrated evolution is quite different to that of a single FLRW model. This lends support to the idea that linear perturbation theory cannot be relied upon to discuss inhomogeneities below the scale of statistical homogeneity at the present epoch.

In LS08, the Christoffel symbols of a perturbed FLRW metric are used to determine the ADM expansion scalar (derived from the covariant derivative of the velocity field of an observer comoving with pressureless dust— see Section 2.2). Calculation of the perturbations to second order yields a simple relation between the domain scale factor $a_{\mathcal{D}}$ from the Buchert average and the scale factor of the perturbed evolution equations, thus making an explicit connection between backreaction and the EdS background:

$$\frac{\dot{a}_{\mathcal{D}}}{a_{\mathcal{D}}} = \frac{\dot{a}}{a} - \langle\dot{\Psi}\rangle_{\mathcal{D}1} = \frac{2}{3t} - \frac{2\langle A\rangle_{\mathcal{D}1}}{3t^{1/3}}, \tag{5.2}$$

where Ψ is the usual comoving synchronous metric perturbation, A is its amplitude, $\langle\rangle_{\mathcal{D}1}$ represents an average over perturbations up to second order (prescriptions for calculating Ψ and $\langle\rangle_{\mathcal{D}1}$ are given in LS08), and t is the usual (i.e. single-valued) cosmic time. This has solution

$$\frac{a_{\mathcal{D}}(t)}{a_{\mathcal{D}}(t_0)} = \left(\frac{t}{t_0}\right)^{2/3} [1 - \langle A\rangle_{\mathcal{D}1}(t^{2/3} - t_0^{2/3})]. \tag{5.3}$$

The perturbative nature of the solution from the matter-dominated background is evident. If the averaged amplitude $\langle A\rangle_{\mathcal{D}1}$ is negative, the scale factor grows faster than EdS, consistent with the intuition that underdense regions expand faster than overdense ones. The relative fluctuation of the Hubble rate δH due to backreaction and cosmic variance was thus found to be inversely proportional to the square of the radial distance, declining from ∼15% at 30 Mpc (21.6 h^{-1} Mpc with their value of H_0), where the validity of the perturbative equation for the variance of the expansion breaks down, to about 2% at 100 Mpc. By this method, backreaction gives rise to effects that are observable in principle up to scales of ∼ 200 Mpc. As can be seen in Fig. 5.2, comparison with the HST Key project data of Freedman et al. (2001) is suggestive but rather inconclusive[1]: the Hubble fluctuation in the Key project data is not inconsistent with zero.

There are four issues with Fig. 5.2 that we aim to address here. Firstly, the insignificant deviation from zero is perhaps partly due to the contribution to the errors from the small sample size ($N = 54$). Secondly, the errors in each bin are correlated because new objects at greater radial distances are added in each successive bin—the averaging domains are concentric spheres. This correlation makes the interpretation problematic. Thirdly, the observed velocities in the HST Key data already incorporate a correction for the local flow field[2] based on three mass concentrations corresponding to the Local Supercluster, the Great Attractor, and the Shapley concentration. (Freedman et al., 2001). Finally, the HST Key velocities are given in the rest frame of the CMB—the "rest frame of the observable Universe". Because the frame in which we measure an isotropic

[1]The data was chosen for the precision of its determinations of H_0 for each datapoint.

[2]The theoretical treatment is linear, however, and the subtracted local flow field is assumed to be nonlinear (Schwarz, *pers. comm.*), hence the cutoff at $r = 30$ Mpc (21 h^{-1} Mpc).

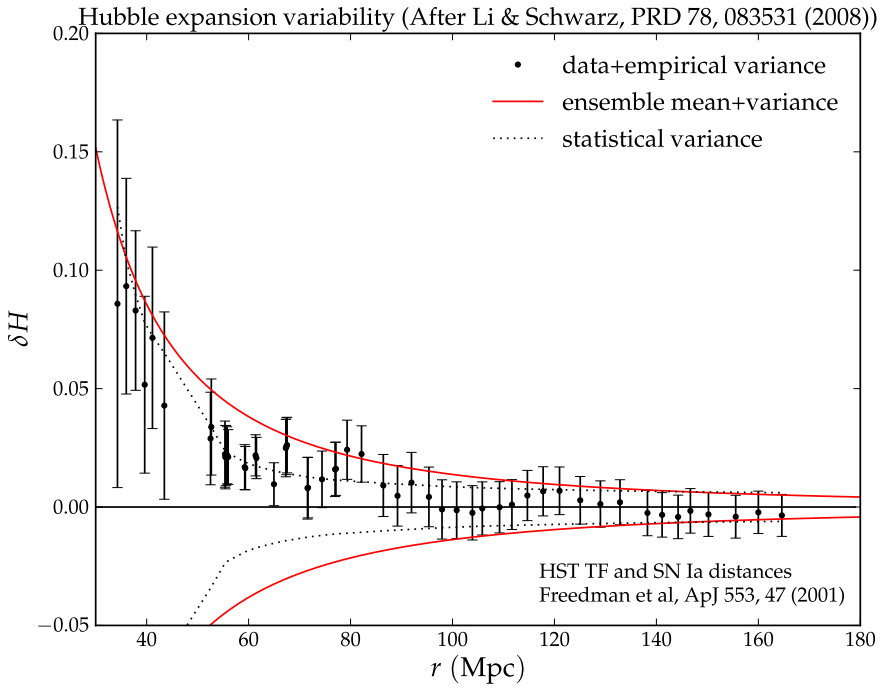

Figure 5.2: Local radial variation in the Hubble constant. The red lines come from a Buchert average over linear perturbations about an EdS background. The bins have been filled by adding datapoints from successively larger radial distances, so the points are not statistically independent. Note the magnitude of the statistical uncertainties. The plot comes from Li and Schwarz (2008).

CMB is not necessarily that in which nearby observers would measure an isotropic CMB, making this correction can introduce distortions to the redshifts of nearby objects. To test this, we will transform the velocities into the rest frame of the Local Group and Local Sheet, to see if the variation in local expansion rates is significantly altered.

In contrast to this cumulative binning method, we now consider separate concentric shells of thickness $12.5\,h^{-1}$ Mpc. This shell thickness is sufficient to include the largest bound structures. From the point of view of interpretation, this has the virtue that each shell is statistically independent. We compute a Hubble "constant" in successive independent radial shells $r_s < r \leq r_{s+1}$ by minimizing the sum $\sum_i [\sigma_i^{-1}(r_i - cz_i/H)]^2$ with respect to H, as a means of fitting a Hubble

law by linear regression. From setting the derivative of the χ^2 equal to zero, and from the standard method for propagating uncertainties in a function $f(x)$, i.e. $\sigma_f^2 = \sum_i^N \sigma_{x_i}^2 (\partial f/\partial x_i)^2$, the slope of the best-fit line to the data in shell s is given by

$$H_s = \left(\sum_{i=1}^{N_s} \frac{(cz_i)^2}{\sigma_i^2} \right) \left(\sum_{i=1}^{N_s} \frac{cz_i r_i}{\sigma_i^2} \right)^{-1}. \tag{5.4}$$

We then plot

$$\delta H_s = \frac{H_s - \bar{H}}{\bar{H}}, \tag{5.5}$$

where $\bar{H}$ is an asymptotic value of H that will be determined from the data. The fitted Hubble constant in the sth shell, H_s, has uncertainty

$$\sigma_s = \frac{1}{H_0} \left(\sum_{i=1}^{N_s} \frac{(cz_i)^2}{\sigma_i^2} \right)^{3/2} \left(\sum_{i=1}^{N_s} \frac{cz_i r_i}{\sigma_i^2} \right)^{-2}. \tag{5.6}$$

In these equations, σ_i is the measurement uncertainty in the distance r_i. It is related to the velocity uncertainties σ_V given in the COMPOSITE data by $\sigma_{r_i} = \sigma_V/H_0$. The uncertainty σ_s is combined in quadrature with a term representing the uncertainty in the origin chosen for the linear determination of the Hubble constant,

$$\sigma_{0,s} = H_s \frac{\sigma_0}{\bar{r}_s}. \tag{5.7}$$

Here $\bar{r}_s = \left(\sum_{i=1}^{N_s} \frac{r_i}{\sigma_i^2} \right) \left(\sum_{i=1}^{N_s} \frac{1}{\sigma_i^2} \right)^{-1}$ is the weighted mean distance in shell s and $\sigma_0 = 0.201\,h^{-1}$ Mpc is the distance uncertainty arising from the 20 km s^{-1} in the uncertainty in the sun's velocity in the LG frame given in T08, combined in quadrature with the 0.4% uncertainty in the magnitude of the CMB temperature dipole from Fixsen et al. (1996). Clearly, shells near the origin will be more affected by the zero-distance uncertainty than more distant shells. The mean of the distances in shell s is $\bar{r}_s$, where each distance is weighted by its inverse variance, and the factor of $\bar{H}^{-1}$ arises because we work with the fractional variation (5.5).

The asymptotic value of the Hubble constant must be determined. This is the value towards which measured values will approach within certain minimal

limits on scales beyond that of statistical homogeneity. We cannot simply fit a whole-sample line to the COMPOSITE data because nearly all the data come from within the scale of statistical homogeneity and will therefore be subject to variation due to the inhomogeneous foreground. Our binning of the COMPOSITE data extends to $156.25\,h^{-1}$ Mpc, beyond which the data becomes sparse. We take our asymptotic Hubble constant $\bar{H}$ from all the data beyond this distance, between 156.25 and $417.44\,h^{-1}$ Mpc. There are 91 distances in this shell, and we find that in the CMB frame,

$$\bar{H}_{\rm CMB} = 100.11 \pm 1.68\ h\ \text{km s}^{-1}\ \text{Mpc}^{-1}, \tag{5.8}$$

while in the Local Group frame,

$$\bar{H}_{\rm LG} = 101.02 \pm 1.70\ h\ \text{km s}^{-1}\ \text{Mpc}^{-1}. \tag{5.9}$$

These values are consistent with each other to within the uncertainties, and consistent with the overall normalization $H_0 = 100\,h$ km s^{-1} Mpc^{-1}. When we compute δH from (5.5) we then have an extra term that accounts for our uncertainty in the asymptotic global Hubble constant $\bar{H}$. The full uncertainty in δH_s then becomes

$$\bar{\sigma}_s^2 = \left(\frac{\sigma_s}{\bar{H}}\right)^2 + \left(\frac{\sigma_{\bar{H}} H_s}{\bar{H}^2}\right)^2. \tag{5.10}$$

We use an overbar to denote the fact that this uncertainty applies to the whole shell s.

One such fit example, from the fourth shell, is shown in Fig. 5.3. In this distance range (25.0–37.5 h^{-1} Mpc) there are 514 distances, and their sky coverage is shown in the inset. One can see from this plot that the uncertainty in the zero-distance value of the Hubble expansion will have more impact on nearby shells than more distant ones.

Finally, we are interested the variation of expansion locally. Velocities are generally quoted with respect to the CMB reference frame since this is assumed to correct for local flows in the same way that the motion of the sun around the galactic standard of rest is corrected for. Such a correction is therefore assumed to result in a more uniform Hubble flow. We compare results in this frame with the

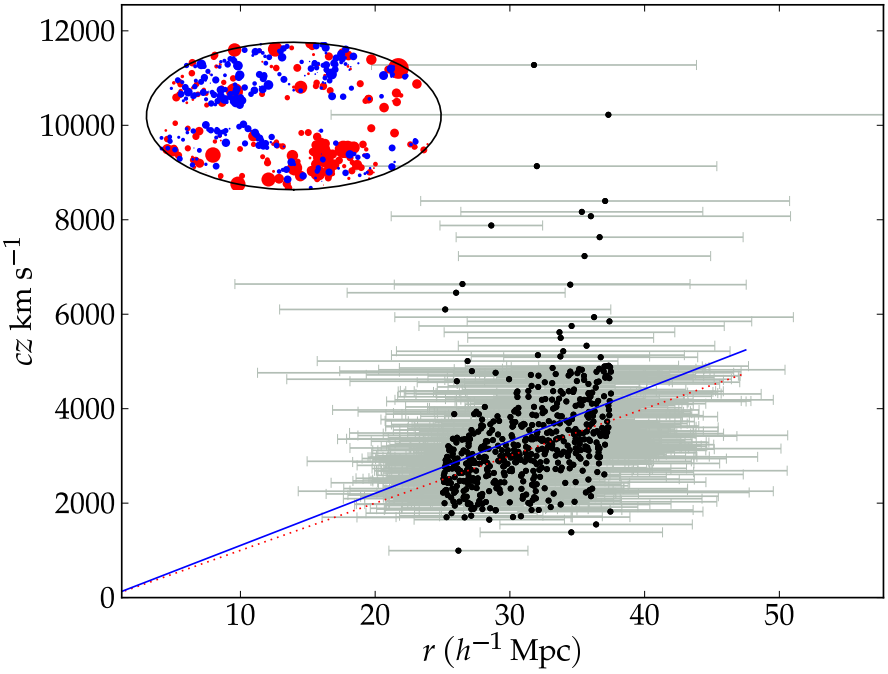

Figure 5.3: Hubble constant calculated from linear best fit, LG frame, in one example shell. The Hubble constant computed from a linear least squares best fit of velocity to distance for galaxies and groups in the shell between 25 and 37.5 h^{-1} Mpc is $106.48 \pm 1.04\,h$ km s^{-1} Mpc^{-1} (the blue line). The red dotted line is the asymptotic best-fit line to the data beyond $156.25\,h^{-1}$ Mpc: $\bar{H}_{\rm LG} = 101.02\,h$ km s^{-1} Mpc^{-1}. The intercept of the line is fixed to be exactly zero, but the observed uncertainty in our motion in the LG frame contributes to the uncertainty in the final δH_k for the shell. The angular distribution of the points is shown in the sky map, with red points having positive peculiar velocities, and blue points negative. The point size is proportional to the peculiar velocity magnitude.

Local Group and Local Sheet frames. Transformation of velocities from the CMB frame to either of the other frames requires two steps. First, we transform from the CMB frame to the heliocentric frame using the sun's velocity with respect to the CMB (371 km s^{-1} toward $(\ell, b) = (264.14°,\ 48.26°)$ (Fixsen et al., 1996). We use the Fixsen et al. direction rather than a more recent determination because the transformations from the heliocentric velocities to the CMB-frame velocities

in most of the COMPOSITE subsamples will have used the 1996 determination. Then we transform from the heliocentric frame to the LG or LS frame using the fit of T08 to a reference sample of 40 galaxies within 1.1 Mpc: 318.6 km s^{-1} toward $(\ell, b) = (106 \pm 4°, -6 \pm 4°)$. For the Local Sheet reference frame the subtracted velocity is 318.2 km s^{-1} toward $(\ell, b) = (95 \pm 4°, -1 \pm 4°)$ (Tully et al., 2008). We will show that correcting for the CMB dipole adds or subtracts a significant amount to the measured radial velocity of objects close to the LG, greatly increasing the variance in H_0 in smaller local volumes.

In fact, *any* boost will introduce a radial variation — a positive perturbation, in fact — in the measured value of the local Hubble constant, as we now show[1]. First, consider a situation of zero Hubble variance and then boost to a random frame, making an effective transformation $cz_i \rightarrow cz_i + c\Delta z_i$, where $\Delta z_i \ll 1$. Plugging this into the equation for the best fit slope (5.4), we obtain $H_s \rightarrow H_s + \Delta H$, where

$$\Delta H = \left(\sum_{i=1}^{N_s} \frac{(c\Delta z_i)^2}{\sigma_i^2} \right) \left(\sum_{i=1}^{N_s} \frac{cz_i r_i}{\sigma_i^2} \right)^{-1} . \tag{5.11}$$

Note that with this substitution the terms linear in Δz will average to zero in the limit of a perfectly sampled volume, since there will as many data points for which this quantity will be positive as there will be for which it is negative. Now, in each shell, we can write the observed redshifts roughly as $cz_i = H_s r_i + v_i$, where v_i is the peculiar velocity that produces scatter about the shell best fit line. To leading order, since $v_i \ll H_s r_i$, $cz_i \approx H_s r_i$, and the change in the boosted Hubble expansion becomes

$$\Delta H \approx \left(\sum_{i=1}^{N_s} \frac{(c\Delta z_i)^2}{\sigma_i^2} \right) \left(\sum_{i=1}^{N_s} \frac{H_s r_i^2}{\sigma_i^2} \right)^{-1} . \tag{5.12}$$

With the weighted average distance $\bar{r}_s$ defined as in § 5.3 above, this represents an effective monopole perturbation in each shell that decreases as $(\Delta z)^2/\bar{r}_s^2$. So, from the hypothetical zero-Hubble variance frame, any boost will produce a larger Hubble constant in radial shells locally, and the difference will be larger the greater the difference between the redshift in the zero-Hubble variance frame and that in the boosted frame.

[1] This argument is due to Rick Watkins.

5.3.1 Radial variability: Results

The variation of the Hubble expansion from the fiducial $\bar{H}$ is shown in Figures 5.4 and 5.5. The values of the best-fit Hubble constants in each shell and in each frame $(H_s)_{\rm CMB}$ and $(H_s)_{\rm LG}$ along with their uncertainties are given in Table 5.2. In order to better detect the variation the data has been analysed twice with the same shell thickness of $12.5\,h^{-1}$ Mpc: once starting at $0\,h^{-1}$ Mpc, shown by the filled circles, and again starting at $6.25\,h^{-1}$ Mpc, shown as empty circles. Hence the open and filled points are correlated with each other, but taken separately, they represent statistically independent shells. The error bars are greatly reduced compared to those in Fig. 5.2 because of the much larger sample size. The size of the error bars here increases at the larger scales because these shells contain fewer objects. For comparison, the predicted variation due to perturbative density fluctuations and cosmic variance in a Euclidean volume for seven different CDM models is calculated in Shi and Turner (1998) and shown in their Fig. 1 to be between 1.5 and 4% at 7500 km s^{-1} ($75\,h^{-1}$ Mpc), decreasing to about 0.2% at 10000 km s^{-1} ($100\,h^{-1}$ Mpc).

Note from the figures that the variation is always positive. It is perhaps a reasonable expectation that the variation should be negative as often as it is positive, but this expectation does not take into account the void statistics observed in 2dFGRS by Hoyle and Vogeley (2004) and in SDSS DR7 by Pan et al. (2011). We use spherically symmetric averaging domains, so even if the Hubble variance is negative in a particular direction, as it would be in the direction of the Virgo cluster, this anisotropy will be over-compensated for in an average over the whole spherical shell because voids dominate the volume of the Universe. Clearly, a given void expansion rate is larger than the volume average because of its underdensity. Moreover, the average void diameter is $\sim 30\,h^{-1}$ Mpc, less than a third of the scale of statistical homogeneity. Hence, the more sophisticated expectation is that on scales of 30–60 h^{-1} Mpc the volume will be "void-dominated", and the Hubble variance will be correspondingly positive. In small volumes within a wall, a negative Hubble variance is certainly possible, but we have seen that this is not the case for the Milky Way. Living as we do on the edge of a roughly "average" void, we might expect an increased Hubble variance at roughly the dominant

void scale. In Figs 5.4 and 5.5 there are bumps in the Hubble variance at exactly this scale. If we apply the Copernican principle to a Universe dominated by $30\,h^{-1}$ Mpc voids, with walls typically $\sim 15\,h^{-1}$ Mpc then a typical wall observer will find several $30\,h^{-1}$ Mpc voids within a range 30–$50\,h^{-1}$ Mpc. In a universe whose volume is dominated by voids, cosmic variance is no longer restricted to local scales, since a void is a single entity that fills a considerable fraction of the nearby volume. In both frames the variation converges to zero by $100\,h^{-1}$ Mpc, consistent with our rough estimates of the scale of statistical homogeneity and also with the observation by Hogg et al. (2005) that at this scale the number density of SDSS luminous red galaxies in comoving spherical volumes varies only within the limits imposed by cosmic variance predicted by the ΛCDM power spectrum that fits the CMB data.

The figures show clearly that there is more variation nearby in the CMB frame than in the LG frame. In the CMB frame, there is also an enhancement of redshift distortions nearby from the correction for the CMB dipole, but there is still more variation in this frame out to about more than $40\,h^{-1}$ Mpc. In both frames, the Hubble variance is less than 2σ from uniform in almost all shells beyond $50\,h^{-1}$ Mpc. There is one exception: in the CMB frame the variance in the shell $100 \lesssim r_s \lesssim 112.5\,h^{-1}$ Mpc is 2.1σ from zero. In the nearer shells, the LG frame data shows only weak variation, with $\delta H_{\rm LG}$ within 1.5σ of zero except in the first shell, which has only 92 data points. By contrast, $\delta H_{\rm CMB}$ for the corresponding CMB-frame bins is between 2.9 and 7σ. Clearly, the frame of minimal variance of the Hubble flow must be closer to the Local Group frame than the CMB frame.

The extent to which the LG frame is more uniform than the CMB frame can be quantified by a Bayes factor (Kass and Raftery, 1995), which quantifies the degree of preference we can reasonably have in one model with respect to another as a ratio of their probabilities. Here we calculate the probability that the variation will be more different from zero than that observed in each shell in each frame. This corresponds to the probability that the χ^2 in a given shell will be greater than the one observed. We calculate the χ^2 values for each shell, and then sum these over shells with a minimum radius that steps from the lower bound of the outermost shell down to the zero-velocity surface $r = 2\,h^{-1}$ Mpc,

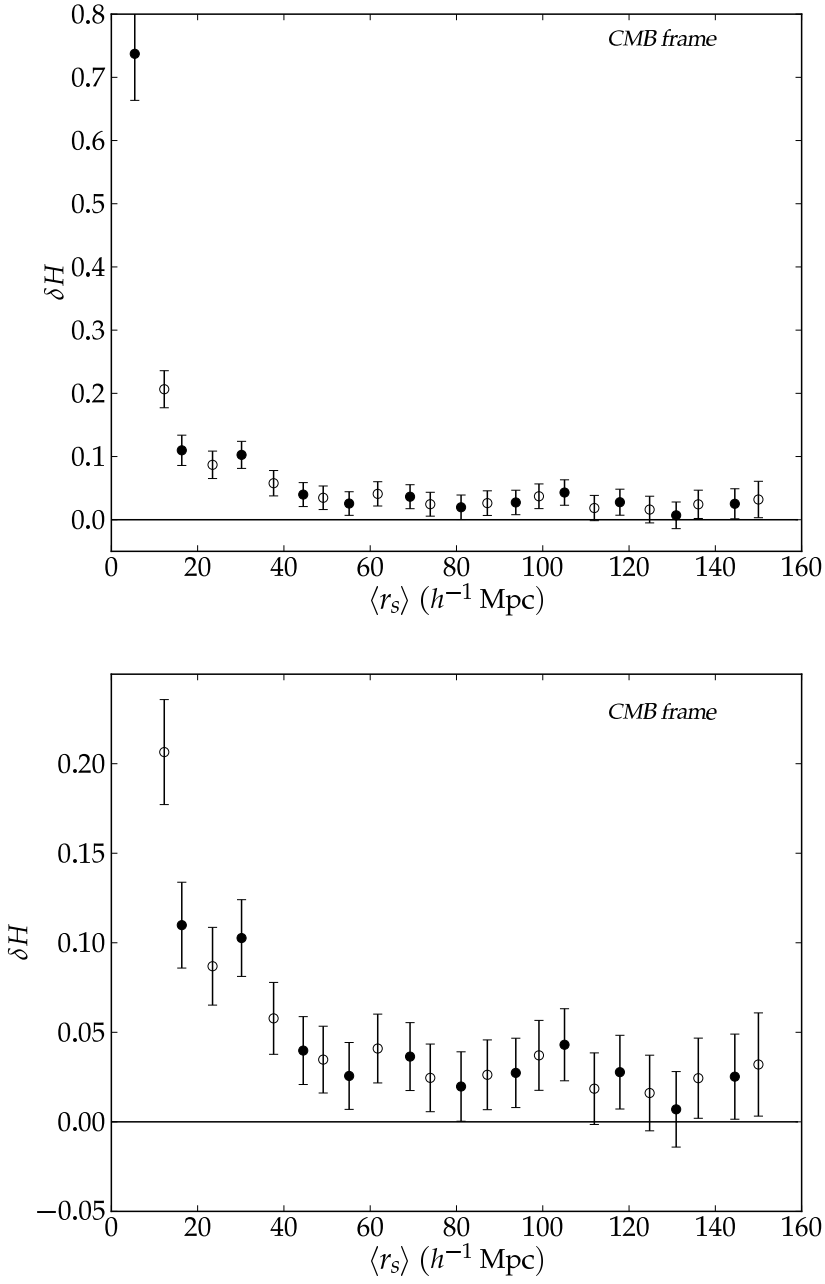

Figure 5.4: Local radial variation in the Hubble constant (CMB frame). The filled data points represent the first choice of shells in Table 5.2, and the open circles the alternative second choice of shells. The variation is around an asymptotic value of $\bar{H}_{\rm CMB} = 100.11 \pm 1.68\, h$ km s^{-1} Mpc^{-1}. We show the same data at two different scales. The upper plot shows the large variation in the first shell, while the lower plot shows in more detail the variation in the other shells.

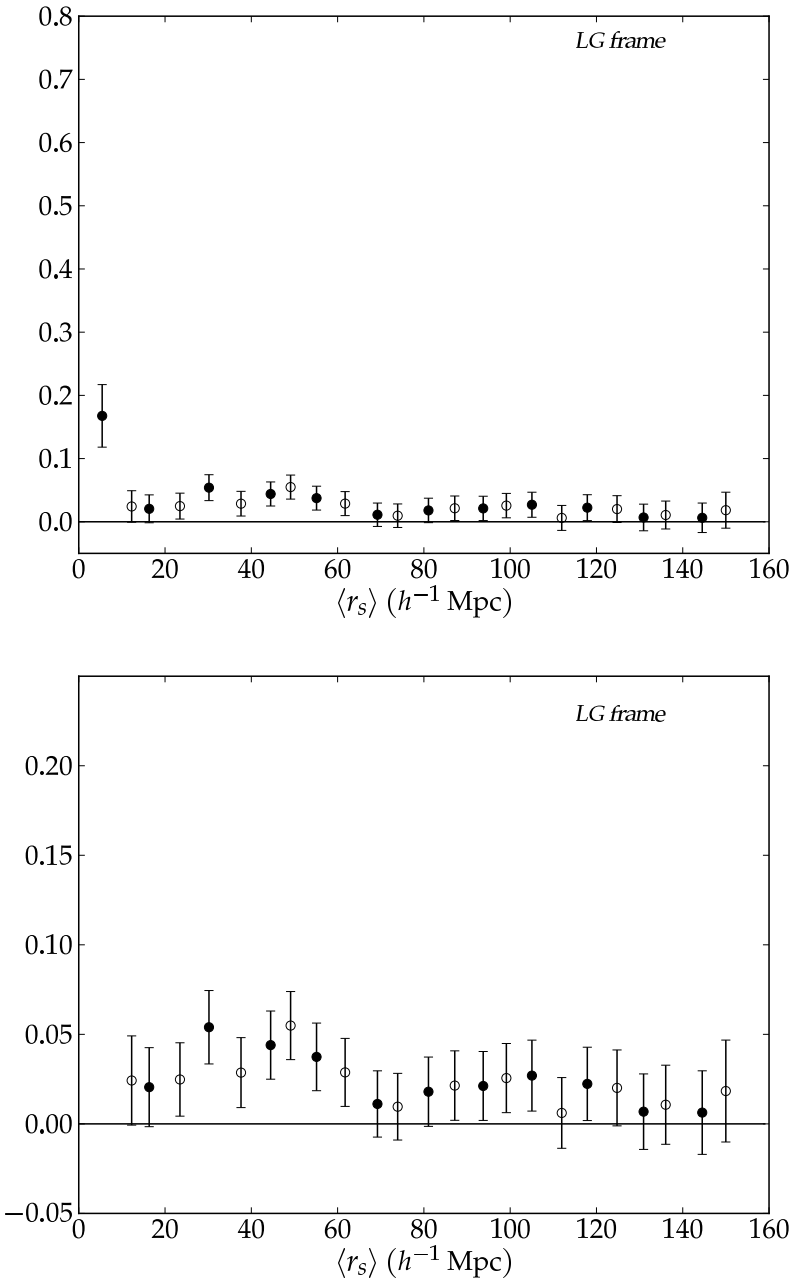

Figure 5.5: Local radial variation in the Hubble constant (Local Group frame). As for Fig. 5.4 but in the LG frame. Variation is with respect to an asymptotic value $\bar{H}_{\rm LG} = 101.02 \pm 1.70\ h$ km s^{-1} Mpc^{-1}. From the point of view of variation in the expansion rates, expansion in this frame is clearly more uniform than in the CMB frame, shown in Fig. 5.4 with the same Y-axis scales for comparison.

Table 5.2. Hubble flow variance in radial shells in CMB and LG frames, for two different choices of shells, the second choice labelled by primes, with a common final shell. In each case $r_s < r \leq r_{s+1}$. We tabulate the inner shell radius, r_s; the weighted mean distance, $\bar{r}_s$; the shell Hubble constants, $(H_s)_{\rm CMB}$ and $(H_s)_{\rm LG}$ in the CMB and LG frames, and their uncertainties; $\ln B$ where B is the Bayes factor for the relative probability that the LG frame has more uniform $\delta H_s = 0$ than the CMB frame when χ^2 is summed in all shells with $r > r_s$. H_s and $\bar{\sigma}_s$ are given in units h km s^{-1} Mpc^{-1}.

Shell s	1	2	3	4	5	6	7	8	9	10	11	12	13
N_s	92	505	514	731	819	562	414	304	222	127	95	58	91
r_s (h^{-1}Mpc)	2.00	12.50	25.00	37.50	50.00	62.50	75.00	87.50	100.00	112.50	125.00	137.50	156.25
$\bar{r}_s$ (h^{-1}Mpc)	5.43	16.33	30.18	44.48	55.12	69.24	81.06	93.75	105.04	117.88	130.92	144.52	182.59
$(H_s)_{\rm CMB}$	173.9	111.1	110.4	104.1	102.7	103.8	102.1	102.8	104.4	102.9	100.8	102.6	100.1
$(\bar{\sigma}_s)_{\rm CMB}$	6.8	1.5	1.1	0.7	0.7	0.8	0.9	0.9	1.0	1.1	1.3	1.6	1.7
$(H_s)_{\rm LG}$	117.9	103.1	106.5	105.5	104.8	102.1	102.8	103.2	103.7	103.3	101.7	101.7	101.0
$(\bar{\sigma}_s)_{\rm LG}$	4.6	1.4	1.0	0.7	0.7	0.7	0.9	0.9	1.0	1.1	1.3	1.6	1.7
$\ln B$ ($r \geq r_s$)	57.69	16.53	8.32	1.87	2.02	2.55	1.63	1.73	1.59	0.62	0.53	1.00	
Shell s	1'	2'	3'	4'	5'	6'	7'	8'	9'	10'	11'	12'	13
N_s	321	513	553	893	681	485	343	273	164	101	73	32	91
r_s (h^{-1}Mpc)	6.25	18.75	31.25	43.75	56.25	68.75	81.25	93.75	106.25	118.75	131.25	143.75	156.25
$\bar{r}_s$ (h^{-1}Mpc)	12.26	23.46	37.61	49.11	61.74	73.92	87.15	99.12	111.95	124.77	136.05	149.99	182.59
$(H_s)_{\rm CMB}$	120.8	108.8	105.9	103.6	104.2	102.6	102.7	103.8	102.0	101.7	102.5	103.3	100.1
$(\bar{\sigma}_s)_{\rm CMB}$	2.1	1.2	0.9	0.7	0.8	0.8	0.9	0.9	1.0	1.2	1.4	2.3	1.7
$(H_s)_{\rm LG}$	103.5	103.5	103.9	106.6	103.9	102.0	103.2	103.6	101.6	103.1	102.1	102.9	101.0
$(\bar{\sigma}_s)_{\rm LG}$	1.8	1.1	0.9	0.7	0.8	0.8	0.9	0.9	1.0	1.3	1.4	2.3	1.7
$\ln B$ ($r \geq r_s$)	29.22	8.72	3.26	1.13	2.34	1.58	1.33	1.22	0.63	0.54	0.89	0.67	

i.e. we include increasing numbers of more nearby objects in each step. The χ^2 in each subset of shells is therefore given by

$$\chi^2(r_s) = \sum_{j=s}^{12} \frac{\bar{H}_0^4 \delta H_j^2}{\bar{H}_0^2 \sigma_{H_j}^2 + H_j^2 \sigma_{\bar{H}_0}^2}, \tag{5.13}$$

where the s now runs over successively *smaller* radii. E.g. In the first bin are the δH values from the outermost two shells—$N = 2$; in the second are those from the outermost three shells ($N = 3$), and so on, until the sum runs over all shells. Given the χ^2 from (5.13), the probabilities are then given by the complement of the cumulative density function, which we calculate as the complementary incomplete gamma function $\Gamma(\nu, \chi^2/2)/\Gamma(\nu)$ (Press et al., 1986). Because this gives the probability that a χ^2 value will exceed that observed, and the LG δH_k are generally less than their CMB-frame counterparts, we expect Bayesian evidence to favour the LG frame in general, and also to give us an indication of the confidence we can have in this preference. Table 5.2 lists the resulting Bayes factors and they are plotted in Figure 5.6.

The points in the figure are consistent with expectations from the previous two figures. The overall relative uniformity of the LG frame compared to the CMB frame is reflected in the fact that the Bayes factor is everywhere positive. There is little to distinguish the different frames in the data beyond larger distances where the Bayes factor indicates differences between the frames are not worth more than a bare mention, but as more data from closer in is included the greater variability in the CMB frame starts to count against it. The evidence for a more uniform LG frame only gets stronger so that when the innermost bins are included, the Bayesian evidence for greater uniformity in the LG frame is very strong, or decisive, in Jeffreys' terminology (Kass and Raftery, 1995).

There is a slight dip in the Bayes factors between 35 and $60\,h^{-1}$ Mpc. Table 5.2 shows that the Hubble constants in the CMB frame between distances of 37.5 and 68.75 h^{-1} Mpc are closer to uniform than their counterparts in the LG frame. As a result, the Bayes factors tend to favour the CMB frame a little more. We interpret this as evidence for the effects of a significant foreground inhomogeneity. This is roughly the distance to the far edge of the Local Void.

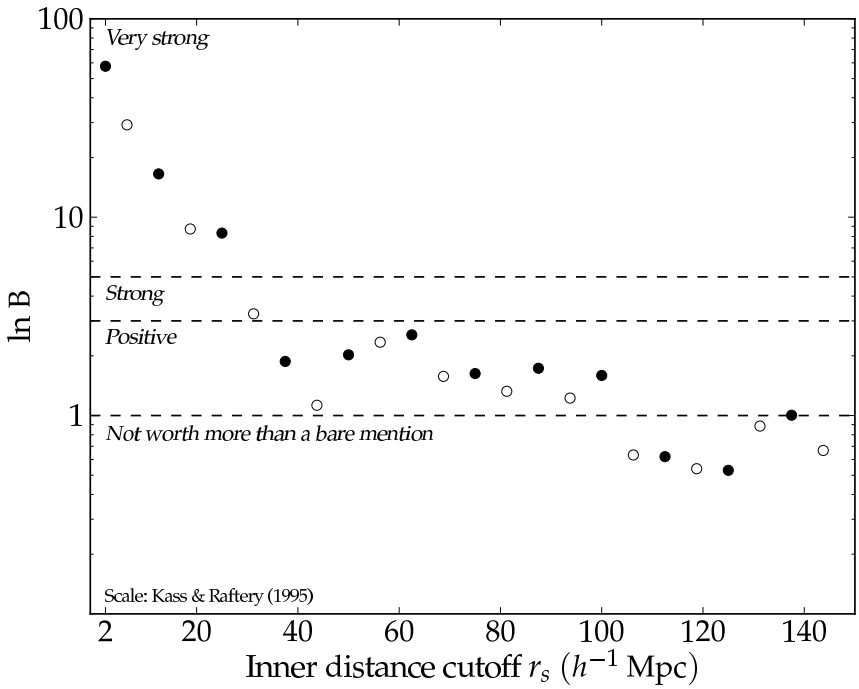

Figure 5.6: Bayes factors for concentric shells with decreasing inner radii. This figure depicts the degree of confidence we can have in our conclusion from Figs. 5.5 and 5.4 that the LG frame is more consistent with a uniform nearby Hubble flow than the CMB frame. The filled and open markers have the same meaning as they did in the previous figures. The scale indicating the strength is from the convention due to Jeffreys.

We summarize the results from this section as follows. Although there are significant foreground structures which distort the spherically averaged Hubble flow in a statistically significant manner, the LG frame has a much smaller Hubble flow variance than the CMB frame. Nevertheless, there is a particular range of distances, roughly $35 \lesssim r \lesssim 60\,h^{-1}$ Mpc, in which the boost to the CMB frame produces an apparently more uniform flow. This is the first evidence for the hypothesis that we will present in Section 5.5, namely that rather than being a transformation which puts us in the frame in which the Hubble flow is most uniform at our own point, the boost to the CMB frame is actually compensating for the effects of foreground structures largely associated with distance scales

of order 35 h^{-1} to 65 h^{-1} Mpc. To better understand these structures we now consider angular averages.

5.4 Angular variation in the cosmic expansion rate

Given the inhomogeneous distribution of galaxies in the nearby Universe it is natural to expect significant angular variation in the Hubble expansion. We now investigate this angular variation by averaging the Hubble ratios cz_i/r_i of COMPOSITE objects over the sky using the same bins as in the previous section.

Galaxy and type Ia supernova distances from the HST Key project data were used to map variations in the cosmic expansion by McClure and Dyer (2007) (hereafter MD07). In this study, the ratio $H_0 = cz/r$ was measured at different locations on the sky to assess angular variation. Large bulk flows in the peculiar velocity framework should be manifest as an angular variation of H_0 from the Hubble variance viewpoint. The HST Key project data had the most precise distance estimates available, but with only 76 data points the sky coverage is rather sparse, and only variations with large spatial extents could be studied. The aim was to detect variation over and above that expected from measurement errors in the data, and a statistically significant variation of 9 km s^{-1} Mpc^{-1} ($6.4\,h^{-1}$ Mpc), or 12.5%, was found across the whole sky.

MD07 used the values of cz/r from the Key project to produce contour maps of the sky using a Gaussian smearing technique. At each grid point on the sky, a mean H_0 is calculated in which each data point is weighted according to its angular separation from the grid point. The Gaussian profile was generally given a standard deviation of 25° in MD07, since with a narrower width the variation became dominated by the measurement errors, and angular resolution was compromised with a greater width.

At a given grid point, labelled α, with galactic coordinates (ℓ, b), the weighting of the ith datapoint is given by

$$W_{\alpha,i} = \frac{1}{\sqrt{2\pi}\sigma} \exp\left(\frac{-\theta_{\alpha,i}^2}{2\sigma^2}\right), \tag{5.14}$$

where $\sigma = 25°$ is the smoothing scale and $\cos\theta_{\alpha,i} = \vec{r}_{\rm grid} \cdot \vec{r}_i$. With the weights $W_{\alpha,i}$, a weighted mean Hubble constant at each grid point is calculated by

$$H_\alpha = \frac{\sum_i^N W_{\alpha,i} c z_i r_i^{-1}}{\sum_j^N W_{\alpha,j}}. \tag{5.15}$$

The variance of this sample mean at each grid point is

$$\bar{\sigma}_\alpha^2 = \frac{\sum_i^N W_{\alpha,i}^2 \sigma_{H_\alpha}^2}{(\sum_j^N W_{\alpha,j})^2}, \tag{5.16}$$

where, as in the previous section, the overbar indicates the uncertainty due to the averaging of the whole sample, and

$$\sigma_{H_i} = c z_i r_i^{-2} \sigma_i \tag{5.17}$$

from the standard formulae for the propagation of errors. Finally, we define

$$\Delta H = H_{\rm max} - H_{\rm min}, \tag{5.18}$$

to be the difference between the maximum and the minimum in a given map.

A weighted mean is conventionally computed using weights derived from the uncertainties in each measurement of the quantity in question. No such uncertainty weighting was used in MD07, since the impact of the errors in the individual data points is averaged out by the Gaussian smearing. However, the H_0 uncertainties in the HST Key data are small—about 5% at most, compared with the distance measurement uncertainties in the COMPOSITE data. For this reason it is desirable to incorporate some sort of contribution to the weight (5.14) from the measurement uncertainties, because as it stands, the weighting scheme only accounts for the angular separation of grid point and datum, and assumes the distance is known with complete confidence. A maximum likelihood-like inverse variance (IV) weight will be discussed in what follows. The weight combining the angular separation and the distance uncertainties is then

$$W'_{\alpha,i} = W_{\alpha,i}/\sigma_{H_i}^2. \tag{5.19}$$

The maximum likelihood approach to uncertainties can bias the results. Because the IV weights are determined by the distance uncertainty, which increases

with distance, the maximum likelihood approach can be dominated by the nearby objects, which have smaller distance uncertainties. The effects of this on the COMPOSITE sample have been examined in detail by Feldman et al. (2010); Watkins et al. (2009), and Fig. 5.7 from the paper by the latter authors illustrates the point. The size of the points on the Aitoff projections is proportional to the object weights, for a maximum likelihood (ML) treatment (in Fig. 5.7(a)) and from an alternative treatment, dubbed "minimum variance" (MV) weighting (in Fig. 5.7(b)), designed to address the shortcomings of the ML scheme by minimizing the variance of the sample with respect to an ideal perfectly sampled 3D Gaussian survey volume. In particular, there is a preponderance of strongly weighted points along the $\ell = 300°$ meridian (along the supergalactic plane) in the ML weighted data, while points in the region $(\ell, b) = (30\text{–}60°, -45\text{–}60°)$ (roughly in the region of the Local Voids) are very uncertain. The MV method results shown in the right hand panel show reduced weights for the galaxies along the supergalactic plane, and enhanced weights for galaxies in the void regions and along the margins of the zone of avoidance.

The MV weights calculated here were designed for a peculiar velocity analysis in supergalactic Cartesian coordinates. This calculation will need to be recast in terms of the Hubble expansion for a complete and robust characterization of the angular variation in the Hubble expansion, but this is left for future work. In the meantime, we investigate the variation both with and without inverse variance distance weighting. We find that the difference between the two approaches turns out to be sufficiently small not to affect our general conclusions.

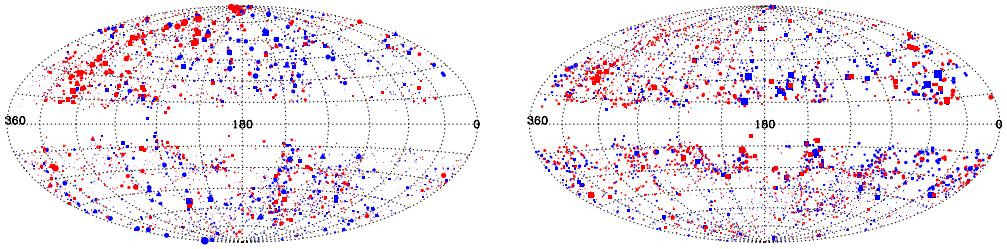

(a) Maximum likelihood weights (b) Minimum variance weighting

Figure 5.7: The effects of different weighting schemes. Source: Feldman et al. (2010)

A direct calculation of the mean H_α at each gridpoint including a contribution to the weights from the uncertainties σ_{H_i} yields a full-sample average weighted mean (including uncertainty weights) of e.g. $\bar{H}_\alpha = 93.5\ h$ km s^{-1} Mpc^{-1}, to be compared with the average calculated *without* uncertainty weights of $\bar{H}_\alpha = 103.2\ h$ km s^{-1} Mpc^{-1}. This is much lower than the normalization we have been using, $H_0 = 100$ km s^{-1} Mpc^{-1}, because the method of determining the propagation of uncertainties dictates that if the Hubble constant is calculated at each grid point via cz_i/r_i, the associated uncertainty is $\sigma_{H_i} \propto r_i^{-2}$, as in equation (5.17). Because the distance uncertainties are relatively large, and increase with distance, the weighted mean Hubble ratio at each gridpoint is skewed towards a lower value. We overcome this bias by working with the weighted *inverse* Hubble ratios at each grid point:

$$H_\alpha^{-1} = \frac{\sum_i^N W_{\alpha,i} r_i c z_i^{-1}}{\sum_j^N W_{\alpha,j}}, \tag{5.20}$$

(c.f. Eq. (5.15)). Now the uncertainties in the Hubble ratio for each data point are

$$\sigma_{H_i^{-1}} = \frac{\sigma_i}{cz_i}, \tag{5.21}$$

so that now the average weighted mean including uncertainty weights is $\bar{H}_\alpha = 103.9\ h$ km s^{-1} Mpc^{-1}. With the uncertainty (5.21), the uncertainty in the weighted mean Hubble ratio at each grid point is

$$\bar{\sigma}^2_{H_\alpha^{-1}} = \frac{\sum_i^N W_{\alpha,i}^2 \sigma^2_{H_i^{-1}}}{(\sum_j^N W_{\alpha,j})^2} \tag{5.22}$$

so that

$$\bar{\sigma}_\alpha = \bar{\sigma}_{H_\alpha^{-1}} H_\alpha^2. \tag{5.23}$$

Working with the inverse Hubble ratios, the average weighted mean of the gridpoint Hubble constants is $\bar{H}_\alpha = 98.2\ h$ km s^{-1} Mpc^{-1}. Since this method of calculating the weighted mean results in a smaller deviation of the Hubble constant values at each grid point from the survey normalization of $H_0 = 100\ h$km s^{-1} Mpc^{-1}, we compute the values of the Hubble ratio at each grid point by this method. This is actually also consistent with the analysis in the previous section

in the case of the radial shells, where we chose to minimize $\sum_i (r_i - cz_i/H)$ with respect to H for the same reason.

Given the various issues of bias associated with the IV weightings, we first simply use the unweighted data points, as MD07 did, to explore gross angular features of the Hubble variance, and defer discussion of the uncertainties until Section 5.4.3.

5.4.1 Hubble anisotropy: Results

In this section we first obtain a qualitative understanding of the angular variance of the Hubble flow using a smearing width of $\sigma = 25°$, following MD07. The first figure from MD07 is reproduced here in Fig. 5.8(a). Here we use galactic coordinates on a Mollweide projection, since we will be comparing maps of the Hubble anisotropy with the CMB dipole map which is most often depicted on a Mollweide projection. In all maps shown here, $(\ell, b) = (0°, 0°)$ (the galactic centre) lies at the right hand edge of the plot. For easier comparison with the COMPOSITE data, we have converted the values of the H_α to units of $h$km s^{-1} Mpc^{-1} using $H_0 = 72$ km s^{-1} Mpc^{-1} from Freedman et al. (2001). This figure is computed from CMB-frame velocities. The 76 galaxy and type Ia supernova distances are shown as black dots.

We used the COMPOSITE data to calculate the weighted mean H_0 at each grid point with the weight function equation (5.14). Initially, we also do not incorporate measurement uncertainties.

Figure 5.8: (page 175) **Angular Hubble variance.** Mollweide projection in galactic coordinates of Hubble expansion calculated from HST Key (above) and COMPOSITE (below) data. For reference, the galaxies of the HST key data are plotted on Fig. 5.8(a) as black dots, and some bulk flow directions and approximate positions of prominent structures are shown on Fig. 5.8(b): GA=Great Attractor; SC=Shapley Concentration; BF50=Direction of bulk flow with characteristic depth $50\,h^{-1}$ Mpc (Watkins et al., 2009); VC=Virgo cluster; Pers=Perseus cluster; Fo=Fornax cluster; the CMB dipole direction is shown as a blue cross.

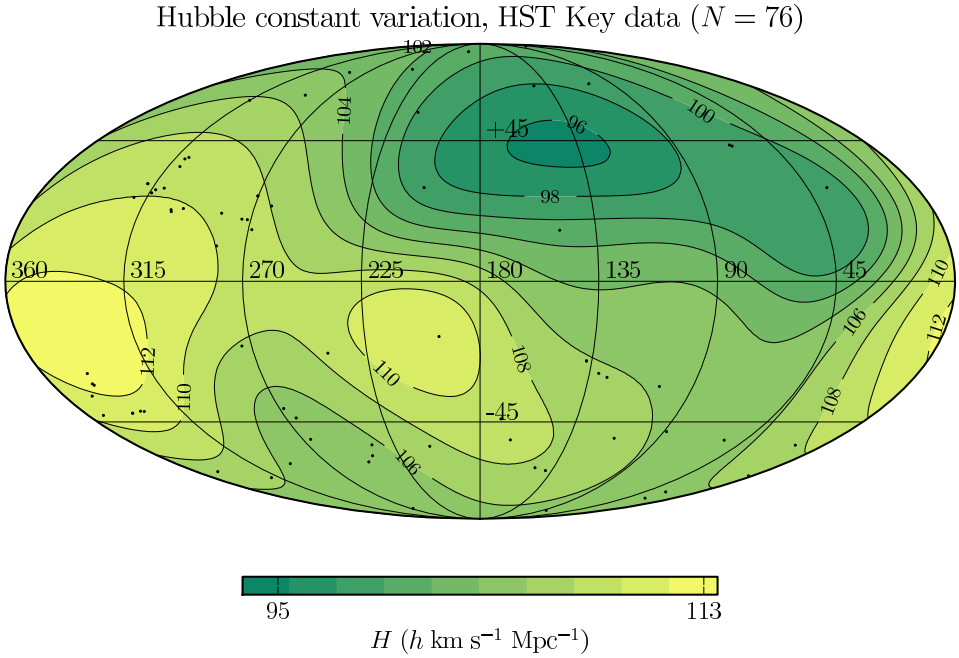

(a) Anisotropy of the Hubble ratio, HST Key data.

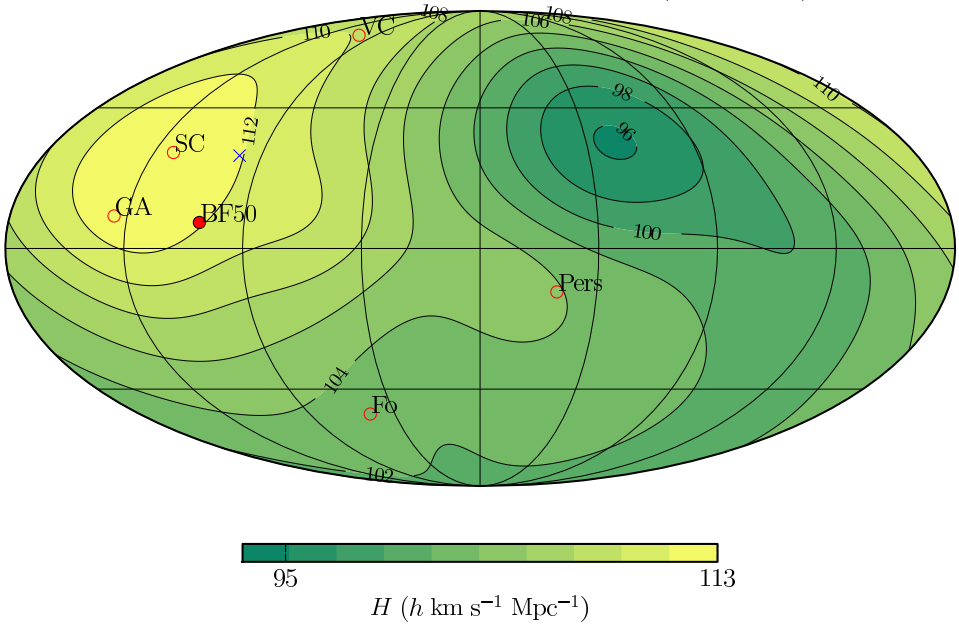

(b) Anisotropy of the Hubble ratio, COMPOSITE data.

The equivalent of Fig. 5.8(a) for the COMPOSITE data is shown in Fig. 5.8(b). The 4534 data points enhance the robustness of the basic rough dipolar pattern revealed in Fig. 5.8(a). The weighted mean and standard deviation of the Hubble ratios (5.15) is $H_\alpha = (104.3 \pm 3.7)\, h^{-1}$ Mpc. The difference between the maximum and the minimum for the COMPOSITE sample is about 18%. While the minimum at $(\ell, b) = (150°, +35°)$ has hardly shifted, the maximum has moved to a higher galactic latitude. Centred at roughly $(300°, +15°)$, this now coincides within $\sim 30°$ with the directions of the CMB dipole and the bulk flow from WFH09, which are marked on the map by the crosses at "CMBd" and "BF50", respectively. In the CMB rest frame, we observe space in the upper left quadrant to be expanding faster than it is in the galactic "eastern" half of the sky. The secondary maximum extending towards the Perseus cluster at $(150°, -15°)$ near the centre of the projection is less significant than it appeared in the HST map, but an imprint of its form remains.

We now use the inverse transformation method (5.20) to compute the H_α. In Figure 5.9(a) we show the resulting sky map for the full CMB-frame sample for comparison to the previous figure, to show the effects of the different computation. The gross features of the anisotropy are unchanged. The mean Hubble value $\langle H_\alpha \rangle$ has fallen to $(98.8 \pm 3.8)\, h^{-1}$ Mpc. The variation has increased slightly: the maximum is now +9.8% greater than the mean and the minimum is −10.6% below it. Interestingly, the remnant of the secondary maximum in the figure from MD07 visible in Fig 5.8(b) extending towards Perseus has all but disappeared. We will see below that the reciprocal transform method reduces noise due to some very nearby points with anomalously large velocities whose presence affects even the whole-sample results.

In Fig. 5.9(b) we show the Hubble variation in the rest frame of the Local Group. The dipole pattern is much "cleaner" in this frame, in the sense that the extrema are closer to 180° apart. The weighted mean and standard deviation of the Hubble ratios is $\langle H_\alpha \rangle = (97.7 \pm 5.8)\, h^{-1}$ Mpc. The maximum is 10.2% larger, and the minimum is 9.1% less. We quote these values for comparison; the aim in this section will be not to determine the variability of the Hubble ratio relative to some absolute global value, so much as to characterize statistically the general features of the relative angular variance.

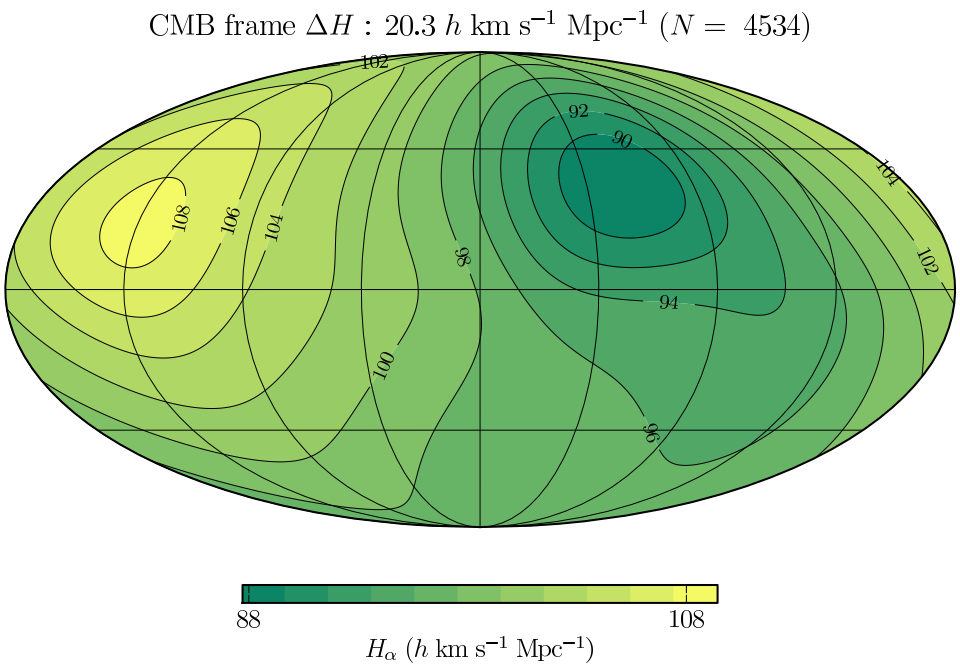

(a) Hubble variance, CMB frame

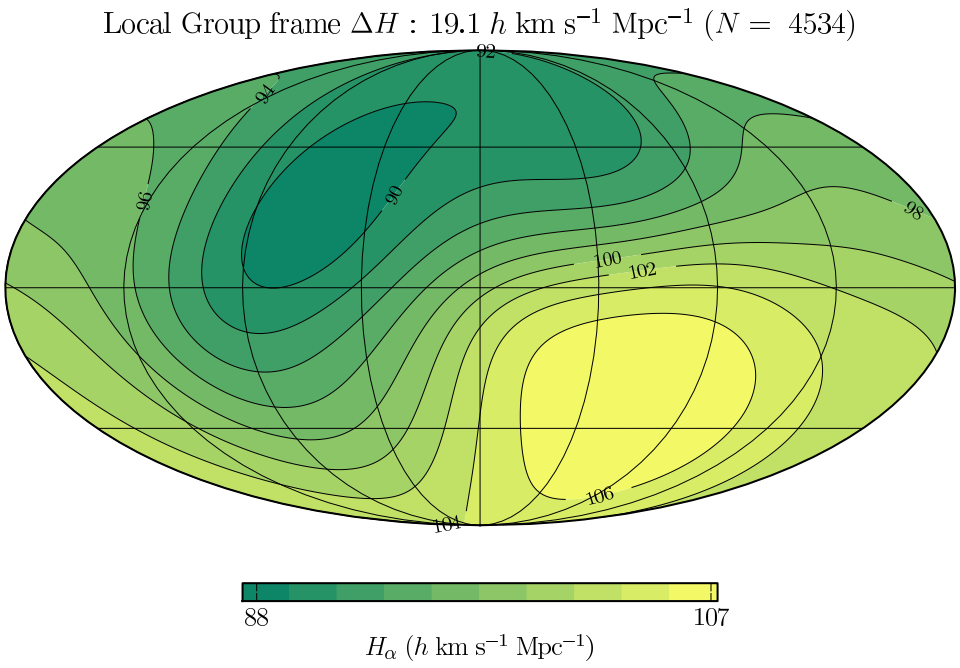

(b) Hubble variance, LG frame

Figure 5.9: (page 176) **Angular Hubble variance** as for previous figure but calculated using the inverse transformation equation (5.20). CMB frame (above) and Local Group frame (below).

5.4.2 Radial changes in the angular Hubble expansion variation

We have seen from the analysis of the radial variance of the Hubble expansion that the Hubble expansion is more uniform in the Local Group rest frame than in that of the CMB, the so-called "cosmic rest frame". Can we see this in a sky map of the angular variation of the Hubble constant?

In Figs. 5.10, 5.11 and 5.12 we plot contour maps of the angular variation in the Hubble flow in the CMB, LS, and LG frames, with the data divided into two spheres, with the boundary between the two spheres varying in steps. In each case, in the left column, we show the Hubble anisotropy within an inner sphere, with $r \leq r_0$, and in the right column, the corresponding map for the data in the outer sphere $r > r_0$, with r_0 taking the values 15 h^{-1}, 30 h^{-1}, 45 h^{-1}, and 60 h^{-1} Mpc. The coordinate system in each subfigure is the same as that in Fig. 5.8(a). The LG comprises galaxies within 1 Mpc of the Milky Way, while the LS rest frame is that in which the average motion of galaxies between 1 and 7 Mpc away is zero. Since there is very little relative motion between the LG and the LS, the two reference frames yield results that are very similar— the maps for the LS frame are substantially the same as those for the LG frame, but we include them here for completeness. In Figs. 5.13, 5.14 and 5.15, we plot the same subvolumes but this time using the inverse Hubble averaging method from equation (5.20).

The inner spheres of the CMB-frame maps in the left column of Fig. 5.10 are dominated by shot noise until the volume within $60\,h^{-1}$ Mpc. Even at this point, an imprint of the variation from the innermost inner volume remains. The outer volumes, in the right column, are initially similar to the full-sample map in Fig. 5.8(b), as expected, with both poles of the "dipole" lying in the northern galactic hemisphere. These poles migrate southward as the inner boundary of the outer

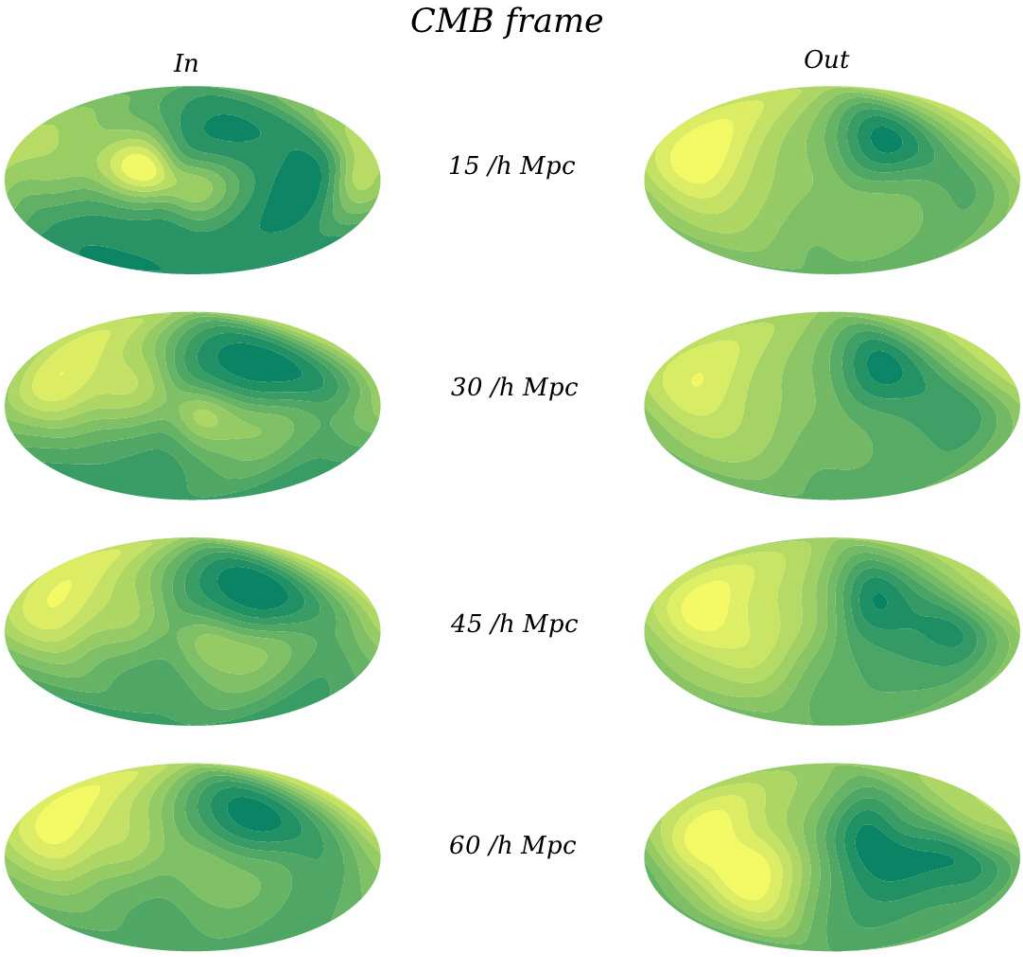

Figure 5.10: Hubble anisotropy restricted to spherical domains, CMB frame. These are mollweide projections of galactic coordinates with $\ell = 0^\circ$ at the right edge and $\ell = 360^\circ$ at the left edge. The H_α were calculated using equation (5.15).

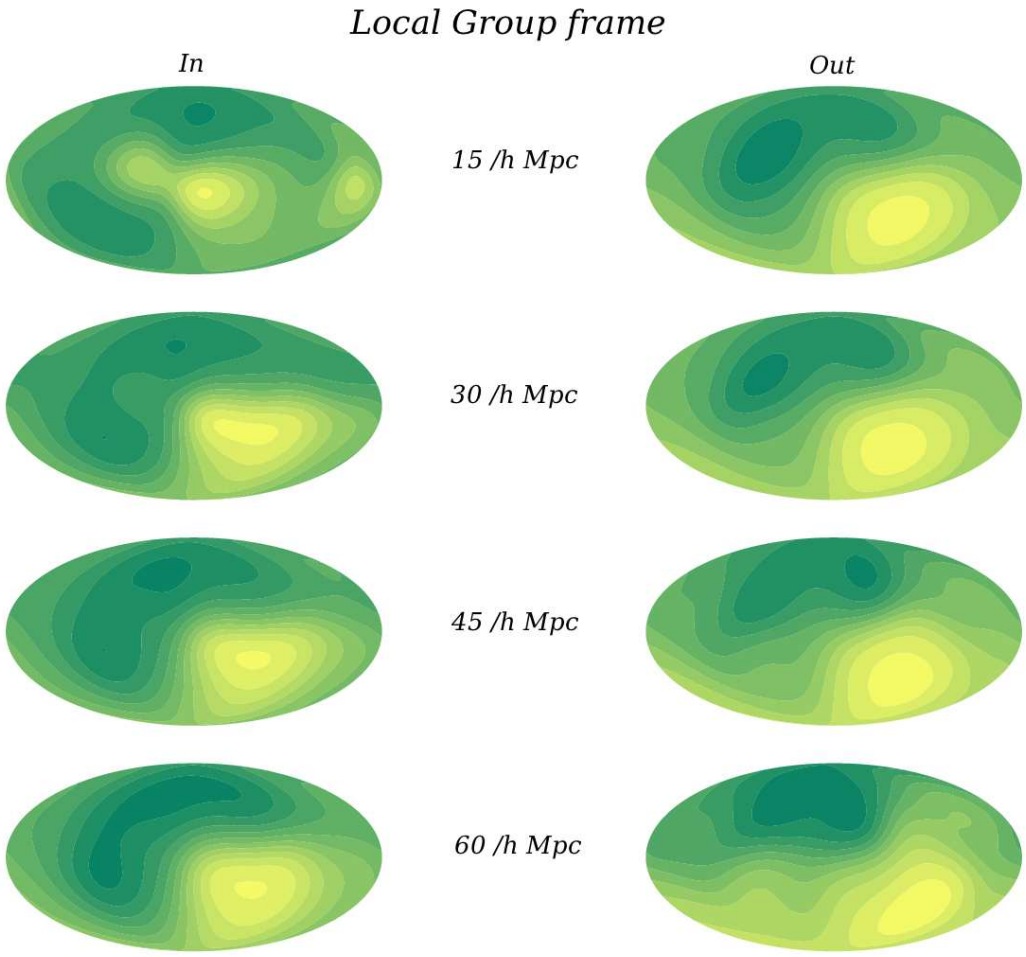

Figure 5.11: Hubble anisotropy restricted to spherical domains, LG frame. These are mollweide projections of galactic coordinates with $\ell = 0°$ at the right edge and $\ell = 360°$ at the left edge. The H_α were calculated using equation (5.15).

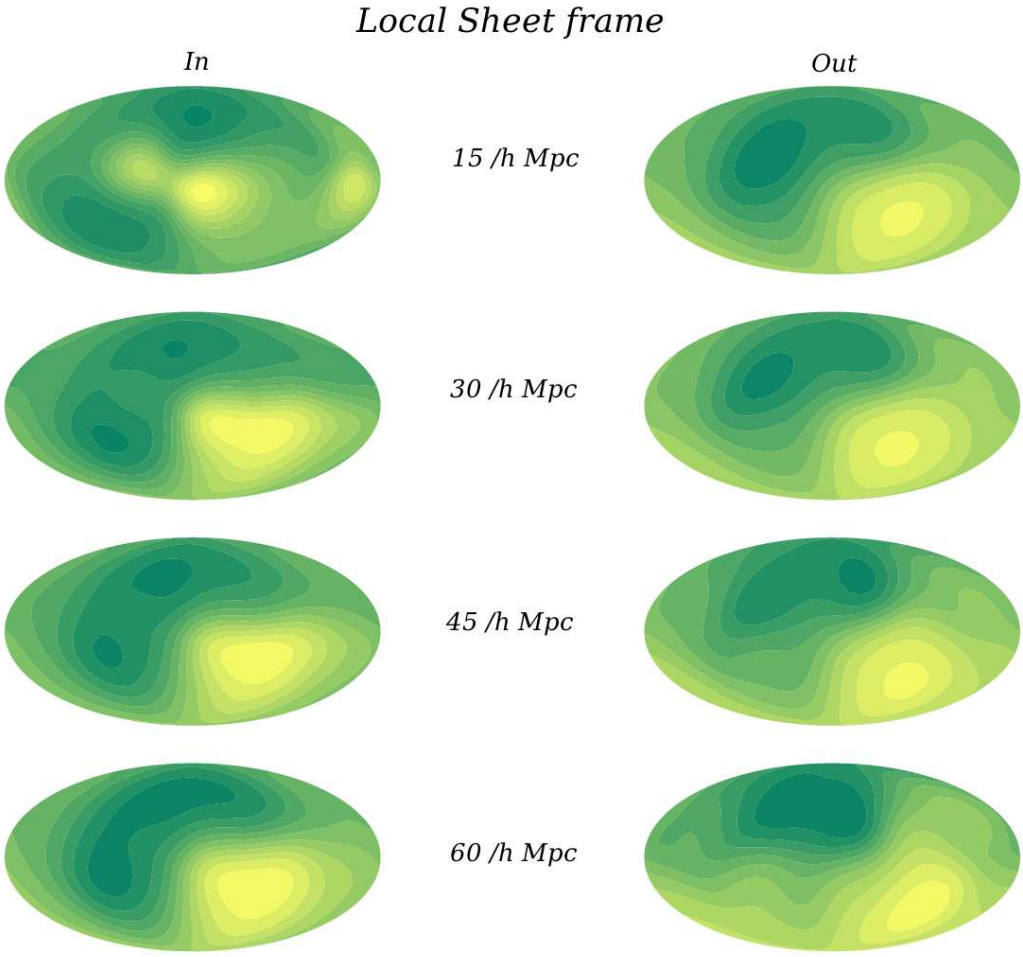

Figure 5.12: Hubble anisotropy restricted to spherical domains, LS frame. These are mollweide projections of galactic coordinates with $\ell = 0^\circ$ at the right edge and $\ell = 360^\circ$ at the left edge. The H_α were calculated using equation (5.15).

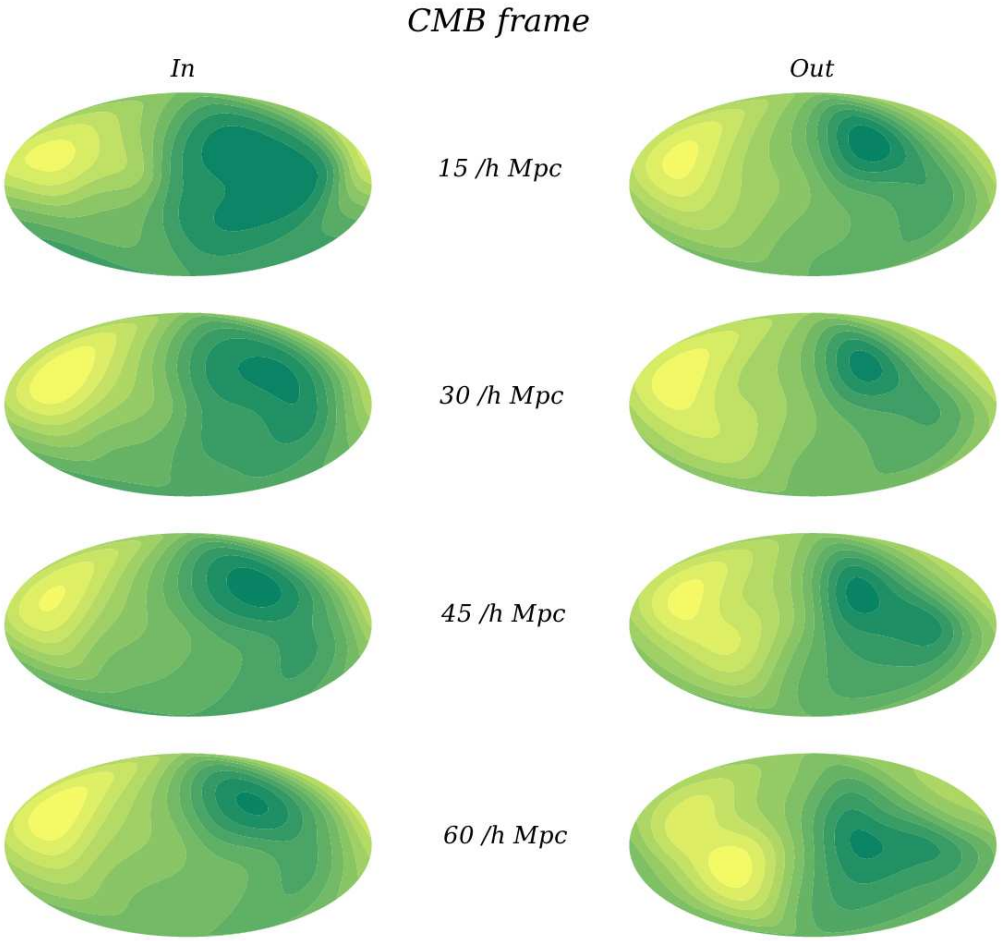

Figure 5.13: Hubble anisotropy restricted to spherical domains, CMB frame. These are mollweide projections of galactic coordinates with $\ell = 0°$ at the right edge and $\ell = 360°$ at the left edge. The H_α were calculated using the reciprocal transform method.

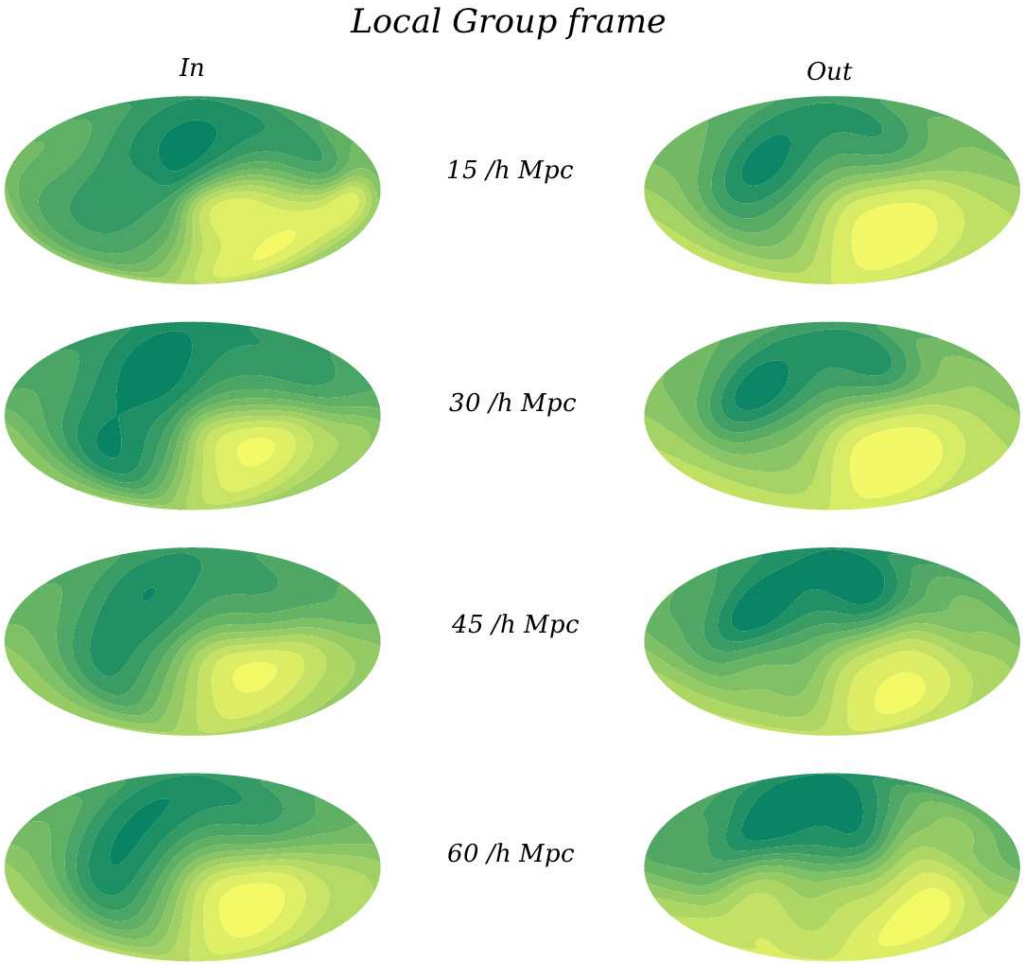

Figure 5.14: Hubble anisotropy restricted to spherical domains, LG frame. These are mollweide projections of galactic coordinates with $\ell = 0°$ at the right edge and $\ell = 360°$ at the left edge. The H_α were calculated using the reciprocal transform method.

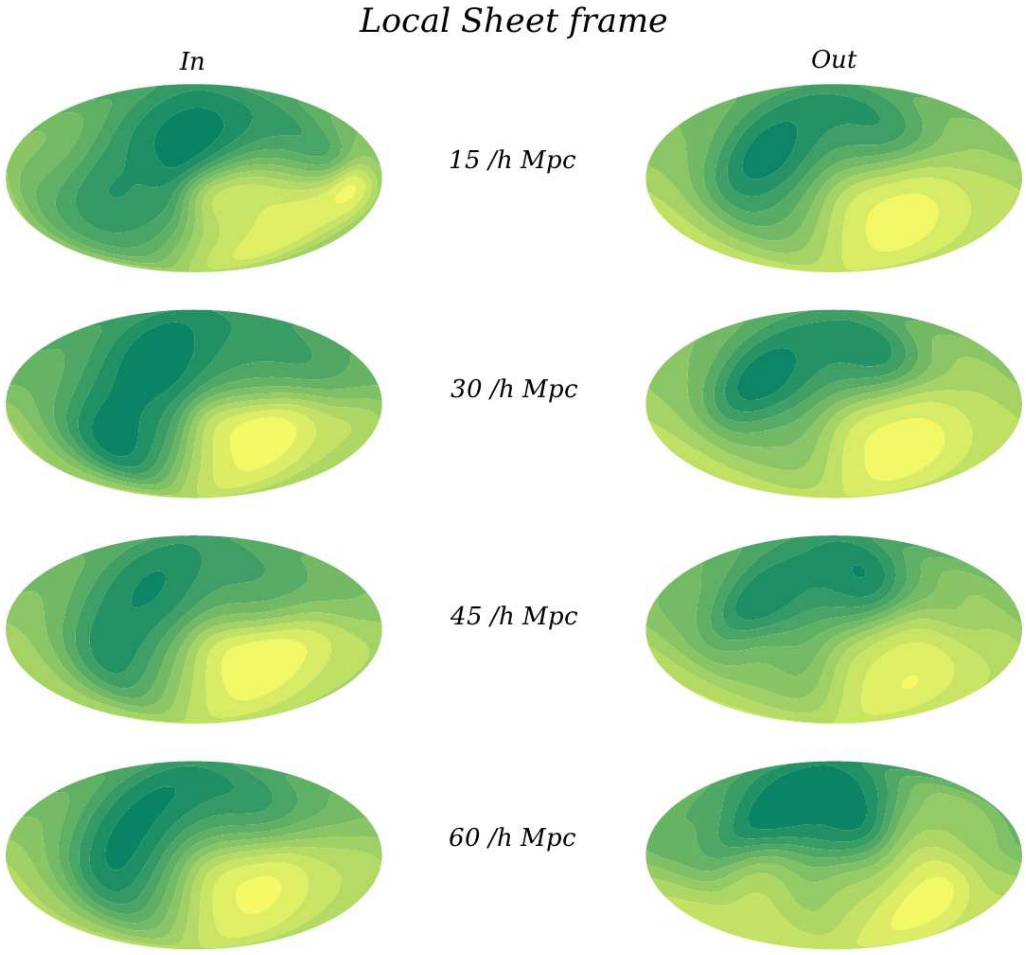

Figure 5.15: Hubble anisotropy restricted to spherical domains, LS frame. These are mollweide projections of galactic coordinates with $\ell = 0°$ at the right edge and $\ell = 360°$ at the left edge. The H_α were calculated using the reciprocal transform method.

sphere is increased and more objects from nearby are excluded, so that in the spherical shell beyond $60\,h^{-1}$ Mpc they lie along the galactic equator.

This pattern of the evolution of the dipole is repeated in the LG frame in Fig. 5.11 in the inside spheres. As in the CMB frame the pattern of the full volume is substantially reproduced by the inside map once the outer boundary of the volume has reached $60\,h^{-1}$ Mpc, and this same pattern is apparent in the volume outside $15\,h^{-1}$ Mpc at the top of the right column. In the LG frame, however, the poles of the dipole are much closer to 180° apart, and in the spherical shell beyond $60\,h^{-1}$ Mpc the pole in the northern hemisphere has moved slightly northward towards the North galactic pole.

The Local Sheet frame results in Fig. 5.12 are very similar to those of the LG, and are shown here for completeness.

Figs. 5.13–5.15 were computed using the inverse transformation method, and the outer volumes show very similar trends to their counterparts in the previous figures. Now, however, the inner volumes are much less different to the corresponding outer volumes.

These figures show the virtue of using the inverse transformation in the computation of the H_α. In Fig. 5.16 are plotted the 92 points in the volume $\lesssim 12.5\,h^{-1}$ Mpc radius (let us call this "shell 1"). Red points have peculiar velocities that are greater than zero. For the sake of argument, in the perturbed FLRW picture, these points are "moving away" from us in a rest frame that is comoving with the uniform expansion. Conversely, the blue points are said to be "moving toward" us[1]. The size of the points is proportional to the magnitude of their peculiar velocity. It is apparent that just a handful of points are governing the pattern of nearby Hubble anisotropy. These are the points responsible for the large radial variance in the first shell in Figs. 5.4 and 5.5. These velocities are so large that they still remain considerable even after they have been transformed to the LG frame. They therefore cause significant positive skew in the Hubble ratio histogram, in the sense that the mean of this distribution will be greater than the median. Now consider first the MD07 method of eq. (5.15) applied to the inner volumes out to $40\,h^{-1}$ Mpc, the results of which are shown in the left columns of

[1]Of course, all these points are moving away from us, with the expansion of the Universe. The blue points are just moving away from us slower than the red ones.

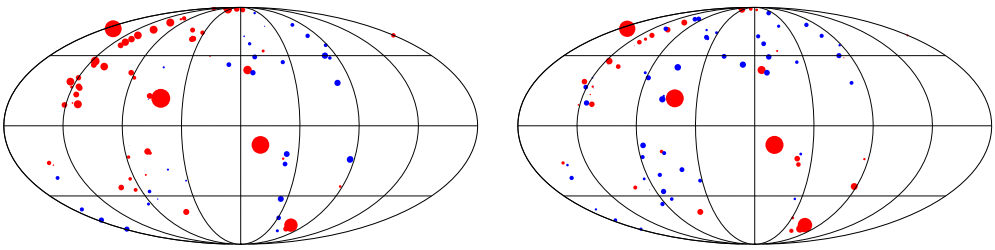

(a) CMB frame (b) LG frame

Figure 5.16: Velocities cz_i for objects within $12.5\,h^{-1}$ Mpc. Red points have positive velocities (in the sense that in that frame they are moving "away" from us), while blue points are moving "toward" us. The point size is proportional to the magnitude of the peculiar velocity $cz_i - H_0 r_i$.

Figs. 5.10, 5.11 and 5.12. This comparison shows that it is the large red point in the upper left quadrant near the centre that dominates the signal in that shell in the CMB frame, and the large point in the lower right quadrant near the centre that dominates the signal in the LG frame. The maps for the volumes $\lesssim 20\ h^{-1}$ and $\lesssim 40\ h^{-1}$ Mpc show the influence of these points gradually reducing.

Using the inverse transform method of eq. (5.20) in the computation of the H_α greatly diminishes the signal from these few points, and the inner volume sky maps in Figs. 5.13, 5.14 and 5.15 show much better the pattern of the smoothed angular variance of the Hubble expansion, particularly in the CMB frame. The inverse transform therefore compensates for the positive skew in the distribution of nearby cz_i/r_i values. From the sky maps in the right hand columns, however, there are always sufficient numbers of datapoints, and their distribution is sufficiently Gaussian for the sky maps to be very similar regardless of the whether the inverse transform is used or not.

We now therefore focus on the sky maps generated by using the inverse transformation in the computation of the Hubble expansion at each grid point on the sky, i.e. Figs. 5.13–5.19.

Sky maps computed with a contribution to the weighting from the measurement uncertainties are shown in Figs. 5.17 and 5.19, for the CMB and LG frames respectively. Clearly the shot noise problem that was reduced by the reciprocal

transform method has reappeared in the inner volumes: the variance in the innermost inner spheres is dominated by shot noise and remnants of this spurious signal are still apparent in the sphere within $60\,h^{-1}$ Mpc. The patterns in the spheres within $60\,h^{-1}$ Mpc are now less like those in the volumes beyond $15\,h^{-1}$ Mpc in each frame, but it seems likely that this excess variation is due to the lingering influence of the shot noise in the nearby inner volumes.

We have noted that the dipole structure in the LG and LS frames is much clearer than it is in the CMB frame. One can also see that the maps for the volumes outside $15\,h^{-1}$ Mpc in each frame are very similar to the maps for the full volumes shown in Figs. 5.8(b) and 5.9(b). This pattern remains in the volume beyond 20 h^{-1} Mpc, but by 60 h^{-1} Mpc it is the inner volume that contains the substance of the full-sample pattern. This indicates that the distribution of the 2434 galaxies between 12.5 and 60 h^{-1} Mpc is responsible for the major features of the full anisotropy map. Moreover, it suggests that the variance of the spherically symmetric averaged shells with $r_s < 62.5\,h^{-1}$ Mpc in the previous section on spherically symmetric radial averaging is *associated with structures on those scales whose smoothed angular signature is predominantly that of a dipole.*

These observations are supported by a spherical harmonic decomposition of the sky maps, undertaken using the `anafast` subroutine from HEALPIX[1]. We use this decomposition to quantify the relative strength of the lowest multipoles. For example, what we consider to be a "clean" dipole will be represented by small values for the ratios of the quadrupole power and octupole power to the dipole power: C_2/C_1, and $C_3/C1$, respectively. In Figures 5.18 and 5.20 are shown the resulting power spectra (calculated with the reciprocal transform) for the subsamples shown in Figs. 5.10–5.19, with volumes without IV weighting in the left columns and volumes with it in the right columns. The monopole has been subtracted in each case and so the magnitude of the dipole is indicated by the Y-intercept. The thin dotted line in each plot shows the power spectrum for the full sample. In each case, both with and without the IV weighting, one can see that the power spectrum of the inside sphere starts a long way from that of the full sample, but tends towards it as the radius is increased. The outer volumes closely resemble the full volume initially, at $15\,h^{-1}$ Mpc, but their power spectra

[1] `http://healpix.jpl.nasa.gov/`

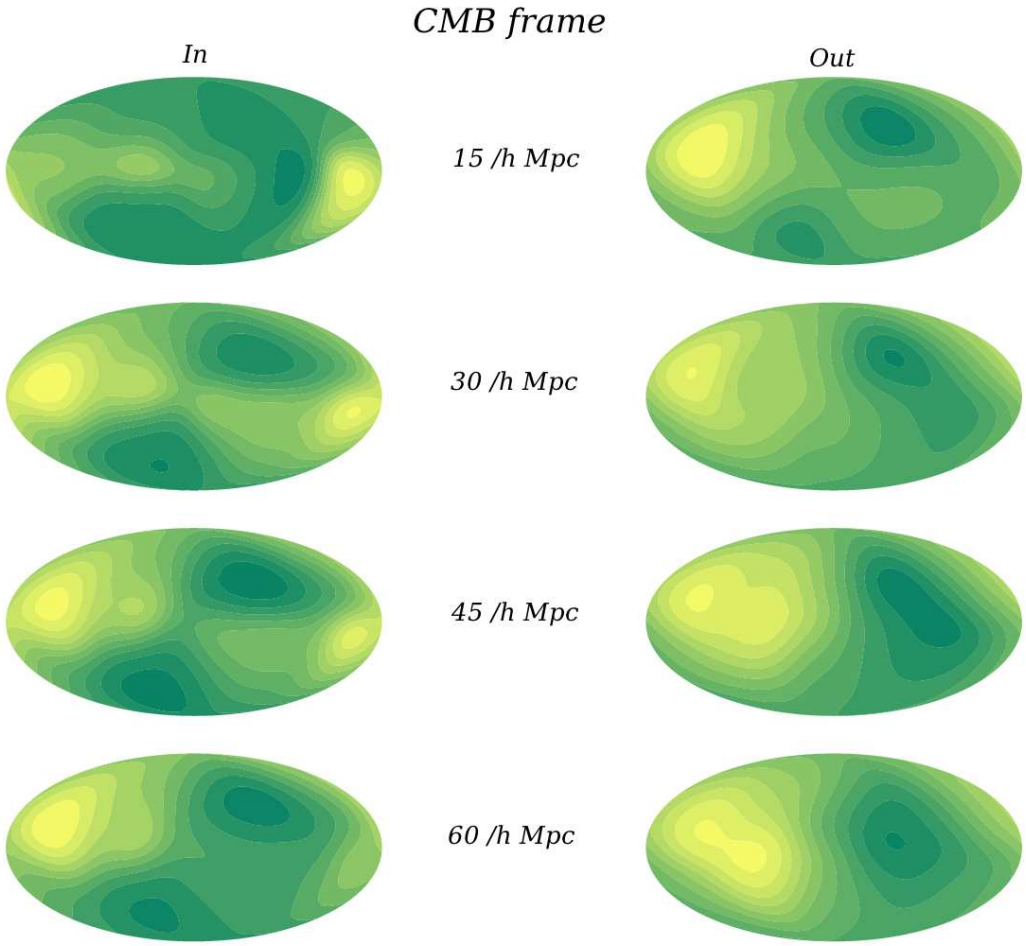

Figure 5.17: Weighted Hubble anisotropy restricted to spherical domains, CMB frame. These are mollweide projections of galactic coordinates with $l = 0°$ at the right edge and $l = 360°$ at the left edge. The H_α were calculated using the inverse transformation method, combined with inverse variance weighting to incorporate the uncertainties due to measurement errors.

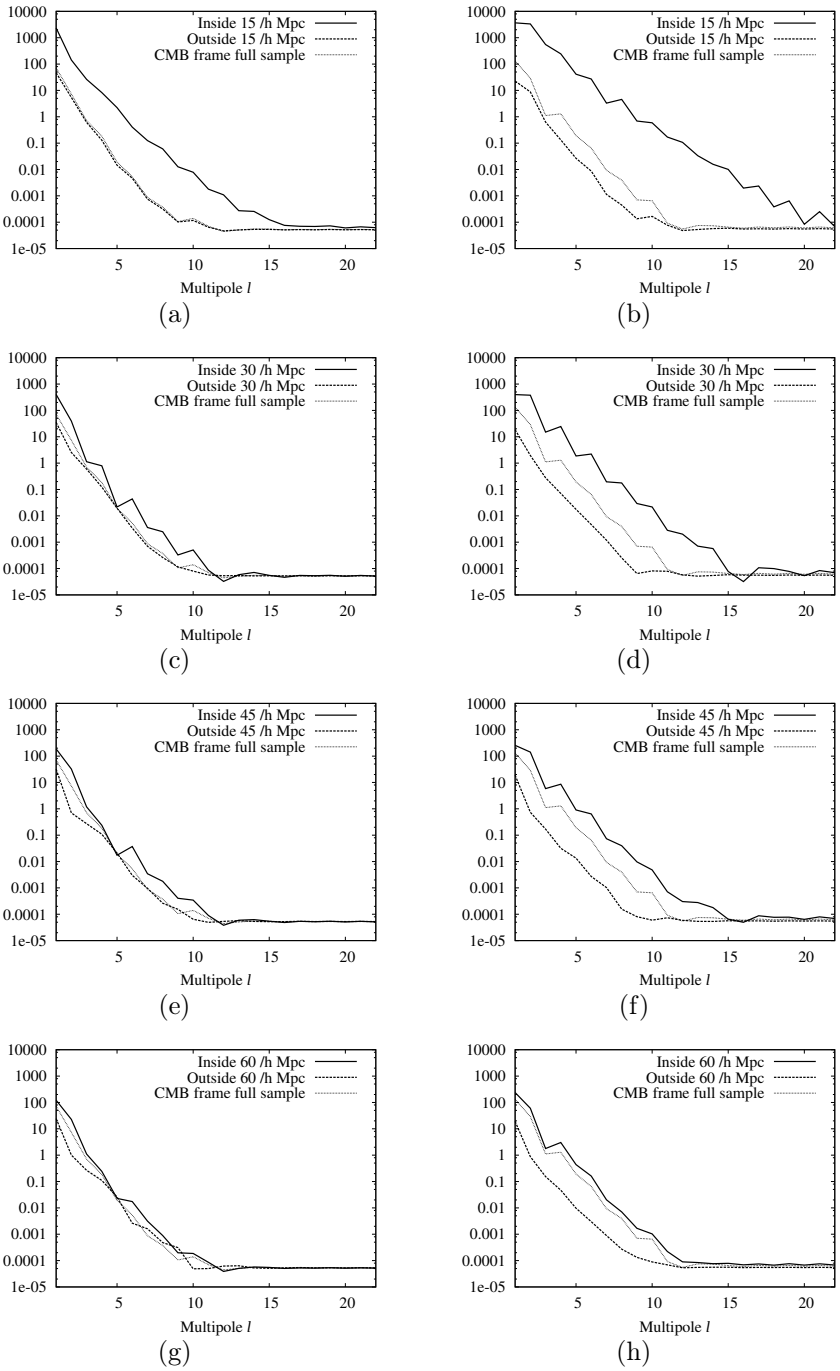

Figure 5.18: CMB frame power spectra. Unweighted (left column) and weighted (right column) power spectra for the Hubble anisotropy in the CMB frame, for comparison with Figs. 5.13 and 5.17. Ratios of the quadrupoles and octupoles to the dipoles are given in Tables 5.3 and 5.4.

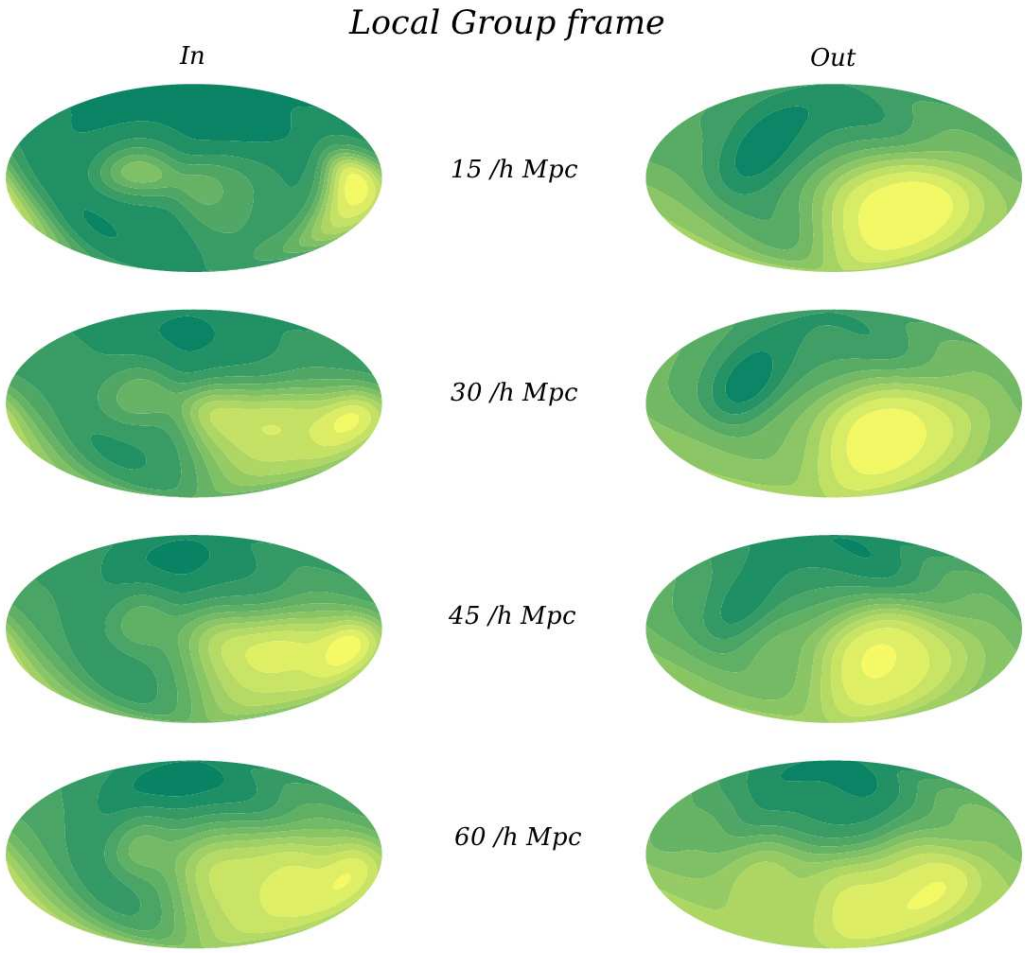

Figure 5.19: Weighted Hubble anisotropy restricted to spherical domains, LG frame. These are mollweide projections of galactic coordinates with $l = 0°$ at the right edge and $l = 360°$ at the left edge. The H_α were calculated using the inverse transformation method, combined with inverse variance weighting to incorporate the uncertainties due to measurement errors.

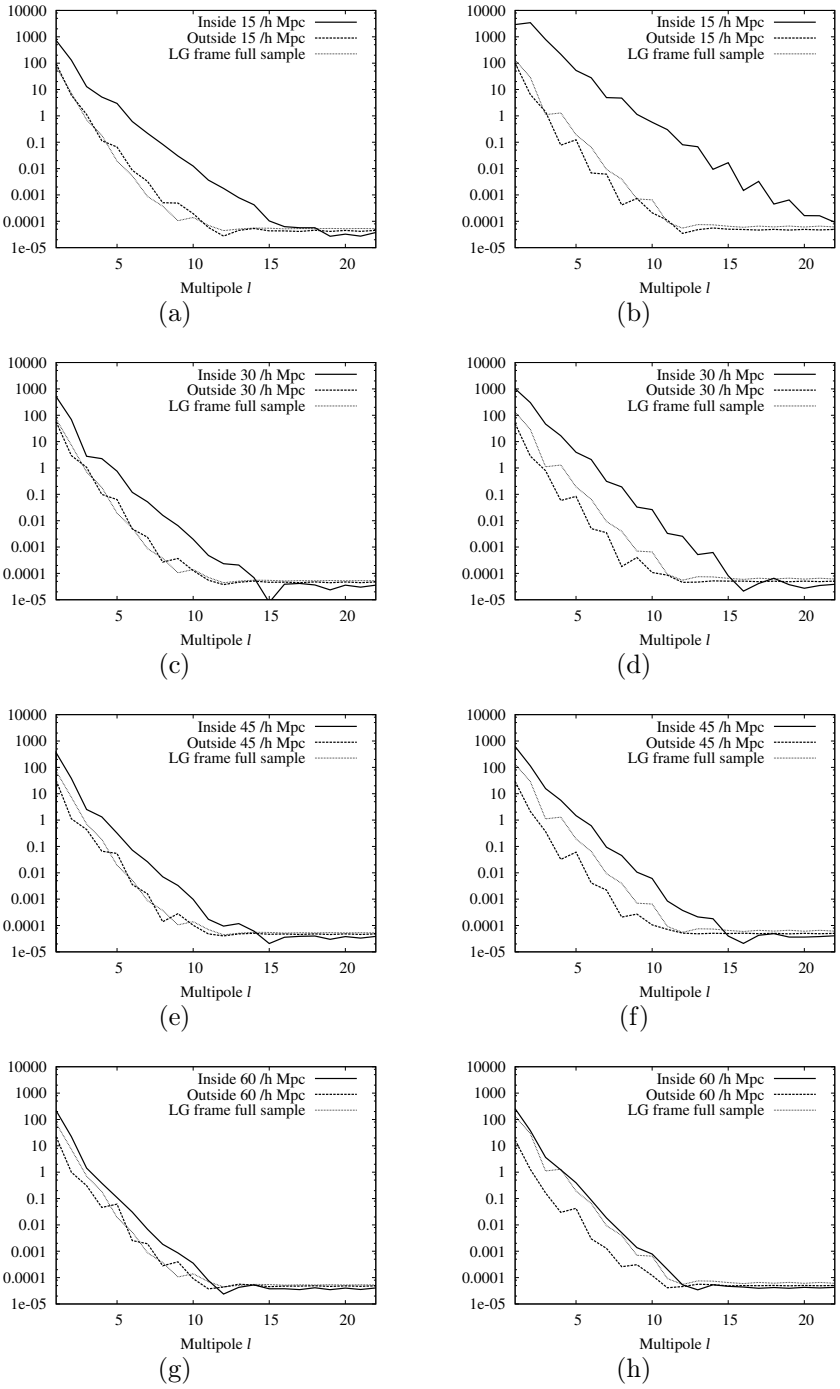

Figure 5.20: LG frame power spectra. Unweighted (left column) and weighted (right column) power spectra for the Hubble anisotropy in the LG frame, for comparison with Figs. 5.14 and 5.19. Ratios of the quadrupoles and octupoles to the dipoles are given in Tables 5.3 and 5.4.

move apart as the inside radius of the spherical shell increases and more objects from the regions of the sample near the origin are excluded.

Clearly, the Gaussian smearing will contribute some signal to the power spectra, and ideally these would be corrected for the beam width effect, but the aim in this chapter is to quantify the general features of the variation, and a rigorous treatment is beyond its scope. We show the effect on the power spectra of different smearing widths in Fig. 5.24. In this figure, the LG-frame power spectrum for $\sigma_\theta = 25°$ is shown in each plot for comparison. We observe that a reduced smearing width increases the power on smaller scales. There is increased power at all the multipoles shown compared to the 25° case for the volumes within $15\,h^{-1}$ Mpc where the data are sparser and more variable (this is discussed in the following section). Our method for obtaining a measure of the strength of the dipole using just the quadrupoles and octupoles is justified by the fact that compared to the higher order multipoles, their amplitudes relative to the dipole's are roughly similar in all cases except that of the very narrow smearing width, where the signal is dominated by the measurement uncertainties.

Since the multipoles with $\ell \geq 4$ are very much suppressed, the ratios of the power in the quadrupoles and octupoles to that in the dipoles provides a rough measure of the relative strength of the apparent dipole. In Tables 5.3 and 5.4 we list the quadrupole to dipole ratios C_2/C_1, and the octupole to dipole ratios C_3/C_1 for both inside and outside the boundary distance r_0 in the CMB, LG and LS reference frames.

Table 5.3 was computed using the standard weighted average of the Hubble ratios, while Table 5.4 was computed using the reciprocal transform method. The reduced impact of the handful of high-velocity points in the reciprocal transform method is reflected in the reduced ratios of quadrupole and octupole to dipole in the inside volumes in Table 5.4. For this reason, we focus on the numbers in this table in the following analysis.

In the LG frame $C_2/C_1 = 0.061$ in the outer $r > 12.5\,h^{-1}$ Mpc sphere, representing a small quadrupole compared with the dipole. In the corresponding inner sphere, $C_2/C_1 = 0.653$, indicating that the dipole and the quadrupole are roughly comparable. By contrast, in the CMB frame the same ratio is $C_2/C_1 = 0.096$ for the outer sphere and $C_2/C_1 = 0.123$ sphere. This shows that these maps are

Table 5.3. Ratios C_2/C_1, C_3/C_1 of quadrupole/dipole and octupole/dipole for the multipoles of angular Hubble variance maps in the CMB, LG and LS frames, using Eq. (5.15) with no inverse variance weighting. In each case the multipole ratios are computed inside ($r < r_o$) and outside ($r > r_o$) a bounding shell.

$r < r_o$ (h^{-1} Mpc)		< 12.5	< 15	< 20	< 30	< 40	< 50	< 60	< 70	< 80	< 90	< 100
CMB C_2/C_1		0.400	0.513	0.225	0.782	0.814	0.492	0.342	0.279	0.230	0.228	0.211
CMB C_3/C_1		0.091	0.088	0.028	0.043	0.074	0.041	0.027	0.023	0.025	0.025	0.023
LG C_2/C_1		0.889	1.079	0.484	0.179	0.154	0.137	0.141	0.147	0.127	0.129	0.127
LG C_3/C_1		0.243	0.224	0.095	0.021	0.023	0.016	0.016	0.018	0.021	0.022	0.022
LS C_2/C_1		1.192	1.431	0.584	0.198	0.167	0.148	0.154	0.161	0.140	0.142	0.139
LS C_3/C_1		0.314	0.282	0.105	0.021	0.024	0.016	0.018	0.019	0.022	0.023	0.023
$r > r_o$ (h^{-1} Mpc)	> 2	> 12.5	> 15	> 20	> 30	> 40	> 50	> 60	> 70	> 80	> 90	> 100
CMB C_2/C_1	0.183	0.187	0.187	0.200	0.092	0.046	0.022	0.042	0.136	0.128	0.174	1.498
CMB C_3/C_1	0.017	0.018	0.027	0.027	0.020	0.011	0.009	0.011	0.022	0.122	0.146	0.308
LG C_2/C_1	0.103	0.065	0.072	0.070	0.071	0.058	0.037	0.048	0.060	0.047	0.046	0.140
LG C_3/C_1	0.018	0.012	0.017	0.016	0.020	0.013	0.014	0.012	0.009	0.027	0.031	0.016
LS C_2/C_1	0.106	0.069	0.076	0.074	0.074	0.060	0.039	0.052	0.065	0.047	0.047	0.147
LS C_3/C_1	0.018	0.012	0.017	0.016	0.020	0.013	0.014	0.012	0.009	0.029	0.035	0.018

Table 5.4. Ratios C_2/C_1, C_3/C_1 of quadrupole/dipole and octupole/dipole for the multipoles of angular Hubble variance maps in the CMB, LG and LS frames, using the reciprocal transform method with no MLE variance weighting. In each case the multipole ratios are computed inside ($r < r_o$) and outside ($r > r_o$) a bounding shell.

$r < r_o$ (h^{-1} Mpc)		< 12.5	< 15	< 20	< 30	< 40	< 50	< 60	< 70	< 80	< 90	< 100
CMB C_2/C_1		0.123	0.061	0.044	0.098	0.136	0.191	0.187	0.167	0.141	0.134	0.120
CMB C_3/C_1		0.010	0.011	0.007	0.003	0.005	0.010	0.009	0.011	0.011	0.012	0.012
LG C_2/C_1		0.653	0.179	0.123	0.135	0.116	0.103	0.104	0.103	0.092	0.089	0.085
LG C_3/C_1		0.067	0.018	0.008	0.005	0.008	0.006	0.007	0.009	0.011	0.011	0.011
LS C_2/C_1		0.861	0.197	0.133	0.146	0.124	0.112	0.113	0.112	0.101	0.097	0.093
LS C_3/C_1		0.068	0.015	0.006	0.005	0.007	0.006	0.007	0.009	0.011	0.012	0.011
$r > r_o$ (h^{-1} Mpc)	> 2	> 12.5	> 15	> 20	> 30	> 40	> 50	> 60	> 70	> 80	> 90	> 100
CMB C_2/C_1	0.102	0.096	0.115	0.124	0.073	0.038	0.023	0.041	0.093	0.093	0.090	0.327
CMB C_3/C_1	0.010	0.009	0.013	0.015	0.017	0.009	0.007	0.011	0.018	0.078	0.069	0.076
LG C_2/C_1	0.072	0.061	0.064	0.064	0.053	0.042	0.032	0.045	0.068	0.077	0.066	0.151
LG C_3/C_1	0.010	0.009	0.012	0.014	0.019	0.013	0.013	0.014	0.010	0.048	0.051	0.016
LS C_2/C_1	0.079	0.065	0.068	0.068	0.054	0.044	0.033	0.048	0.074	0.079	0.070	0.162
LS C_3/C_1	0.010	0.009	0.012	0.014	0.019	0.013	0.013	0.014	0.011	0.053	0.062	0.020

more similar to each other than they are in the LG frame, and the dipole is less clearly defined.

In the inner volumes, the quadrupole to dipole ratio in the LG frame drops substantially, and it remains at about a sixth of its initial value in the range $50 \leq r_0 \leq 90$. This is higher than the same ratio for the corresponding outer spheres, but this is on account of the contribution to the inner volumes from the first volume, in which the dipole and quadrupole are comparable.

The ratios in the tables support the observation that the dipole is generally less distinct in the CMB frame than in the LG frame. But recall that in Section 5.3.1 above for the spherical averages, we found that the Hubble variance in the CMB frame was slightly less in the range $35 \lesssim r_0 \lesssim 60\,h^{-1}$ Mpc. Comparison of the ratios in Table 5.3.1 in this range reveals that the spherical harmonic decomposition supports this observation too, despite the overall smaller ratios in the LG frame. In particular, at $r_0 = 40$, 50, or $60\,h^{-1}$ Mpc, both the quadrupole to dipole ratio and the octupole dipole ratio are less in the CMB frame than they are in the LG frame for the outer volumes. Beyond $70\,h^{-1}$ Mpc the CMB dipole becomes less distinct again. This shows that the boost to the CMB frame is producing a more dipole-like angular variation in the Hubble expansion over this particular range.

How many points are enough?

It is worth taking a more detailed look at the innermost inside volumes, those whose outer bounds lie at 12.5 and $15\,h^{-1}$ Mpc, because they reveal a fundamental difference in the analysis undertaken by MD07 and the one undertaken here. Although we are ultimately obtaining individual "Hubble constants" for each datum, the measurement uncertainties in the COMPOSITE sample are such that we cannot take each point on its own as an equally precise estimate of the Hubble flow at that distance. By contrast, the HST Key data was collected with precisely this aim. Consequently, MD07 could create a full sky map from only 76 points, and even considered a radial weighting scheme to investigate radial variation in the Hubble expansion.

Because of the larger uncertainties in the COMPOSITE sample, we rely on having a statistically sufficient number of points to obtain the smoothed variation of the Hubble expansion across the sky. We now demonstrate that the number of points in the closer inner volumes is insufficient to determine the smoothed map, despite being greater than the number of points in the entire HST Key sample.

We refer to Figures 5.21 and 5.22. Here we show the locations of the data within 12.5 (Fig. 5.21(a)) and $15\,h^{-1}$ Mpc (Fig. 5.22(a)). The points in the $12.5\,h^{-1}$ Mpc volume are the same as those in Fig. 5.16, but now we include more information about the velocities. As in Fig. 5.16, the size of each point is proportional to the magnitude of its peculiar velocity. But now each point is coloured with either a pale orange to red colour scale or a pale blue to purple colour scale depending on whether its peculiar velocity $cz_i - H_0 r_i$ is positive or negative, respectively. The strength of the colour of each point represents the uncertainty in the measurement of its distance. There are some very faint points. Figures 5.21 and 5.22 show contour maps for the volumes within $12.5\,h^{-1}$ Mpc and within $15\,h^{-1}$ Mpc, weighted with just the Gaussian smearing (above) and with both smearing and inverse variance weights (below). The contour lines are lines of constant Hubble expansion, and, for the $12.5\,h^{-1}$ Mpc case, correspond to the filled contours shown in the upper left maps in Figs. 5.14 and 5.19 (Those for the volume inside $15\,h^{-1}$ Mpc have not yet been shown). The filled contours in Figs. 5.21 and 5.22 represent the uncertainties σ_α (eq. (5.23)) from computing the values of H_α at each grid point.

From the angular distribution of the points, it is clear that the uncertainties thus calculated are driven by the measurement errors, especially when the inverse variance weighting is used. There is evidently only a very weak contribution to the uncertainty from insufficient sky coverage. The dearth of data in the zone of avoidance (ZoA) along the galactic plane and in the Local Void and behind the galactic centre at the right-hand ends of the maps in Figs. 5.21(a) and 5.22(a) contributes very little, if anything, to the uncertainties. Instead these are associated mainly with just a handful of points, namely the more isolated point points with large uncertainties. A couple of these also have unusually large velocities— these are the large, faint points near the centres of the maps in Figs. 5.21(a) and 5.22(a). The velocities of these points are so large (the two "fastest"

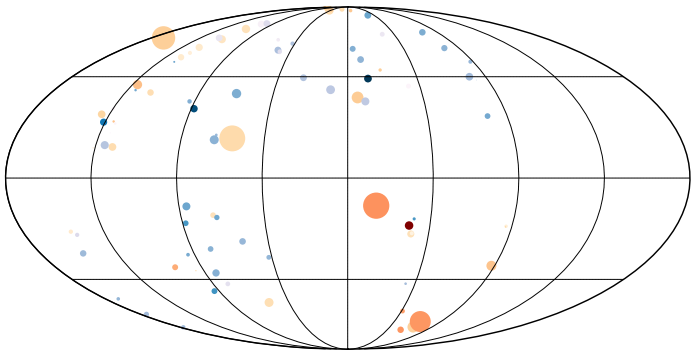

(a) COMPOSITE galaxies with $r_0 = 12.5\,h^{-1}$ Mpc

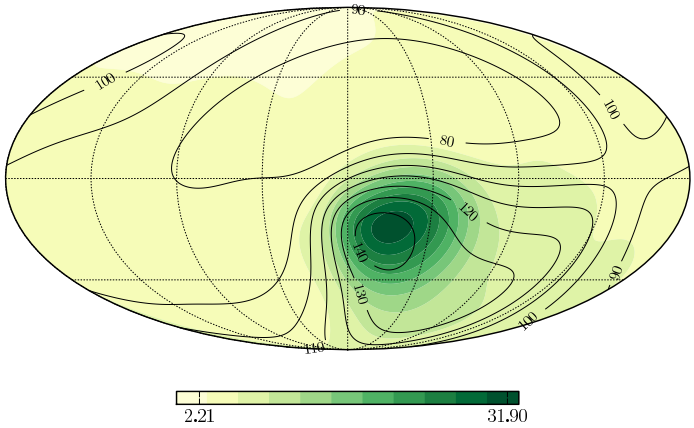

(b) Hubble anisotropy within $r_0 = 12.5\,h^{-1}$ Mpc, no IV weighting

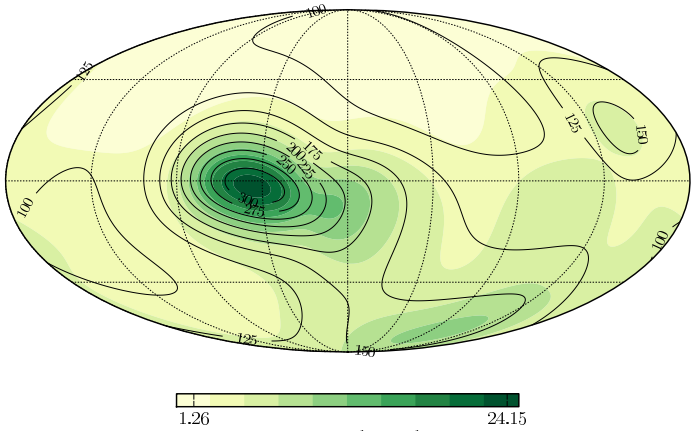

(c) Hubble anisotropy within $r_0 = 12.5\,h^{-1}$ Mpc, with IV weighting

Figure 5.21: Shot noise in nearest shells: within $12.5\,h^{-1}$ Mpc.

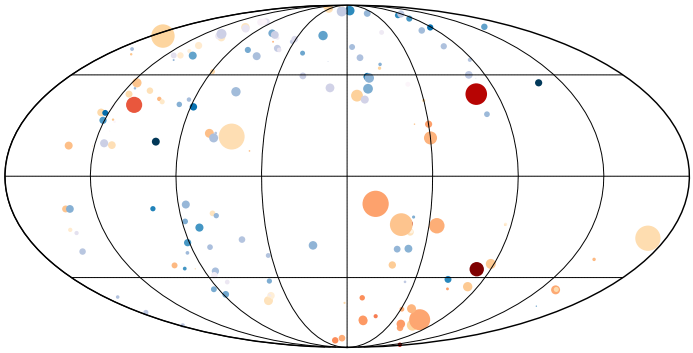

(a) COMPOSITE galaxies with $r_0 = 15\,h^{-1}$ Mpc

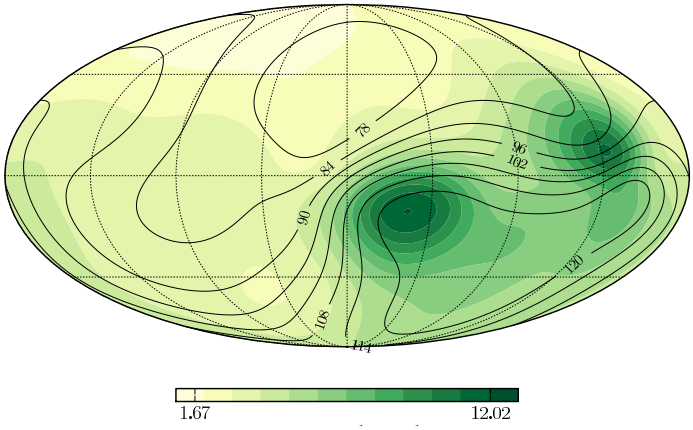

(b) Hubble anisotropy within $r_0 = 15\,h^{-1}$ Mpc, no IV weighting

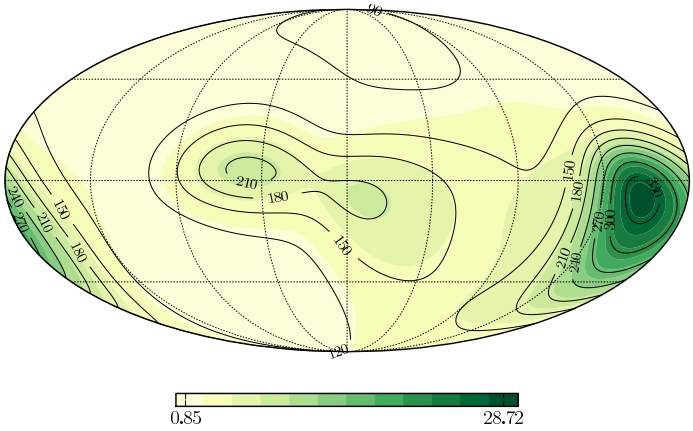

(c) Hubble anisotropy within $r_0 = 15\,h^{-1}$ Mpc, IV weighting

Figure 5.22: As for Fig. 5.21 but for $r < 15\,h^{-1}$ Mpc.

galaxies are moving at more than 5500 km/s) that they remain large even after the transformation to the LG frame.

Because they are so close, these points yield very large Hubble ratios, and it is these points in particular which determine the pattern of the sky maps for nearby volumes. Because of their unusually high velocities, and their large uncertainties, it is unreasonable to presume that these points can tell us anything about cosmic expansion. This is another manifestation of shot noise: in the nearby volumes from the COMPOSITE sample, there is inadequate sky coverage and a few statistical outliers are generating the variation, particularly in the inverse variance-weighted maps. Since these points are included in the subsequent volumes, the effect of these points can still be seen in the volumes inside $60\,h^{-1}$ Mpc. This is especially strong in the LG frame plots shown in Fig. 5.19.

It is an indication of the precision of the HST Key measurements that the map of Hubble variance produced in MD07 has a similar underlying form to the map computed here from roughly 60 times the number of measurements.

The aim of the following sections is to provide statistical constraints on the angular orientation of the dipole feature in the LG-frame Hubble anisotropy. To counter the effects of the shot noise just described, we therefore as an initial step exclude the objects from within $15\,h^{-1}$ Mpc, thereby avoiding the foreground effects that produce the large variance in the first bins in the figures (however, two of the shells giving rise to the strong Bayesian evidence in Fig. 5.6 still remain). For example, the high-H_α region near $\ell = 0^\circ$ visible in the volumes within $20\,h^{-1}$ Mpc in Figs. 5.17 and 5.19 is removed with this cut. Our sample therefore now comprises 4534-175=4359 distances.

Figures 5.21 and 5.22 (pages 175 and 176): Shot noise in nearest shells. The locations of nearby COMPOSITE objects within $12\,h^{-1}$ Mpc are shown in the top figure. Fig. 5.21(a), and Fig. 5.22(a) include more velocity information than was shown in Fig. 5.16. Points coloured pale orange to red have positive velocities, while pale blue to purple points have negative peculiar velocities. The measurement uncertainties are represented by the strength of the colour of the point. The point size is proportional to the magnitude of the peculiar velocity $cz_i - H_0 r_i$. Hubble anisotropy maps are shown without (middle) and with (bottom) inverse distance variance weighting for $r_0 < 12.5\,h^{-1}$ Mpc. Shot noise produces large uncertainties, which drive the Hubble anisotropy.

5.4.3 Constraining the angular variation in the Hubble expansion

5.4.3.1 MD07 uncertainty estimation

To assess the statistical significance of the Hubble anisotropy they detected in the HST Key data, MD07 used Monte Carlo methods, determining how often randomly generated samples showed variation as great or greater than that observed, assuming that the measurement uncertainties were correct. Statistically significant (95% C.L.) variation in the data was deemed to be detected when the simulated variation was as great as the observed variation less than 5% of the time. This shows that the measurement uncertainties are generally not large enough to produce the observed variation. By this criterion, MD07 detected a statistically significant variation in H_α of 12.5% for the 25° smearing angle.

Following MD07, assuming the 1σ measurement errors to be correct, we generated 1000 Monte Carlo simulations of the COMPOSITE data, choosing a new distance for each data point from a gaussian distribution centred on the quoted distance with width equal to the quoted 1σ distance error. Note that for this analysis we used no IV weighting and we calculated H_α using eq. (5.15), i.e. without the inverse transformation. We then recalculated the sky maps and the difference ΔH between the mean H_0 maximum and minimum. The results for various smearing widths are shown in Table 5.5. For the HST Key data of MD07, with the 25° smearing width, the variation in the simulated samples was as great

Survey	*N*	15°	25°	35°	45°
MD07	76	64.72 (24.82)	13.80 (13.0)	5.57 (8.76)	4.51 (6.28)
MD07 (publ.)	76	-	13.08 (12.9)	4.93 (8.8)	3.82 (6.3)
COMP.	4535	13.3 (27.3)	0.43 (18.18)	0.6 (12.35)	0.7 (8.99)
SBF	88	0.80 (90.48)	0.38 (57.13)	0.10 (41.78)	0.30 (32.84)
ENEAR	697	2.20 (32.11)	5.77 (20.51)	0.30 (13.95)	0.50 (10.15)
EFAR	50	48.66 (26.76)	32.17 (14.09)	23.26 (9.61)	23.22 (6.87)
SFI++	3456	5.00 (31.08)	13.56 (16.65)	14.29 (11.57)	9.76 (8.82)
SMAC	56	19.38 (26.71)	12.78 (16.44)	6.04 (12.85)	2.90 (10.08)
SC	70	36.42 (14.43)	22.40 (7.86)	15.14 (5.02)	18.95 (3.19)
SN	103	0.00 (95.6)	0.00 (55.13)	0.00 (36.5)	0.00 (26.75)
Willick	15	86.56 (22.13)	31.37 (16.95)	16.16 (11.45)	20.72 (7.32)

Table 5.5: MC Simulation results: H_0 anisotropy. N is the number of objects in the survey. The numbers in each column are the percentages of the 1000 MC simulations for each Gaussian smearing width for which the simulated variation was as great as that in the real data. The H_α were calculated without IV weights and using eq. (5.15)—i.e. without using the reciprocal transform. The bracketed numbers are the true differences ΔH in units of km s^{-1} Mpc^{-1} for the MD07 data, and in units of h km s^{-1} Mpc^{-1} for the COMPOSITE data and its subsamples. The published results from MD07 from 10000 simulations are also shown for comparison.

as that observed 13% of the time (MD07 obtained 12.9%). MD07 do a second Monte Carlo run based on scattering the H_0 values from the HST Key project data. In the HST Key data, several estimates of H_0 were used for each data point. We only have one corresponding value for each data point so this method cannot be adapted for the COMPOSITE data. A combination of the MC method used here and the H_0 scattering method permitted MD07 to quote the statistically significant variation of 12.5%. For the COMPOSITE data, the simulated variation was as great as that observed (18%) only 0.43% of the time. Therefore, the MC simulations seem to demonstrate that an 18% variation in the Hubble constant is significant with a 99% confidence level.

By this method, there appear to be some large H_0 variations in Table 5.5 that are statistically significant. In particular, for the SN supernova subsample in each

window width the simulated variation is as great as that observed 0% of the time. MD07 obtain the same results for the $N = 36$ SN subsample of the HST Key data they use. This is interesting because the supernova distances have relatively small uncertainties, and suggests that the variation is indeed significant. In the light of the discussion in the previous section, we suggest that the sparser samples are showing the effects of shot noise.

As the smearing window size is reduced, ΔH_0 increases as the uncertainties have more impact. Thus, for a smearing width of 15°, the ΔH_0 for the whole COMPOSITE sample is 27.3%, but the confidence we can have in its significance is less than 90%. At larger window sizes, the Hubble variation is the dominant effect, but its resolution is smeared out.

There is a conceptual issue with this method however. The aim with the Monte Carlo methods is to propagate the data errors into uncertainties in the final measurements. The assumption is that measurement uncertainties produce a certain amount of variation, and that if there is variation over and above that produced by the measurement uncertainties, then that variation is caused by something other than the uncertainties. However, if scattering the distances by the uncertainties generally gets rid of the variation (if the simulated variation is generally less than that observed), then this should indicate that is precisely the distance uncertainties that are causing the variation[1]. In other words, to detect significant variation, one should look for simulated variation being greater than that observed *more* than 95% of the time. Preliminary work has been carried out to address this conundrum, but the issue remains tangential to the one at hand. We therefore take the statistical significance claim of MD07 at face value, and leave a detailed investigation of the issue to future work. This possibility makes sense for the sparse datasets in Table 5.5 like the SBF and SN samples which each show what amounts to an infeasibly large yet significant variation.

5.4.3.2 New alternative method of uncertainty estimation

With the larger sample size, a measure of statistical confidence in the expansion variation is more readily obtained by plotting the uncertainties as filled contours

[1] I am indebted to Dr Rick Watkins for pointing this out.

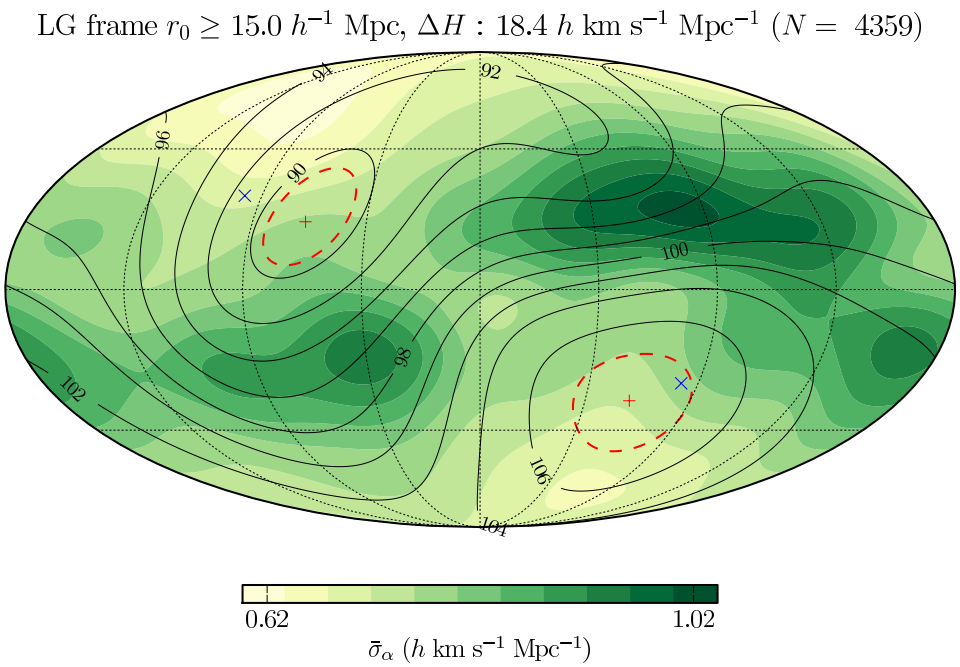

(a) Without IV weighting

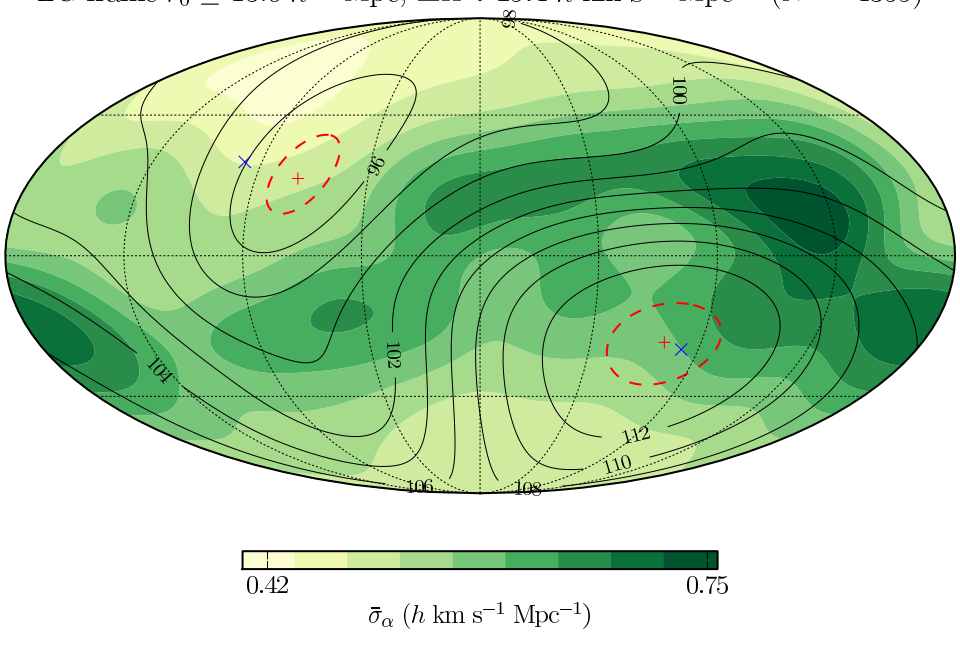

(b) With IV weighting

on the same map as lines of constant Hubble expansion. We have already shown the resulting Hubble anisotropy uncertainty maps for the innermost regions of the COMPOSITE sample in the LG frame (Figs. 5.21 and 5.22(a)). In Figure 5.23 we show maps computed from all the data beyond $15\,h^{-1}$ Mpc[1].

In Fig. 5.23 the smearing width and the spatial distribution of the data combine to produce a maximum in the Hubble expansion uncertainty in the north-eastern region of the galactic coordinate system. The large COMPOSITE sample size brings the statistical errors down to the point where we can discern more statistically significant variation than that detected from the 76 objects in the HST Key sample. The mean value and the weighted standard deviation of the H_α plotted in the figure are 98.2 ± 5.4 h km s^{-1} Mpc^{-1}, and the corresponding values for the IV-weighted map are 102.6 ± 5.3 h km s^{-1} Mpc^{-1}. With the maximum uncertainty shown on the colorbar under the figure, the Hubble anisotropy $\Delta H = 18.4$ h km s^{-1} Mpc^{-1} is clearly significantly different from zero. In Fig. 5.23(a) the maximum and minimum values of H_α are $+9.3\%$ and -9.4% from the mean respectively. The corresponding values for the IV-weighted variance shown in Fig. 5.23(b) are $+11\%$ for the maximum and -7.9% for the minimum. In each case the differences are considerably larger than the standard uncertainty, which, as seen in the figure, is of order 1% of the mean. The regions of greatest uncertainty appear to follow roughly the contours which define the mean expansion value.

Also shown in Figure 5.23 are the positions of the H_α extrema, shown as red plus signs. The 1σ contour is shown as a dashed red line, and has been taken to be the maximum shown on the map, i.e. 1.01 h km s^{-1} Mpc^{-1} for the case without IV weighting. The pole positions here are $(\ell, b) = (117°, -35°)$ for the maximum and $(\ell, b) = (249°, 21°)$ for the minimum. The corresponding values for Fig. 5.23(b) with IV weighting are $(\ell, b) = (105°, -27°)$ for the maximum and $(\ell, b) = (252°, 25°)$ for the minimum. In Fig. 5.23(b) the minimum of the CMB temperature dipole lies within 1σ of the Hubble variance maximum. We checked

[1]We note here that in plotting the CMB temperature extrema we have not accounted for the uncertainty in the boost to the LG frame given in Tully et al. (2008). These are small (see the end of § 5.3 above), and will not affect the significance of our conclusions, but a comprehensive error analysis should take these into account.

that the CMB temperature dipole maximum lies within 3σ of the Hubble variance minimum. We note that the poles are slightly squeezed in galactic longitude compared with the poles of a pure dipole.

Figure 5.23: (page 181) **Local Group-frame Hubble anisotropy uncertainty maps** for COMPOSITE data beyond $15\,h^{-1}$ Mpc (No IV weighting). The filled contours represent the uncertainty, and the contour lines represent the H_α. The upper map is calculated wihout inverse variance weighting, the lower map with it. The red plus signs mark the extrema of the Hubble anisotropy dipole, and the dashed red lines mark the one standard deviation confidence level. The blue crosses mark the extrema of the CMB temperature dipole (see § 5.4.5 below).

5.4.4 Fitting Hubble anisotropy to the distribution of structure

The distribution of large-scale structure within $30\,h^{-1}$ Mpc has been described by Tully et al. (2008) and is summarized in Section 5.1.1 above. The observed dipole in the Hubble ansiotropy is consistent with a foreground density gradient with an average overdensity on one side of the sky and an average underdensity on the opposite side. This breakdown of the overall structure, as probed by the Hubble variation we have observed, is much more complicated on local scales, even without considering the question of galaxy bias.

The Milky Way galaxy, within the Local Group, is situated in a thin filamentary sheet, the Local Sheet. The Local Sheet defines the supergalactic (X, Y) plane, and lies right on the edge of a complex of voids separated from each other by filamentary wall structures of total diameter at least $30\,h^{-1}$ Mpc (Tully et al., 2008). In the plot in Fig. 5.1, looking along the supergalactic plane, the Inner Local Void, the nearest of three in the void complex, is clearly visible as the relatively empty region in the upper left, and the Local Sheet is visible as the collection of yellow and green points on its margin. The other two voids in the complex are denoted Local Voids North and South. Here "north" and "south" refer to the supergalactic coordinate system, in which the north pole lies at galactic $(\ell, b) = (47.37°, 6.32°)$. The Inner Local Void, which is ellipsoidal, with its major axis roughly parallel to the Local Sheet, is the structure that covers the largest

fraction of the sky in the Local Void complex. From Fig. 10 in Tully et al. (2008) we estimate that the centre of the Local Void is located at approximately $(\ell, b) = (107°, -7°)$. From Euclidean geometry, assuming a spherical "top hat" void with radius 15 Mpc whose edge lies 3 Mpc from us, one can estimate that the fraction of one hemisphere taken up by the void apparent from our position is 40–60%[1], given the uncertainties due to redshift space distortions. This is too large a fraction of the sky to produce a pure dipole in the Hubble variance.

The dipole axis appears to be defined by structures within $60\,h^{-1}$ Mpc, about twice the scale of the survey of Tully et al. (2008). However, since the Hubble relation will include the contribution of foregrounds, the important question is in what direction is there an alignment of a void in the range $35 \lesssim r \lesssim 60\,h^{-1}$ Mpc and the Local Void in the foreground? The position of the Hubble variance maximum in Fig. 5.23 seems to indicate that such a void lies behind the Local Void North but is not directly aligned with an axis through its centre. The opposite side of the sky is dominated by wall regions, most notably the Hydrus, Centaurus and Norma superclusters, constituting what has become known as the Great Attractor (see Fig. 5.8(b)). The nearest cluster to the Milky Way, the Virgo cluster, lies in the supergalactic plane, in a direction almost at right angles the direction of the overall density gradient.

Given therefore that the Milky Way lies in the transition region between a wall and a void, a dipole in the Hubble expansion measured from the velocities and distances of nearby objects is to be expected. If the Milky Way was situated in the middle of a large void, one might expect a more isotropic Hubble expansion, while a situation within a wall with large voids to either side would produce more of a quadrupole pattern.

One might wonder if reducing the smoothing width can help to demarcate structure in the COMPOSITE sample. We leave an in-depth analysis of this for future work, but we make some preliminary, cursory investigations now.

[1]It can be shown that with these assumptions, with r the distance to the edge of the void, and R the void radius, the fraction of one hemisphere taken up by the void is given by (Mattsson, *pers. comm.*)

$$f\left(\frac{r}{R}\right) = \frac{1}{2}\left(1 - \sqrt{1 - \frac{1}{1 + (r/R)^2}}\right). \tag{5.24}$$

We have so far not experimented with changing the smoothing width, but in principle one might hope that reducing it from 25° might even help us to pick out some of the larger concentrations. Because the COMPOSITE sample is so much larger than the HST Key sample, we can perhaps be justified in reducing the smearing width and achieving better resolution of the expansion field. In practice this is not the case because the uncertainties are too large, and below a certain smearing scale they will come to dominate the variation. In Figure 5.25 we show the maps derived from 5, 15, 25, and 40 degree smearing widths. By changing the smearing width σ_θ in (5.14) and showing the uncertainties as well, we can determine a width that is appropriate for the data that we have. We show the resulting uncertainty maps for 5, 15, 25 and 40 degree smearing widths in Fig 5.26.

Figure 5.25 shows the expected better resolution of the Hubble expansion field with a narrower smearing width. At 15° the dipole is still present but has become indistinct. With a smearing width of 5° we see a lot of variation, including some along the galactic equator. In Fig. 5.26 we see that this level of variation from this data cannot be real; the effects of the zone of avoidance are clear from the larger uncertainties along the galactic equator. For $\sigma_\theta = 5°$ the difference ΔH is 60.7 h km s^{-1} Mpc^{-1}, but the standard deviation is 36.1 h km s^{-1} Mpc^{-1}, so clearly the variation is now driven by the fit uncertainties rather than the actual expansion— the variation is large but no longer statistically significant. The 15° uncertainty map shows higher uncertainties still roughly aligned with the galactic equator. The variation in this map is 22.8 ± 2.29 h km s^{-1} Mpc^{-1} so this angle looks promising for potentially resolving the effects of larger structure within the COMPOSITE data on smaller scales than the 25° that we have been using. It is evident that 25° is easily sufficient to smooth over the region $b \lesssim |10°|$ in which observations are sparse. The 40° maps in Figs 5.25 and 5.26 show an almost perfect dipole, in which $\Delta H = 13.6$ h km s^{-1} Mpc^{-1} with a confidence level of 13σ.

We conclude that smoothed above a certain scale, there exists a clear dipole in the Hubble expansion in the Local Group frame. Given the large size of the COMPOSITE sample, we could feel justified in reducing the smoothing angle to at least 15° without losing the statistical significance of this variation. In

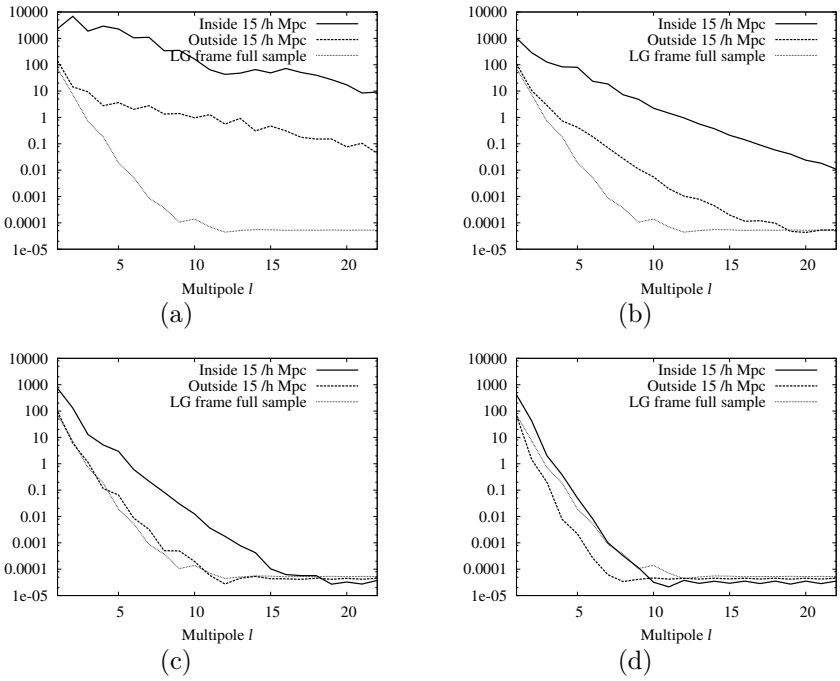

Figure 5.24: LG frame power spectra for different smearing widths. Unweighted power spectra for the Hubble anisotropy in the LG frame, for data inside and beyond $15\,h^{-1}$ Mpc. Smearing widths and rough corresponding multipole scales (for angular scales of twice the Gaussian width) are: (5.24(a)), $(\sigma_\theta, \ell_\theta) = (5°, 18)$; (5.24(b)), $(\sigma_\theta, \ell_\theta) = (15°, 6)$; (5.24(c)), $(\sigma_\theta, \ell_\theta) = (25°, 4)$; (5.24(d)), $(\sigma_\theta, \ell_\theta) = (40°, 2)$. The power spectrum for the full LG sample with a 25° smearing width is shown in each case for comparison. Note that the relative amplitudes of the dipole and quadrupole are compratively stable with respect to the full 25° spectrum for all the outside shells. Although the smearing clearly contributes to the signal, this justifies our rough estimation of the relative strength of the dipole from looking at just the ratios of the power in the quadrupole C_2 and octupole C_3 to the dipole power C_1 for the data beyond $15\,h^{-1}$ Mpc. More explanation is given in § 5.4.2.

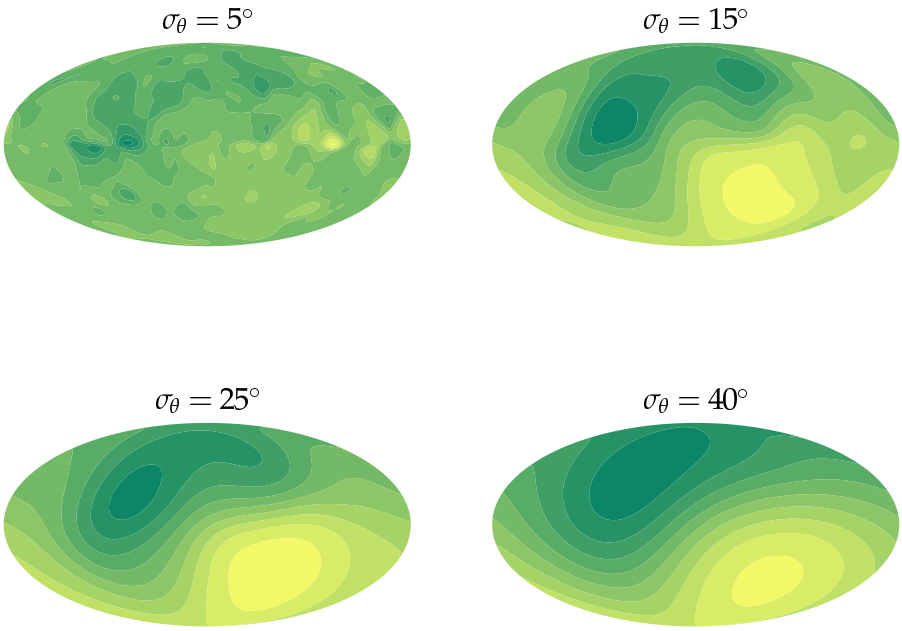

Figure 5.25: Hubble anisotropy from different smearing widths. We show here only LG-frame data from beyond $15\,h^{-1}$ Mpc without IV weighting. The corresponding power spectra are shown as dotted lines in Fig. 5.24. The weighted maps look very similar.

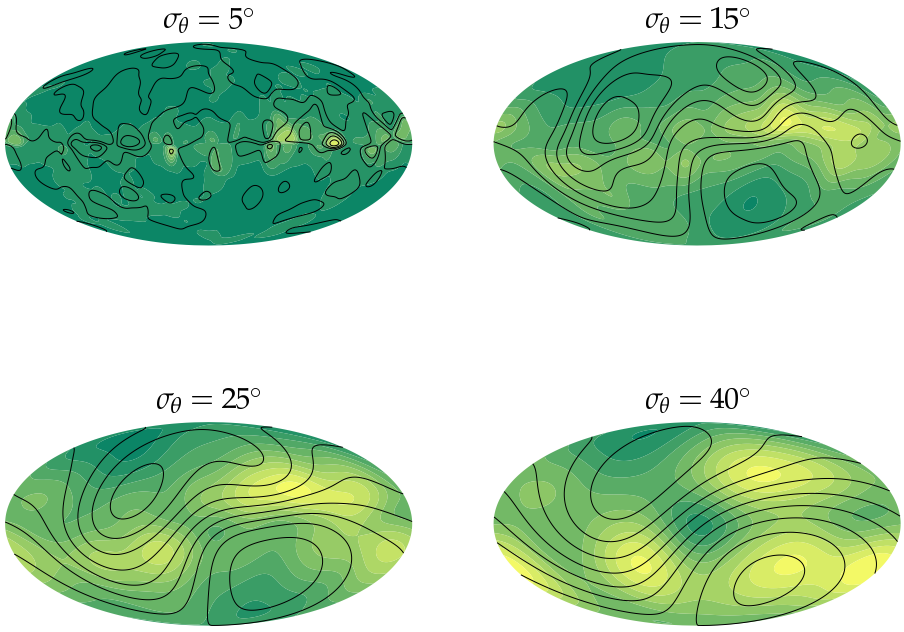

Figure 5.26: Uncertainties in Hubble anisotropy from different smearing widths. We show here only LG-frame data from beyond 15 h^{-1} Mpc without IV weighting. The weighted maps look very similar. The smaller smearing widths pick out the uncertainties along the zone of avoidance, but the uncertainty due to the paucity of data in this region is much less than that derived from the data uncertainties.

future work, we would like to compare the Hubble anisotropy smoothed on these scales with current maps of large-scale structure with the aim of constraining the relationship between over- or underdensities and the cosmic expansion. In the present investigation however, we limit ourselves to constraining the dipole feature.

In the following, final part of this chapter, we compare the strength and alignment of the Hubble anisotropy dipole with that of the temperature dipole in the cosmic microwave background.

5.4.5 Constraining the Hubble dipole

The Hubble anisotropy map calculated from the 4359 COMPOSITE distances and velocities beyond $15\,h^{-1}$ Mpc is shown in Fig. 5.27(b). This map is strongly reminiscent of the CMB temperature dipole and we investigate this similarity further in this section.

We are assuming that the dipole in the CMB temperature is a perfect one, in the sense that we use the same "aether drift" model dipole that is subtracted from the satellite measurements in order to discern the intrinsic μK primordial microwave anisotropies. To make this comparison, we must first compensate for the sun's motion with respect to the LG (or LS) by transforming to that frame and then look at the residual CMB temperature dipole in that frame. The temperature dipole has been calculated as the difference between the temperature distribution induced by the sun's motion with respect to the CMB, 371.0 km s^{-1} towards $(\ell, b) = (264.14^\circ \pm 0.15^\circ, 48.26^\circ \pm 0.15^\circ)$ (Fixsen et al., 1996), and the motion of the sun with respect to the LG, 318.6 ± 20.0 km s^{-1} towards $(\ell, b) = (106^\circ \pm 4^\circ, -6^\circ \pm 4^\circ)$ (Tully et al., 2008), using equation (5.1). We use the monopole temperature $T_{CMB} = 2.728$ K, from Fixsen et al. (1996). The velocity is relative to the LG or the LS frame, as appropriate.

Figure 5.27(a) shows the residual temperature dipole in the CMB in the LG reference frame. The poles have amplitudes of ± 5.77 mK in the LG frame and ± 5.73 mK in the LS frame. They are located at $(\ell, b) = \{(97.0, -29.3), (277.0, 29.3)\}$ in the LG frame and $(\ell, b) = \{(90.0, -26.6), (270.0, 26.6)\}$ in the LS frame. There is a 6.3% uncertainty in the dipole amplitudes arising from the uncertainty in the

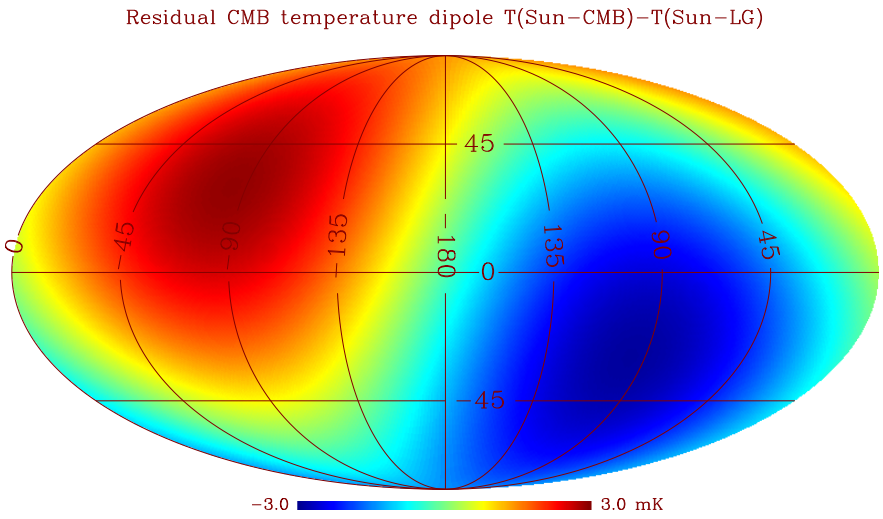

(a)

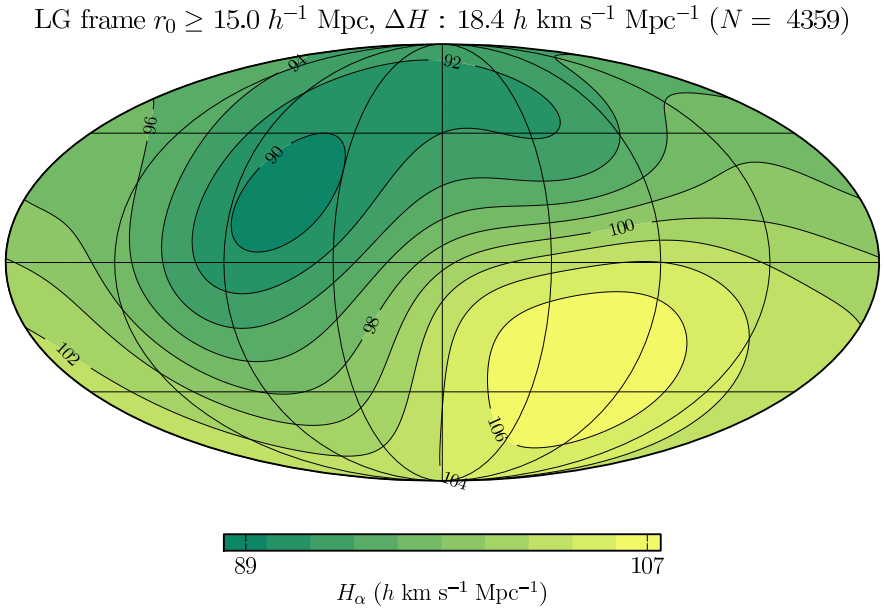

(b)

Figure 5.27: The temperature dipole in the CMB (corrected for the heliocentric motion in the LG frame) (a), and the Hubble expansion dipole in the Local Group frame (b), showing their similarity.

heliocentric velocities in each frame. Since we are here only interested in alignments, this will not concern us further. There is a strong resemblance between these two sky maps, despite their independent origins. The simplest explanation is that we are observing the same LG velocity dipole seen by Jha et al. (2007) and Gordon et al. (2008).

In Figure 5.23 are plotted blue crosses at the positions of the extrema of the CMB temperature dipole. Also plotted in this figure are red crosses indicating the location of the Hubble anisotropy extrema and their 1σ contours. The CMB temperature extrema lie within 2σ of the Hubble expansion extrema. We can further quantify the degree to which these features are correlated by calculating the Pearson correlation coefficient

$$\rho_{HT} = \frac{\sqrt{N_p}\sum_\alpha \bar{\sigma}_\alpha^{-2}(H_\alpha - \bar{H})(T_\alpha - \bar{T})}{\sqrt{\sum_\alpha \bar{\sigma}_\alpha^{-2}\sum_\alpha \bar{\sigma}_\alpha^{-2}(H_\alpha - \bar{H})^2\sum_\alpha (T_\alpha - \bar{T})^2}}\ , \tag{5.25}$$

where $N_p = 49152$ is the number of HEALPIX pixels, the summations go over the whole sky, T_α is the temperature in the pixel with angular coordinates α, $\bar{T}$ is the mean temperature,

$$\bar{H} = \frac{\sum_\alpha^{N_p} \bar{\sigma}_\alpha^{-2} H_\alpha}{\sum_\alpha^{N_p} \bar{\sigma}_\alpha^{-2}}, \tag{5.26}$$

H_α is given by (5.20) and $\bar{\sigma}_\alpha$ by (5.21). Since HEALPIX partitions the celestial sphere into pixels of equal area, and since the CMB temperature dipole is assumed to be ideal, the only weighting in the sum comes from the measurement uncertainties of the Hubble flow.

With $\sigma_\theta = 25°$ we performed a correlation analysis between the Hubble variance dipole and the residual CMB temperature dipole in both the LG and LS frames, as the division radius, r_o, between the inner and outer spheres was varied. In Fig. 5.28 are plotted the correlation coefficients as a function of the distance cuts r_0 between inner and outer spheres, a subset of which is shown in Figures 5.10–5.19. We observe firstly that the correlation coefficient is negative since the maximum value of the Hubble parameter coincides with the minimum residual CMB temperature. The strongest anticorrelation is therefore represented by those values which are closest to -1. The similarity between the LG and LS frames is immediately apparent. The correlation coefficients for the inner volumes reflect

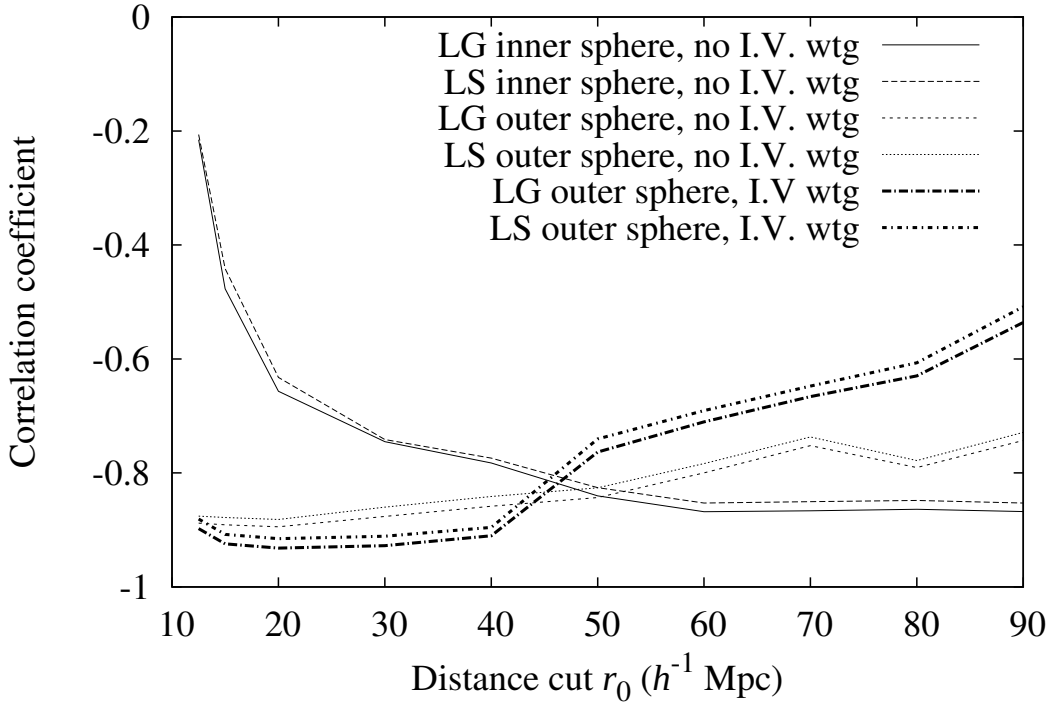

Figure 5.28: Pearson correlation coefficients for the CMB temperature dipole and the Hubble anisotropy. .

Table 5.6. Correlation coefficient between the residual CMB temperature dipole in the LG and LS rest frames, as compared to the Hubble flow variance in the $r > 15\,h^{-1}$ Mpc sphere, for different choices of Gaussian smearing angle σ_θ. Unweighted (u) and IV weighted (w) smearing is considered in each case.

σ_θ	LG u	LG w	LS u	LS w
15°	-0.8909	-0.9056	-0.8695	-0.8750
20°	-0.8945	-0.9197	-0.8774	-0.8965
25°	-0.8905	-0.9240	-0.8782	-0.9077
30°	-0.8847	-0.9237	-0.8769	-0.9133
40°	-0.8752	-0.9187	-0.8739	-0.9160

the fact that their dipoles are initially weak, but become stronger as the distance cut increases and the sample number grows. We do not show the correlation coefficients for the weighted inner volumes since we have seen that the inverse variance weighting enhances the shot noise in these volumes.

In all cases the result for the LS frame does not differ greatly from that of the LG frame. However, the anticorrelation is generally a bit stronger in the LG frame. The anticorrelation is stronger for the IV weighted sky maps in both frames. The anticorrelation is strongest in the outer sphere for $r_o = 15\,h^{-1}$ Mpc. As might be expected from Section 5.4.2, the anticorrelation remains strong in the outer sky maps for values of r_o up to $40\,h^{-1}$ Mpc. By contrast, the anticorrelation in the inner sphere is not at all strong for $r \leq r_o$ with small values of r_o. However, the anticorrelation in the inner sphere improves dramatically as r_o is increased, and by the stage that we reach $r_o = 50\,h^{-1}$ Mpc the anticorrelation is comparable in both spheres for the unweighted case, and stronger in the inner sphere than in the outer sphere for the IV weighted case. There is no further improvement in the anticorrelation in the inner sphere for $r_o > 60\,h^{-1}$ Mpc, which is again consistent with the earlier indications that the structures responsible for the Hubble variance dipole are within $60\,h^{-1}$ Mpc.

One final question is the extent to which the correlation depends on the Gaussian smearing width, σ_θ. We have therefore recomputed the correlation coefficient

for a range of values of σ_θ for the $r > 15\,h^{-1}$ Mpc map, the case which shows the strongest anticorrelation. The results are shown in Table 5.6. We find that the anticorrelation in the IV weighted map is stronger than the unweighted map for different choices of σ_θ. Moreover, as well as the correlation coefficient in the LS frame being slightly weaker, it also varies a little more with smearing angle. In the LG frame the correlation coefficient varies the least for varying σ_θ in the IV weighted case. Indeed to two significant figures the correlation coefficient of -0.92 is unchanged for $\sigma_\theta = 25^\circ \pm 5^\circ$.

A correlation coefficient of -0.92 between the residual CMB temperature sky map and the LG frame Hubble variance sky map for $r > 15\,h^{-1}$ Mpc strongly suggests that the dipole features of the two maps are related. From Figure 5.23 we see that in the IV weighted sky map the cooler residual CMB temperature pole (marked by a cross) lies just 7.4° from the maximum of the Hubble flow variance, well within the 1σ contour. The hotter residual CMB temperature pole is separated by 22° from the minimum of the Hubble flow variance, however, and lies 10° outside the 1σ contour but is within 3σ. It remains to be seen whether the uncertainty estimates in this case are significantly affected by the choice of weighting scheme. In particular, the left hand panel of Figure 1 of FWH10 shows that with a maximum likelihood estimate based on traditional IV weightings there are a substantial number of very strongly weighted data points in the COMPOSITE sample in the region which coincides with that of minimum $\bar{\sigma}_\alpha$ to the north of residual CMB temperature pole in Figure 5.23(b). With the alternative minimum variance weightings shown in the right hand panel of Fig. 5.7(b) the same data points are not strongly weighted.

5.5 Discussion

The origin of the CMB dipole

A dipole in the LG-frame Hubble expansion field is expected given the results described in the introduction of Jha et al. (2007) and Gordon et al. (2008). Our results extend and corroborate these results, but it is the dipole in the *Hubble expansion field* in our data that converges to the CMB dipole, as distinct from

the peculiar velocity dipole. The correlation coefficient of -0.92 is evidence for a convergence of the Hubble expansion field to the CMB dipole at the depths probed by the data.

Although the dipole motion has been found to be generated substantially at scales $\lesssim 60\,h^{-1}$ Mpc (e.g Courtois et al., 2011; Tonry et al., 2003; Tully et al., 2008), finding convergence on larger scales has proved challenging, as shown by the WFH09 result from the COMPOSITE sample and also by Lavaux et al. (2010). We have shown that there is significant variation in the Hubble flow on these scales, based only on the assumption of an average linear Hubble law, and that the pattern of this variation is closely aligned to the CMB dipole. Although further work is required to show conclusively that this is in fact the long sought-after convergence, we here suggest a possible contributing mechanism for the production of the Hubble variance that is independent of the assumptions inherent in the peculiar velocity interpretation. A recurring theme in this thesis has been what is one of the basic postulates of relativistic cosmology: that expansion rates increasingly differentiated by the evolution of structure will produce a small variation in the distance-redshift relation that increases with time. We suggest[1] that the component of the CMB dipole that is usually attributed to a peculiar motion of the LG is instead a consequence of a small anisotropy in the average redshift-distance relation on scales up to $65\,h^{-1}$ Mpc. In what follows, we will not attempt a model-independent theoretical estimate of this effect, but we will derive an order-of-magnitude estimate of the Hubble expansion variation required to produce the observed residual temperature dipole.

The Universe was homogeneous at the epoch of last scattering, with a temperature very close to uniform. In contrast, the Universe of the present epoch is inhomogeneous. If the inhomogeneities are sufficiently evolved, the distance to the surface of last scattering will be slightly different in different directions because the regional expansion rates vary with the density field, and increasingly as the inhomogeneities evolve.

Assuming the expansion of the Universe is governed by some average scale factor, we can give an order of magnitude estimate of the variation of the distance to the last scattering surface and compare it with the observed residual temperature

[1] I am indebted to my supervisor, David Wiltshire, for this idea

dipole. This assumption accommodates both the exact FLRW models and the timescape scenario in which an average scale factor describes a Buchert average over an ensemble of void and wall regions.

The scale factor, which by (1.22) is related to the observed cosmological redshift $1 + z = a_0/a$ is inversely proportional to the mean CMB temperature: $T \propto 1/a$. A fractional change δz in the redshift of the last scattering surface, brought about by the differential evolution of structures in the foreground, will induce a corresponding CMB temperature increment $T = T_0 + \delta T$, where, as before, $T_0 = 2.728$ K is the mean temperature at the present epoch,

$$\frac{\delta T}{T_0} = \frac{-\delta z}{1 + z_{\rm dec}}, \tag{5.27}$$

and $z_{\rm dec} = 1089$ is the redshift of the photon decoupling. In the LG frame, the temperature increment $\delta T = \pm(5.77 \pm 0.36)$ mK corresponds to a redshift increment $\delta z = \mp(2.31 \pm 0.14)$.

In the spatially flat ΛCDM model the comoving distance to the surface of last scattering is given by

$$D = \frac{c}{H_0} \int_1^{1+z_{\rm dec}} \frac{{\rm d}x}{\sqrt{\Omega_{\Lambda 0} + \Omega_{\rm m0} x^3 + \Omega_{\rm R0} x^4}} \tag{5.28}$$

in the spatially flat ΛCDM model[1], where $\Omega_{\Lambda 0} = 1 - \Omega_{\rm m0} - \Omega_{\rm R0}$, $\Omega_{\rm R0} = 4.15 h^{-2} \times 10^{-5}$ and a numerical estimate can be made by putting $\Omega_{\rm m0} = 0.25$. Assuming that the anisotropy is generated by foregrounds near $z = 0$ we find that the residual dipole in the CMB temperature can be generated by a comoving distance increment of $\delta D = \mp(0.33 \pm 0.02)\, h^{-1}$ Mpc. According to the results of the foregoing sections, this difference is due to structures within $65\, h^{-1}$ Mpc, so we can expect a variation of the order of 0.5% in the distance-redshift relation within this scale. This variation is small enough to be plausible even if it is all induced by structures within $30\, h^{-1}$ Mpc, producing a ∼1% variation, given the Hubble anisotropy observed in the COMPOSITE sample.

[1]Numbers of a similar order will hold for the timescape model, but the exact computation is not done here since the redshift of last scattering is beyond $z \sim 37$, where the exact tracker solution that we have been using for the distance-redshift relationship in the low-z Universe begins to deviate from the numerical results. Work is in progress to include the radiation density in these computations (James Duley MSc., *in process*).

We have a general picture therefore of a ∼1% variation in the distance-redshift relation brought about by the differential expansion of void and wall regions at late times on 30–60 h^{-1} Mpc average distance scales. All observers will see some sort of anisotropy in the distance-redshift relation, though the nature and amplitude of it will vary with position. In the case of Milky Way observers, within this distance there is a strong density gradient between the Local Void complex on one side of the sky, and the overdensities on the other. Correspondingly, there is an increment in the CMB temperature in the direction of the smaller-than-average distance, and decrement in the CMB temperature due to larger-than-average distances in the direction of the clusters.

The $\sim \pm 10\%$ variation we saw in § 5.4.2 is much greater than the variation in the distance-redshift relation we have estimated here. However, note that the analysis of § 5.4.2 assumed a single radial linear Hubble law over the whole sample. The same data producing angular variation in the Hubble flow produces radial variation as well, and the $\pm 10\%$ variation includes distortions due to this underlying radial variance in the sample range.

If a substantial fraction of the CMB dipole is due to the influence on the passage of light of foreground inhomogeneities, why is the CMB dipole so perfect? The fact that the amplitude of the CMB dipole is roughly two orders of magnitude larger than the higher multipoles is usually taken as evidence of its origin from a peculiar velocity. Even considering the problem of realistic galactic foreground removal in the CMB temperature maps, in the higher frequency bands the galactic foreground occupies a sufficiently narrow band along the galactic equator to allow clear resolution of the dipole (Tegmark et al., 2003). We also have the evidence of the data: there is a strong dipole in the variance of the Hubble flow, and it is strongly aligned with the CMB temperature dipole.

Further investigation of the variation of the distance-redshift relation requires a greater number of more precise observations on the empirical side and ray-tracing through suitably averaged foreground density fields on the theoretical side. A study of ray tracing of the CMB sky as seen by an off-centre observer through a large Lemaître-Tolman-Bondi void has shown that it is possible for foregrounds to generate a CMB dipole without simultaneously generating significant higher-order multipoles (Alnes and Amarzguioui, 2006): The quadrupole and octupole

coefficients a_{20} and a_{30} were very small compared to the the dipole coefficient a_{10}. For example, a Newtonian approximation numerically close to the ray-traced result yields

$$\frac{a_{20}}{a_{10}} = \sqrt{\frac{15}{4}}\frac{(h_{\rm in} - h_{\rm out})d_{\rm off}}{2998\ {\rm Mpc}} \tag{5.29}$$

where $H_{\rm in\,0} = 100\,h_{\rm in}$ km s^{-1} Mpc^{-1} and $H_{\rm out\,0} = 100\,h_{\rm out}$ km s^{-1} Mpc^{-1} are the Hubble constants inside and outside the void, and $d_{\rm off}$ is the distance of the observer from the centre in Mpc. Even for the relatively large values $d_{\rm off} = 50\,h^{-1}$ Mpc and $h_{\rm in} - h_{\rm out} = 0.2$, we would still have a ratio of a_{20}/a_{10} of order 1%.

Since all light that we receive must travel to us through the highly differentiated structure within $60\,h^{-1}$ Mpc—structure which we have observed to produce a temperature dipole—we expect small residual corrections to be made to the distance-redshift relation, even on large scales. The strong correlation between the Hubble variance dipole and the residual CMB temperature dipole suggest that this mechanism is a major component of the CMB dipole, along with a local boost. With this interpretation, we can expect that on scales $\gg 100\,h^{-1}$ Mpc the typical distance for a given redshift will be subject to some variation from the average of up to $0.35\,h^{-1}$ Mpc. This result will have important implications for cosmology.

5.5.1 Future work

The central results of our work on the variance of the Hubble flow have been presented. We have come across several issues in the course of this analysis that were beyond the scope of a preliminary exposition and which demand further study.

From bulk flows to Hubble variance

There are statistical issues that need to be fleshed out. Firstly, if we would like to estimate the convergence of the LG-frame dipole then we will need to perform a more sophisticated error analysis. For example, although clustering has been accounted for in the compilation of the COMPOSITE sample, it remains the case that each galaxy or supernova measurement does not represent a completely

independent realization of the velocity field, so one issue will be accounting for correlations between velocities in the manner of the analysis of Gordon et al. (2007, 2008). The extent to which these correlations are already accounted for in the angular smearing we have used needs further investigation. However, because our analysis of the expansion dipole only focuses on larger angular scales, we do not expect that this should greatly affect the strength of the general conclusions so far.

Secondly, the most appropriate weighting scheme is probably not the inverse variance one used here, for the reasons elaborated in the discussion of Fig. 5.7(a) above. The Minimum Variance weighting scheme developed in Watkins et al. (2009) and Feldman et al. (2010) is couched in terms of peculiar velocities but it is conceivable that an analogous method could be developed for Hubble ratios.

These considerations suggest the need for a dedicated method for computing a multipole expansion of the Hubble expansion field. The radial variation in the averaged Hubble law will have to be factored out before the additional angular variation can be correctly determined. Following MD07, we have not attempted this in the present study, but it will be contributing to the angular variance that we have observed. One might accomplish this by defining an average comoving distance D to a particular redshift z within the redshift of statistical homogeneity $z_{\rm hom}$

$$D = c \int_0^z \frac{\mathrm{d}z_s}{H_s(z_s)}, \tag{5.30}$$

where $H_s(z_s)$ is calculated with equation (5.4) in the same way as it was in the radial shells above, except that here the shells are defined by the redshift ranges $z_s < z \leq z_s + \sigma_z$ for shell thickness σ_z. The thickness of the shell $c\sigma_z/H_0$ must be sufficient to include the largest bound structures, since the regression can only be calculated on scales over which space is expanding and a Hubble law is defined. In Section 5.3, mainly for this reason, we chose a shell width $12.5\,h^{-1}$ Mpc, which corresponds to $c\sigma_z = 1250\,\mathrm{km\ s^{-1}}$, or $\sigma_z = 0.0042$.

One can then subtract the spherically averaged Hubble expansion from the the angular Hubble variation determined over the shell volume. The difference $H(z_s, \theta, \phi) - H(z_s)$ will lead to corrections to the mean comoving distance (5.30).

Equation (5.30) defines a monopole about which the corrections can then be expanded in terms of spherical harmonics. We can claim convergence of the Hubble flow variance if the dipole anisotropy reduces to a fixed value at some redshift $z > z_{\rm conv}$, where our cursory investigation suggests a convergence redshift $z_{\rm conv} \simeq 0.02$. A residual anisotropy of order $\pm 0.35\,h^{-1}$ Mpc in $D(z)$ would account for the residual CMB temperature dipole, with the exact anisotropy depending on the cosmological model.

One intriguing question is whether an echo of the baryon acoustic oscillation (BAO) scale could show up in a future survey on $\lesssim 150\,h^{-1}$ Mpc scales if the sample statistics were greatly improved. In Figure 5.4 there are some hints of a deviation from uniformity in shells around $r \simeq 100\,h^{-1}$ Mpc. However, the effect is less than 2σ in the LG frame. Since the BAO is a statistical phenomenon, there is also a question of how it might manifest itself in Hubble flow variance in our nearby volume. If the BAO enhances wall to wall correlations, then we would have to account for the fact that our location is on the edge of a wall and not in a wall centre. Although the distance-redshift relation offset calculated here is only $0.35\,h^{-1}$ Mpc — much smaller than the $\sim 20\,h^{-1}$ Mpc FWHM of the baryon acoustic peak — this could produce a broadening of the BAO feature between $r_{\rm bao} \pm r_{\rm off}$, where $r_{\rm bao}$ is the effective comoving BAO scale and $r_{\rm off}$ is the distance by which we are offset from the centre of the Local Wall. Although this is small, high resolution (ΛCDM) reconstructions of the BAO feature have been incorporated to enhance measurement precision in the distance to redshifts less than 0.5 to less than 1% (e.g. Seo et al., 2010), so such a broadening is discernible in principle.

A further question which might be resolved by future surveys is the splitting between what in the standard cosmology are known as the linear and nonlinear regimes. In particular, the BAO enhancement is assumed to be in the linear regime of perturbation theory about a FLRW model in the standard model. If we were to find convergence of Hubble flow variance by $z_{\rm conv} \simeq 0.021$, apart from very small deviations at $r_{\rm bao} \pm r_{\rm off}$, then it would be consistent with the notion that scales $z \lesssim z_{\rm conv}$ are in the "nonlinear regime" while the BAO scale is in the "linear regime"[1].

[1]We note that such an interpretation just relies on there existing a scale of statistical

The rest frame of minimum Hubble variance

The multipole expansion proposed above should properly be performed in the rest frame in which the radial variance in the Hubble flow relative to the global average flow beyond the scale of statistical homogeneity is minimized. We have seen that this frame is closer to the Local Group frame than the CMB frame. Within the uncertainties, the radial variance of the Hubble expansion in the Local Sheet frame is equally uniform. However, this frame may still be different to that of minimum Hubble variance. What is the best way to determine the minimum Hubble variance frame? The simplest way would be to minimize the sum of the H_s in each shell, since the estmated effective perturbation to H_s, δH, from eq. (5.12) above is expected to go to zero in the limit of large r.

The possibility that the Local Group has some other peculiar velocity with respect to the minimum Hubble variance frame should be considered. Another question is whether the frame with the greatest anticorrelation between the residual CMB temperature dipole and the Hubble flow variance dipole coincides with the minimum Hubble variance frame to within the uncertainties.

Relation between Hubble variance and structure

Armed with a multipole expansion of the Hubble expansion field and larger numbers of data points from future surveys, we hope future investigations will pin down the relation between the Hubble variance and the distribution of large-scale structures in detail. A more thorough analysis than the preliminary one presented here could be undertaken by varying the smearing angle according to an assessment of the attendant error variation, and comparing this with the known distribution of matter.

Type Ia supernova systematics

Systematic uncertainties in SN Ia observations were discussed extensively in Chapter 3. Suffice it to say here that supernova cosmology has reached a point where systematic uncertainties are the main factor limiting better precision. This

homogeneity above which an average cosmological evolution can be described. It is not necessary for the average evolution to be described exactly by a homogeneous isotropic FLRW model.

means that the result from Section 5.3 that the radial Hubble flow variance is not minimized in the CMB frame has some interesting consequences for the light-curve reduction methods discussed in Chapter 3.

Both the MLCS2k2 and SALT/SALT-II fitters involve minimizing the distance modulus residuals with a nearby global linear Hubble law, and this is done in the CMB frame. If the Hubble variance in the LG frame is more uniform, then the Hubble variance in the CMB frame must be contributing systematic effects to the calibration of the SN Ia light curves. The Union, Union2 and Constitution samples all contain a significant number of data points in the range $0.015 \lesssim z \lesssim 0.02$, which, although conventionally deemed to be "within the Hubble flow", is below the scale $z_{\rm conv}$ estimated above[1].

It is interesting that the redshift range $0.012 \lesssim z \lesssim 0.02$ corresponds to the range $35 \lesssim r \lesssim 60\,h^{-1}$ Mpc over which the LG frame Hubble variance was found to be further from uniform than that in the CMB frame, despite it being closer to uniform overall. It may be that the boost to the CMB frame actually best compensates for structures within this range, but that this has also led to a misidentification of the minimum redshift $z_{\rm conv}$ at which a single global linear Hubble law can be safely assumed.

The data in Figs. 5.5 and 5.4 and in Table 5.2 indicate that convergence to a uniform Hubble flow has occurred by $r \equiv 68.75\,h^{-1}$ Mpc or $z_{\rm conv}$. This scale coincides roughly with the redshift scale of the Hubble bubble cutoff first observed in the supernova data by Zehavi et al. (1998) and confirmed by Jha et al. (2007)—$z = 0.024$. The best fit value of H_0 was found to be $6.5 \pm 2.2\%$ larger within this redshift range. Here we have observed a Hubble bubble within a similar redshift range from a large sample of distances of which only a small fraction are derived from SNe Ia. We can compare our results directly with a similar analysis from the COMPOSITE sample, by fitting a linear Hubble law to the 2222 data points in the interval $30 \lesssim r \lesssim 70\,h^{-1}$ Mpc. In the CMB frame, we find $H_0 = (104.5 \pm 0.6)$ $h$km s^{-1} Mpc^{-1}, and $H_0 = (105.1 \pm 0.6)$ $h$km s^{-1}

[1]By contrast, the full Nearby+SDSS+SNLS+ESSENCE+HST MLCS2k2 sample (Kessler et al., 2009) exclude SNe Ia from below $z = 0.0218$, as discussed in Section 3.4.2. There are differences in the cosmological parameters estimated from this sample and the three SALT samples listed here.

Mpc^{-1} in the LG frame. These values are $4.40 \pm 0.08\%$ and $4.06 \pm 0.07\%$ larger respectively than the global asymptotic values of H_0 determined in Section 5.3.1. This is somewhat lower, but still consistent with the value from the MLCS2k2 samples, but Zehavi et al. (1998) and Jha et al. (2007) worked with a very simple single cut, dividing the Hubble flow variance into inner and outer spheres.

The $30 \lesssim r \lesssim 70\,h^{-1}$ Mpc range chosen by Zehavi et al. (1998) is equally divided between regions in which we find the LG frame Hubble variance to be closer to uniform and in which the CMB frame is closer to uniform. An alternative estimate of the Hubble bubble effect can be obtained by comparing the fit of a single linear Hubble law to the whole COMPOSITE sample and the global asymptotic values. From fits to the whole sample, $H_0 = (108.9 \pm 1.5)$ $h$km s^{-1} Mpc^{-1}, in the CMB frame, and $H_0 = (104.4 \pm 1.4)$ $h$km s^{-1} Mpc^{-1} in the LG frame, amounting to differences of $8.8 \pm 0.2\%$ and $3.37 \pm 0.07\%$ respectively. In each frame, the larger Hubble variance nearby affects H_0 values obtained from the whole sample, and more so in the CMB frame.

As discussed in Section 3.4.2, the presence of a Hubble bubble in the data has a mysterious connection to the treatment of extinction and reddening by dust by the different light-curve fitters (Conley et al., 2007). The two MLCS2k2 supernova samples mentioned above used a reddening parameter $R_V = 3.1$. Hicken et al. (2009) find no evidence of a similar Hubble bubble in the SALT-reduced data if $R_V = 1.7$. Our results suggest that a combination of the boost to the CMB frame compensating for structures in the range $35 \lesssim r \lesssim 60\,h^{-1}$ Mpc and the treatment of parameters such as R_V as adjustable in the light curve reduction, my be significant contributors to the systematic uncertainties associated with SNe Ia. Ideally, rather than reaching erroneous conclusions about the nature of dust in other galaxies from minimizing Hubble residuals in supernova calibrations, reddening by dust should be measured independently of the SNe Ia and then incorporated into the calibrations. Efforts are currently underway to determine the reddening laws in other galaxies (Finkelman et al., 2008, 2010). For the combined sample of dust lanes in 15 E/S0 galaxies (see the discussion in Section 3.6.1.1), one obtains $R_V = 2.77 \pm 0.41$. Our results could be taken so far as to suggest that for consistency the MLCS2k2 supernovae should be calibrated with this independent reddening parameter.

The bulk flow analysis of Turnbull et al. (2011) includes a comparison of results for 162 SNe Ia computed with different values of the reddening law parameter: $R_V = 1.7$ and $R_V = 3.1$. The bulk flow results are consistent with each other to within the uncertainties, but differ considerably considering they are not independent. They note that this is a reflection of the large systematic errors for bulk flow surveys. It would therefore be interesting to know the extent to which the bulk flow of WFH09 depends on the choice of R_V for the 103 SNe Ia in the COMPOSITE sample.

The global Hubble constant

We can determine the relative Hubble flow from the COMPOSITE sample, but this sample does not well constrain the overall normalization of the distance scale and, consequently, the global asymptotic Hubble constant.

The high-precision estimate of the global Hubble constant $H_0 = 73.8 \pm 2.4$km s^{-1} Mpc^{-1} from the SH0ES survey (Riess et al., 2011) should be compared with other high-precision estimates from the baryon acoustic oscillation scale at different redshifts: $H_0 = 68.2 \pm 2.2$km s^{-1} Mpc^{-1} (Percival et al., 2010); $H_0 = 67.0 \pm 3.2$km s^{-1} Mpc^{-1} (Beutler et al., 2011); $H_0 = 68.1 \pm 1.7$km s^{-1} Mpc^{-1} (Blake et al., 2011). These results are all consistent at the 2σ level but a further increase in precision could lead to tension. A major difference between the estimates is that the SH0ES value relies on establishing a cosmic distance ladder from such standard candles as Cepheid variables on very nearby scales. The BAO estimates are more model-dependent, relying on fits to the FLRW model at larger redshifts $0.1 \lesssim z \lesssim 0.6$.

If the cosmic rest frame is identified with the frame of minimum Hubble flow variance, then the impact of performing cosmological tests in this frame rather than the CMB frame needs to be carefully considered. Tests using direct measurements on $z \lesssim 0.023$ scales will be most significantly affected. Whether or not this has an impact on measurements that establish the cosmic distance ladder is a question that should be investigated once the minimum Hubble variance frame is positively identified.

Large-angle CMB anomalies

Several observations concerning the large-angle multipoles of the CMB anisotropy power spectrum my be considered anomalous, with varying degrees of statistical significance. These include: (i) the power asymmetry between the northern and southern galactic hemispheres (Tegmark et al., 2003); (ii) the low power of the quadrupole (de Oliveira-Costa et al., 2004; Tegmark et al., 2003); the alignment of the quadrupole and octupole (Copi et al., 2006; de Oliveira-Costa et al., 2004; Land and Magueijo, 2005; Schwarz et al., 2004); and the parity asymmetry (Kim and Naselsky, 2010). It is beyond the scope of this thesis to investigate all these anomalies and they are here mentioned only for completeness. However, it is clear that our proposal to revisit the CMB dipole analysis will introduce systematics which will require a reassessment of all these issues.

In particular, two lines of enquiry suggest themselves:

- The propagation of photons through the foreground contributing to the Hubble expansion variance may produce a multipole signature that differs subtly from the pure dipole due to a Lorentz boost;
- Since the dipole subtraction is an integral part of the CMB map-making procedure, differences in dipole subtraction may lead to subtle differences in the cleaning of galactic foregrounds (Tegmark et al., 2003).

Freeman et al. (2006) found that of several possible systematic errors, a 1–2% error in the CMB dipole subtraction could potentially be result in the observed power asymmetry anomalies.

While a 1–2% change in the dipole would not affect the power on very small scales, its effect on the large angle multipoles would require a redrawing of the CMB sky maps, and may thereby alter other large angle features, such as the CMB Cold Spot.

The dark flow

As a method of determining peculiar velocities, the method of Kashlinsky et al. (2008, 2009) is particularly interesting because it uses the decrements in the CMB temperature due to the kinetic Sunyaev-Zel'dovich effect rather than directly

looking at the distance redshift relation. Moreover, the large bulk flow from these observations seems to be at odds with other bulk flow measurements, such as the recent result of Turnbull et al. (2011). However, another bulk flow determination by the same method, but using different filtering of the WMAP band maps, finds no such anomalous flow, but suggests that there is a thermal SZ effect which could be mistakenly measured as a large-amplitude bulk motion (Osborne et al., 2011).

Further kSZ measurements from the Atacama Cosmology and South Pole Telescopes will provide increasingly accurate estimations of peculiar velocities. Although we have not gone through all the details of the work of either Kashlinsky et al. (2008, 2009) or Osborne et al. (2011), we note that the determination of the kinetic and thermal SZ effects involves a determination of the temperature of the thermal plasma in the galaxy cluster. This is achieved iteratively using empirical relations along with the cluster redshift. The total rest frame [0.1–2.4] keV band cluster luminosities are then determined from the recalculated fluxes using a standard conversion with the cosmological luminosity distance and a temperature-dependent K-correction (Kashlinsky et al., 2009). All these will have been performed using a perfectly isotropic distance-redshift relation. If, as we suggest, the distance-redshift relation has some small anisotropy, then this will introduce systematics into the above procedure.

5.5.2 Hubble Variation: Conclusions

This concludes our investigation of the radial and angular variation of the Hubble ratio from the COMPOSITE peculiar velocity sample. From the radial variation found from averaging over spherical shells we found that the Hubble expansion is more uniform in the reference frame of the Local Group than it is in the reference frame of the CMB. A Bayes factor analysis revealed that the boost to the CMB frame works slightly better, in terms of the extent to which it results in a uniform Hubble flow, within the range $35 \lesssim r \lesssim 60\,h^{-1}$ Mpc. We suggest that this is because the boost to the CMB frame is compensating for the effect of foreground structures on these scales.

In Section 5.4 we investigated the angular variation of the Hubble expansion using a smoothed average of the COMPOSITE Hubble ratios over the sky. To ensure adequate statistical properties in the sample we considered only objects beyond $15\,h^{-1}$ Mpc. We find a strong dipole in the angular Hubble variance. It is strongly correlated (with a coefficient of -0.92) with the temperature dipole in the cosmic microwave background. Moreover, we observe that the dipole is substantially generated by objects within $65\,h^{-1}$ Mpc, adding credence to the suggestion from § 5.3.1 that the transformation to the CMB reference frame corrects for the effect of structures on these scales, where the dominant Hubble anisotropy is a dipole.

Our work suggests that a fundamental revision of the treatment of peculiar velocities can shed new light on some of the puzzles raised by bulk flows. If, as our results suggest, a substantial fraction of the CMB dipole is due to a residual anisotropy in the distance-redshift relation, then this will have important consequences for understanding the large-angle features in the CMB anisotropy spectrum.

We do not wish to understate the importance of peculiar velocities in cosmology —galaxies in clusters exhibit peculiar velocities with respect to the cluster barycentres which are directly observed in the "fingers of god" redshift space distortions. However, the natural conclusion of the work in this chapter in that on scales larger than gravitationally bound systems the variance of the Hubble flow should be treated as the differential expansion of regions of varying density, which have decelerated by different amounts from the initial uniform expansion at the epoch of last scattering. While directional forces are the basis of Newtonian mechanics in Euclidean space, and may apply on small scales within gravitationally bound systems, there is nothing in general relativity which demands that such notions should also apply to the scale of tens of megaparsecs over which space is expanding.

There has been some discussion in recent years about whether it is correct to treat the expansion of space as a Doppler law on a fixed background (Abramowicz et al., 2007; Bunn and Hogg, 2009; Francis et al., 2007). This debate has been limited to discussions of thought experiments about how one might in principle distinguish the two circumstances observationally, mainly from the viewpoint of

a homogeneous isotropic expansion. The results of this chapter suggest that as far as observations are concerned, variance in the Hubble law over scales of tens of megaparsecs cannot simply be reduced to a boost at a point; space really is expanding, and by differential amounts.

Chapter 6

Conclusions

The world is everything that is the case
– Wittgenstein, *Tractatus Logico-Philosophicus*

The subject of this thesis has been the issue of accounting for inhomogeneities in the interpretation of cosmological observations. In the introduction we began by introducing the standard cosmological model, which has been very successful in describing the Universe. This success has come at the price of the introduction of an enigmatic "dark energy", which is responsible for the accelerated expansion of the Universe observed in the type Ia supernova distances. In the second chapter we introduced the timescape model, which aims at incorporating the inhomogeneous matter distribution *ab initio*. This model provides a physical reinterpretation of the averaging scheme of Buchert (2000) which attributes the apparent cosmic acceleration to the differences in estimates of an overall average smooth geometry made by different observers. The clocks and rulers of the different observers acquire cumulative differences as their local regional expansion histories change with the growth of structure. The work in this thesis has centred around applying these considerations in the interpretation of cosmological observations.

We began with a detailed analysis of the systematic uncertainties that currently limit the precision of type Ia supernova observations. These are of great interest in observational cosmology because SNe Ia are bright enough to be seen over cosmological distances, and their physics is sufficiently well understood for

them to be accurate standard candles within the redshift range over which structure began to "go non-linear" (or, in terms of the ΛCDM model, over which the Universe went from matter-dominated decelerating expansion to dark energy-dominated accelerating expansion). The results of Leith et al. (2007) found a concordance of physically reasonable cosmological parameters for the timescape model using SNe Ia, the angular diameter of the sound horizon at last scattering, and the scale of baryon acoustic oscillations. A study by Kwan et al. (2009) applied the timescape model to some newer supernova samples, and found unreasonably low best-fit values for the matter density, concluding that newer, better data was ruling out the timescape scenario—a conclusion which we found to be flawed.

Our analysis found that the results of the fits for the timescape model depend strongly on the method used to translate the supernova light curves into distances. We looked in detail at two currently widely used such methods: MLCS2k2 (Jha et al., 2007) and SALT (Guy et al., 2005) (these methods are constantly evolving). We concluded that rather than being ruled out by the new data, the fit results for the timescape model were being compromised by the inclusion in the SALT samples of SNe Ia within the scale of statistical homogeneity. Since the timescape scenario is based on an spatial averaging scheme, such a scale is expected, and below it variance is too great to conclude anything about global parameter values. We showed that exclusion of SNe Ia from within this scale led to more physically reasonable parameter values. We also found that

- even though the SALT method incorporates a process in which the ΛCDM model is invoked to determine intrinsic errors such that they make the χ^2 equal to one, it is only very weakly dependent on the input cosmology;
- selection cuts and assumptions about systematic uncertainties were much more important in contributing to the TS results, especially the assumptions regarding the putative Hubble bubble and reddening/extinction due to dust;
- the timescape model works best with MLCS2k2-reduced supernova samples, because they usually assume 1) a Hubble bubble, 2) a host galaxy reddening law parameterized by best-fit the Milky Way value $R_V = 3.1$;

- this is due to the degeneracy between treatment of reddening and the presence of a Hubble bubble (Conley et al., 2007)—the SALT data we used assumed (a very low) $R_V = 1.7$ (the result of a fit to a low-z subsample of SNe Ia), which reduced the statistical significance of any Hubble bubble to the point where they could be justified in including low-z objects that were excluded from MLCS2k2 samples;

- there is evidence to show that $R_V = 1.7$ is anomalously low, and that other galaxies do in fact obey reddening laws with R_V closer to the Milky Way value.

In summary: provided that reddening and extinction by dust in other galaxies is Milky Way-like, and appropriate selection cuts are made, physically reasonable parameter values could also be found from the supernova data for the timescape model with χ^2 values very close to those for the ΛCDM parameters. In Chapter 5 we found strong evidence for radial variance in the Hubble flow which might naively be interpreted as a Hubble bubble. Since the COMPOSITE data contains only $\sim 5\%$ supernova distances, it shows that independently of the SN Ia systematics there is a Hubble bubble in the expansion field.

Perhaps much like SNe Ia a couple of decades ago, Gamma ray bursts (GRBs) have yet to be established as standard candles, but there has been much work dedicated to making them such. Occurring out to redshifts $z \sim 8$, they offer a unique means of discriminating between cosmological models that may, like the timescape and ΛCDM models, be difficult to distinguish at lower redshifts. A fit of the timescape luminosity distance (2.38) to a Hubble diagram constructed from 69 GRBs from Schaefer (2007) resulted in a best-fit value of the present void fraction $f_{\rm v0} = 0.84^{+0.14}_{-0.21}$, with a reduced χ^2 of 1.04, to be compared with a reduced χ^2 of 1.05 for the ΛCDM fit which gave $\Omega_{M0} = 0.21^{+0.22}_{-0.11}$, which coincided within a standard deviation with the value found by Schaefer (2007). Recent work on the luminosity indicators used to place the GRBs on the Hubble diagram suggests that the satellite gamma ray detector triggering thresholds may be introducing some spurious redshift dependence that invalidates the luminosity relations used here (Shahmoradi and Nemiroff, 2011).

The third section of the thesis was devoted to characterizing the variance in the Hubble rate in the local Universe (within $100\,h^{-1}$ Mpc) using the COMPOSITE sample of 4536 peculiar velocities of Watkins et al. (2009). The Local Group (LG) has some peculiar velocity with respect to the CMB that is observed as a dipole in the CMB temperature. There is a long ($\sim$ 30-year) history of attempts to reconstruct the peculiar velocity of the Local Group using linear Newtonian perturbation theory and find its convergence with the CMB dipole, but this convergence is proving elusive. Furthermore, there have been many detections of a bulk flow on scales greater than $50\,h^{-1}$ Mpc. Apart from the "dark flow", measured from the kSZ effect, these flows show some consistency in direction, but their amplitudes vary considerably.

This lack of agreement suggested a return to first principles, and motivated our investigation of the Hubble expansion variance in the COMPOSITE sample, since this analysis does not make the assumption that local motions are driven by Newtonian gravity. In fact this analysis is model-independent apart from the assumption of the existence of a suitably averaged linear Hubble law.

From an analysis of radial variation in spherically symmetric shells, we discovered that the Local Group rest frame yields a Hubble flow that is closer to uniform than that of the CMB rest frame, with decisive Bayesian evidence. This is an important result, since much observational analysis is done in the CMB frame in the belief that it is also that of the most uniform Hubble flow—in particular, e.g. in calibrations of SN Ia distances. Although the LG frame yields a more uniform Hubble flow overall than the CMB frame, there is a region between approximately 35 and $60\,h^{-1}$ Mpc in which the CMB frame Hubble flow is slightly more uniform.

We then observed significant angular variation in the Hubble expansion after excluding 92 objects within $15\,h^{-1}$ Mpc as contributing shot noise. Consistent with previous supernova peculiar velocity studies (Gordon et al., 2008; Jha et al., 2007), we observed a strong dipole in the LG frame, mostly formed within $60\,h^{-1}$ Mpc. A comparison of this dipole with that in the temperature of the CMB yielded a Pearson correlation cofficient of -0.92. This correlation combined with the observation that the Hubble flow becomes statistically uniform in the LG frame beyond $70\,h^{-1}$ Mpc, strongly suggests we are observing convergence to the

CMB dipole. We conclude that the differential expansion of regions of varying density which have decelerated by different amounts from the initial uniform distribution at the epoch of last scattering manifests itself as a variance in the distance-redshift relation on scales $r \lesssim 70\,h^{-1}$ Mpc.

The Hubble variance analysis has raised many further questions. Specifically, we would like to develop a statistical method involving multipole expansions that characterizes the Hubble variance. Such an analysis will also involve the development of statistical techniques to account for the measurement errors and peculiar velocity correlations. Armed with this new method, and with more data, we can hope to determine a frame of minimum Hubble variance and better elucidate the relation between the Hubble variance and the distribution of structure. More generally, this work can inform studies that, among other things, seek to reduce the systematic uncertainties in supernova cosmology, to address the large-angle multipoles in the CMB anisotropy spectrum, and to determine the cosmic distance ladder. It can also potentially help to explain the disagreements between various bulk flow detections and between the various predictions of the depth of convergence of the clustering dipole with the CMB temperature dipole. This work suggests that when interpreting cosmological observations on large scales, the expansion of space really cannot be approximated as a Doppler shift on a fixed background.

The aim of this thesis has been to investigate the feasibility of applying a cosmological model that accounts for the inhomogeneous cosmological distribution of matter. We have seen that accounting for inhomogeneity requires some spatial averaging methodology, and that the position of the observer within local-scale structure is a crucial contributing factor to the values obtained for cosmological parameters, since all radiation reaching the observer is received having traveled through this foreground.

A more general, implicit, aim of this thesis has been the characterization of the true cosmology from a minimal set of geometrical assumptions. In particular, we wish *not* to impose the constraint that space be flat FLRW. We believe that such assumptions can obscure the relativistic nature of space, potentially complicating the interpretation of observations even to the point of engendering extraneous possibilities to "save the hypothesis". It may be true that without

the Newtonian approximation "all bets are off" (Bob Wald, *remark overheard at conference dinner*), but we have shown, particularly in the last chapter, that significant understanding can still be gained by a straightforward statistical analysis even without the Newtonian-flat space assumptions. In this way, for example, rather than obstructing the determination of some unique true Hubble constant, the Hubble variance can be seen as a clue to establishing a fully relativistic treatment of the universe on local scales as well as large.

Finally: the Universe is, by definition, all that is. It is both homogeneous and inhomogeneous. One could say, in answer to the question posed by Coles and Ellis (1997), that it is both open and closed. It is a question of scale. On small scales, quantum mechanics in particular has taught us that there is more to the world than our intuition has evolved to deal with. After imagining that the Universe and our galaxy constituted the whole Universe only 100 years ago, we are just beginning, with the help of advancing technology, to obtain a working knowledge of just how big the Universe really is. The timescape scenario represents an attempt to account for the effects of gravitational collapse on all scales. It makes the claim that many putative anomalies can potentially be solved by adequately accounting for inhomogeneities. It provides a recipe for averaging that is as simple as possible, and in so doing, shows us just how complicated such an analysis could be, and might necessarily be. In this thesis, we have shown that the timescape scenario cannot yet be ruled out by current observations, and that the treatment of inhomogeneities in cosmology is a fundamental aspect of the science that is still in its infancy. The statistical challenge is considerable.

My work so far in inhomogeneous cosmology reminds me on a daily basis of the words of J.B.S. Haldane:

> ... the Universe is not only queerer than we suppose, but queerer than we can suppose.

Dark energy is queer, but gravitational collapse in an expanding Universe is just as queer.

Appendix A

Appendix A

A.1 Timescape GRB calibration curve equations

The five calibrations in figures 4.4–4.8 are based on the bisector of the two ordinary least squares fits (Isobe et al., 1990). For the ith luminosity indicator, the best-fit line has the form $Y_i = a + bX_i$, where $X_i = \log(\text{indicator}) \pm \log(1+z)$, where the sign of the redshift factor depends on the indicator. The five best-fit lines for the TS model (those for which the HD χ^2 is a minimum), their associated uncertainties, and the corresponding ΛCDM values for a and b, are given below.

1. *Lag time vs. Luminosity*:
   For the timescape model:

$$\log\ L = 52.37 - 1.02 \log\left[\frac{\tau_{\rm lag}(1+z)^{-1}}{0.1\ {\rm s}}\right]; \tag{A.1}$$

$$\begin{aligned}\sigma^2_{\log\ L} = \quad & \sigma_a^2 \quad + \left\{\sigma_b \log\left[\frac{\tau_{\rm lag}(1+z)^{-1}}{0.1\ {\rm s}}\right]\right\}^2 \\ & + \quad \left(\frac{0.4343 b \sigma_{\rm lag}}{\tau_{\rm lag}}\right)^2 + \sigma^2_{\rm lag,sys},\end{aligned} \tag{A.2}$$

   where $\sigma_a = 0.13$, $\sigma_b = 0.09$, and $\sigma^2_{\rm lag,sys} = 0.37$ gives a reduced χ^2 of one. For the ΛCDM calibration, we find $a = 52.30 \pm 0.13$, $b = -1.00 \pm 0.09$ and $\sigma^2_{\rm lag,sys} = 0.36$.

2. *Variability vs. Luminosity*:
   For the timescape model:

$$\log\ L = 52.57 + 1.80 \log\Big[\frac{V(1+z)}{0.02}\Big]; \tag{A.3}$$

$$\begin{aligned}\sigma^2_{\log\ L} = \quad & \sigma_a^2 \quad + \Big\{\sigma_b \log\Big[\frac{V(1+z)}{0.02}\Big]\Big\}^2 \\ & + \quad \Big(\frac{0.4343 b \sigma_V}{V}\Big)^2 + \sigma^2_{V,\mathrm{sys}},\end{aligned} \tag{A.4}$$

   where $\sigma_a = 0.34$, $\sigma_b = 0.20$, and $\sigma^2_{V,\mathrm{sys}} = 0.35$ gives a reduced χ^2 of one. For the ΛCDM calibration, we find $a = 52.50 \pm 0.34$, $b = 1.77 \pm 0.20$ and $\sigma^2_{V,\mathrm{sys}} = 0.35$.

3. E_{peak} *vs. Luminosity*:
   For the timescape model:

$$\log\ L = 52.31 + 1.71 \log\Big[\frac{E_{\mathrm{peak}}(1+z)}{300\ \mathrm{keV}}\Big]; \tag{A.5}$$

$$\begin{aligned}\sigma^2_{\log\ L} = \quad & \sigma_a^2 \quad + \Big\{\sigma_b \log\Big[\frac{E_{\mathrm{peak}}(1+z)}{300\ \mathrm{keV}}\Big]\Big\}^2 \\ & + \quad \Big(\frac{0.4343 b \sigma_{E_{\mathrm{peak}}}}{E_{\mathrm{peak}}}\Big)^2 + \sigma^2_{E_{\mathrm{peak}},\mathrm{sys}},\end{aligned} \tag{A.6}$$

   where $\sigma_a = 0.24$, $\sigma_b = 0.10$, and $\sigma^2_{E_{\mathrm{peak}},\mathrm{sys}} = 0.34$ gives a reduced χ^2 of one. For the ΛCDM calibration, we find $a = 52.24 \pm 0.24$, $b = 1.69 \pm 0.10$ and $\sigma^2_{E_{\mathrm{peak}},\mathrm{sys}} = 0.34$.

4. E_{peak} *vs.* E_γ:
   For the timescape model:

$$\log\ E_\gamma = 50.64 + 1.63 \log\Big[\frac{E_{\mathrm{peak}}(1+z)}{300\ \mathrm{keV}}\Big]; \tag{A.7}$$

$$\begin{aligned}\sigma^2_{\log\ E_\gamma} = \quad & \sigma_a^2 \quad + \Big\{\sigma_b \log\Big[\frac{E_{\mathrm{peak}}(1+z)}{300\ \mathrm{keV}}\Big]\Big\}^2 \\ & + \quad \Big(\frac{0.4343 b \sigma_{E_{\mathrm{peak}}}}{E_{\mathrm{peak}}}\Big)^2 + \sigma^2_{E_\gamma,\mathrm{sys}},\end{aligned} \tag{A.8}$$

where $\sigma_a = 0.28$, $\sigma_b = 0.10$, and $\sigma^2_{E_\gamma,\mathrm{sys}} = 0.17$ gives a reduced χ^2 of one. For the ΛCDM calibration, we find $a = 50.58 \pm 0.28$, $b = 1.62 \pm 0.10$ and $\sigma^2_{E_\gamma,\mathrm{sys}} = 0.15$.

5. *Rise time vs. Luminosity*:
   For the timescape model:

$$\log\ L = 52.61 - 1.25 \log\left[\frac{\tau_{\mathrm{RT}}(1+z)^{-1}}{0.1\ \mathrm{s}}\right]; \tag{A.9}$$

$$\begin{aligned}\sigma^2_{\log\ L} = \quad & \sigma_a^2 \quad + \left\{\sigma_b \log\left[\frac{\tau_{\mathrm{RT}}(1+z)^{-1}}{0.1\ \mathrm{s}}\right]\right\}^2 \\ & + \quad \left(\frac{0.4343 b \sigma_{E_{\mathrm{peak}}}}{E_{\mathrm{peak}}}\right)^2 + \sigma^2_{\tau_{\mathrm{RT}},\mathrm{sys}},\end{aligned} \tag{A.10}$$

   where $\sigma_a = 0.11$, $\sigma_b = 0.11$, and $\sigma^2_{\tau_{\mathrm{RT}},\mathrm{sys}} = 0.48$ gives a reduced χ^2 of one. For the ΛCDM calibration, we find $a = 52.54 \pm 0.11$, $b = -1.23 \pm 0.11$ and $\sigma^2_{\tau_{\mathrm{RT}},\mathrm{sys}} = 0.47$.

References

Abramowicz, M. A., S. Bajtlik, J.-P. Lasota, and A. Moudens (2007, June). Eppur si Espande. *Acta Astronomica 57*, 139–148. 207

Alnes, H. and M. Amarzguioui (2006). CMB anisotropies seen by an off-center observer in a spherically symmetric inhomogeneous universe. *Phys. Rev.* **D 74**, 103520. 197

Amanullah, R., C. Lidman, D. Rubin, et al. (2010). Spectra and Hubble Space Telescope Light Curves of Six Type Ia Supernovae at $0.511 < z < 1.12$ and the Union2 Compilation. *ApJ* **716**, 712–738. 48, 51, 73, 74, 75

Amati, L. (2010). The Ep,i - Eiso correlation and Fermi Gamma-Ray Bursts. arXiv:1002.2232. 117

Amati, L., C. Guidorzi, F. Frontera, M. Della Valle, F. Finelli, R. Landi, and E. Montanari (2008). Measuring the cosmological parameters with the $E_{p,i}$-E_{iso} correlation of gamma-ray bursts. *MNRAS* **391**, 577–584. 117

Arnowitt, R., S. Deser, and C. W. Misner (2008). Republication of: The dynamics of general relativity. *Gen. Relativ. Grav.* **40**, 1997–2027. 26

Astier, P., J. Guy, N. Regnault, et al. (2006). The Supernova Legacy Survey: Measurement of $\Omega_{\rm m}$, Ω_Λ and w from the First Year Data Set. *Astron. Astrophys.* **447**, 31–48. 49, 56

Band, D., J. Matteson, L. Ford, et al. (1993). BATSE observations of gamma-ray burst spectra. I - Spectral diversity. *ApJ* **413**, 281–292. 107

Barbary, K., G. Aldering, R. Amanullah, et al. (2010). The Hubble Space Telescope Cluster Supernova Survey: The Type Ia Supernova Rate in High-Redshift Galaxy Clusters. *ArXiv e-prints*. arXiv:1010.5786. 100

Barbary, K., G. Aldering, R. Amanullah, et al. (2011). The Hubble Space Telescope Cluster Supernova Survey: VI. The Volumetric Type Ia Supernova Rate. *ArXiv e-prints*. arXiv:1110.6442. 100

Behrend, J., I. A. Brown, and G. Robbers (2008). Cosmological backreaction from perturbations. *JCAP* **1**, 13–. 134

Bennett, C. L., M. Halpern, G. Hinshaw, N. Jarosik, et al. (2003). First-Year Wilkinson Microwave Anisotropy Probe (WMAP) Observations: Preliminary Maps and Basic Results. *ApJ* **148**, S1–S27. 126

Bernardi, M., M. V. Alonso, L. da Costa, et al. (2002). Redshift-Distance Survey of Early-Type Galaxies. I. The ENEARc Cluster Sample. *AJ* **123**, 2990–3017. 133

Beutler, F. et al. (2011). The 6dF Galaxy Survey: Baryon Acoustic Oscillations and the Local Hubble Constant. arXiv:1106.3366. 38, 71, 204

Bianchi, E. and C. Rovelli (2010). Why all these prejudices against a constant? arXiv:1002.3966. 8

Bilicki, M., M. Chodorowski, T. Jarrett, and G. A. Mamon (2011). Is the Two Micron All Sky Survey Clustering Dipole Convergent? *ApJ* **741**, 31. 124

Blake, C., F. Abdalla, S. Bridle, and S. Rawlings (2004). Cosmology with the SKA. *New Astron. Rev.* **48**, 1063–1077. 7

Blake, C., A. Collister, S. Bridle, and O. Lahav (2007). Cosmological baryonic and matter densities from 600000 SDSS luminous red galaxies with photometric redshifts. *MNRAS* **374**, 1527–1548. 21, 131

Blake, C., E. Kazin, F. Beutler, et al. (2011). The WiggleZ Dark Energy Survey: mapping the distance-redshift relation with baryon acoustic oscillations. *ArXiv e-prints*. arXiv:1108.2635. 131, 204

Blake, C. and J. Wall (2002, March). A velocity dipole in the distribution of radio galaxies. *Nature 416*, 150–152. 126

Blomqvist, M. and E. Mörtsell (2010). Supernovae as seen by off-center observers in a local void. *JCAP* **5**, 6. 67

Blondin, S., J. L. Prieto, F. Patat, et al. (2009). A Second Case of Variable Na I D Lines in a Highly Reddened Type Ia Supernova. *ApJ* **693**, 207. 98

Bolejko, K. and C. Hellaby (2008). The Great Attractor and the Shapley Concentration. *Gen. Relativ. Grav.* **40**, 1771–1790. 123

Brown, P. J., R. P. W. A., P. Milne, et al. (2010). The absolute magnitudes of type ia supernovae in the ultraviolet. *ApJ* **721** (2), 1608–1626. 59

Buchert, T. (2000). On average properties of inhomogeneous fluids in general relativity I: Dust cosmologies. *Gen. Relativ. Grav.* **32**, 105–125. 25, 27, 209

Bunn, E. F. and D. W. Hogg (2009). The kinematic origin of the cosmological redshift. *American Journal of Physics 77*, 688–694. 207

Butler, N. R., D. Kocevski, J. S. Bloom, and J. L. Curtis (2007). A Complete Catalog of Swift Gamma-Ray Burst Spectra and Durations: Demise of a Physical Origin for Pre-Swift High-Energy Correlations. *ApJ* **671**, 656–677. 117

Cardelli, J. A., G. C. Clayton, and J. S. Mathis (1989). The relationship between infrared, optical, and ultraviolet extinction. *ApJ* **345** (1). 53, 62, 64

Clarkson, C. and O. Umeh (2011). Is backreaction really small within concordance cosmology? *Class. Quantum Grav.* **28** (16), 164010–. 134

Coles, P. and G. F. R. Ellis (1997). *Is the Universe Open or Closed? The Density of Matter in the Universe*. Cambridge University Press. 1, 214

Colin, J., R. Mohayaee, S. Sarkar, and A. Shafieloo (2011). Probing the anisotropic local Universe and beyond with SNe Ia data. *MNRAS* **414**, 264–271. 123

Colless, M., R. P. Saglia, D. Burstein, et al. (2001). The peculiar motions of early-type galaxies in two distant regions - VII. Peculiar velocities and bulk motions. *MNRAS* **321**, 277–305. 133

Conley, A., R. G. Carlberg, J. Guy, et al. (2007). Is There Evidence for a Hubble Bubble? The Nature of Type Ia Supernova Colors and Dust in External Galaxies. *ApJ Lett.* **664**, L13–L16. 66, 203, 211

Copi, C. J., D. Huterer, D. J. Schwarz, and G. D. Starkman (2006). On the large-angle anomalies of the microwave sky. *MNRAS* **367**, 79–102. 205

Courbin, F. et al. (2010). COSMOGRAIL: the COSmological MOnitoring of GRAvItational Lenses IX. Time delays and N-body realisations of the lens in HE 0435-1223. arXiv:1009.1473. 38, 71

Courtois, H. M., Y. Hoffman, R. B. Tully, and S. Gottlober (2011). 3D Velocity and Density Reconstructions of the Local Universe with Cosmicflows-1. *ArXiv e-prints*. arXiv:1109.3856. 130, 195

da Costa, L. N., M. Bernardi, M. V. Alonso, et al. (2000). Redshift-Distance Survey of Early-Type Galaxies. I. Sample Selection, Properties, and Completeness. *AJ* **120**. 133

Dale, D. A., R. Giovanelli, M. P. Haynes, L. E. Campusano, and E. Hardy (1999). Seeking the Local Convergence Depth. V. Tully-Fisher Peculiar Velocities for 52 Abell Clusters. *AJ* **118**. 133

de Oliveira-Costa, A., M. Tegmark, M. Zaldarriaga, and A. Hamilton (2004). Significance of the largest scale CMB fluctuations in WMAP. *Phys. Rev.* **D 69**, 063516. 205

de Vaucoleurs, G. (1970). The Case for a Hierarchical Cosmology. *Science 167*(3922). 23, 131

Efstathiou, G. and M. J. Rees (1988). High-redshift quasars in the Cold Dark Matter cosmogony. *MNRAS* **230**. 23

Einstein, A. (1917). *The Principle of Relativity*, Volume 142, pp. 177. Methuen 1923, reprinted by Dover Publications. 19

Eisenstein, D. J. and W. Hu (1998). Baryonic Features in the Matter Transfer Function. *ApJ* **496**, 605. 122

Ellis, G. F. R. (1984). Relativistic cosmology - Its nature, aims and problems. In B. Bertotti, F. de Felice, & A. Pascolini (Ed.), *General Relativity and Gravitation Conference*, pp. 215–288. 29

Ellis, G. F. R. and T. Rothman (1993). Lost Horizons. *American Journal of Physics 61*(10), 883–893. 10

Ellis, G. F. R. and W. R. Stoeger (2009). The evolution of our local cosmic domain: effective causal limits. *MNRAS* **398** *398*, 1527–1536. 29

Erdoğdu, P., O. Lahav, J. P. Huchra, et al. (2006). Reconstructed density and velocity fields from the 2MASS Redshift Survey. *MNRAS* **373**, 45–64. 124

Feldman, H. A., R. Watkins, and M. J. Hudson (2010). Cosmic flows on 100 h^{-1} Mpc scales: standardized minimum variance bulk flow, shear and octupole moments. *MNRAS* **407**, 2328–2338. 150, 199

Finkelman, I., N. Brosch, A. Y. Kniazev, et al. (2008). Determining the extragalactic extinction law with SALT. *MNRAS* **390**, 969–984. 64, 96, 103, 203

Finkelman, I., N. Brosch, A. Y. Kniazev, et al. (2010). Determining the extragalactic extinction law with SALT-II. Additional sample. *MNRAS* **409**, 727–736. 64, 96, 103, 203

Fixsen, D. J., E. S. Cheng, J. M. Gales, et al. (1996). The Cosmic Microwave Background Spectrum from the Full COBE FIRAS Data Set. *ApJ* **473**, 576. 137, 139, 189

Folatelli, G., M. M. Phillips, C. R. Burns, et al. (2010). CSP: Analysis of the first sample of SNe Ia. *ApJ* **139**, 120–. 51, 96, 97, 98, 99

Francis, M. J., L. A. Barnes, J. B. James, and G. F. Lewis (2007). Expanding Space: the Root of all Evil? *Pub. Astron. Soc. Aust. 24*, 95–102. 207

Freedman, W. L., C. R. Burns, M. M. Phillips, et al. (2009). The Carnegie Supernova Project. *ApJ* **704**, 1036–1058. 51, 83, 88, 95

Freedman, W. L., B. F. Madore, B. K. Gibson, et al. (2001). Final Results from the Hubble Space Telescope Key Project to Measure the Hubble Constant. *ApJ* **553**, 47–72. 20, 68, 125, 135, 152

Freeman, P. E., C. R. Genovese, C. J. Miller, et al. (2006). Examining the Effect of the Map-making Algorithm on Observed Power Asymmetry in WMAP Data. *ApJ* **638**, 1–19. 205

Gabrielli, A., F. Sylos Labini, M. Joyce, and L. Pietronero (2005). *Statistical Physics for Cosmic Structures*. Springer. 21

Ghirlanda, G., G. Ghisellini, and C. Firmani (2006). Gamma-ray bursts as standard candles to constrain the cosmological parameters. *New Journal of Physics 8*, 123. 109, 115

Ghirlanda, G., G. Ghisellini, D. Lazzati, and C. Firmani (2004). Gamma-Ray Bursts: New Rulers to Measure the Universe. *ApJ Lett.* **613**, L13–L16. 110, 112, 115, 116

Ghirlanda, G. (2009). Advances on GRB as cosmological tools. In *Probing Stellar Populations out to the Distant Universe, AIP Conference Proceedings* **1111**, pp. 579–586. 115

Giovanelli, R., D. A. Dale, M. P. Haynes, et al. (1999). No Hubble Bubble in the Local Universe. *ApJ* **525** *525*, 25–30. 66

Giovanelli, R., M. P. Haynes, J. J. Salzer, et al. (1998). The Motions of Clusters of Galaxies and the Dipoles of the Peculiar Velocity Field. *AJ* **116**, 2632–2643. 133

Glazebrook, K., R. G. Abraham, P. J. McCarthy, et al. (2004). A high abundance of massive galaxies 3-6 billion years after the Big Bang. *Nature 430*, 181–184. 23

Goobar, A. (2008). Low R_V from Circumstellar Dust around Supernovae. *ApJ Lett.* **686**, L103. 98

Gordon, C., K. Land, and A. Slosar (2007). Cosmological Constraints from Type Ia Supernovae Peculiar Velocity Measurements. *Phys. Rev. Lett.* **99**, 081301. 199

Gordon, C., K. Land, and A. Slosar (2008). Determining the motion of the Solar system relative to the cosmic microwave background using Type Ia supernovae. *MNRAS* **387**, 371–376. 121, 191, 194, 199, 212

Guy, J. et al. (2007). SALT2: using distant supernovae to improve the use of Type Ia supernovae as distance indicators. *Astron. Astrophys.* **466**, 11. 55, 56

Guy, J., P. Astier, S. Nobili, N. Regnault, and R. Pain (2005). SALT: a spectral adaptive light curve template for type Ia supernovae. *Astron. Astrophys.* **443**. 50, 55, 56, 210

Hamuy, M., M. M. Phillips, J. Maza, N. B. Suntzeff, R. A. Schommer, and R. Aviles (1995). A Hubble diagram of distant type IA supernovae. *AJ* **109**. 47, 100

Hamuy, M., M. M. Phillips, J. Maza, N. B. Suntzeff, R. A. Schommer, and R. Aviles (1996). The Absolute Luminosities of the Calan/Tololo Type IA Supernovae. *AJ* **112**, 2391. 47

Hicken, M., W. M. Wood-Vasey, S. Blondin, et al. (2009). Improved Dark Energy Constraints from ∼100 New CfA Supernova Type Ia Light Curves. *ApJ* **700**, 1097–1140. 51, 58, 61, 66, 67, 73, 74, 75, 78, 79, 83, 89, 91, 92, 93, 95, 98, 203

Höflich, P., K. Krisciunas, A. M. Khokhlov, et al. (2010). Secondary Parameters of Type Ia Supernova Light Curves. *ApJ* **710**, 444. 100

Hogg, D. W., D. J. Eisenstein, M. R. Blanton, et al. (2005). Cosmic Homogeneity Demonstrated with Luminous Red Galaxies. *ApJ* **624**, 54–58. 21, 42, 131, 142

Hook, I. M. et al. (2005). Spectra of High-Redshift Type Ia Supernovae and a Comparison with their Low-Redshift Counterparts. *AJ* **130**, 2788–2803. 65

Howell, D. A., M. Sullivan, A. Conley, and R. Carlberg (2007). Predicted and Observed Evolution in the Mean Properties of Type Ia Supernovae with Redshift. *ApJ Lett.* **667**, L37. 100

Hoyle, F. and M. S. Vogeley (2002). Voids in the Point Source Catalogue Survey and the Updated Zwicky Catalog. *ApJ* **566**, 641–651. 21, 22

Hoyle, F. and M. S. Vogeley (2004). Voids in the 2dF Galaxy Redshift Survey. *ApJ* **607**, 751–764. 21, 22, 39, 130, 141

Huchra, J., M. Davis, D. Latham, and J. Tonry (1983). A survey of galaxy redshifts: 4. The data. *ApJ Suppl.* **52**, L89–L119. 1

Hudson, M. J., R. J. Smith, J. R. Lucey, and E. Branchini (2004). Streaming motions of galaxy clusters within 12 000 km s^{-1}- V. The peculiar velocity field. *MNRAS* **352**, 61–75. 66, 133

Hudson, M. J., R. J. Smith, J. R. Lucey, D. J. Schlegel, and R. L. Davies (1999). A Large-scale Bulk Flow of Galaxy Clusters. *ApJ Lett.* **512**. 133

Isobe, T., E. D. Feigelson, M. G. Akritas, and G. J. Babu (1990). Linear regression in astronomy. *ApJ* **364**, 104–113. 110, 215

Iwata, I. and P. Chamaraux (2011). Is the far border of the Local Void expanding? *Astron. Astrophys.* **531**, A87–. 130

Jarosik, N., C. L. Bennett, J. Dunkley, et al. (2011). Seven-year Wilkinson Microwave Anisotropy Probe (WMAP) Observations: Sky Maps, Systematic Errors, and Basic Results. *ApJ Suppl.* **192**, 14–. 11, 20

Jha, S., A. G. Riess, and R. P. Kirshner (2007). Improved distances to type Ia supernovae with multicolor light-curve shapes: MLCS2k2. *ApJ* **659**, 122–148. 49, 50, 53, 62, 66, 67, 83, 91, 120, 191, 194, 202, 203, 210, 212

Karachentsev, I. D., O. G. Kashibadze, D. I. Makarov, and R. B. Tully (2009). The Hubble flow around the Local Group. *MNRAS* **393**, 1265–1274. 29, 133

Kashlinsky, A., F. Atrio-Barandela, and H. Ebeling (2012). Measuring bulk motion of X-ray clusters via the kinematic Sunyaev-Zeldovich effect: summarizing the "dark flow" evidence and its implications. Available from: `http://www.kashlinsky.info/bulkflows/physicsreport`. 123

Kashlinsky, A., F. Atrio-Barandela, D. Kocevski, and H. Ebeling (2008). A Measurement of Large-Scale Peculiar Velocities of Clusters of Galaxies: Results and Cosmological Implications. *ApJ Lett.* **686**, L49–L52. 122, 123, 205, 206

Kashlinsky, A., F. Atrio-Barandela, D. Kocevski, and H. Ebeling (2009). A Measurement of Large-Scale Peculiar Velocities of Clusters of Galaxies: Technical Details. *ApJ* **691**, 1479–1493. 122, 123, 205, 206

Kass, R. E. and A. E. Raftery (1995). Bayes Factors. *J. Amer. Statistical Assoc.*. 114, 142, 146

Kazin, E. A., M. R. Blanton, R. Scoccimarro, et al. (2010). The Baryonic Acoustic Feature and Large-Scale Clustering in the Sloan Digital Sky Survey Luminous Red Galaxy Sample. *ApJ* **710**, 1444–1461. 21

Kelly, P. L., M. Hicken, D. L. Burke, K. S. Mandel, and R. P. Kirshner (2010). Hubble Residuals of Nearby Type Ia Supernovae are Correlated with Host Galaxy Masses. *ApJ* **715**, 743–. 101

Kessler, R., A. Becker, D. Cinabro, et al. (2009). First-year Sloan Digital Sky Survey-II Supernova Results. *ApJ Suppl.* **185**, 32–84. 9, 51, 54, 58, 60, 67, 73, 74, 75, 77, 95, 202

Kim, J. and P. Naselsky (2010). Anomalous Parity Asymmetry of the Wilkinson Microwave Anisotropy Probe Power Spectrum Data at Low Multipoles. *ApJ Lett.* **714**, L265–L267. 205

Kirshner, R. P. (2003). Hubble's diagram and cosmic expansion. *Proceedings of the National Academy of Science 101*, 8–13. 18, 19, 20

Kirshner, R. P. (2009). Foundations of Supernova Cosmology. arXiv:astro-ph/0910.0257. 4, 46, 47, 51

Kogut, A., C. Lineweaver, G. F. Smoot, et al. (1993). Dipole Anisotropy in the COBE Differential Microwave Radiometers First-Year Sky Maps. *ApJ* **419**, 1–. 126

Kolb, E. W., S. Matarrese, A. Notari, and A. Riotto (2005). Effect of inhomogeneities on the expansion rate of the universe. *Phys. Rev.* **D 71** *71*(2), 023524–. 134

Komatsu, E., K. M. Smith, J. Dunkley, et al. (2011). Seven-year Wilkinson Microwave Anisotropy Probe (WMAP) Observations: Cosmological Interpretation. *ApJ Suppl.* **192**, 18. 51, 60

Kowalski, M., D. Rubin, G. Aldering, et al. (2008). Improved cosmological constraints from new, old and combined supernova datasets. *ApJ* **686**, 749–778. 50, 56, 61, 73, 75, 79, 82

Krasinski, A. (1997). *Inhomogeneous Cosmological Models*. Cambridge University Press. 10

Kwan, J., M. J. Francis, and G. F. Lewis (2009). Fractal Bubble cosmology: a concordant cosmological model? *MNRAS* **399**, L6–L10. 71, 72, 73, 75, 76, 77, 101, 102, 210

Lampeitl, H., M. Smith, R. C. Nichol, et al. (2010). The Effect of Host Galaxies on Type Ia Supernovae in the SDSS-II Supernova Survey. *ApJ* **722**, 566–576. 95, 101, 102

Land, K. and J. Magueijo (2005). Examination of Evidence for a Preferred Axis in the Cosmic Radiation Anisotropy. *Phys. Rev. Lett.* **95**, 071301. 205

Lavaux, G., R. B. Tully, R. Mohayaee, and S. Colombi (2010). Cosmic Flow From Two Micron All-Sky Redshift Survey: the Origin of Cosmic Microwave Background Dipole and Implications for ΛCDM Cosmology. *ApJ* **709**, 483–498. 121, 124, 195

Leith, B. M., S. C. C. Ng, and D. L. Wiltshire (2007). Gravitational energy as dark energy: concordance of cosmological tests. *ApJ Lett.* **672**, L91. 31, 38, 39, 40, 42, 69, 71, 72, 73, 105, 210

Li, L.-X. (2007). Variation of the Amati relation with cosmological redshift: a selection effect or an evolution effect? *MNRAS* **379**, L55–L59. 117

Li, N. and D. J. Schwarz (2007). Onset of cosmological backreaction. *Phys. Rev.* **D 76** (8), 083011–. 43, 134

Li, N. and D. J. Schwarz (2008). Scale dependence of cosmological backreaction. *Phys. Rev.* **D 78** (8), 083531–. 70, 120, 124, 133, 136

Linder, E. V. (2006). Importance of Supernovae at $z < 0.1$ for Probing Dark Energy. *Phys. Rev.* **D 74**, 103518–. 49

Maddox, S. J., G. Efstathiou, W. J. Sutherland, and J. Loveday (1990). Galaxy correlations on large scales. *MNRAS* **242**, 43P–147P. 3

Mattsson, T. and M. Ronkainen (2008). Exploiting scale dependence in cosmological averaging. *JCAP* **2**, 4. 10

McClure, M. L. and C. C. Dyer (2007). Anisotropy in the Hubble constant as observed in the HST extragalactic distance scale key project results. *New Astron. 12*, 533–543. 125, 148

Melia, F. (2009). *High-Energy Astrophysics*. 106

Ménard, B., M. Kilbinger, and R. Scranton (2010). On the impact of intergalactic dust on cosmology with type Ia supernovae. *MNRAS* **406** (3), 1815–1920. 99

Ménard, B., R. Scranton, M. Fukugita, and G. Richards (2010). Measuring the galaxy–mass and galaxy–dust correlations through magnification and reddening. *MNRAS* **405** (2), 1025–1039. 99

Mortlock, D., S. J. Warren, B. P. Venemans, et al. (2011). A luminous quasar at a redshift of z=7.085. *Nature* ***474***, 616–619. 23

Muñoz, J. A. and A. Loeb (2008). The density contrast of the Shapley supercluster. *MNRAS* **391**, 1341–1349. 123

Nusser, A. and M. Davis (2011). The Cosmological Bulk Flow: Consistency with ΛCDM and $z \approx 0$ Constraints on σ_8 and γ. *ApJ* **736**, 93. 122

Oguri, M. (2007). Gravitational lens time delays: A statistical assessment of lens model dependencies and implications for the global Hubble constant. *ApJ* **660**, 1. 71

Osborne, S. J., D. S. Y. Mak, S. E. Church, and E. Pierpaoli (2011). Measuring the Galaxy Cluster Bulk Flow from WMAP Data. *ApJ* **737**, 98–. 123, 206

Padmanabhan, T. (1993). Structure Formation in the Universe. Book, Cambridge University Press. 7

Pan, D. C., M. S. Vogeley, F. Hoyle, Y.-Y. Choi, and C. Park (2011). Cosmic Voids in Sloan Digital Sky Survey Data Release 7. `arXiv:1103.4156`. 22, 39, 65, 130, 141

Patat, F., D. Baade, P. Höflich, et al. (2009). VLT spectropolarimetry of the fast expanding type Ia SN 2006X. *Astron. Astrophys.* **508**, 229. 98

Patat, F., P. Chandra, R. Chevalier, et al. (2007). Detection of Circumstellar Material in a Normal Type Ia Supernova. *Science 317*, 924. 98, 99

Patil, M. K., S. K. Pandey, D. K. Sahu, and A. Kembhavi (2007). Properties of dust in early-type galaxies. *Astron. Astrophys.* **461**, 103–113. 64

Peacock, J. A. (1999). *Cosmological Physics*. Cambridge University Press. 25

Peebles, P. J. E. (1993). *Principles of Physical Cosmology*. Princeton Series in Physics. 17, 125

Peebles, P. J. E. (2001). The Void Phenomenon. *ApJ* **557**, 495–504. 23

Peebles, P. J. E. and D. T. Wilkinson (1968). Comment on the anisotropy of the Primeval Fireball. *Phys. Rev.* **174**, p 2168. 126

Percival, W. J., B. A. Reid, D. J. Eisenstein, et al. (2010). Baryon acoustic oscillations in the Sloan Digital Sky Survey Data Release 7 galaxy sample. *MNRAS* **401**, 2148–2168. 204

Perlmutter, S., G. Aldering, G. Goldhaber, et al. (1999). Supernova Cosmology Project Collaboration. *ApJ* **517**, 565. 47, 48

Perlmutter, S., S. Gabi, G. Goldhaber, et al. (1997). Measurements of the Cosmological Parameters Ω and Λ from the First Seven Supernovae at $z \geq 0.35$. *ApJ* **483**, 565–581. 47

Petrosian, V., A. Bouvier, and F. Ryde (2009). Gamma-Ray Bursts as Cosmological Tools. `arXiv:0909.5051`. 115, 116

Phillips, M. M. (1993). The absolute magnitudes of Type IA supernovae. *ApJ* **413**, L105–L108. 47

Press, W. H., B. P. Flannery, S. A. Teukolsky, and W. T. Vetterling (1986). *Numerical Recipes: The Art of Scientific Computing*. Cambridge University Press. 146

Rawlings, S., F. B. Abdalla, S. L. Bridle, et al. (2004). Galaxy evolution, cosmology and dark energy with the Square Kilometer Array. *New Astron. Rev.* **48**, 1013–1027. 7

Reese, E. D., H. Kawahara, T. Kitayama, N. Ota, S. Sasaki, and Y. Suto (2010). Impact of Chandra Calibration Uncertainties on Galaxy Cluster Temperatures: Application to the Hubble Constant. *ApJ* **721**, 653–669. 71

Riess, A. G. et al. (1998). Supernova Search Team Collaboration. *AJ* **116**, 1009. 47, 53

Riess, A. G. et al. (2004). Type Ia supernova discoveries at $z > 1$ from the Hubble Space Telescope: Evidence for past deceleration and constraints on dark energy evolution. *ApJ* **607**, 665. 67, 112

Riess, A. G., W. Li, P. B. Stetson, et al. (2005). Cepheid calibrations from the hubble space telescope of the luminosity of two recent type ia supernovae and a redetermination of the hubble constant. *ApJ* **627**, 579. 69

Riess, A. G., L. Macri, S. Casertano, et al. (2011). A 3Space Telescope and Wide Field Camera 3. *ApJ* **730**, 119. 20, 38, 68, 69, 70, 204

Riess, A. G., W. H. Press, and R. P. Kirshner (1996). A precise distance indicator: Type Ia supernova multicolor light-curve shapes. *ApJ* **473**, 88. 47, 62

Riess, A. G., L. G. Strolger, S. Casertano, et al. (2007). New Hubble Space Telescope Discoveries of Type Ia Supernovae at $z = 1$: Narrowing Constraints on the Early Behavior of Dark Energy. *ApJ* **659**, 98–121. 38, 49, 50, 53, 62, 67, 69, 73, 83, 99, 106, 107

Ross, A. J., S. Ho, A. J. Cuesta, et al. (2011). Ameliorating systematic uncertainties in the angular clustering of galaxies: a study using the SDSS-III. `arXiv:1105.2320`. 131

Sandage, A. (1986). The redshift-distance relation. IX - Perturbation of the very nearby velocity field by the mass of the Local Group. *ApJ* **307**, 1–19. 29

Sandage, A. R. (1995). Practical cosmology - Inventing the Past. In A.R. Sandage, R.G. Kron, & M.G. Longair (Ed.), *The Deep Universe. SAAS-Fee Advanced Course 23, Lecture notes 1993*, pp. 2–233. Springer. 18, 19, 23

Sandage, A. R., G. A. Tammann, and E. Hardy (1972). Limits on the Local Deviation of the Universe from a Homogeneous Model. *ApJ* **172**, 253–263. 23, 131

Sandage, A. R., G. A. Tammann, A. Saha, B. Reindl, F. D. Macchetto, and N. Panagia (2006). The Hubble Constant: A Summary of the Hubble Space Telescope Program for the Luminosity Calibration of Type Ia Supernovae by Means of Cepheids. *ApJ* **653**, 843–860. 68, 69

Sari, R., T. Piran, and J. P. Halpern (1999). Jets in Gamma-Ray Bursts. *ApJ Lett.* **519**, L17–L20. 110

Scannapieco, E. and L. Bildsten (2005). The Type Ia Supernova Rate. *ApJ Lett.* **629**, L85. 100

Schaefer, B. E. (2007). The Hubble Diagram to Redshift greater than 6 from 69 Gamma-Ray Bursts. *ApJ* **660**, 16. 105, 106, 108, 109, 110, 111, 112, 211

Schaefer, B. E. (2008). talk given at Sixth Huntsville Gamma Ray Symposium, `http://grbhunstville2008.cspar.aah.edu/content/Talks/Schaefer.pdf`. 114

Schmidt, B. P., N. B. Suntzeff, M. M. Phillips, et al. (1998). The High-Z Supernova Search: Measuring Cosmic Deceleration and Global Curvature of the Universe Using Type IA Supernovae. *ApJ* **507**, 46–63. 47, 53

Schwarz, D. J., G. D. Starkman, D. Huterer, and C. J. Copi (2004). Is the Low-ℓ Microwave Background Cosmic? *Phys. Rev. Lett.* **93**, 221301. 205

Seo, H.-J., J. Eckel, D. J. Eisenstein, et al. (2010). High-precision Predictions for the Acoustic Scale in the Nonlinear Regime. *ApJ* **720**, 1650–1667. 200

Shahmoradi, A. and R. J. Nemiroff (2011). The possible impact of gamma-ray burst detector thresholds on cosmological standard candles. *MNRAS* **411**, 1843–1856. 117, 211

Shi, X. and M. S. Turner (1998). Expectations for the Difference between Local and Global Measurements of the Hubble Constant. *ApJ* **493**, 519. 141

Sinclair, B., T. M. Davis, and T. Haugbølle (2010). Residual Hubble-bubble Effects On Supernova Cosmology. *ApJ* **718**, 1445–1455. 65, 67

Smale, P. R. (2011). Gamma ray burst distances and the timescape cosmology. *MNRAS* **418**, 2779–2784. 40

Smale, P. R. and D. L. Wiltshire (2011). Supernova tests of the timescape cosmology. *MNRAS* **413**, 367–385. 40, 45, 105

Sollerman, J., E. Mörtsell, T. M. Davis, et al. (2009). First-Year Sloan Digital Sky Survey-II (SDSS-II) Supernova Results: Constraints on Nonstandard Cosmological Models. *ApJ* **703**, 1374–1385. 77

Sparke, L. S. and J. S. Gallagher (2007). *Galaxies in the universe: an introduction*. Cambridge University Press. 16, 46, 64

Springob, C. M., K. L. Masters, M. P. Haynes, R. Giovanelli, and C. Marinoni (2007). SFI++. II. A New I-Band Tully-Fisher Catalog, Derivation of Peculiar Velocities, and Data Set Properties. *ApJ Suppl.* **172**, 599–614. 133

Sullivan, M., A. Conley, D. A. Howell, et al. (2010). The dependence of Type Ia Supernovae luminosities on their host galaxies. *MNRAS* **406**, 782–802. 95, 101, 102

Sullivan, M., D. Le Borgne, C. J. Pritchet, et al. (2006). Rates and Properties of Type Ia Supernovae as a Function of Mass and Star Formation in Their Host Galaxies. *ApJ* **648**, 868. 100

Sylos Labini, F., N. L. Vasilyev, L. Pietronero, and Y. V. Baryshev (2009). Absence of self-averaging and of homogeneity in the large-scale galaxy distribution. *Europhysics Letters 864*, 49001–. 42, 131

Teerikorpi, P. (1997). Observational Selection Bias Affecting the Determination of the Extragalactic Distance Scale. *Ann. Rev. Astron. Astroph. 35*, 101–136. 15

Tegmark, M., A. de Oliveira-Costa, and A. J. Hamilton (2003). High resolution foreground cleaned CMB map from WMAP. *Phys. Rev.* **D 68** (12), 123523. 126, 197, 205

Thomas, S. A., F. B. Abdalla, and O. Lahav (2011). Excess Clustering on Large Scales in the MegaZ DR7 Photometric Redshift Survey. *Phys. Rev. Lett.* **106** *106*(24), 241301. 21, 131

Tonry, J. L., A. Dressler, J. P. Blakeslee, et al. (2001). The SBF Survey of Galaxy Distances. IV. SBF Magnitudes, Colors, and Distances. *ApJ* **546**, 681–693. 133

Tonry, J. L., B. P. Schmidt, B. Barris, et al. (2003). Cosmological Results from High-z Supernovae. *ApJ* **594**, 1–24. 133, 195

Trotta, R. (2008). Bayes in the sky: Bayesian inference and model selection in cosmology. *Contemporary Physics* ***49***(2), 71–104. 81, 85

Tully, R. B., E. J. Shaya, I. D. Karachentsev, H. M. Courtois, D. D. Kocevski, L. Rizzi, and A. Peel (2008). Our Peculiar Motion Away from the Local Void. *ApJ* **676**, 184. 24, 65, 121, 127, 128, 129, 130, 140, 182, 183, 184, 189, 195

Turnbull, S. J., M. J. Hudson, H. A. Feldman, et al. (2011). Cosmic flows in the nearby universe from Type Ia supernovae. `arXiv:1111.0631`. 122, 123, 204, 206

Umeh, O., J. Larena, and C. Clarkson (2011). The Hubble rate in averaged cosmology. *JCAP* **3**, 29–+. 134

van Putten, M. (2009). Cosmological flashes from rotating black holes. In D. Wiltshire, M. Visser, and S. Scott (Eds.), *The Kerr Spacetime: Rotating Black Holes in General Relativity. Cambridge University Press*, pp. 281–308. 107

Wald, R. M. (1984). *General Relativity*. The University of Chicago Press. 2, 7, 26

Wang, H., H. J. Mo, X. Yang, and F. C. van den Bosch (2011). Reconstructing the Cosmic Velocity and Tidal Fields with Galaxy Groups Selected from the Sloan Digital Sky Survey. `arXiv:1108.1008`. 123

Wang, X. et al. (2009). Improved Distances to Type Ia Supernovae with Two Spectroscopic Subclasses. *ApJ Lett.* **699**, L139. 97, 98, 102

Wang, X., W. Li, A. V. Filippenko, et al. (2008a). Optical and Near-Infrared Observations of the Highly Reddened, Rapidly Expanding Type Ia Supernova 2006X in M100. *ApJ* **675**, 626. 98

Wang, X., W. Li, A. V. Filippenko, et al. (2008b). The Detection of a Light Echo from the Type Ia Supernova 2006X in M100. *ApJ* **677**, 1060. 98

Wang, X., L. Wang, A. V. Filippenko, G. Aldering, P. Antilogus, et al. (2011). Evidence for Type Ia Supernova Diversity from Ultraviolet Observations with the Hubble Space Telescope. arXiv:1110.5809. 59

Watkins, R., H. A. Feldman, and M. J. Hudson (2009). Consistently large cosmic flows on scales of 100 h^{-1}Mpc: a challenge for the standard ΛCDM cosmology. *MNRAS* **392**, 743–756. 120, 122, 132, 133, 150, 152, 199, 212

Waxman, E., S. R. Kulkarni, and D. A. Frail (1998). Implications of the Radio Afterglow from the Gamma-Ray Burst of 1997 May 8. *ApJ* **497**, 288. 106

Wegner, G., M. Bernardi, C. N. A. Willmer, et al. (2003). Redshift-Distance Survey of Early-Type Galaxies: Spectroscopic Data. *AJ* **126**, 2268–2280. 133

Wiegand, A. and D. J. Schwarz (2011). Inhomogeneity-induced variance of cosmological parameters. *ArXiv e-prints*. arXiv:1109.4142. 125

Willick, J. A. (1999). The Las Campanas Observatory/Palomar 10,000 Kilometer per Second Cluster Survey. II. Constraints on Large-Scale Streaming. *ApJ* **522**, 647–660. 133

Wiltshire, D. L. (2005). Viable inhomogeneous model universe without dark energy from primordial inflation. arXiv:0503099. 25

Wiltshire, D. L. (2007). Cosmic clocks, cosmic variance and cosmic averages. *New J. Phys* ***9***(377), 1–66. 5, 23, 24, 29, 134

Wiltshire, D. L. (2007). Exact Solution to the Averaging Problem in Cosmology. *Phys. Rev. Lett.* **99** (25), 251101. 37, 40

Wiltshire, D. L. (2008). Cosmological equivalence principle and the weak-field limit. *Phys. Rev.* **D 78** (8), 084032. 22, 24, 30, 82

Wiltshire, D. L. (2009). Average observational quantities in the timescape cosmology. *Phys. Rev.* **D 80** (12), 123512. 37, 42, 103, 106, 107

Wiltshire, D. L. (2011). What is dust? - Physical foundations of the averaging problem in cosmology. arXiv:1106.1693. 27, 28

Wiltshire, D. L., P. R. Smale, T. Mattsson, and R. Watkins (2012). Hubble flow variance and the cosmic rest frame. arXiv:1201.5371. 119

Wood-Vasey, W. M., G. Miknaitis, C. W. Stubbs, et al. (2007). Observational constraints on the nature of dark energy: First cosmological results from the ESSENCE supernova survey. *ApJ* **666**, 694–715. 9, 49, 58, 59, 62, 63

Yahil, A., G. A. Tammann, and A. Sandage (1977). The Local Group - The solar motion relative to its centroid. *ApJ* **217**, 903–915. 128

Zehavi, I., A. G. Riess, R. P. Kirshner, and A. Dekel (1998). A Local Hubble Bubble from Type IA Supernovae? *ApJ* **503** *503*, 483–+. 50, 66, 202, 203

Zhang, B.-B., B. Zhang, E.-W. Liang, et al. (2011). A Comprehensive Analysis of Fermi Gamma-ray Burst Data. I. Spectral Components and the Possible Physical Origins of LAT/GBM GRBs. *ApJ* **730**, 141. 109

Zhang, P. and A. Stebbins (2011). Confirmation of the Copernican Principle at Gpc Radial Scale and above from the Kinetic Sunyaev-Zel'dovich Effect Power Spectrum. *Phys. Rev. Lett.* **107** (4), 041301. 67

Zibin, J. P. and A. Moss (2011). Linear kinetic Sunyaev-Zel'dovich effect and void models for acceleration. *Class. Quantum Grav.* **28** (16), 164005. 131